Memòria presentada per a l'obtenció del grau de doctor

Programa de Doctorat en Ciència de Materials

Controlling Vortex Pinning and Dynamics of Nanostructured YBCO Thin Films Grown by Chemical Solution Deposition

Víctor Rouco Gómez

Gener 2014

Direcció

Dra. Anna Palau Masoliver

Prof. Teresa Puig Molina

Tutoria

Prof. Jordi Sort Viñas

Universitat Autònoma de Barcelona

Departament de Física, Facultat de Ciències

Institut de Ciència de Materials de Barcelona ICMAB-CSIC

Departament de Materials Superconductors i Nanoestructuració a Gran Escala

Anna Palau Masoliver, Científica Titular a l'Insitut de Ciència de Materials de Barcelona, **Teresa Puig Molina**, Professora d'investigació a l'Insitut de Ciència de Materials de Barcelona, i **Jordi Sort Viñas**, Professor d'investigació ICREA a la Universitat Autònoma de Barcelona

CERTIFIQUEN

que en Víctor Rouco Gómez, Llicenciat en Física, ha dut a terme sota la seva direcció el treball que porta per títol "Controlling Vortex Pinning and Dynamics of Nanostructured YBCO Thin Films Grown by Chemical Solution Deposition" i queda recollit en aquesta memòria per optar al Grau de Doctor en Ciència de Materials.

I per a que així consti, signen el present certificat.

Dra. Anna Palau Masoliver Prof. Teresa Puig Molina Prof. Jordi Sort Viñas

Llic. Víctor Rouco Gómez

Bellaterra, Gener 2014

Contents

Acknowledgments **1**

Motivation **3**

1. Introduction to Superconductivity **5**
1.1. High Temperature Superconductors: $YBa_2Cu_3O_{7-x}$ . . . 8
1.1.1. Laminar Anisotropy in HTS . . . 9
1.2. Vortex Matter in HTS . . . 11
1.2.1. The Irreversibility Line . . . 12
1.2.2. Vortex Pinning . . . 13
1.2.3. The Bean Critical State Model . . . 15
1.3. Thermally Activated Vortex Motion . . . 18

2. Sample growth, electrical contacts and characterization techniques **23**
2.1. Growth of YBCO thin films . . . 23
2.2. Artificial nanostructure in YBCO thin films . . . 24
2.2.1. In-situ nanocomposites . . . 25
2.2.2. Focused Ion Bean nanostructures . . . 25
2.2.3. Focused Electron Beam nanostructures . . . 26
2.2.4. Focused Electron Beam Induced Deposition nanostructures . . . 27
2.3. Physical characterization of nanostructured films . . . 27
2.3.1. Inductive measurements . . . 28
2.3.2. Electrical Transport measurements . . . 30
2.3.3. Bitter Decoration experiments . . . 37

3. Vortex pinning in CSD-YBCO/BYTO nanocomposite thin films **39**
3.1. State of the art . . . 39
3.2. Nanostructural defects . . . 40
3.2.1. Stacking faults along the ab-plane . . . 40
3.2.2. Twin boundaries along the c-axis . . . 43
3.3. Study of the irreversibility line and effective anisotropy . . . 45
3.4. Study of the upper critical field and intrinsic anisotropy . . . 49
3.5. Study of J_c angular dependence . . . 51
3.6. Study of J_c with applied magnetic field parallel to the c-axis . . . 55
3.6.1. Magnetic field dependence of $J_c(H_a||c)$ . . . 55
3.6.2. Temperature dependence of $J_c(H_a||c)$ . . . 58
3.7. Role of nanostrain in vortex pinning . . . 61
3.8. Role of twin boundaries in vortex pinning . . . 63
3.8.1. Role of twin boundaries in YBCO/LAO pristine films . . . 64

3.8.2. Role of twin boundaries in YBCO/CeO_2 buffered films 67
3.8.3. Role of twin boundaries in YBCO nanocomposite films 68
3.9. Study of the magnetic flux relaxation 69
3.10. Conclusions 73

4. YBCO thin films patterned with assymetric arrays 75
4.1. State of the art 75
4.2. Experimental ratchet effect in asymmetric pinning potentials 76
4.2.1. Ratchet effect in FIB patterns 77
4.2.2. Ratchet effect in FEBL patterns 81
4.3. Vortex motion in ratchet systems 82
4.3.1. Evaluation of the field dependence on the ratchet effect 84
4.3.2. Evaluation of the temperature dependence on the ratchet effect . . 85
4.3.3. Role of the patterned array geometry on the ratchet effect 86
4.3.4. Dynamic differences between direct and reversal ratchet effect: H_a and T dependences 92
4.4. Conclusions 95

5. YBCO thin films patterned with Cobalt nanorods 97
5.1. State of the art 97
5.2. Patterning of ferromagnetic nanostructures 98
5.3. Magnetic characterization of one single Co-nanorod 99
5.4. Hysteretic effect on the irreversibility line of hybrid systems 100
5.5. Hysteretic effect on J_c of hybrid systems 103
5.6. Return magnetic fields of hybrid systems 108
5.6.1. Hysteretic J_c behavior as a function of H_{mag} 108
5.6.2. Hysteretic J_c behavior as a function of the initial magnetic state . . 111
5.6.3. Hysteretic J_c behavior as a function of temperature 116
5.7. Conclusions 118

General conclusions 121

A. Analytical simulation of the hysteretic $J_c(H_a)$ in a strip with antidots 125

Bibliography 129

Nomenclature 145

Acknowledgments

I would like to say that the work described in this thesis would not have been possible without the help, knowledge and friendship of several people:

First of all, I would like to express my deep gratitude to my supervisors: Dra. Anna Palau and Prof. Teresa Puig. I would like to thank them for all the time and discussions dedicated to this work, for all the opportunities and advices that they have given to me and specially, for having always their o ce doors opened when I needed.

Very special acknowledgments again to Prof. Teresa Puig and Prof. Xavier Obradors for bringing me the opportunity of realize this work and form part of the Superconducting materials group.

Obviously, I would like to thank to the "Consejo Superior de Investigaciones Cientificas" ($CSIC$) for the JAE-fellowship and for bringing me the opportunities of visiting two different foreign centers by means of short term stays. On the other hand, these work would have not been possible without the financial support of the projects: $MAT2008-01022$ (Superconductores nanoestructurados basados en deposición de soluciones químicas para aplicaciones energéticas), $NESPA$, $EUROTAPES$, $MAT2011-28874-SENY$ (Strain engineered nanostructures for effective cost-performance $YBCO$ coated conductors), $Xarmae$ and $SGR770$ projects.

I give thanks to Dr. Javier E. Villegas for all the facilities, discussions and friendship that he gave me during my stay in "Centre National de la Recherche Scientifique" ($CNRS$-$THALES$).

Also to Dr. Leonardo Civale for all the time that he dedicated to me and for the profitable scientific discussions that we held during my stay in "Los Alamos National Laboratory" ($LANL$). To Dr. Boris Maiorov for his friendliness, and for his help in the ultra-high magnetic field experiments at "National High Magnetic Field Laboratory" ($NHMFL$-$LANL$) during the same stay.

Special thanks to Dra. Rosa Córdoba and Prof. José María de Teresa from "Instituto de Nanociencia de Aragón" (INA) for the growth and $MOKE$-characterization of Co-nanorods appearing in chapter 5. Regarding this last issue, I give thanks also to Dr. Rafael Morales from "Ikerbasque Foundation" for the same $MOKE$-measurements.

Thanks also to Dr. Guillem Vía, Dra. Nuria del Valle, Dr. Carles Navau and Prof. Àlvar Sànchez from "Universitat Autònoma de Barcelona" (UAB) for the theoretical simulations and the deeply discussions that we shared in order to understand our model systems.

I am also very grateful to Dr. Roger Guzmán, Dr. Jaume Gàzquez and Dr. Jordi Arbiol for the TEM measurements, analyses and discussions about the microstructural defects in $YBCO$.

Also thanks to Shuai Ye, Paula Garcés, Pablo Callado and Dra. Mariona Coll for the growth and structural analyses of the $YBCO/BYTO$ nanocomposites studied in chapter 3.

Thanks to Xavier Palmer and Victor Rodriguez for the precursor $YBCO$ solution preparation and for helping me when I need something at the laboratory.

I want to acknowledge also the $ICMAB$ technicians: Bernat Bozzo ($PPMS$ and $SQUID$), Edgar León, Neus Romà and Enrique Irisarri (Clean Room Facilities), Judith Oró and Anna Esther Carrillo (SEM) and Andrés Gómez and Maite Simón (AFM) for all their work and friendliness.

A very special thank to Dr. Roberto Luccas for teaching me the Bitter Decoration technique and for the useful discussions that we had about the physics and the things that it involves.

Also, a very deeply acknowledgment to Dr. Carlos Montón for being my instructor during the firsts months that I was at $ICMAB$ before finishing the Physics degree. For their patient, friendship and friendliness.

A toda la gente que ha pasado por el despacho; por el buen rollo que siempre ha habido: Adrián, Aziz, Coco, David, Ferrán, Josh, Juan Carlos, Macià, María, Marta, Mateusz, Ondrej y Roberto.

Como no, a tod@s l@s compañer@s pasados y presentes del $ICMAB$, en especial al grupo de superconductividad, por haber hecho del Instituto un lugar muy agradable en el que trabajar (no nombro a tod@s porqué la lista podría ser enorme y me saldría muy cara la impresión de la tesis).

A la Bea, la Candela, el Dani, el Dano, el Fran, el Javito, el Jonish, el Karlangas, la María, la Marta, la Natalia, el Negro, el Pau, el Primo, el Ramón, la Sandra, el Solis y el Vecino (los colegas los del barrio) por todas nuestras reuniones semanales y en especial por la bienvenida que tuve cuando volví de Los Alamos. Sobre todo a la Bea, por haber soportado convivir conmigo este último año.

Al Ferrán, al Juan, al Miguel, al Pol y al Sergio (los colegas de la UB) por el interés en mi trabajo y las ganas de seguir viéndonos después de tanto tiempo.

Obviamente, agradecer a mi familia más cercana toda la preocupación porque las cosas siempre me fueran bien.

A tots vosaltres, moltes gràcies!

Motivation

Since the discovery of high-temperature superconductors (HTS) in 1986, a huge effort has been devoted in order to optimize the electric power properties of these materials. The possibility to achieve the superconducting state using liquid nitrogen, rather than liquid helium required for conventional low-temperature superconductors (LTS), makes these materials much more attractive for technological applications due to their reduced operating costs. Consequently, HTS allows offering performance advantages to electric power devices such an increase of the e ciency in the generation, transmission, distribution and storage of energy.

On the other hand, HTS materials have been deeply studied in the field of electronics. In particular, HTS nanowires can be functionally scaled to smaller sizes due to their extremely short intrinsic lengths. Furthermore, their characteristic fast relaxation rates offer higher counting rates in photodetection experiments when compared to LTS.

One of the most important issues to take into account in the study of HTS, is the presence of quantified magnetic flux lines, referred as vortex, into their phase diagram. It became apparent that the vortex dynamics in HTS was quite different from that of LTS. Among the non-conventional characteristics that were early identified are: the large drop of the critical current density with temperature; the existence of an "irreversibility line" in the $H-T$ phase diagram above which the critical current density is zero and the magnetic response is reversible; and the very fast time relaxation of the persistent currents in the irreversibility regime (orders of magnitude faster than in low temperature superconductors). Is why thousands of reports and researches have been focused in the study of the new vortex matter present in HTS strongly influenced by thermal fluctuations.

The ceramic $YBa_2Cu_3O_{7-x}$ ($YBCO$) is the HTS that presents the widest working temperature range and therefore, the best candidate towards these applications. On the other hand, the chemical solution deposited (CSD) methodology used at $ICMAB$'s group to grow films of this material, allows reducing the production costs making it much more attractive to large scale applications.

One of the strong possibilities to the understanding of vortex matter in $YBCO$ is through the nanostructuration of the material. With that, new vortex-defect interactions are emerged and consequently, an enormous control on the vortex dynamics and the pinning energies can be obtained. In this thesis, different examples of nanostructurated $YBCO-CSD$ will be presented in *chapters* 3, 4 and 5.

Previously to these analyses, in *chapter* 1 we will present the main properties of superconductors, and in particular, those concerning vortex pinning in $YBCO-CSD$ thin films. In *chapter* 2, the different experimental techniques used in the next chapters to study and nanostructurate our material will be exposed.

In *chapter* 3 we will present the results obtained in $YBCO-CSD$ thin films where a chemical nanostructuration is performed. It consists of the spontaneous segregation of non-superconducting nanoparticles into the $YBCO$ matrix resulting in a new pinning landscape which strongly enhance J_c and reduces its anisotropy [1]. Our aim is to understand the mechanism controlling the interaction between vortices and defects in these films in order to optimize their critical current density behavior.

On the other hand, exploring ways to control the motion of vortices has turned out to be useful for the understanding of vortex physics, for the improvement of existing superconducting devices, and for the development of innovative fluxtronic devices that employ vortices instead of electrons [2]. In particular, a new generation of solid-state devices can be achieved by exploiting the manipulation of flux quanta, such as flux pumps, vortex diodes, and lenses to concentrate magnetic flux [3]. Thus, many experiments involving patterned thin films with arrays of dots or antidots have been developed in order to control the strength and location of the pinning centers for tuning vortex motion [4–9]. However, most of these works have concentrated in LTS although the study of this subject with HTS as also acquired interest specially regarding the asymmetric motion of vortex matter [10]. In *chapters* 4 and 5 we have devoted strong effort in understanding vortex matter in patterned $YBCO-HTS$ films grown by CSD. We present two different studies with the aim of analyzing vortex dynamics in model system with specially designed pinning centers. In *chapter* 4, directed transport at the nanoscale has been explored by using asymmetric pinning potentials, able to induce guided vortex ratchets effects. In *chapter* 5, vortex dynamics has been modified by inserting ferromagnetic nanostructures in previouly pattern films with antidots and therefore, ferromagnetic/superconductor interactions are studied in a model HTS hybrid system.

Finally, the general conclusions of the present work are summarized.

In the appendix, the analytical procedure of a simulation presented in *chapter* 5 is presented.

1. Introduction to Superconductivity

Superconductivity was discovered in 1911 by H. Kamerling Onnes in Leiden (Holland) 3 years after he liquefied helium for first time at the temperature of $4.2K$, giving him the refrigeration technique required to reach temperatures of a few degrees Kelvin. He measured the mercury resistivity at low temperatures and observed that at $4.15K$, the resistivity dropped to zero since the material became superconductor, avoiding the electrical resistance (perfect conductivity). The temperature at which the superconducting materials make this transition is known as critical temperature, T_c. According to the microscopic theory proposed by Bardeen, Cooper and Schiffer in 1957, (the BCS theory) [11], in the superconducting state, electrons are coupled forming Cooper pairs which, behaving as bosons, fall into the ground state forming a bose condensate. Cooper pairs are energetically coupled together in the presence of a weak attractive interaction mediated by the lattice (electron-phonon interaction). The movement of the pairs is coherent, and does not dissipate energy. Thus the system behaves as a superfluid.

In 1933 Meissner and Ochsenfeld discovered the second most important property of the superconductors, which is based on the exclusion of magnetic flux from the superconductor at temperatures below T_c (perfect diamagnetism or Meissner effect). This magnetic field expulsion is produced by supercurrents circulating at the surface of the sample which are able to screen the external magnetic field that drops exponentially within the superconductor.

In 1950 Gindburg and Landau developed a very successful phenomenological theory to explain the superconductivity phenomena by applying general principles of second order phase transitions to the superconducting transitions under applied magnetic fields. Depending on the contribution of the boundary energy between normal and superconducting regions to the total system energy, superconductors can be separated analytically in type I and type II. If this boundary energy is positive, the superconductor is type I, and type II if it is negative [12]. The sign of the normal-superconductor interface energy depends on the relative values of and . is the penetration depth where the magnetic field drops exponentitally from its applied value at the outside, to zero inside the superconductor. The other characteristic distance, , called the coherence length, is the distance over which the density of Cooper pairs, n_c (also known as order parameter), changes from 0 to its maximum (see Fig. 1.1).

The two lengths present the same temperature dependence provided by the relation [13]:

$$(T), \ \ (T) \propto (1 - T/T_c)^{-1\ 2} \tag{1.1}$$

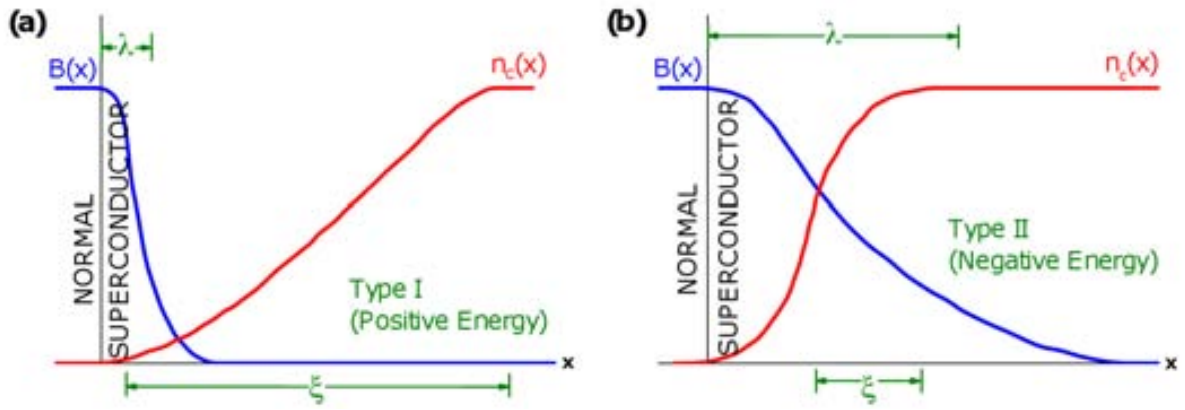

Figure 1.1.: Schematic representation of the coherence length and penetration depth in the boundary between a normal region and a **(a)** type I and **(b)** type II superconducting regions.

and their ratio:

$$= - \tag{1.2}$$

is the so called Ginzburg-Landau parameter, which distinguish between type I ($< 1/\ \overline{2}$) and type II ($> 1/\ \overline{2}$) superconductors.

Type I and type II superconductors can be also distinguished depending on how the magnetic field penetrates into the superconductor. In type I superconductors, magnetic flux is totally excluded from the material (Meissner State) for external magnetic fields below the critical field, H_c. For external magnetic fields higher than H_c, the material becomes normal, and superconductivity disappears (see Fig. 1.2$-a$). In type II superconductors, the Meissner state occurs when the external magnetic field is below the lower critical field, H_{c1}. For fields between H_{c1} and the upper critical field, H_{c2}, the magnetic flux penetrates into the superconductor. In this region, called the mixed state, the magnetic field penetrates forming quantized cylindrical flux lines called vortices. For magnetic fields higher than H_{c2} the material becomes normal (see Fig. 1.2$-b$).

Vortices have a normal core of radius where the density of Cooper pairs, n_c, is null. The normal core is surrounded by a region of larger radius, , where superconducting currents are flowing generating a flux quantum of $\Phi_0 = 2.07 \cdot 10^{-15} Tm^2$. Fig. 1.3$-a$ shows a schematic representation of a vortex, where the magnetic field profile, $B(r)$ and $n_c(r)$ are shown. In order to minimize the system total energy, in the lack of defects, vortex arrange in a regular array forming a triangular (or hexagonal) lattice, known as the Abrikosov lattice (see Fig. 1.3$-b$, [14]).

A second division of superconducting materials can be done regarding their critical temperature, where they can be classified as Low Critical Temperature Superconductors (LTS) and High Critical Temperature Superconductors (HTS). In LTS, also known as conventional superconductors, charge carriers are coupled via electron-phonon interaction, and they are fully described by the BCS theory. However, in HTS, the interaction

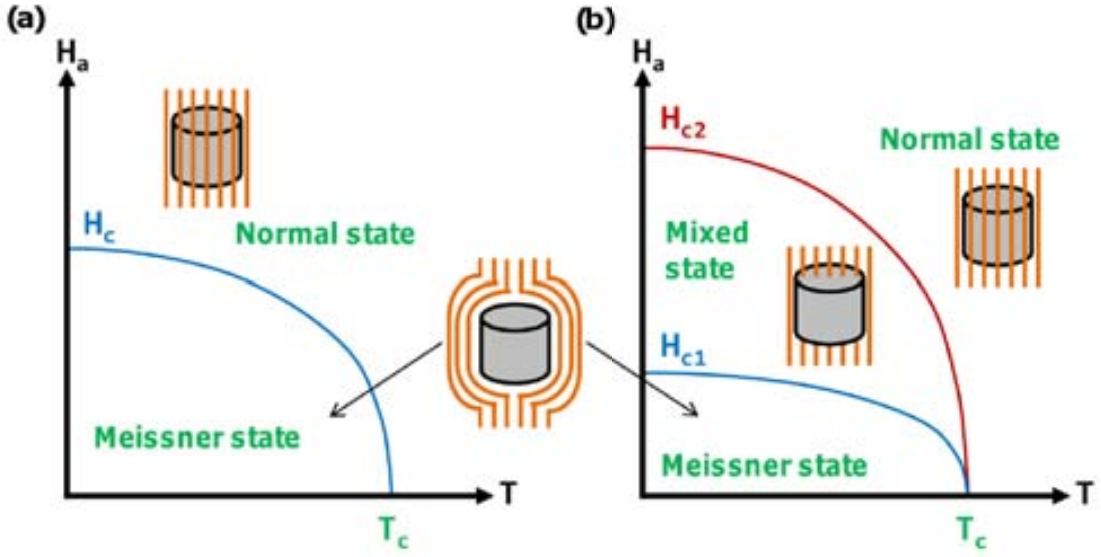

Figure 1.2.: Magnetic phase diagrams of a **(a)** type I and **(b)** type II superconductors.

between charge carriers and phonons cannot explain the large energies needed to break the Cooper pairs, and as a consequence, other mechanisms promoting their formation are required. Since the discovery of the first high temperature superconductor in 1986, $(La, Ba)_2Cu_4$ with $T_c = 37K$ [15], the search for the origin of charge attraction in HTS has been one of the main items. Although, different theories have been proposed, the formation of Cooper pairs in HTS is still an open issue until now.

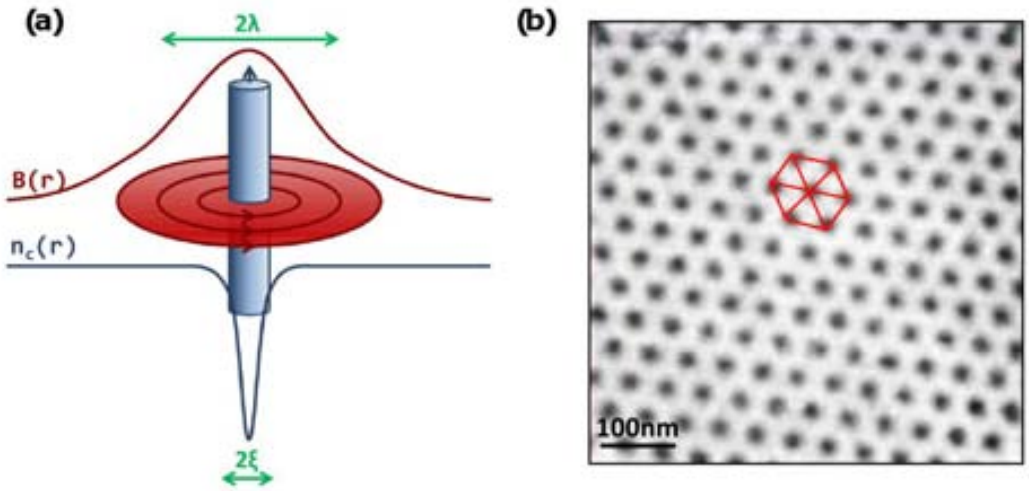

Figure 1.3.: **(a)** Schematic representation of a vortex formed by a normal core and surrounding supercurrents. **(b)** Scanning Tunneling Microscopy image of vortices in a type II superconductor showing the hexagonal lattice [14].

1.1. High Temperature Superconductors: $YBa_2Cu_3O_{7-x}$

The discovery of high temperature superconductors by Bednorz and Müller opened a new area for superconductivity applications since cooling to cryogenic temperatures is one of the critical factors for the use of superconductors. HTS are mostly ceramic cuprate compounds with transition temperatures close to $100K$. Up to now, all discovered HTS are type II, which means that the phase diagram is governed by the presence of vortices.

One of the most relevant technological HTS, and the one studied in this thesis, is $YBa_2Cu_3O_{7-x}$ $(YBCO)$ which presents a critical temperature of $92K$. This temperature is high enough to use liquid nitrogen as a refrigerant, making easy its technological applications.

The crystallographic structure of the superconducting $YBCO$ phase is a triple perovskite with an orthorhombic symmetry. Fig. 1.4 shows a schematic representation of its structure, where the different crystallographic axes are indicated. The structure is formed by a succession of CuO_2 planes lying normal to the c-axis. These planes are the superconducting planes, which contain mobile charge carriers, and there is where supercurrents flow. The maximum current density that can flow in the superconductor without dissipation is known as critical current density, J_c. CuO_2 planes are separated by charge-reservoir interleaved layers which contain CuO chains. In particular, these charge reservoir layers are the responsible of a proper carrier density in the superconducting CuO_2 planes.

In $YBCO$ the superconductivity is controlled by the oxygen content in the material, determining the carrier density in the CuO_2 planes and modifying the final $YBCO$ critical temperature, Fig. 1.5, [16].

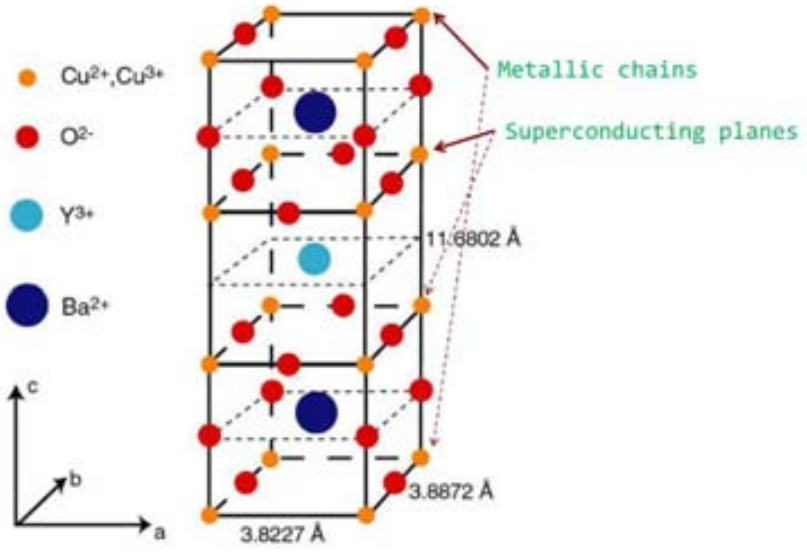

Figure 1.4.: Crystallographic structure of $YBCO$ where different lattice parameters are indicated.

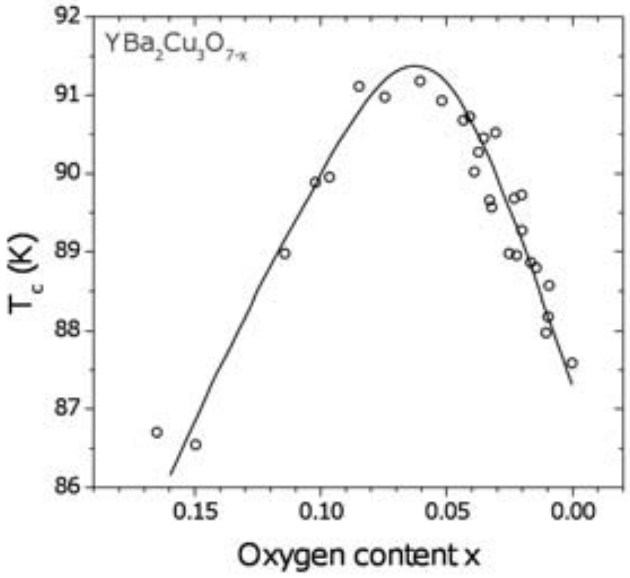

Figure 1.5.: Critical temperature of $YBCO$ as a function of the oxygen content x, [16].

As a consequence of the planar structure of $YBCO$, it presents anisotropic properties. The critical current density parallel to the CuO_2 planes (ab-planes), J_c^{ab}, is much higher than that flowing through the c-axis, J_c^c. That is the reason for which in a $YBCO$ superconductor the current should be applied parallel to the ab-planes to reach their maximum value in technological applications. Therefore, in a $YBCO$ thin film, the material should be grown highly epitaxial with the c-axis normal to the substrate.

1.1.1. Laminar Anisotropy in HTS

The anisotropy derived from the layered structure of $YBCO$ is reflected by a directional dependence of both, and . It means that the vortex structure will depend on the relative magnetic orientation with respect to the crystallographic axes of the material. As

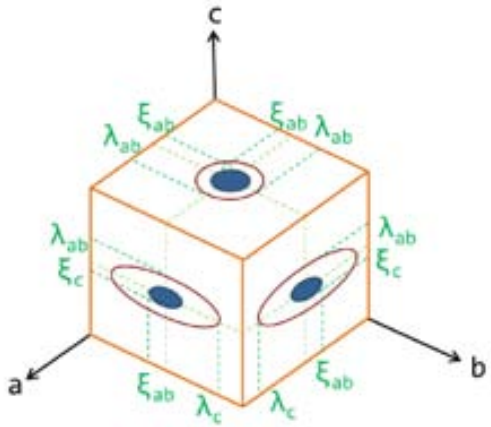

Figure 1.6.: Coherence length and penetration depth along the different crystallographic axis in an anisotropic superconductor where a b. .

a consequence, different characteristic and parameters for the vortex should be defined. Regarding the coherence length, the vortex core radius is defined by the parameters $_{ab}$ and $_{c}$ when the core is parallel to CuO_2 planes or along the c-axis, respectively. On the other hand, $_{ab}$ and $_{c}$ are the penetration depths for supercurrents flowing parallel to the ab-plane and the c-axis respectively. These different parameters are illustrated in Fig. 1.6, and indicated in Tab. 1.1 at 0K [12].

YBCO (T=0K)	**c**	**ab**
(nm)	890	135
(nm)	0.24	1.6

Table 1.1.: Coherence length and penetration depth for $YBCO$ at $T = 0K$.

In cuprates, the anisotropy is directly related with the separation between CuO_2 planes (parameter d, in Fig. 1.7) and therefore, to the electronic coupling between them. In the case of Bi, Tl and Hg cuprates compounds, where this separation is much larger than 2 $_{c}$, the vortex is broken in the so called "pancake vortices" and a 2-dimensional approximation of the flux line should be used, see Fig. 1.7$-a$. In the case of $YBCO$, the order parameter along the c-axis is not fully suppressed due to the metallic behavior of the charge-reservoir interleaved layers (CuO chains) situated between the superconducting CuO_2 planes. Consequently, in that case, vortices can be described with a 3-dimensional approximation, see Fig. 1.7$-b$.

To determine the anisotropy of a HTS, it is very useful to use the anisotropic parame-

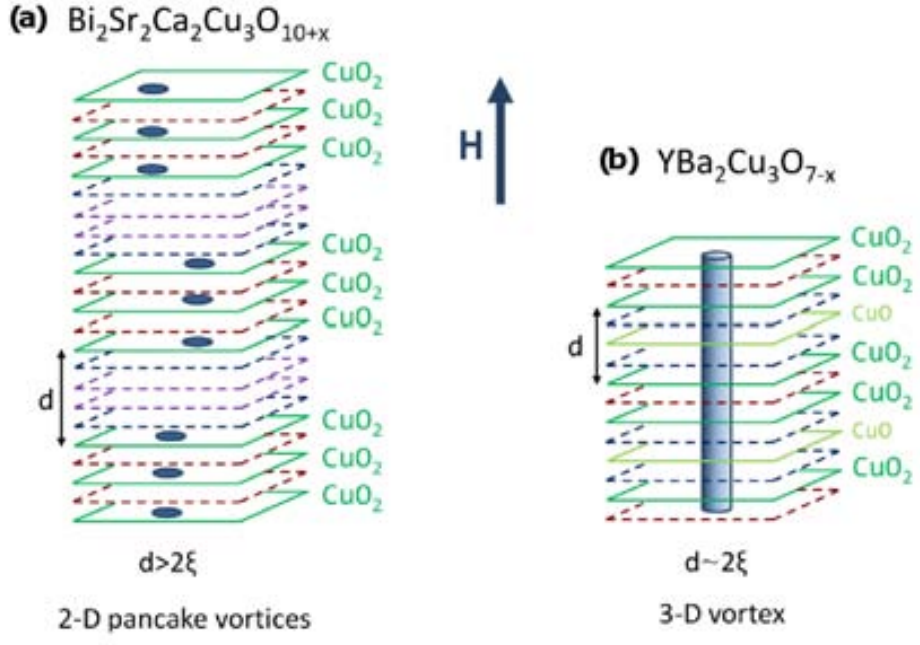

Figure 1.7.: **(a)** Scheme of a $2-D$ ux line structure in $Bi_2Sr_2Ca_2Cu_3O_{10+x}$. **(b)** Scheme of a $3-D$ ux line in $YBa_2Cu_3O_{7-x}$.

ter, , proportional to the mass anisotropy ratio along the two crystallographic directions:

$$= \quad \overline{\frac{m_c}{m_{ab}}} = \frac{c}{ab} = \frac{ab}{c} \tag{1.3}$$

Due to the layered structure of the superconducting cuprates, the value of is always greater than unity since $m_c > m_{ab}$. In the case of Bi-compounds, where the $2-D$ approximation is used due to their large value of d, achieves values between $50-200$ [17]. In contrast, in $YBCO$, the value of is between $5-7$, being one of the lowest anisotropic superconducting cuprate. According to the Gindburg-Landau approximation (which can be used for $YBCO$ due to its $3-D$ behavior), different superconducting parameters (as the critical field or the critical current density) can be scaled into an isotropic contribution by using the angular dependence of an anisotropic factor, $\varepsilon(\theta)$, proposed by Blatter [18]:

$$\varepsilon(\theta) = \quad \overline{cos^2(\theta) + \frac{1}{2} sin^2(\theta)} \tag{1.4}$$

where θ is the angle between the magnetic field and the crystallographic c-axis.

1.2. Vortex Matter in HTS

Since the discovery of HTS, vortex matter physics has called the attention of researchers in many fields due to the role of vortices in the major part of the HTS phase diagram. Different phases are observed in the mixed state of HTS, induced by the interplay of vortex-vortex interactions, thermal fluctuations, different kind of disorder and the anisotropic behavior [13]. However, the main characteristic of a type II superconductor phase diagram, and specially in HTS, is the existence of two different states: a magnetically irreversible zero-resistance state, called vortex solid phase, and a reversible state with dissipative transport properties, called vortex liquid state [19]. In the absence of disorder, as in clean systems free of defects, the solid phase presents topological order (forming the Abrikosov lattice), and it is separated from the liquid phase, by a first order transition (melting line) [13]. In samples containing disorder (defects), a second order transition (irreversibility line) is found between the solid and liquid phases [20, 21]. Moreover, various glassy vortex states have been suggested for this solid state.

In $YBCO$, a variety of disordered vortex solid states have been proposed, depending on the type and dimensionality of the defects. In the presence of isotropic weak random point disorder, like impurities, oxygen vacancies or electron irradiation, a vortex glass phase has been predicted [20]. In contrast, in the presence of correlated disorder, such as dimensional columnar defects, amorphous defects induced by heavy ion irradiation or $2-D$ planar defects as twin boundaries, a Bose glass phase is expected [22, 23]. These different solid phases are present in Fig. 1.8 where a schematic illustration of a typical $YBCO$ phase diagram is displayed.

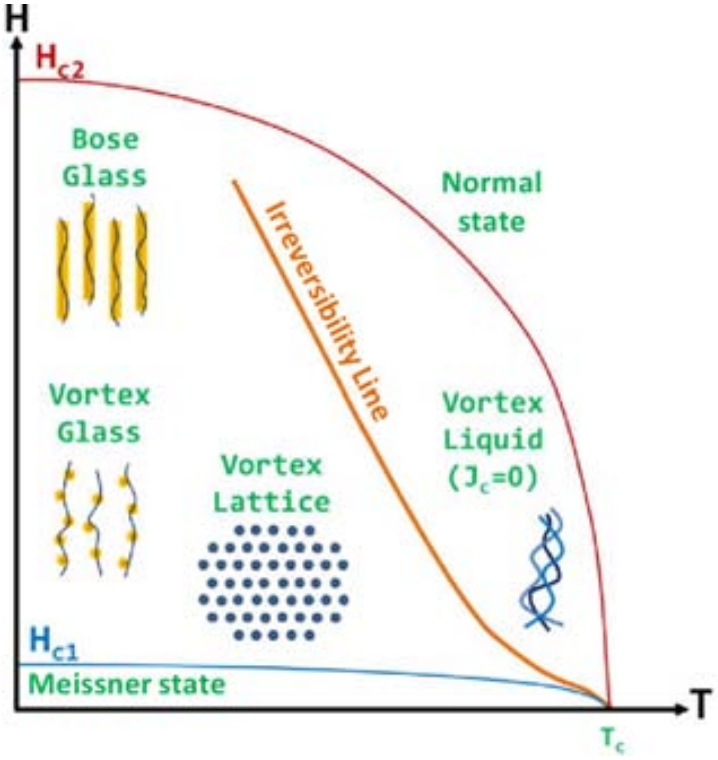

Figure 1.8.: Representation of the magnetic phase diagram of $YBCO$.

1.2.1. The Irreversibility Line

As commented above, the magnetic field-temperature $(H-T)$ region where the zero electrical resistance state is observed, is limited by the irreversibility line (IL) in the case of $YBCO$ thin films. Above the IL, the material is in the superconducting state in the sense that it has a finite order parameter however, it presents a finite electrical resistance due to spontaneous vortex motion, even in the lack of applied electrical current. In this regime, vortices move since the thermal energy is larger than the energy able to pin vortices in the material (pinning energy) inducing therefore an electrical resistance due to the motion of normal electrons present at the vortex core. Below the IL, the material presents zero electrical resistance since in that case, the pinning energy is effective enough to immobilize the vortices. Therefore this non-dissipative region is the relevant for technological applications of $YBCO$.

Fig. 1.9 [17] shows the values of H_{c2} and IL for some superconductors. Differences between phase diagrams are related with the physical parameters and crystal structure of each superconductor. It should be noticed that $YBCO$ is the superconductor which shows the highest IL making it as the optimum candidate for technological applications.

It should be commented that, in HTS, the IL can be enhanced closer to H_{c2} by introducing defects in the system and thus enhancing the pinning force and preventing the loss of the vortex line tension [24].

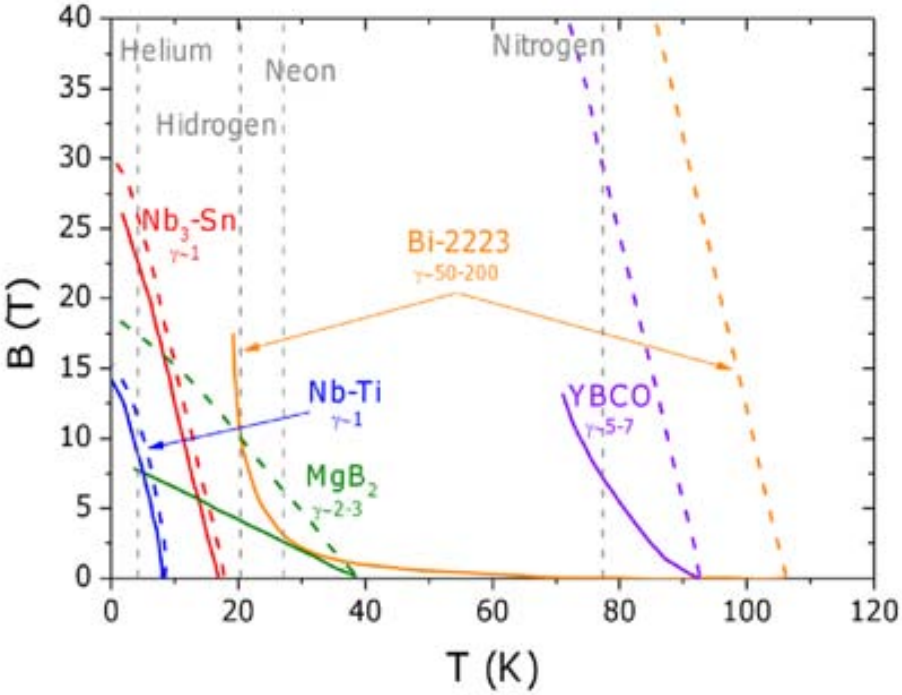

Figure 1.9.: Irreversibility field (solid lines) and H_{c2} (dashed lines) as a function of the temperature for different materials with different anisotropy. Vertical dashed lines shown the temperatures of different cryogenic gases [17].

1.2.2. Vortex Pinning

The presence of a current in the presence of magnetic field, induce a Lorentz like force which tries to move vortices, according to:

$$\overrightarrow{F_L} = \overrightarrow{J} \times \overrightarrow{B} \tag{1.5}$$

where $\overrightarrow{F_L}$ is the Lorentz force, $\overrightarrow{J}$ is the current density and $\overrightarrow{B}$ is the magnetic field into the superconductor. In the region below the IL, defects present into the materials can act as effective pinning sites for the vortices, avoiding their movement and thus, the electrical dissipation [25–27]. When the Lorentz force exceeds the pinning force created by defects ($\overrightarrow{F_p}$) vortices start to move inducing a voltage drop in the superconductor. Another important parameter that characterizes the material is the critical current density ($\overrightarrow{J_c}$) which is defined as the current density necessary to equal the pinning force, i.e. $\overrightarrow{J_c} \times \overrightarrow{B} = \overrightarrow{F_p}$. Therefore, when $J > J_c$, an electrical field will appear due to the vortex movement in agreement with the Faraday's law. This electrical field, $\overrightarrow{E}$, can be related with the velocity that vortices develop according to [28]:

$$\overrightarrow{E} = \overrightarrow{v} \times \overrightarrow{B} \tag{1.6}$$

where $\overrightarrow{v}$ is the local velocity of the flux lines.

As we will comment along this thesis, the value of the critical current density depends on temperature, magnetic field, and orientation between the magnetic field and the crystallographic axis of the superconductor.

Classification of vortex pinning sites

Pinning centers in a superconductor result from structural inhomogeneities in the material, that yield in a local reduction of the order parameter. As a consequence, the vortex can reduce its free energy when it is positioned on a pinning center. These defects can appear spontaneously during the growth of the superconductor (natural defects), or artificially introduced on purpose (Artificial Pinning Centers, APCs) to optimize their particular applications.

Different criterions can be used in order to classify the pinning centers. One can use their dimensionality, their anisotropic behavior or their pinning strength:

According to their dimensionality, different kinds of defects can be mentioned. The case of foreign element substitutions at the Y, Ba or Cu sites of $YBCO$, oxygen vacancies or point defects, are commonly referred as zero-dimensional $(0-D)$. Dislocations or columnar defects are examples of one-dimensional $(1-D)$ [29–41]; low angle grain boundaries, twin boundaries, stacking faults or intergrowths, as two-dimensional $(2-D)$ [42–51], and nanoparticles or local strained regions, as three-dimensional $(3-D)$ [52,53]. It is important to note that usually, natural defects or APCs with different dimensionalities, are simultaneously found in the material [54,55]. Fig. 1.10 shows a schematic representation of defects with different dimensionality.

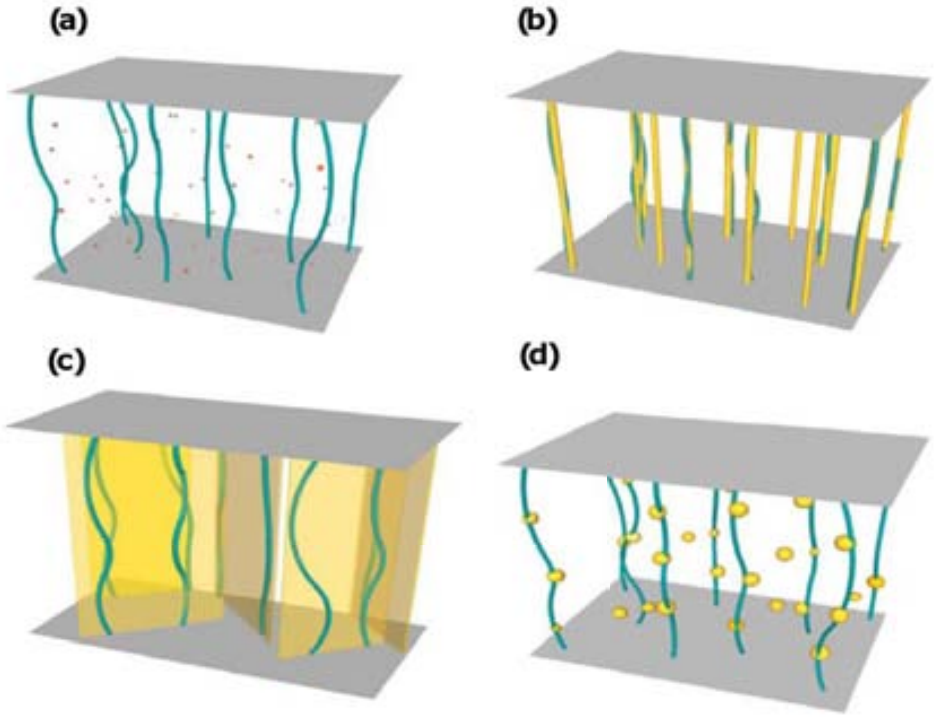

Figure 1.10.: Schematic representation of the dimensionality of pinning centers with examples of typical defects for each case **(a)** $0-D$, **(b)** $1-D$, **(c)** $2-D$ and **(d)** $3-D$.

Regarding the orientation of the applied magnetic field, and the anisotropy of defects, they can be separated as isotropic or anisotropic pinning centers. The former corresponds to defects which are equally effective for all magnetic field directions, like oxygen vacancies, strained localized areas or nanoparticles. The later corresponds to defects which present different pinning force depending on the orientation of the magnetic field, like dislocations or twin boundaries [49]. As we will discuss in chapter 3, isotropic defects follow the Blatter scaling approach if the field is scaled with the anisotropy factor $\varepsilon(\theta)$ introduced in sec. 1.1.1.

Finally, the strength of pinning centers can be evaluated from the temperature dependence of $J_c(T)$. Two different theoretical models have been proposed to describe the $J_c(T)$ dependence of weak and strong pinning centers:

On one hand, the weak collective pinning model [13] predicts a fast decay of $J_c(T)$ following the expression.

$$J_c^{weak}(T) = J_c^{wk}(0) exp\left(-\frac{T}{T_0}\right) \tag{1.7}$$

where $J_c^{wk}(0)$ is the weak pinning contribution at $0K$ and T_0 is associated to the characteristic vortex pinning energy of weak defects (in Kelvin units). In $YBCO$, typically $0-D$ point defects with dimensions smaller than the coherence length , are one source of such weak pinning defects.

On the other hand, for strong correlated defects, the theory predicts a slower temperature decay of J_c derived from [22, 23]:

$$J_c^{strong}(T) = J_c^{str}(0) exp\ \ -3\left(\frac{T}{T^*}\right)^2 \tag{1.8}$$

where $J_c^{str}(0)$ is the strong pinning contribution at $0K$ and T^* is the corresponding characteristic vortex pinning energy of strong pinning defects (again, measured in Kelvin). It is important to note that this smoother temperature dependence of J_c makes them more effective at high temperatures. Usually the contribution of $1-D$ and $2-D$ correlated defects can be described with this strong pinning model.

In this thesis, we will study $YBCO$ thin films where, in general, several natural types of defects are present. Thus, their simultaneous contribution will be responsible of their final pinning performance [55, 56]. Besides the presence of natural defects, we will use different approaches to introduce artificial pinning centers. These approaches go from scalable processes where randomly oriented second phase nanoparticles have been spontaneously segregated into the $YBCO$ matrix (as will be discussed in chapter 3), to designed model systems with ordered nanostructures (chapter 4 and chapter 5).

1.2.3. The Bean Critical State Model

In order to describe the macroscopic magnetic behavior of a superconductor in the mixed state, the Bean Critical State model can be used [57]. Within this model, it is

assumed that the flux starts to penetrate in the sample from $\mu_0 H_a = 0$ (where H_a is the applied or external magnetic field), i.e. the lower critical field, H_{c1}, is equal to zero. Furthermore, critical current density in the sample is supposed to be independent of field. The simplest version of this model assumes the case of an infinitely long cylinder in a parallel field, in which demagnetization effects [58, 59] are not relevant.

To explain the critical state model, it is useful to start with a Zero Field Cooled (ZFC) process and a post-increase of the applied magnetic field. In this condition, vortices start to nucleate at the edges of the sample and move to the center as H_a increases. Pinning forces are opposed to this flow and as a consequence, a non-homogeneous flux distribution is obtained into the material, i.e. the competition between pinning, and Lorentz forces, generates a magnetic field gradient into the superconductor. The model assumes that the field slope (proportional to J_c) is constant and thus, the field decreases linearly with the distance. Consequently, three different values of the current density can be found inside the sample: $+J_c$, $-J_c$ and 0 (Fig. 1.11 and Fig. 1.12).

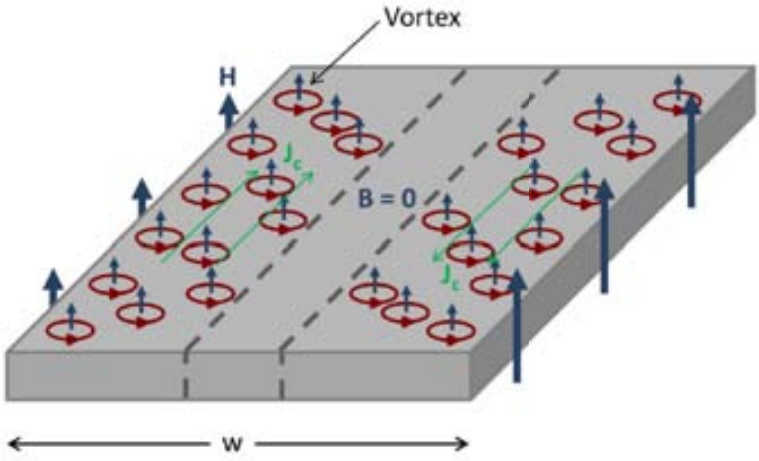

Figure 1.11.: Schematic representation of the introduction of vortices according to the Bean critical state in an infinite slab of width w. The applied magnetic field is $H < H^*$ (see Fig. 1.12).

Fig. 1.12 shows the magnetic field and critical current density profiles generated in an infinitely long cylinder after increasing and decreasing the applied magnetic field. Fig. 1.12$-b$ shows the magnetic flux and current distribution inside the cylinder for several applied fields marked at different hysteretic loop curves shown in Fig. 1.12$-a$. Fig. 1.12$-b_i$, b_{ii} and b_{iii} represent the magnetic flux profile within the sample as the applied magnetic field ($H_a^{\uparrow}$) is increased. In Fig. 1.12$-b_i$, H_a is lower than a characteristic field known as the full penetration field, H^*, and the sample is not fully penetrated by flux lines. The total magnetization, M, can be determined from the area limited by the internal magnetic field profile and the applied magnetic field (zone colored in orange). At $H = H^*$ the flux lines reach the center of the sample and the magnetization saturates, M^{sat}, (Fig. 1.12$-b_{ii}$). The field profile reached at this point stays constant as the magnetic field is furthered increased (Fig. 1.12$-b_{iii}$). When the magnetic field is decreased, flux lines start to leave from the superconductor by its edges, reverting the magnetic flux gradient and hence, the superconducting currents.

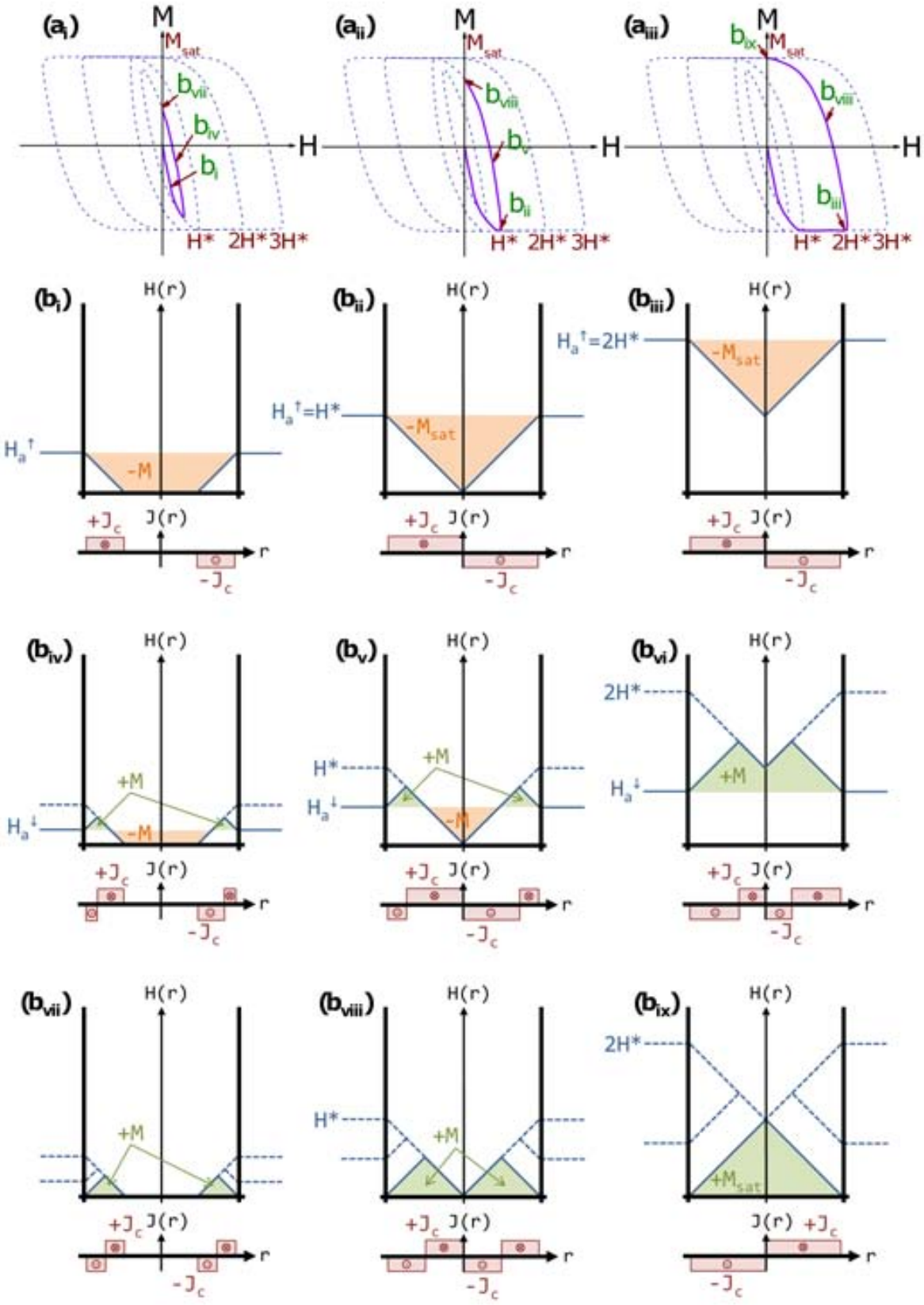

Figure 1.12.: Scheme of the magnetization of an infinite cylindrical superconducting sample of radius R, according to the Beam model, at different stages. Figures **(a)** show in violet color the magnetic hysteresis loops generated afther a maximum applied magnetic field of $H < H^*$, $H = H^*$ and $H = 2H^*$, respectively. Figures **(b)** shows the magnetic field and current profiles correspondent to each hysteresis loop.

Fig. 1.12$-b_{iv}$, b_v, b_{vi} corresponds to the flux profiles obtained by decreasing the field to a value $H_a^{\downarrow}$, starting from the magnetic situations described in Fig. 1.12$-b_i$, b_{ii}, b_{iii}, respectively. Fig. 1.12$-b_{vii}$, b_{viii}, b_{ix} shows the correspondent remanent magnetic states, obtained once the applied magnetic field is suppressed in the three different situations. It should be noted that it is necessary to apply a maximum field of $2H^*$ to saturate the remanent magnetization (Fig. 1.12$-b_{ix}$).

Within the Bean critical state model, the critical current density for an infinitely long cylinder can be evaluated from the saturated magnetization value by using the following equation [57, 60]:

$$J_c = \frac{3\Delta M}{2R} \tag{1.9}$$

where R is the cylinder radius, and ΔM is the width of the saturated hysteresis loop of the saturated magnetization hysteretic loop $M - H$.

With a finite sample, demagnetizing effects must be taken into account and thus, the penetration of the current inside the sample, and the field profiles are affected by edge effects [58, 59]. Moreover, in a real superconductor, the critical current density is not independent of the magnetic field, as it is assumed in the Bean model.

In the case of superconducting thin films, due to their geometry, the value of the internal field is basically equal to the external value, except within a narrow region around $\mu_0 H_a = 0T$ [61, 62]. Therefore, in thin samples, the expression 1.9 can be used to determine the value of J_c, taking into account the magnetic field dependence of the saturated magnetization, $M(H)$.

1.3. Thermally Activated Vortex Motion

In contrast to conventional superconductors (LTS), vortex dynamics in HTS is strongly influenced by thermal fluctuations [20, 21, 63]. This is due to the combination of several factors, namely the higher temperature, the very small superconducting coherence length of HTS, and the large anisotropy resulting from their laminar structure.

As it has been described in sec. 1.2.2, electric currents exert forces on vortices and, in the absence of pinning centers, an arbitrarily small current density J would result in a dissipative vortex motion [25]. The pinning potential created by defects precludes a large scale vortex motion and the associated dissipation, unless J exceeds the value of the critical current density J_c. However, vortex motion still occurs for $J < J_c$, at a much slower rate, due to thermally activated jumps out of the pinning centers [25]. This flux creep mechanism implies a residual dissipation and it is responsible for the time relaxation of persistent currents flowing in a superconducting closed loop. The relaxation rate is controlled by an activation energy that results from the interaction between defects and the vortex lattice.

A simple theory of thermally activated flux motion was developed by Anderson and Kim [64], who consider a sawthooth like activation energy. Fig. 1.13, shows a schematic

representation of the model, where vortices are directed along Z direction, U_0 is the temperature dependent barrier height, and x_{hop} represents the distance that vortices have to move to overcome it. Two different situations can be described. On one hand, in Fig. 1.13$-a$, no force has been applied to the system ($J = 0$). In this case, due to thermal activated processes, the rate of hopping over the barrier may be written as $P = exp(U_0/K_BT)$ where K_B is the Boltzman constant. As a consequence, the probability of jumping is the same for all the directions, and the net vortex velocity is zero. On the other hand, in Fig. 1.13$-b$, a current along the Y direction has been applied and consequently, a driving force along the X direction is generated.

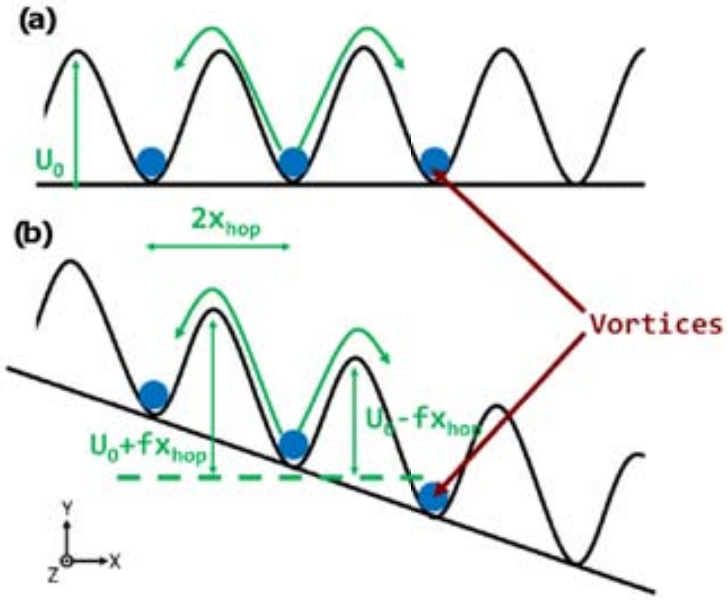

Figure 1.13.: Sawthoot like energy potential model used to explain the thermal activation phenomena. **(a)** No force is applied into the system i.e. $J = 0$. **(b)** A force f is applied to the right. Vortices are represented by blue dots.

The action of the applied force on a given vortex can be expressed as $-fx_{hop}$, and it reduces the potential well on the right to $U_0 - fx_{hop}$, and increases it on the left to $U_0 + fx_{hop}$. Consequently, there is a net rate of vortices jumping to the right, according to the following expression [12]:

$$P \propto exp\left(-\frac{U_0 - fx_{hop}}{K_BT}\right) - exp\left(-\frac{U_0 + fx_{hop}}{K_BT}\right) \tag{1.10}$$

Thus, a general expression for the electric field $E(B, T, J)$ generated by thermally activated flux jumps out of the pinning centers can be expressed as:

$$E(J) \propto x_{hop}Be^{-\epsilon}sinh\left(\epsilon\frac{J}{J_c}\right) \tag{1.11}$$

where $\epsilon = U_0/(K_B T)$ and B is the internal magnetic field. Concerning to this expression, three different regimes on the $E(J)$ curve can be distinguished, depending on the applied critical current density (indicated in Fig. 1.14) [12]. At low current densities ($J << J_c$), one have a linear dependence associated to the $TAFF$ (Thermal Activation Flux Flow) regime where dissipation is promoted by thermal excitations. At very high current densities ($J >> J_c$), the pinning force is much weaker than the driving force and thus, a diffusive vortex motion occurs (Flux Flow regime). At $J \sim J_c$, one has $U_0 \sim f x_{hop}$ and thus, $E \propto exp(J/J_c)$. This regime is the so called flux creep regime.

Therefore, thermally activated flux motion determines the shape of the electric-field/current-density ($E(J)$) curves. According to the Anderson-Kim model, which assumes a linear $U(J)$ dependence, the $E(J)$ curves show an exponential behavior at the flux creep regime. However, more complex potential barriers have been proposed, in order to better describe the creep behavior of high temperature superconductors, resulting in other different $E(J)$ dependences [65, 66].

A common phenomenological way to describe the electric field in the flux creep regime of $YBCO$ thin films, obtained from direct transport measurements, is assuming a power law dependence which can be expressed as [67, 68]:

$$E(J) = E_c \left(\frac{J}{J_c}\right)^n \tag{1.12}$$

where n is the flux creep exponent that provides information about the nature of the dissipation process [69] and E_c is the electric field criterion used to determine J_c. In first approximation, one can consider that $n \propto U_0/(K_B T)$. Thus, from a fundamental point of view, the temperature and field dependence of n can provide insight into the nature of the dissipation process determining the shape of the $E(J)$ curve. From a practical viewpoint, the n-factor describes how fast induced or injected supercurrents decay [70].

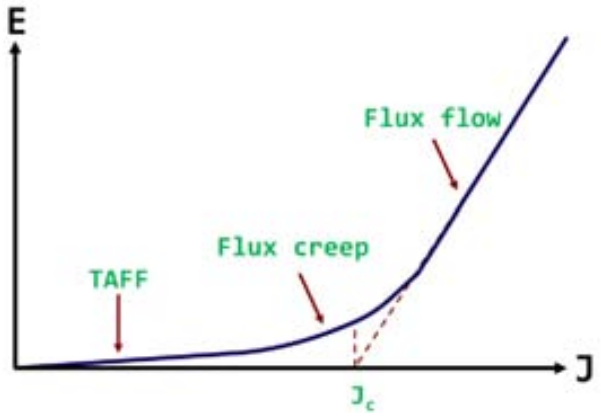

Figure 1.14.: Schematic view of the $E - J$ characteristic in presence of thermal activation processes for a HTS.

Vortex relaxation remarked theories in HTS

Regarding the model proposed by Anderson and Kim [71] the activation energy goes linearly with the current density as commented above. However, it has been found that the time relaxation of the current density derived from this model, and defined by the parameter S:

$$S = -\frac{d\,[ln(J)]}{d\,[ln(t)]} \tag{1.13}$$

does not follow the measured behavior on HTS samples [72, 73].

Experimentally, in HTS, S presents four different regimes when it is plotted as a function of temperature for a given applied magnetic field [65]. At very low temperatures, $T < 10K$, the quantum creep becomes relevant [74–77]. At low temperatures, $10K < T < 20K$, S follows the expected behavior for the Anderson-Kim model. At intermediate low temperatures, S reaches a constant value between $[0.02 - 0.035]$ which arises in the collective flux creep [78]. In the case of correlational defects along the magnetic field direction, a peak in this regime can be observed at fields lower than the matching field[1] due to the formation of Double-Kinks (DK) [55, 73, 79–82]. Ideally, for identical parallel columnar defects, once a DK is created, there is no energy barrier preventing the entire vortex form moving to the next columnar defect so, S, can be arbitrarily large (Fig. 1.15). It is important to note that the large $S(T)$ peak has a negative implication as it induces a fast drop of J_c with increasing T [73,79–81]. At high enough temperatures, the reduction of the current density with time is higher, increasing therefore the value of the S parameter. This last regime is known as plastic-creep, while the former described regimes are within the elastic-creep region.

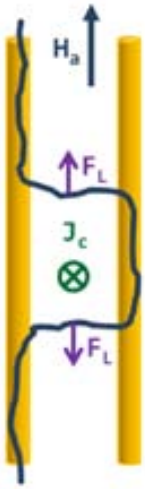

Figure 1.15.: Scheme of two parallel correlated defects with a vortex depinning through the double-kink mechanism

[1] Matching field: Applied magnetic field at which each defect is occupied by one vortex.

Experimental deviations of $S(T)$ from the Anderson-Kim model (where vortices are considered as particles trapped in pinning wells), can be described if the elastic energy of the vortex structure is taken into account. Consequently, an inverse power-law form for the activation energy emerges considering a collective flux creep theory described as [68, 83]:

$$U(J) = \left(\frac{U_0}{\mu}\right) \left(\frac{J_{c0}}{J}\right) - 1 \tag{1.14}$$

where μ is the regime-dependent exponent [66, 84, 85].

Using the Arrhenius expression relation shown in expression 1.15 (where t_{eff} is a characteristic time), and combining expressions 1.14 and 1.13, one can obtain the final expression of the magnetic flux relaxation, which describes accurately the observed elastic-creep in long thermal relaxation studies in $YBCO$ single crystals with non-correlated disorder (such as random point defects) [66, 78] i.e. when DK are not produced.

$$U = K_B T ln\left(\frac{t}{t_{eff}}\right) \tag{1.15}$$

$$S(T,t) = \frac{K_B T}{U_0 + \mu K_B T ln(t/t_{eff})} \tag{1.16}$$

2. Sample growth, electrical contacts and characterization techniques

The zero electrical resistance of the superconductors makes them very usefull as high electrical current conductors for power applications instead of normal metals such as cooper or aluminum. Cuprate superconductors are one of the best candidates to this aim since they present a high irreversibility line. Thus $YBCO$ Coated Conductors (CC) have appeared as one of the most promising technologies to generate high temperature superconducting tapes. They consist of a long metallic substrate tape covered with different buffer layers and a $YBCO$ film grown on top. The interaction between the substrate and the superconducting thin film promotes higher density of defects in the $YBCO$ layer which may act as pinning centers obtaining therefore an increase of the critical current density, J_c.

2.1. Growth of YBCO thin films

By analyzing the properties of the CC, it was found a fast decay of the critical current density with the applied magnetic field due to the presence of grain boundaries [17,86–88]. Consequently, highly textured $YBCO$ thin films should be obtained to get the highest critical current density. To this aim, physical or chemical methodologies can be used to grow $YBCO$ films.

By physical methods, Molecular Beam Epitaxy (MBE) [89], Pulsed Laser Deposition (PLD) or sputtering [90], are the most used techniques. Parallel to them, by chemical methods, Liquid Phase Epitaxy (LPE) [91], Chemical Vapor Deposition (CVD) [92] or Chemical Solution Deposition (CSD) [93] are some alternatives. In particular, CSD is one of the cheapest methodologies due to the unnecessary requirement of vacuum technology.

no high vacuum systems are necessary and deposition of long tapes is possible, decreasing therefore the final cost and thus, making these methodologies more attractive for applications.

In this work, we will study $YBCO$ thin films grown on single crystal substrates using the CSD methodology. The different steps and parameters of the film preparation are well described in [94].

Chemical Solution Deposition through tri uoroacetates

CSD has become one of the most appealing alternatives towards successful development of affordable production of long length HTS tapes. The most challenging issue to reach high critical currents has been to find a suitable methodology for the $YBCO$ layer growth based on CSD, and here, the greatest progress has been made based on the use of trifluoroacetate (TFA) solution as metal-organic precursors [95]. These new precursors allows the formation of BaF_2, instead of $BaCO_3$ which decomposes at much higher temperatures.

An important issue of CSD is to properly pyrolyze the deposited solution. This process is performed at relatively low temperatures ($T \sim 300 - 400^oC$) and leads to a solid which should maintain homogeneity at the nanoscale to allow the growth of high-quality epitaxial films.

The next fundamental processing step corresponds to the nucleation and growth of the $YBCO$ layer at high temperature ($T \sim 800^oC$), including the control of the growth rate and keeping a high epitaxial quality. This step, together with the previous one, needs to be carefully studied to optimize the final $YBCO$ performance [93, 94, 96].

The last step to obtain good superconducting films consists of the oxygenation process where the final superconducting structure is achieved [97, 98].

In this work we have studied $250nm$-thick $YBCO$ films grown on $LaAlO_3$ single crystal substrates with self-field critical current densities (J_c^{sf}[1]) at $77K$ between $3 - 5MA/cm^2$, which indicates a good quality of the films.

2.2. Artificial nanostructure in YBCO thin films

One of the main goals of this thesis is to understand the different mechanism that governs vortex motion in $YBCO$ thin films. Nanostructure control is one of the possibilities that can be used in order to tune vortex pinning and dynamics in $YBCO$ samples. As the typical lengths present in a vortex are in the nanometric range, nanometric techniques should be used in order to induce effective pinning sites.

With this aim, two different approaches can be used. On the one hand, the matrix of $YBCO - CSD$ has been nanostructured by a spontaneous segregation of Ba_2YTaO_6 ($BYTO$) nanoparticles during the growth process of the $YBCO$ thin film (in-situ nanocomposites). With this in-situ technique, vortex pinning, dynamics and anisotropy are successfully controlled as we will study in chapter 3.

On the other hand, $YBCO$ films have been patterned with ordered arrays of Artificial Pinning Centers (APCs) with controlled geometry (shape, size and depth). These samples will be studied in chapter 4 and chapter 5. For this last approach, different techniques can be used to nanostructure the material [99]. However, we have to take into account that each technique can cause secondary effects in the superconducting properties. In this work, we have used different high resolution nanolithography techniques such as Focused

[1] J_c^{sf} is defined as the value of J_c in the lack of applied magnetic field.

Ion Beam, Focused Electron Beam Lithography and Focused Electron Beam Induced Deposition. The study of different APCs has allowed us obtaining a preferential direction for the vortex motion and/or hysteretic controlled behaviors of the critical current density as a function of the applied magnetic field.

2.2.1. In-situ nanocomposites

A modified $YBCO - BYTO$ precursor solution has been prepared by introducing specific amounts of tantalum ethoxide in a stoichimetric $YBCO-CSD$ precursor solution. Consequently, during the growth process of the film, spontaneous nanoparticles of $BYTO$ are segregated within the $YBCO$ matrix.

$BYTO$ nanoparticles are a potential candidate to enhance pinning in $YBCO$ films since due to the large lattice mismatch with $YBCO$ ($\epsilon = 8.5\%$), it is expected that strained-localized areas could be induced at the interface. Nanostrained regions between the $YBCO$ matrix promotes a new vortex pinning mechanism based on strain-induced Cooper pair suppression as it will be discussed in chapter 3.

The molar content of $BYTO$ in the studied samples has been varied from 0% to 15% understanding $x\%$ as $1YBCO + 0.xBYTO$. Strick controll of the stoichiometry of $Y : Ba : Cu$ is ensured to be $1 : 2 : 3$ after the addition of Ta since additional Ba and Y are also added. After sample growth, the final result consists of $YBCO$ nanocomposite with $BYTO$ nanoparticles between $14nm$ and $40nm$ in diameter.

2.2.2. Focused Ion Bean nanostructures

Direct nanopaterning of $YBCO$ films can be performed by using an incident Focused Ion Beam (FIB). In this system, Ga^+ ions are accelerated and focused using electrostatic lenses and coils. Due to the high energy of these ions, milling of the material at nanometric scale is produced at the sample surface without needing any mask. Controlling the beam voltage and the dose (number of ions per unit of time), defects with different shapes can be obtained, with the possibility to tune their sizes and depths.

However, with this technique, some secondary effects near the irradiated areas can be induced modifying the properties of the film. Interstitial or atomic replacement with Ga^+ ions can be produced into the $YBCO$ matrix damaging the superconducting properties (blue dots in Fig. 2.1). Another effect to take into account is the amorphization and redeposition of small amounts of sputtered material (ions and atoms) around the irradiated zones (light grey zone and grey dots in Fig. 2.1, respectively). This effect may change the surface roughness of the film [100] although no variations in the material properties are expected.

An accurate optimization of the milling parameters has been performed in order to minimize these secondary effects and thus, avoid the damage of the material. The optimized parameters used to create the nanostructures studied in chapter 4 and chapter 5 of this thesis were: voltage of $30kV$ and ion current between $30 - 200pA$. The milling time was adjusted to control the depth of the patterned holes.

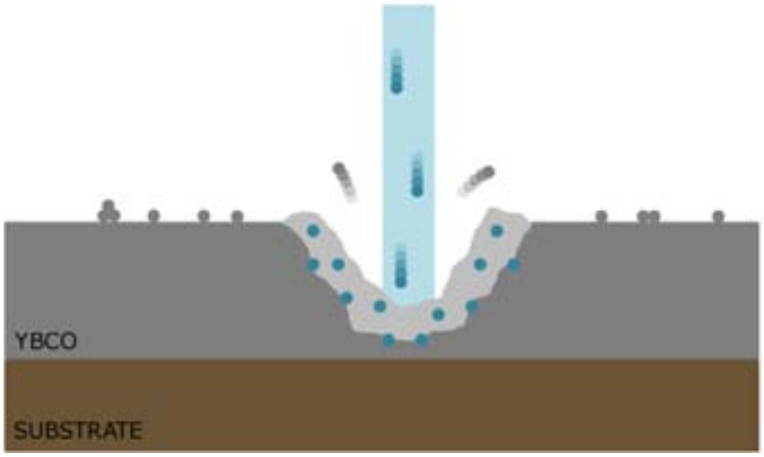

Figure 2.1.: Schematic representation of the Focused Ion Bean etching. Blue column corresponds to the Focused Ion Beam.

2.2.3. Focused Electron Beam nanostructures

In the case of Focused Electron Beam Lithography ($FEBL$), electrons are not heavy enough to directly etch the $YBCO$ film and thus, an electron sensitive resist is necessary to perform a patterning. Thereupon, the etching of the film should be performed using the resist as a mask.

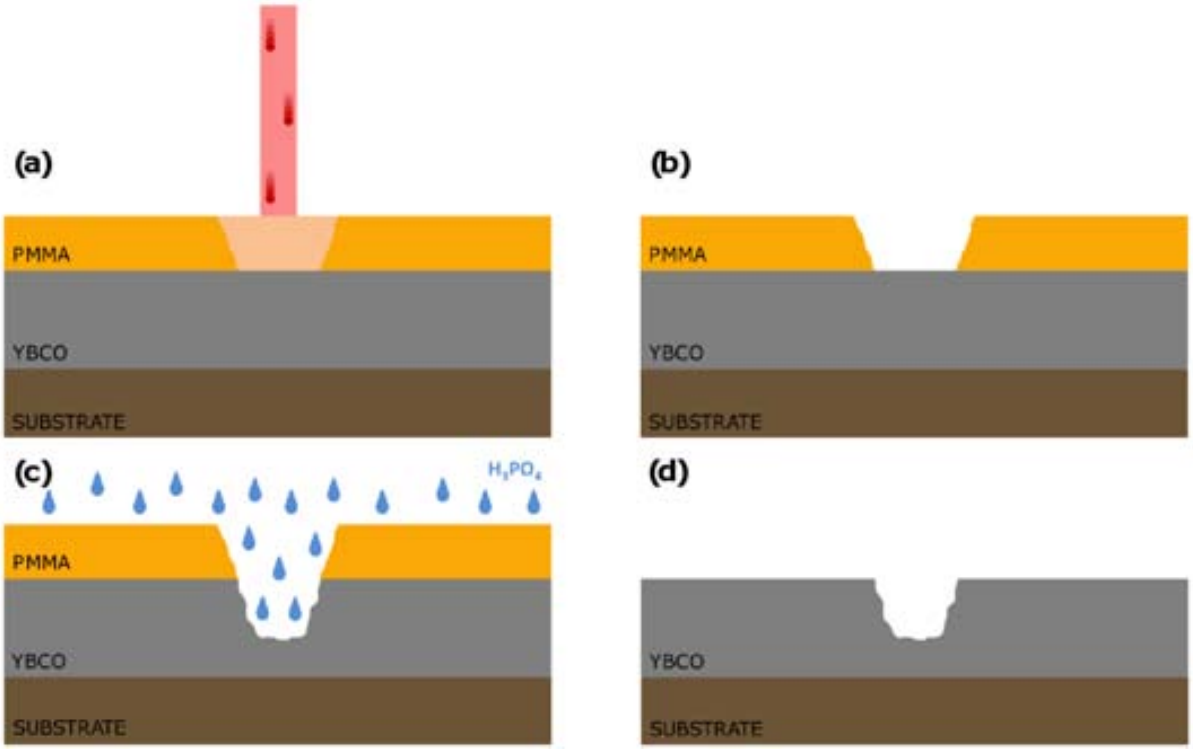

Figure 2.2.: Schematic representation of the Focused Electron Beam Lithography process. Red column corresponds to the electron beam. **(a)** Irradiation of the resist. **(b)** Irradiated resist is removed after a developing process. **(c)** $YBCO$ is etched with H_3PO_4 acid. **(d)** Final form of the nanostructured $YBCO$ film.

Having the sample surface cleaned with acetone and methanol, the deposit of the positive polymethyl metacrylate resist ($PMMA$) is carried out in a spinner. To obtain a layer of $100nm$, we used an acceleration of $3500r.p.m./s$ and velocity of $1500r.p.m.$ during $40s$. Copolymer pre-bake at 180^oC during $60s$ is needed in order to remove the organic solvent of the resist. Next step consists of the e-beam exposure of the resist with the desired pattern (Fig. 2.2$-a$) and a developing process to remove the resist of the exposed zones [101, 102], Fig. 2.2$-b$.

The optimized parameters used to perform the $FEBL$ of samples studied in chapter 4 were a potential of $10kV$, and bean current around $100pA$.

After e-beam lithography, the resulting patterned $PPMA$ layer on top of $YBCO$ is used as a mask in order to perform the etching of the $YBCO$ layer. The etching consists of a chemical attack in which the sample is immersed in a high-diluted acid ($1:10000/H_3PO_4:H_2O$) (Fig. 2.2$-c$) in order to obtain a good control of the mill rate ($80nm/min$). Finally, $PMMA$ mask is removed with acetone and the final pattern is obtained (Fig. 2.2$-d$).

2.2.4. Focused Electron Beam Induced Deposition nanostructures

Another alternative to introduce nanostructures in $YBCO$ films is the growth of an additional material with nanometric size into the $YBCO$ matrix by using the Focused Electron Beam Induced Deposition ($FEBID$) technique. With this powerful technique, an hybrid system at the nanometric scale can be designed without any need of mask [103–105]. $FEBID$ consists of the local deposition of materials using a focused electron beam in the presence of a precursor gas. The electron beam interacts with the gas molecules injected at the film surface and decomposes them. As a consequence, the volatile fragments of the gas are evacuated in the vacuum system while the desired material is deposited (Fig. 2.3).

In our particular case, we are interested in the study of the interaction between ferromagnetic (FM) and superconducting (SC) materials, which can provide interesting effects like field compensation. In order to perform these studies, we have grown an hybrid system consisting of a $YBCO$ film with cobalt nanorods (chapter 5).

To do so, an array of antidots (physical holes which completely perforate the $YBCO$ layer and part of the substrate) was patterned in a sample using the FIB technique (Fig. 2.3$-a$). Next, cobalt was deposited into these antidots using $FEBID$ forming cylindrical Co-nanorods with a high purity of about $85-95\%$ (Fig. 2.3$-b$ and c). Parameters used to grow Co-nanorods were a potential of $5kV$, and ion current of $5.5nA$.

2.3. Physical characterization of nanostructured films

To study vortex pinning and dynamics in $YBCO$ thin films with artificial defects, electric transport and inductive magnetic measurements have been performed throughout this thesis. To this aim, we have used different devices according to the absolute applied

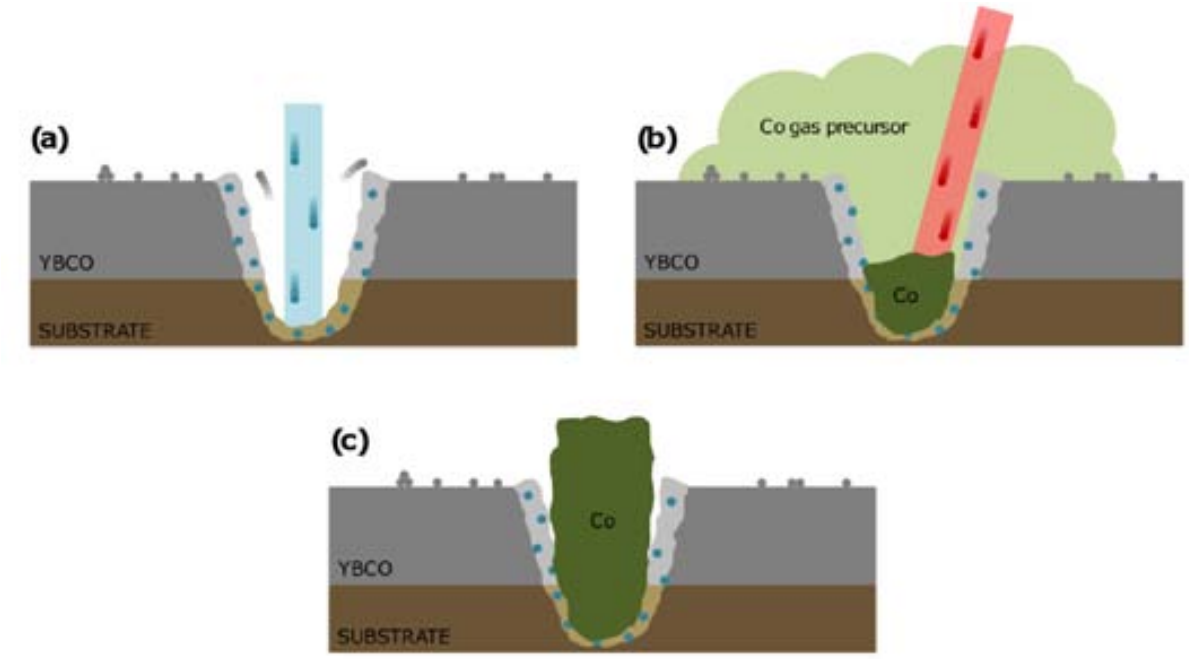

Figure 2.3.: Schematic representation of the Focus Ion Beam etching + Focus Electron Beam Induced Deposition. **(a)** Etching ofthe sample by FIB. **(b)** Cobalt grow through the focused electron beam. **(c)** Final form of the nanostructured $YBCO$ film with Co-nanorods.

magnetic field value needed: in the case of high applied magnetic fields[2], a magnetometer which consists of a Superconducting Quantum Interference Device ($SQUID$) and a Physical Properties Measurement System ($PPMS$) were used for DC-magnetometry and transport measurements, respectively. On the other hand, for H_{c2} studies, where an ultra-high applied magnetic fields[3] were needed, a high-magnetic-pulsed-electromagnet was used.

Bitter decorations studies have been also performed in order to evaluate the position of the vortices, and the pinning energies present at some positions of our material.

Parallel to these techniques, micro and nanostructure of the films, together with surface analysis, have been characterized by means of Scanning Electron Microscopy, Atomic Force Microscopy, X-ray diffraction patterns, and transmission electron microscopy, in collaboration with other members of the group, and also reported in recent PhD thesis [106, 107].

2.3.1. Inductive measurements

Inductive measurements are non-invasive studies of the superconducting properties, which have been carried out in order to perform a first magnetic characterization and to determine the quality of the samples.

The magnetometer used consists of a $SQUID$ detection system and a superconducting coil which is able to provide a maximum applied magnetic field of $7T$. The pick-up

[2]We referred as "high magnetic fields" as $\mu_0 H_a < 7T/9T$ in agreement with standard comercial devices.
[3]The maximum applied magnetic field during the ultra high measurements was $\mu_0 H_a = 65T$.

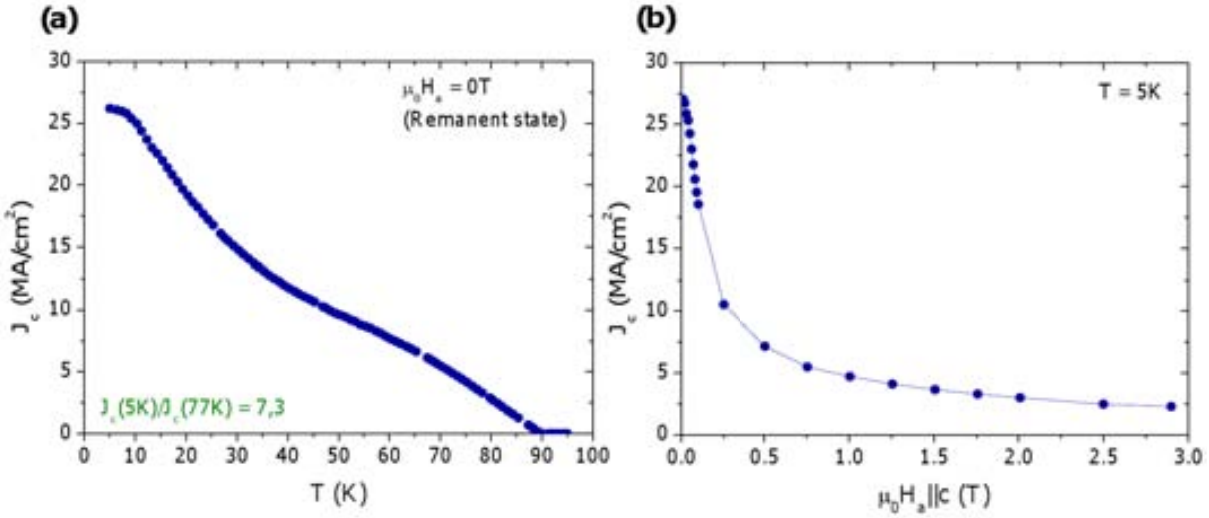

Figure 2.4.: **(a)** Critical current density as a function of the temperature and **(b)** Critical current as a function of the applied magnetic field at $5K$, for an standard YBCO $250nm$-thin film. Both measurements have been performed with $H_a||c$.

detection system is composed by a group of pick-up coils located at the middle of the magnet. Half of these coils are rolled up in one sense and the other half in the opposite one. The sample, which is typically mounted with the c-axis parallel to the applied magnetic field, is moved along the pick-up coils inducing an electrical current on them proportional to the magnetic flux variation. The $SQUID$ functions as a highly linear current-to-voltage convertor so, variations in the current at the detection coil circuit, produce corresponding variations in the $SQUID$ output voltage. This system, which presents a resolution of $10^{-9}Am^2$ ($10^{-6}emu$), is located in a helium cryostat that refrigerates the superconducting coil and allow a temperature control of the sample between 1.8 and $400K$.

Each measurement is performed at a given temperature and magnetic field by moving the sample through the pick-up coils with a $3cm$-displacement. Higher displacements (maximum displacement allowed is $12cm$) can introduce magnetic field and/or temperature variations during the measurement which would result in non-reliable data.

Fig. 2.4$-a$ and Fig. 2.4$-b$ show the temperature and field dependence of J_c determined from magnetic measurements by using the Bean critical state model (sec. 1.2.3) for a standard $YBCO$ thin film. The high values of J_c and the ratio between $J_c(5K)/J_c(77K) = 7.3$ indicates a good quality of the film.

In chapter 3 we will present measurements of magnetization as a function of time which give us information about the magnetic relaxation. In order to perform these experiments, th inductive critical current density at a given field (H_{study}) and temperature is recorded, as a function of time over periods of $1h$ [108]. The relaxation time, t, has been taken to be zero when magnet charging finish, and the first data point has been registered at $t_1 \sim 60s$. Before each measurement at the desired temperature and magnetic field H_{study}, a maximum field (H_{max}) should be applied in order to ensure the saturation of the sample. This maximum magnetic field corresponds to $H_{max} > 4H^* + H_{study}$[4], where H^* is defined in sec. 1.2.3.

[4]Following the Bean critical state model presented in sec. 1.2.3, the value of H_{max} should be $H_{max} >$

Fig. 2.5 shows a typical relaxation measurement performed in a standard $YBCO$ sample. Inset plots the procedure followed to determine the normalized time relaxation in accordance with expression 1.13.

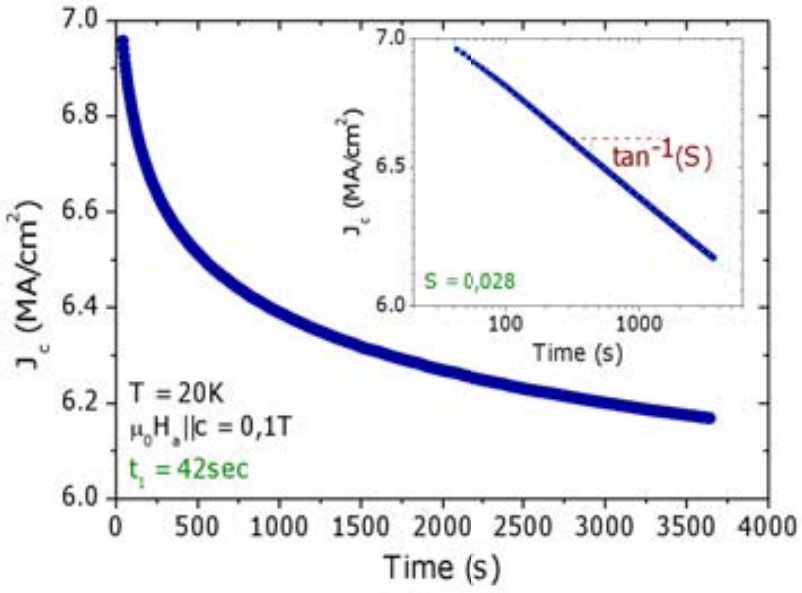

Figure 2.5.: Critical current density as a function of time under an applied magnetic field of $\mu_0 H_{study} = 0.1T$ and temperature of $20K$. Inset shows the log-log representation from which magnetic relaxation can be obtained as the slope of the plot.

2.3.2. Electrical Transport measurements

Electrical transport measurements have been performed in order to deeply study the vortex pinning behavior on nanostructured $YBCO$ films. This technique consists of applying an external electrical current along the sample and measure its voltage drop.

2.3.2.1. Sample preparation

Due to the high electrical current that these materials can support without dissipation, a previous optimization process of the electrical contacts should be performed in order to minimize the electrical resistance between the sample and the external wires. Moreover, a photolithography process to define a 4-point bridge configuration is needed.

Low resistance metal/SC electrical contacts

The requirement to obtain low contact resistance is to avoid sample warming during the transport measurement. Ekin et. al. [109] developed a procedure that allows obtaining low-resistivity contacts ($\sim 10^{-6}\Omega cm^2$ at $76K$) consisting of the deposition of a noble metal

$2H^* + H_{study}$ however, as a consequence of the large demagnetizing factors, a large value is needed to ensure the critical state for a given H_{study}.

layer (silver or gold) on the top of the superconductor at areas where external equipment wires will be connected.

In order to deposit the metal over the film surface, three different steps should be followed:

1. With the aim of obtain the designed pattern contact, a brass shadow mask is located on top of the $YBCO$ film (figure Fig. 2.6$-a$). To fabricate the masks, we use a standard photolithography process (described in the next part).
2. Evaporation of $500nm$ Ag is carried out in a vacuum chamber with a pressure of $10^{-4}Pa$.
3. In order to obtain high quality electrical contacts between the metal and the film, a post-thermal treatment is needed. This annealing consists of a fast warming of the sample ($10^{o}C/min$) from room temperature to $450^{o}C$; a plateau at this temperature during $1h$, and a slow cool down to room temperature (all the process under a $0.17g/min$ oxygen flow atmosphere). The final specimen is shown in Fig. 2.6$-b$ where silver paths (grey squares/rectangles) are observed onto the $YBCO$ film (black surface) with a contact resistance between them as low as $10^{-10} - 10^{-8}\Omega cm^2$.

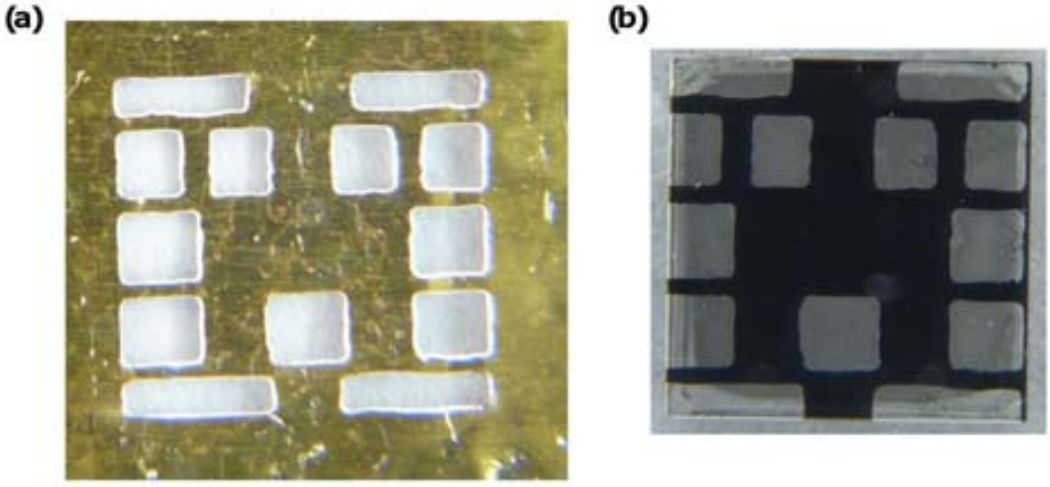

Figure 2.6.: (a) Brass-shadow mask used to pattern the silver contact paths. **(b)** Sample with silver paths.

Photolitography process

One of the main consequences of the high critical current densities of $YBCO$ films is the need to confine the electrical current in bridges with relative low cross-section, to be able to perform transport measurements. By doing so, critical current density ($J_c = I_c/A$, where I_c is the critical current and A the crossection of the bridge) can be reached at these bridges with relative low applied currents. In order to avoid the measurement of the contact resistance, a 4-point bridges configuration should be used (Fig. 2.7). Thus, a photolithography process is required [110].

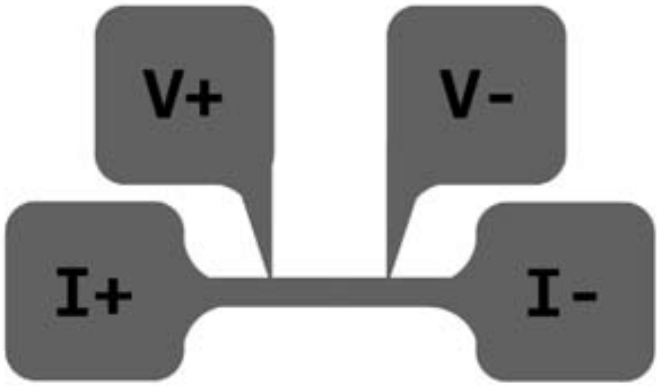

Figure 2.7.: 4-point bridge configuration used in the transport measurements.

Before starting the photolithography process, a previous cleaning of the sample with acetone and methanol must be carried out. After that, the lithography process is performed in a clean room which consists of the following steps:

1. Photo-resist is deposited by spin coating under acceleration of $7500 r.p.m./s$ and velocity of $5000 r.p.m.$ during $25 s$ to obtain a layer of $\sim 1 \mu m$.
2. With the aim to remove the organic solvent of the resist, the film is placed in a hot plate (pre-bake process) at $95^{o}C$ during $60 s$.

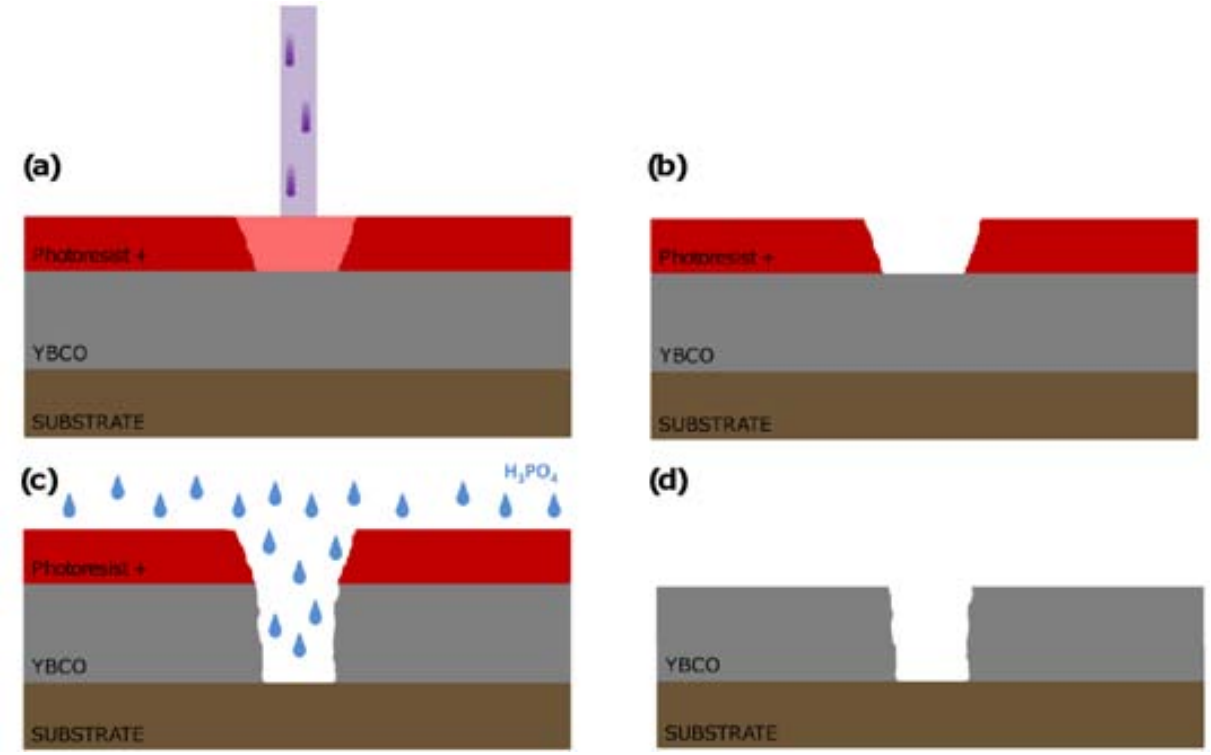

Figure 2.8.: Schematic representation of the photolithography process. Violet column corresponds to the UV light. **(a)** Irradiation of the resist. **(b)** Irradiated resist is removed after a developing process. **(c)** $YBCO$ is etched with H_3PO_4 acid. **(d)** Final scheme of the $YBCO$ film.

3. The required pattern is transferred to the photo-resist by using a Micro Writer equipment with 3 different ultra-violet (UV) lasers of different spots ($0.6\mu m$, $1\mu m$ and $5\mu m$). With this system, one can design the pattern needed in each sample without any need of mask. We use an irradiation dose of $250mJ/cm^2$ determined after a calibration process (Fig. 2.8$-a$).

4. After immersing the sample into a developer during $30s$ the resist in the irradiated areas is removed (Fig. 2.8$-b$).

5. The final step consists of removing $YBCO$ in areas where the resist has been eliminated. To perform this step, the sample is immersed in an acid solution ($1:100\ H_3PO_4/H_2O$) during $15s$ (Fig. 2.8$-c$).

6. Finally, the rest of photo-resist is removed with acetone and the final patterned sample is obtained (Fig. 2.8$-d$).

An example of the design used to irradiate with the ultraviolet lasers is shown in Fig. 2.9$-a$. Since the used photo-resist is type +, the areas which the laser irradiates will be removed in the step 4 of the lithography process described above. Typically, we perform four different bridges in each sample which allows us generating three different arrays of artificial pinning centers in the same sample, and compare the results with a non-patterned reference bridge (see chapter 4 and chapter 5). The typical dimensions of the bridges can vary as a function of the desired study but generally, they are between $100-200\mu m$ length, and $5-50\mu m$ width. Notice that also bridges oriented along the (110) or $(1\bar{1}0)$ planes of the substrate are also patterned (two bridges on the right in Fig. 2.9$-a$) in order to study the interaction of vortices within twin boundaries (see sec. 3.8). The final patterned $YBCO$ thin film is displayed in Fig. 2.9$-b$.

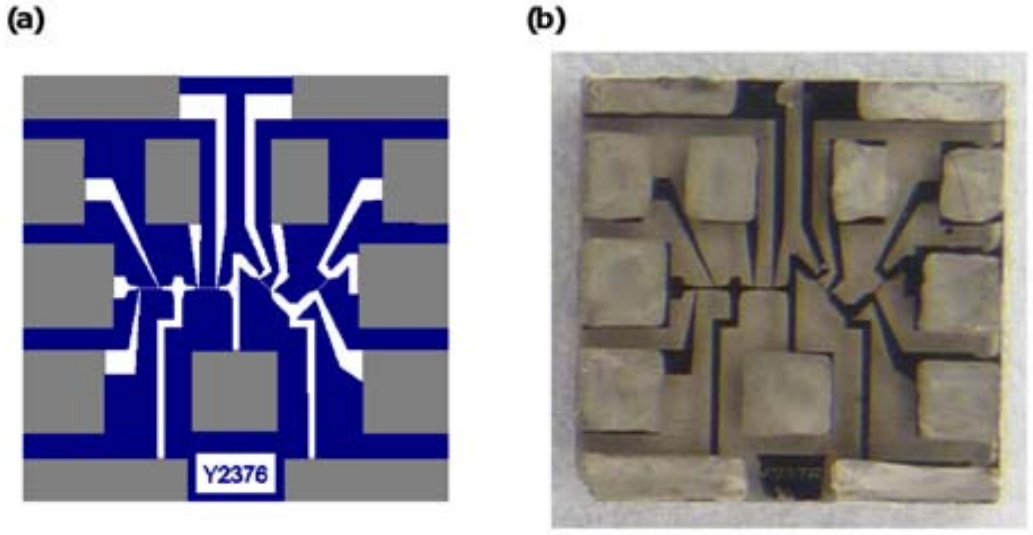

Figure 2.9.: **(a)** Example of the design that the UV laser follows to create the pattern (blue zones are the irradiated zones). **(b)** Final form of a $YBCO$ film patterned with four bridges for transport measurements

2.3.2.2. Transport measurements at high applied magnetic fields

Most of the electrical transport measurements presented along this thesis have been performed in a $PPMS$. It consists of a $9T$ superconducting coil and a cryostat that allows controlling the temperature between 1.8 and $400K$. The sample is mounted in a removable support that allows connecting it with the device through $50\mu m$-diameter Ag wires, to perform transport measurements. Vacuum thermal grease is used to mount the sample to allow thermalizing the sample during the measurements. The support provides a thermometer located just below the sample to accurately control the sample temperature, and it is placed in a single axis rotor that allows rotating the sample an angle θ with 0.1^{o} precision. In all cases, orientation of the sample with respect to the support is chosen to maintain the maximum Lorentz force configuration while the magnetic field is rotated out-of-plane (see Fig. 2.10). To carry out the electrical transport measurements, the $PPMS$ provides a nanovoltmeter and an AC/DC current source which can apply electrical currents between $1\mu A$ and $2A$.

Two different kinds of measurements have been performed in order to analyze the superconducting performances of our samples: resistivity measurements to determine the critical temperature and irreversibility line, and $V(I)$ curves for J_c analysis.

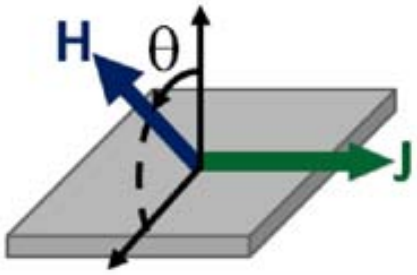

Figure 2.10.: Schematic representation of the field-current configuration in angular transport measurements. θ is the angle between the c-axis of the superconductor and the applied magnetic field.

Critical temperature and irreversibility line

Resistance as a function of temperature is measured in order to determine the transition from normal to superconducting states at different applied magnetic fields. Temperature variation rates and capture of values are modified as a function of the resistance gradient at different temperatures ranges to assure that no differences will be found when measuring increasing or decreasing the temperature.

Following the 4-point bridge configuration displayed in Fig. 2.7, the resistivity is expressed as:

$$\rho = \frac{V^+ - V^-}{I}\frac{t_s w}{l} \tag{2.1}$$

where $V^+ - V^-$ is the voltage drop provided by the nanovoltmeter, I the applied current, t_s the sample thickness, and w and l the bridge width and length, respectively.

Measurements are performed using an AC-current of $10\mu A$ and $33Hz$. In the lack of applied magnetic field, these $\rho(T)$ provide us the value of the critical temperature, T_c. In contrast, in the presence of an external magnetic field, the $\rho(T)$ curves enable us to determine the irreversibility temperature, T_{irr}.

Fig. 2.11 shows a typical $\rho(T)$ transition at zero applied magnetic field. Inset shows the whole $\rho(T)$ curve measured from $300K$ to $80K$ where the ohmic behavior is observed for $T > 100K$. We have defined T_c and T_{irr} as $\rho(T_c, T_{irr})/\rho(100K) = 10^{-3}$. Using this criteria we obtain for the measurement shown in Fig. 2.11 $T_c = 91.8K$ with a ΔT_c, where $\Delta T_c \quad T_c^{onset} - T_c^{drop}$, $\sim 1.9K$, indicating the good quality of the film. T_c^{onset} corresponds to the temperature at which the resistivity diverges from the linear ohmic behavior while T_c^{drop} is defined as the temperature at which the resistivity achieves the experimental offset.

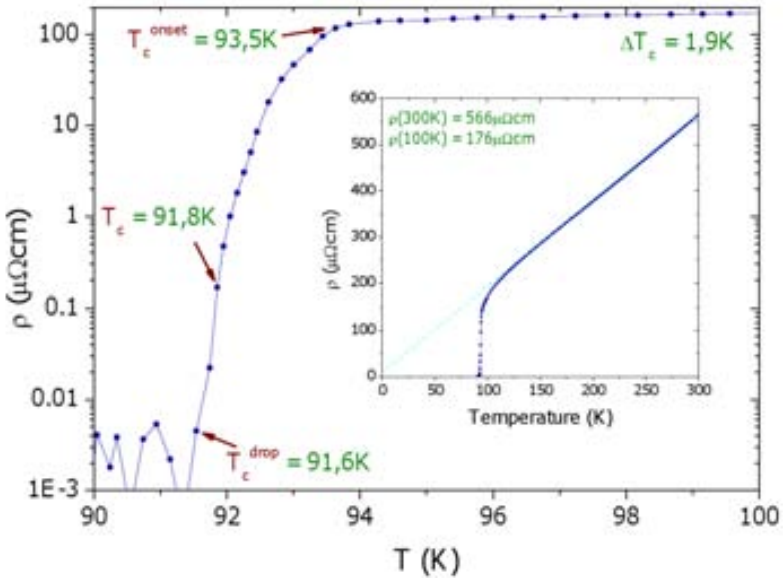

Figure 2.11.: $\rho(T)$ curve measured for a $YBCO$ film. T_c is obtained by using the $\rho(T_c)/\rho(100K) = 10^{-3}$ criterion. Inset shows the linear behavior of the curve where the ohmic resistance in the normal state can be observed.

Critical current density

Voltage drop as a function of applied current is measured in order to determine the critical current density of our samples. Electrical current is increased from 0 to I_{max} in steps of $I_{max}/256$. In order to avoid damaging the sample by injecting too much electrical current, the voltage drop is limited at $3\mu V$ during the measurement.

As commented in sec. 1.3, the $V(I)$ curves of a superconducting material are highly non linear and typically described by a power law behavior, $V \propto I^n$[5]. Ideally, the critical current (I_c) is defined as the maximum current that the superconductor can sustain without dissipation. Experimentally, voltage drops at the nanometric scale are always

[5]In sec. 1.3 we presented the relation $E \propto J^n$ however, they can be transformed to $V \propto I^n$ with geometrical factors.

measured due to offset-measurement devices and so a criterion should be used to determine I_c. The most extended criterion used to define I_c is the current needed to obtain an electrical field of $1\mu V/cm$ where the electric field is $E = V/l$, being l the distance between voltage connections. Nevertheless, since we have used short bridges to be able to perform homogenous patterns along the bridge, we used a criterion of $10\mu V/cm$ (Fig. 2.12). It is important to remark that, due to the exponential form of the $E(J)$ curve, the obtained J_c $(= I_c/t_s w)$ values are almost independent of the criterion used.

In this thesis, $E(J)$ curves will be measured at different values of applied magnetic field, temperature and sample orientation with respect to the c-axis of the $YBCO$, obtaining therefore different dependences of J_c at different conditions.

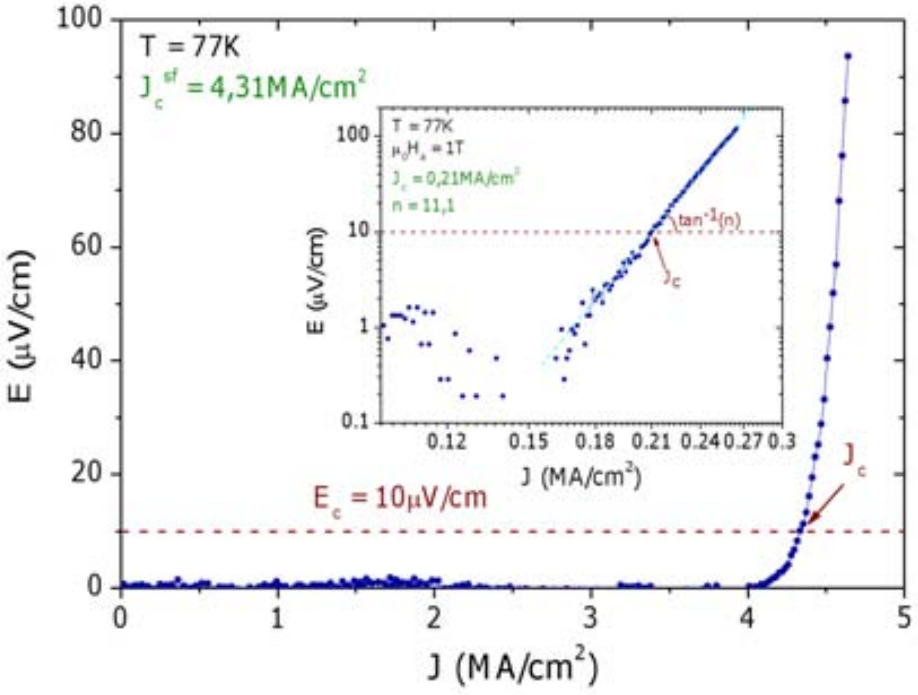

Figure 2.12.: $E(J)$curve of a $YBCO$ thin film at $77K$ and self field showing a critical current density of $4.31MA/cm^2$. Inset shows the log-log representation of the $E(J)$ curve at $77K$ and $1T$ where the slope on the creep regime at $J = J_c$ is the n parameter.

Another parameter which contains information about the pinning properties of the material is the n value [69]. Experimentally, this value is defined as the derivative of the logarithmic of the electric field versus the logarithmic of the current density at the point of the critical current density, (Fig. 2.12$-inset$). As Sun et. al. proposed [111], this parameter is related with the magnetic flux relaxation.

2.3.2.3. Transport measurements at ultra-high magnetic field

In order to perform the experiments to determine the H_{c2} line, it is necessary to use a ultra-high-field-electromagnet system, in our case $\mu_0 H_a < 65T$, due to the strong increase

of the upper critical field when temperature is reduced [6].

Pulsed magnetic fields are generated by a cooper coil immersed into a methacrylate box containing nitrogen liquid. The magnet is powered by a $1.6MJ$ and $10kV$ capacitor bank and the overall pulse width is about $20ms$. Sample is mounted in a external support which allowed to connect it with the equipment external wires. Due to the brief pulse, fast measurements should be performed and as a consequence high electrical current frequencies are needed. External wires should be as close as possible in order to avoid autoinductive phenomenons.

The experimental data is recorded on a digitizer using a high-resolution low-noise synchronous lock-in technique with an applied AC electric current of $10\mu A$ and $110kHz$ along the bridge. An external He cryostat allows the temperature control in the working range. Regarding the measurements performed increasing and decreasing the magnetic field, no heating of the sample was observed in our particular studies.

We have determined the upper critical field, H_{c2}, from the fits of the high-field isothermal $\rho(H)$ measurements by taking the intersection of the normal state asymptote, and the tangent drawn at the zero point of the second derivative (see dashed lines in Fig. 2.13).

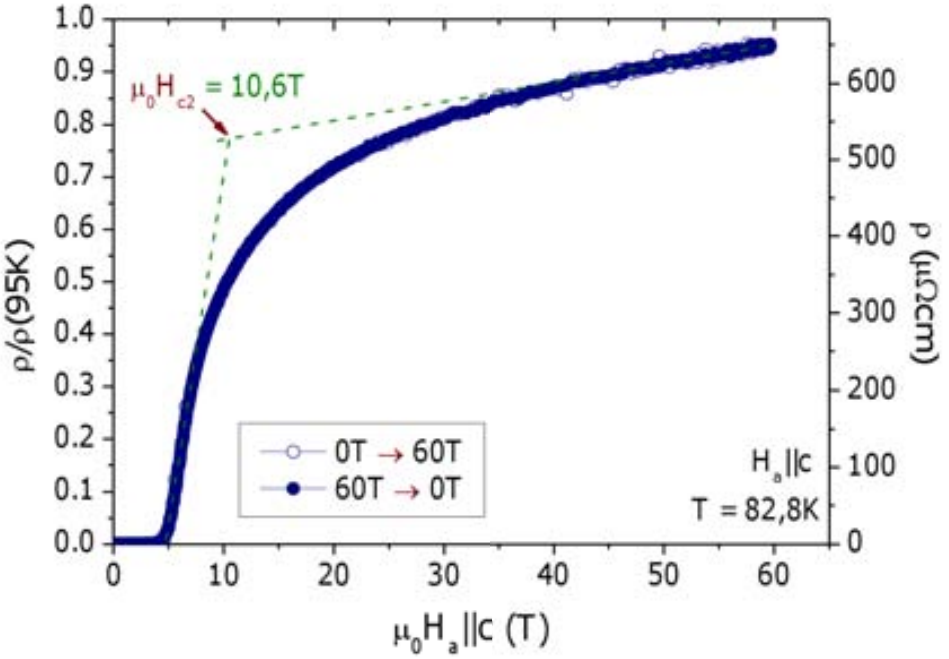

Figure 2.13.: $\rho(H_a)$ curve measured for a $YBCO$ thin film at $82.8K$ to determine de value of $\mu_0 H_{c2}$.

2.3.3. Bitter Decoration experiments

Bitter Decoration technique consists of the observation of magnetic domains at the surface of the material. In the particular case of superconductors, these magnetic domains correspond to the position of vortices. They are detected after the evaporation

[6] These experiments were performed at the National High Magnetic Field Laboratory at Los Alamos National Laboratory ($NHMFL - LANL$)

of a ferromagnetic material, Fe in our case, at the proximities of the material in the superconducting-mixed state.

To do so, we have used a homemade equipment which was designed at the $ICMAB$'s group [100]. It consists of a chamber which is able to work at controlled pressures down to $30mtorr$ ($4Pa$) and temperatures down to $4.2K$. In order to apply the external magnetic field, the equipment also provides a serial of coils which allows the presence of external magnetic field during the experiment.

The Fe evaporation is performed into the chamber with a He pressure of $\sim 200mtorr$ ($\sim 27Pa$). The evaporated ferromagnetic particles collide one each other and with the He molecules, allowing a thermalization of them and forming hosts of large size reaching values of $5-7nm$ [112]. The resulting magnetic moment of these hosts interacts with the magnetic field of the vortices and it results in an attractive force of the hosts towards the position of the vortices. As a consequence, the evaporated material is deposited at the surface of the superconductor decorating the vortex positions.

Forces that control the adhesion between the material surface and hosts are type Van der Waals. This allows the post-observation of the decorated system at room temperature after the evaporated procedure in the mixed state of the superconductor. This observation can be performed through scanning electron microscopy [113], optical microscopy, atomic force microscopy [114] or transmission electron microscopy.

The maximum applied magnetic field that this technique allows is dictated by the modulation of magnetic field produced by vortices. For small magnetic field modulations (obtained at high magnetic fields where vortices are very close to each other), the interaction between vortices and Fe particles decreases and the decoration resolution is lost. The modulation is also determined by the intrinsic characteristics of the material, i.e. the value of . Optimization of the chamber pressure must be performed to obtain good decoration results.

In the case of very thin films, i.e. when $> thickness$, the value of the penetration depth corresponds to $^2/thickness$, which is larger than . Consequently, the vortex field modulation could not be completed, resulting in the presence of magnetic field in all the sample surface, and in the impossibility of vortex discretization through Bitter Decoration experiments.

As a difference from other visualization techniques, like Scanning Tunneling Microscopy or Magnetic Force Microscopy, Bitter Decoration allows the observation of vortices in large areas in the same experiment (in our case $\sim 1cm^2$ due to the dimensions of the chamber). Consequently, interaction between vortices and different defects located at different positions can be studied.

3. Vortex pinning in CSD-YBCO/BYTO nanocomposite thin films

Many efforts have been performed with the aim to improve the superconducting properties of $YBCO$ thin films. A very e cient way to do so is by the introduction of nanoparticles within the structure of the superconductor which provides higher critical current densities [49] and even, in some cases, lower effective anisotropies than standard $YBCO$ films [1]. These new type of materials has been called superconducting nanocomposites. In this section, we will report on our effort in study vortex pinning in different $YBCO$ nanocomposites grown by Chemical Solution Deposition (CSD).

3.1. State of the art

The effectiveness of nanocomposites to enhance vortex pinning was first identified by MacManus-Driscoll in the pioneer work [31]. That work initiated a strong effort within the scientific commuity to reach high performance in nanocomposites. By the introduction of $BaZrO_3$ (BZO) secondary phases, they obtained an enhancement of the pinning properties in $YBCO$ samples grown by pulsed laser depositon (PLD). In this case, the secondary phases form columnar structures compost by self-assembled epitaxial nanodots along the c-axis (nanorods) increasing therefore the pinning properties along this direction. Using the same growth technique, other compositions of nanorods along the c-axis have been achieved in different works [32, 40, 115].

A different situation emerges with nanocomposite films grown by CSD where segregated secondary phases form randomly orientated and distributed nanoparticles within the epitaxial $YBCO$ matrix and, an overall, an enhancement of the pinning properties in a wider region of orientations is achieved [1]. Different compositions can be used to generate these nanoparticles. In particular, in this chapter, Ta metalorganic salts have been added to the $YBCO$ precursor solution which are segregated in the form of Ba_2YTaO_6 ($BYTO$) nanoparticles during the growth process obtaining the final $YBa_2Cu_3O_{7-x}/Ba_2YTaO_6$ nanocomposite as it has been introduced in sec. 2.2.1. These nanocomposites with different amounts of nanoparticles have been compared with the more studied $YBCO/BZO$ nanocomposites and standard films. Furthermore, several $YBCO/Y_2O_3$ and $YBCO/BaCeO_3$ nancomposites, already studied at $ICMAB$ during the lasts years, will be used for comparison.

3.2. Nanostructural defects

Five different samples will be considered in our study: a pristine $YBCO$ sample and four nanocomposites containing 6%, 8%, 10% and 15% molar content of $BYTO$. No significant reduction in T_c has been found when incorporating $BYTO$ nanoparticles in $YBCO$, displaying T_c values $\sim 89-90K$ consistent with the expected non-incorporation of tantalum atoms in the $YBCO$ structure [116]. Fig. 3.1 shows a low magnification Z-contrast TEM image of a $YBCO/BZO$ nanocomposite ($10\%M$) where the presence of nanoparticles is observed in the whole sample.

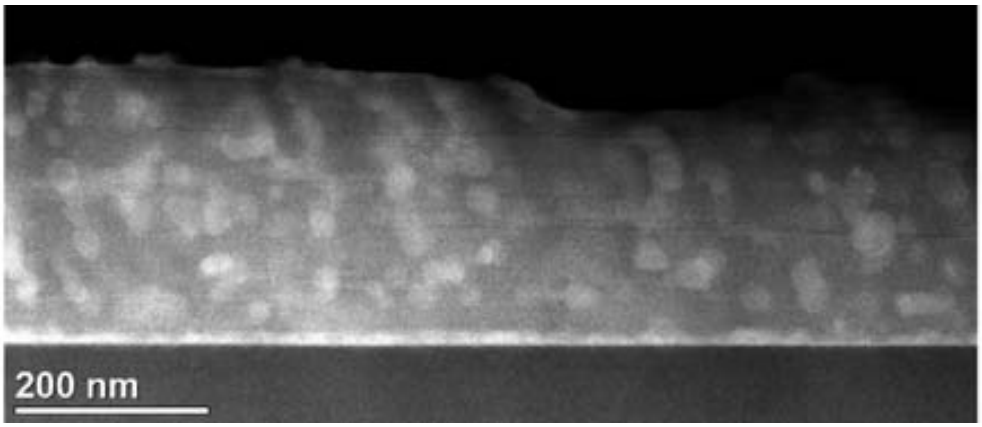

Figure 3.1.: Low magnification Z-contrast image of $YBCO/BZO$ nanocomposite ($10\%M$) where brighter spots correspond to BZO nanoparticles.

Critical current densities of $YBCO$ thin films and nanocomposites depend on the nanoscale defects; their size, length and distribution within the superconductor is of major importance. Consequently, the performance of the material is dictated by their interaction with vortices. Depending on the shape and dimension of microstructural defects, they may act as point-like, linear or planar pinning centers (see sec. 1.2.2). Obviously, defects able to pin a longer lenght of vortex core should provide better pinning e ciency against thermal fluctuations. In CSD nanocomposites, two natural defects appear strongly modified as compared to pristine $YBCO-CSD$ films, mainly induced by the presence of the randomly oriented nanoparticles: stacking faults (SFs) as planar intergrowths along the ab-plane of the $YBCO$, and twin boundaries (TBs) along the c-axis [117].

3.2.1. Stacking faults along the ab-plane

Stacking faults consist mostly of an extra $Cu-O$ chain layer between two $Ba-O$ layers. If they form an ordered array, they result in the $Y_2Ba_4Cu_8O_{16}$ ($Y248$) [118] phase which, in turn, is superconducting with lower $T_c \sim 80K$ [119]. Consequently, measurement of the unit cell of the $Y248$ phase along the c-axis increases from 11.7 to 13.3Å, matching the $Y248$ lattice parameter [120].

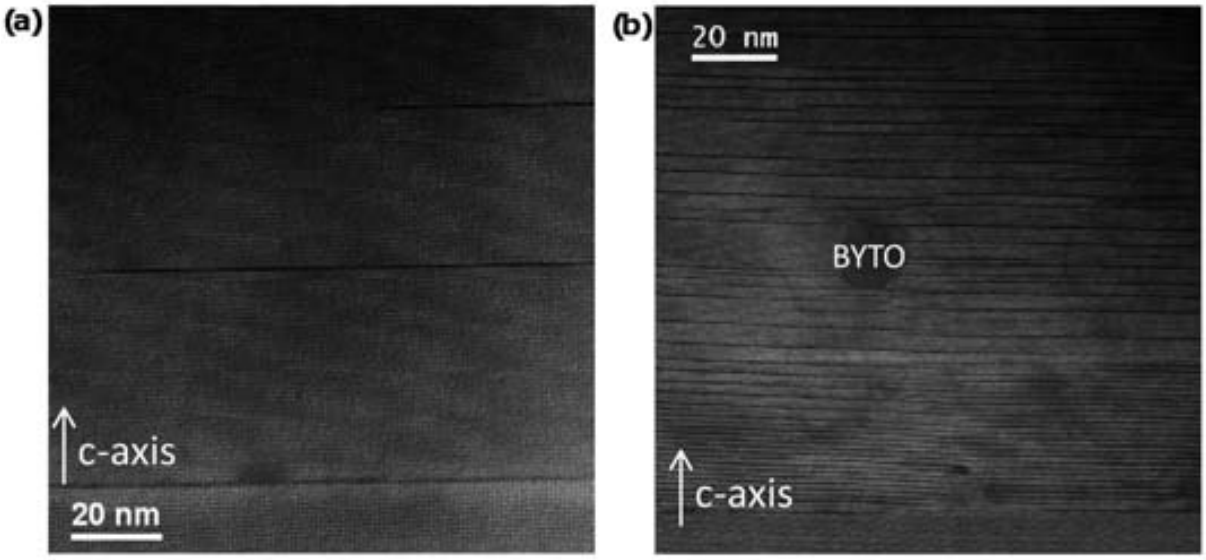

Figure 3.2.: High magnification Z-contrast image of **(a)** $YBCO/Pristine$ sample and **(b)** $YBCO/BYTO$ nanocomposite. Horizontal dark stripes correspond to the $Cu-O$ defects (SF).

Fig. 3.2 shows low magnification Z-contrast Scanning Transmission Electron Microscopy ($STEM$) images for a pristine $YBCO$ films, Fig. 3.2$-a$, and for a typical $BYTO$ nanocomposite, Fig. 3.2$-b$ where intergrowths (horizontal dark stripes in the image) can be observed. A clear difference between the two samples is present since the nanocomposite shows a strong increase of the density of intergrowths.

The use of the high-resolution Z-contrast technique provide atomic resolution images (resolution below $0.1nm$) to clearly observe the formation of intergrowths in the $YBCO$ matrix of nanocomposites near the embedded nanoparticles, see Fig. 3.3 [121]. This intergrowth corresponds to an additional CuO chain identified as a Stacking Fault (SF)

To further analyze the effect of the SFs, Fig. 3.4$-a$ shows a high annular angle dark field ($HAADF$) image where an intergrowth can be observed at the center of the image marked with yellow arrows. In Fig. 3.4$-b$, the analogous low annular angle dark field ($LAADF$) image shows the strained regions at the nanoscale (white zones) emerged from the presence of the SF and strongly localized at the edges of the SF, i.e. at the in-plane partial dislocations that surrounds the SF.

This nanostrain is attributed to elastic distortions of the crystal parameters and it can also be quantified macroscopically by X-ray diffraction through the Williamson-Hall plot method of the $(00l)$ reflections [122]. As it has been demonstrated, the incoherent interface between the randomly oriented nanoparticles and the $YBCO$ epitaxial matrix is the parameter which distorts the superconducting matrix promoting the nucleation of high density of SFs and therefore, the enhancement of the nanostrain [121] (Fig. 3.5). It should be noted that the amount of incoherent interface takes into account the percentage of randomly oriented nanoparticles with respect to the $YBCO$ matrix and the corresponding size of nanoparticles.

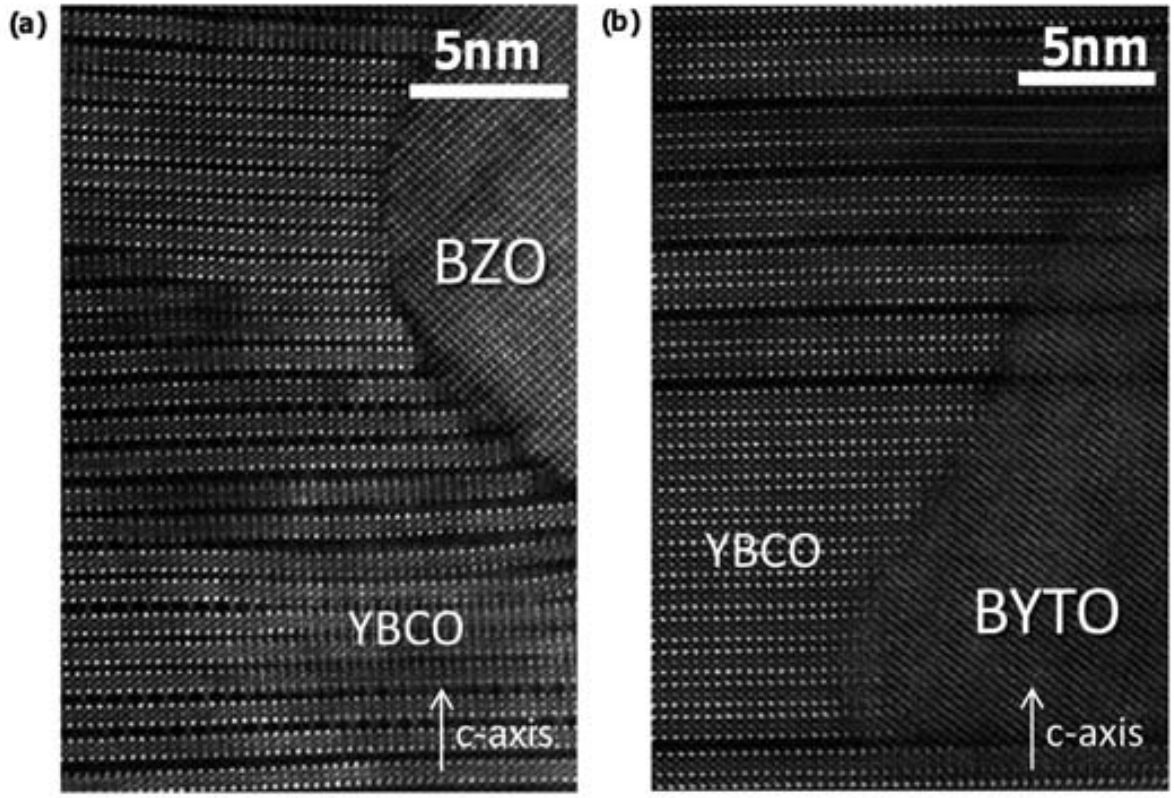

Figure 3.3.: High resolution Z-contrast image where the interface between a nanoparticle **(a)** BZO and **(b)** $BYTO$ and the $YBCO$ is observed. Horizontal black stripes shown the SFs emerging from the nanoparticles.

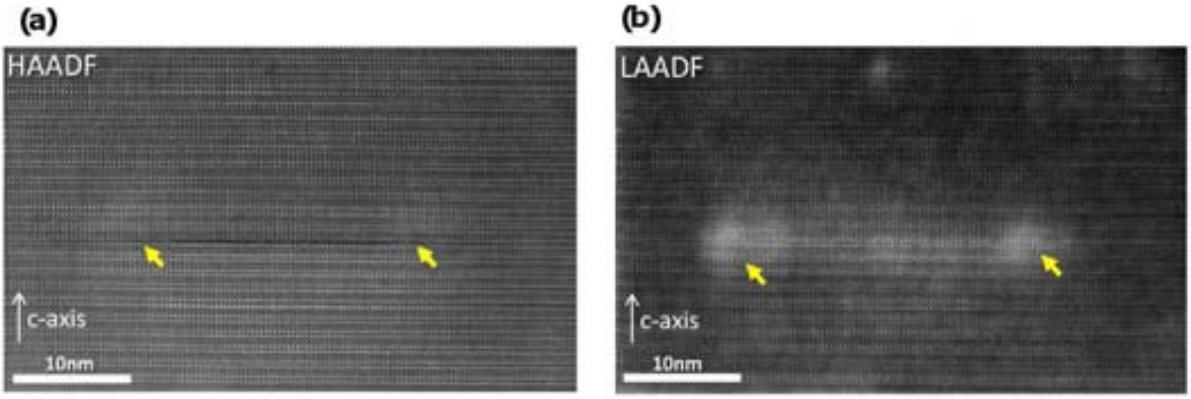

Figure 3.4.: (a) High Annular Angle Dark Field ($HAADF$) image where a SF can be observed in the middle of the image. **(b)** Low Anular Angle Dark Field ($LAADF$) image of the same zone than a) where the distorsion of the lattice parameter, i.e. the strained regions, can be observed as a white "cloud". The yellow symbols point to partial dislocations and arrows to their surrounding strain fields.

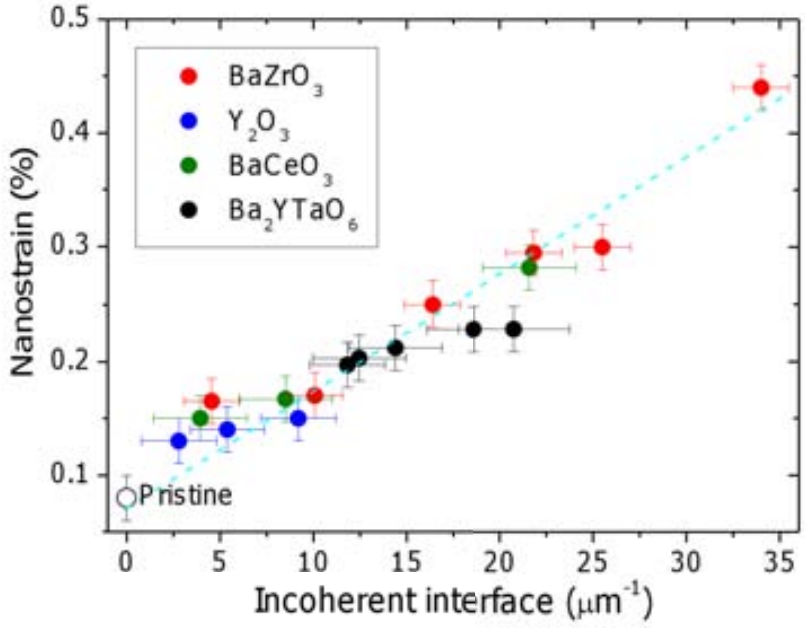

Figure 3.5.: Dependence of the $YBCO$ vertical nanostrain on the incoherent interface of nanoparticles in the different analyzed nanocomposites

3.2.2. Twin boundaries along the c-axis

The structure of a twin boundary consists of a thin plane with disordered and oxygen-hole depleted regions [123]. They are formed during the tetragonal-orthorhombic phase transition which is accompanied by the formation of a-axis and b-axis domains in order

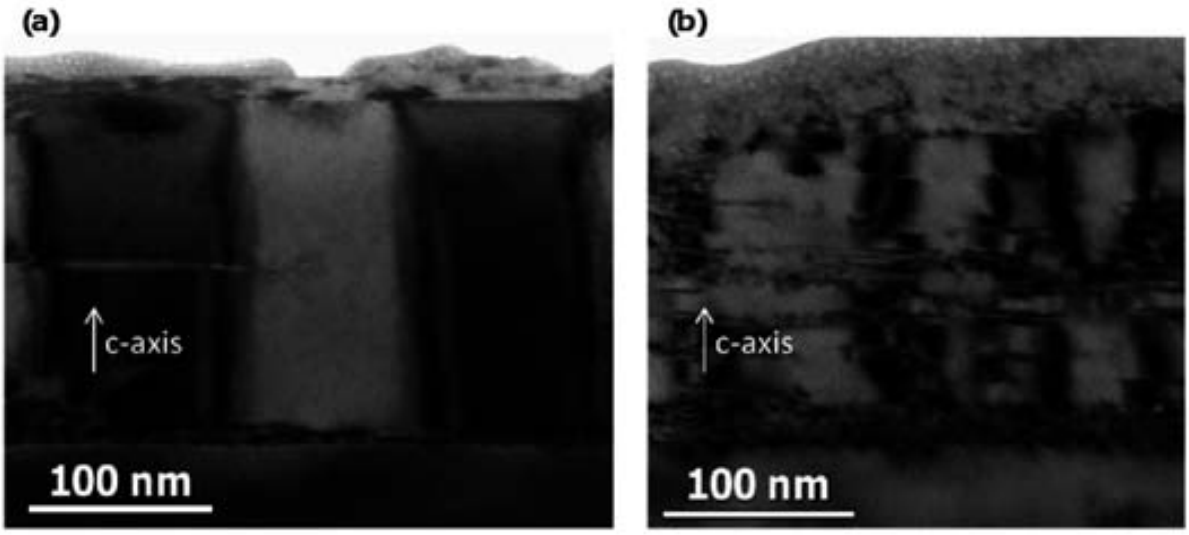

Figure 3.6.: Bright-field TEM image with the $\overrightarrow{g} = (2, 0, 0)$ diffraction vector of a **(a)** $YBCO/Pristine$ sample and **(b)** $YBCO/BYTO$ nanocomposite. Different contrasts correspond to different $a - b$ orientations and the separation between them corresponds to the TBs.

to relieve the spontaneous strains arising from the reduction of symmetry. It means that TBs are formed and oriented in order to maintain a strain compatibility between the a and b orientations of the orthorhombic phase, leading to two twin plane orientations: (110) and $(1\bar{1}0)$.

Fig. 3.6$-a$ shows a cross-sectional TEM image of the pristine $YBCO$ sample where different a-b domains can be observed as different contrasts. Between domains, we find the twin boundaries separated $\sim 50nm$, distance that is smaller than the usual values in bulk $YBCO$ materials or $YBCO$ single crystals (tipically above $\sim 100nm$) [124].

Fig. 3.6$-b$ presents the twin boundaries in the case of a $BYTO$ nanocomposite. In this case, contrary to what we observe for the pristine samples, TBs are completely broken along the c-axis, i.e. they are non-coherent throught the sample thickness. A more detailed view of this non-coherence can be observed in Fig. 3.7 were a high resolution image from the same sample is shown. Different colors represent the different domains and white dashed lines the TBs. It is possible to distinguish each domain in this image since the SFs involve a shift of half unit cell along the b-axis of the $YBCO$, inset of Fig. 3.7. The lenght of the coherent TB extends only $< 5nm$.

As different defects appear at different growth states, the resulting microstructure in a $YBCO$ film will be the result of their mutual interaction. A clear example is that of the TBs which appear at the oxygenation step [97, 98] (last stage of the growth process) interacting therefore with intergrowths and another defects that have been already formed during growth. In the case of our nanocomposites, TBs will encounter a rather complex microstructure formed by the high density of SFs that might alter their size and distribution, yielding to a new pinning landscape [125]. It is important to note that previous work of the group [106] could demonstrate that the SF intergrowth in nanocomposites are mostly formed during growth and not at the oxygenation step. Discussion about the consequences of all these different microstructures on the physical properties will be performed in the next sections.

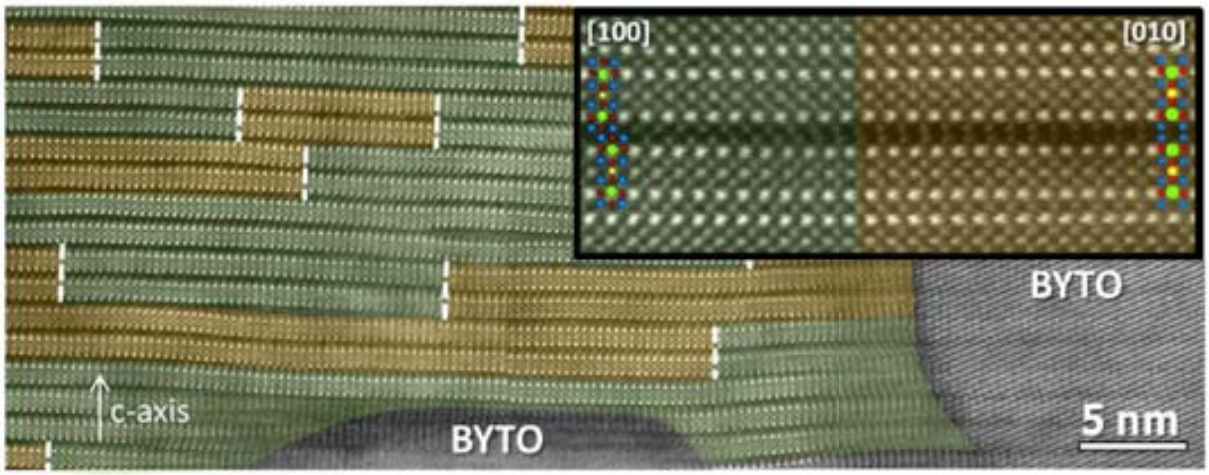

Figure 3.7.: High-resolution Z-contrast TEM image. Green and brown colored regions mark different twin domains, where green corresponds to [100] $YBCO$ zone axis orientation and brown to [010] zone axis. Inset shows a detail of the methodoloy followed to determine each orientation since the $Y248$ intergrowths involves a shift of half unit cell along the b-axis of the $YBCO$.

3.3. Study of the irreversibility line and effective anisotropy

We will first start with the study of the angular dependence of the irreversibility line (IL) in nanocomposites. To do so, we have performed a serial of $\rho(T)$ curves under different applied magnetic fields and orientations, always with the maximum Lorentz force configuration. The criterion used to determine the value of the irreversibility temperature, $T_{irr}(H_a)$, is indicated in sec. 2.3.2.2.

Fig. 3.8 presents the $\rho(T,\theta)$ curves at $\mu_0 H_a = 9T$ obtained for a pristine sample. It should be noted that the $\rho(T)$ curve at $\theta = 180^o$ presents a drop at low temperatures which is related with the presence of c-axis correlated defects [22,23,126–130]. In our case, as we have commented in the previous section, these c-axis correlated defects correspond to TBs.

The full angular behavior of the IL, $T_{irr}(\theta)$, at different applied magnetic fields can be observed in Fig. 3.9. The most important feature observed is the angular variation of the T_{irr} due to the electronic mass anisotropy of the material [13], which give rise to a maximum at $\theta = 90^o$ (when $H_a||ab$). Additional anisotropic pinning contributions are present at this orientation, arising from the periodic pinning potential associated to the layered structure of the material (intrinsic pinning) and the existence of the SFs. At $\theta = 180^o$, $H_a||c$, the presence of a peak at high fields corresponds to an enhancement of the T_{irr} due to the presence of twin boundaries.

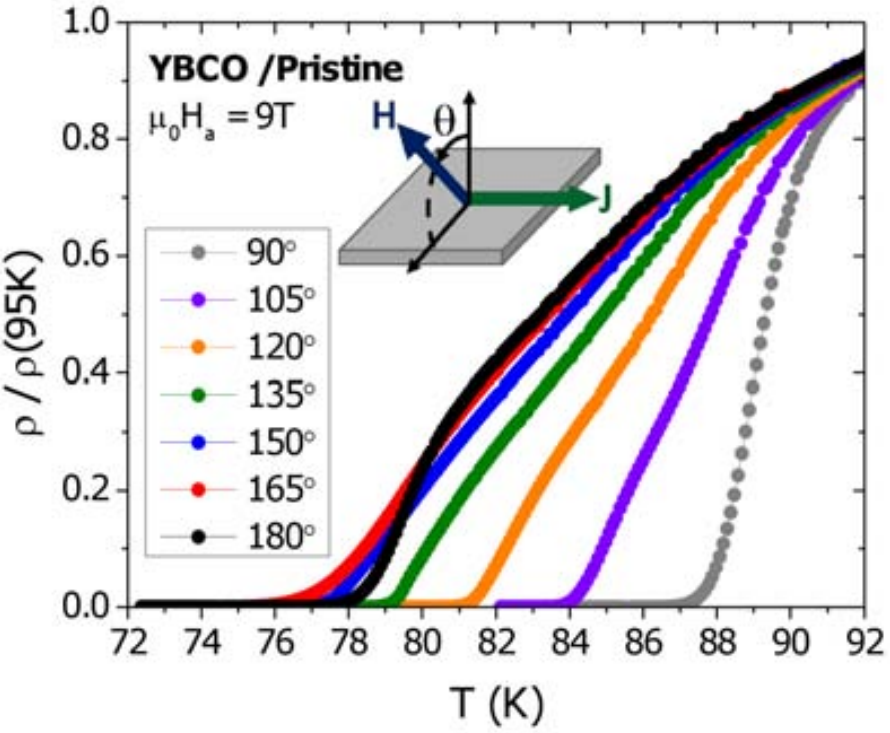

Figure 3.8.: $\rho(T,\theta)$ curves at $9T$ and different orientations for the pristine sample. The detail displays the detail of current and field during the measurement and the rotation angle θ.

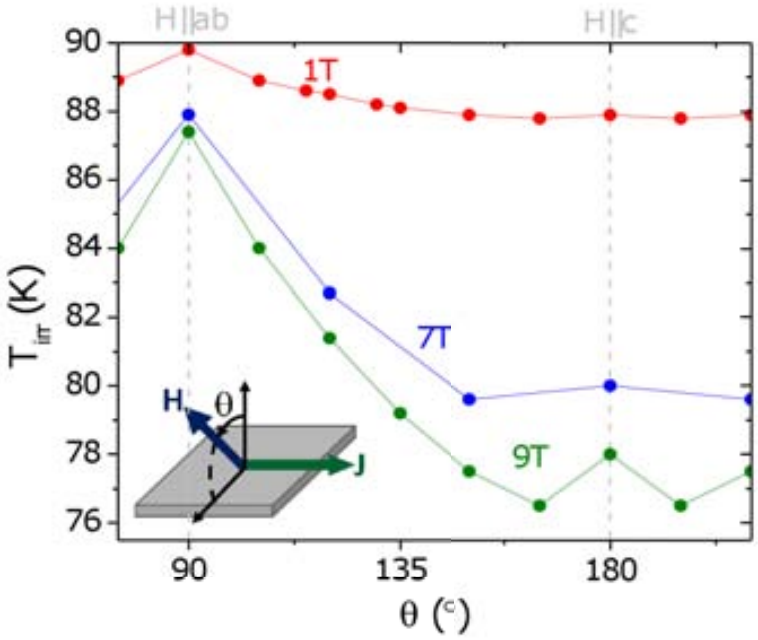

Figure 3.9.: T_{irr} as a function of orientation for $YBCO/Pristine$ sample at different applied magnetic fields.

An additional analysis that can be performed through the angular dependence of the IL is the study of the material anisotropy, which can be determined by using the Blatter scaling approach [18]. With this method, any superconducting parameter which depends on the orientation of the magnetic field with respect to the crystallographic axis of $YBCO$ (θ) can be collapsed into a single isotropic curve by using the anisotropy parameter, $\varepsilon(\theta)$. An example of this is presented in Fig. 3.10 where the IL curves of a pristine $YBCO$ sample are studied. Fig. 3.10$-a$ shows the IL curves obtained at different

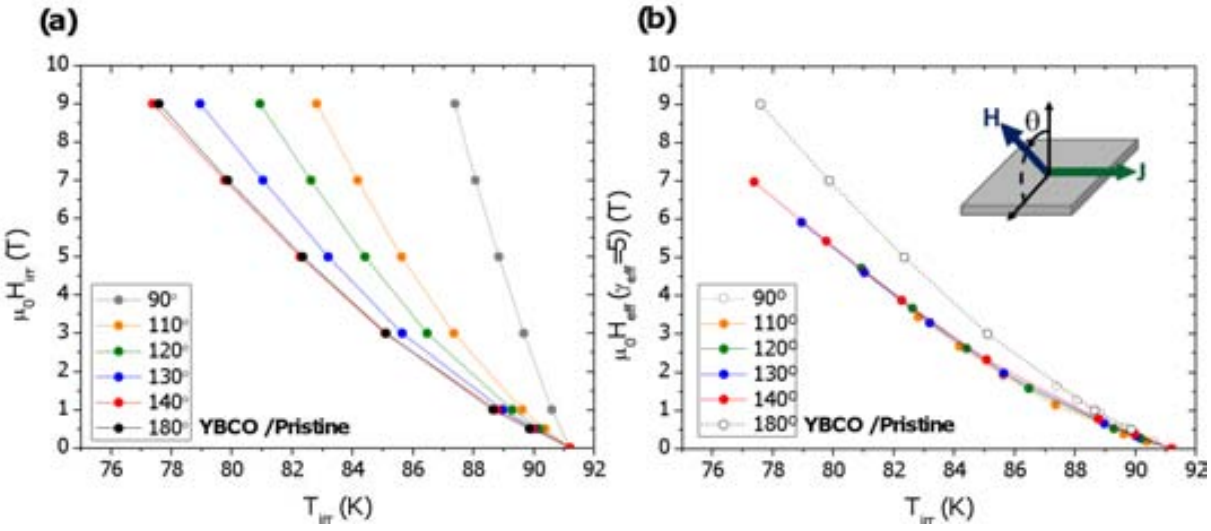

Figure 3.10.: **(a)** H_{irr} as a function of T_{irr} for different orientations for the $YBCO/Pristine$ sample. **(b)** Isotropic collapse with $\gamma_{eff} = 5$ of (a) following the Blatter scaling approach.

applied magnetic fields and orientations. Fig. 3.10$-b$ shows the same plotted curves with the correspondent effective field, H_{eff}, where:

$$H_{eff} = H_a\varepsilon(\theta) = H \quad \overline{cos^2\theta + \frac{1}{2}sin^2\theta} \tag{3.1}$$

being the anisotropic parameter defined as $= \overline{m_c/m_{ab}} = {}_c/{}_{ab} = {}_{ab}/{}_c$. We observe that the IL curves collapse when the value of is equal to 5, which is in agreement with the intrinsic mass anisotropy of $YBCO$ [131]. It should be noted that, for this type of study, only the H_{irr} curves arround 180º and 90º ($H_a||c$ and $H_a||ab$ respectively) do not collapse since at these two particular orientations, anisotropic defects (TBs and SFs) govern the vortex dynamics and therefore, they do not fit the isotropic collapse.

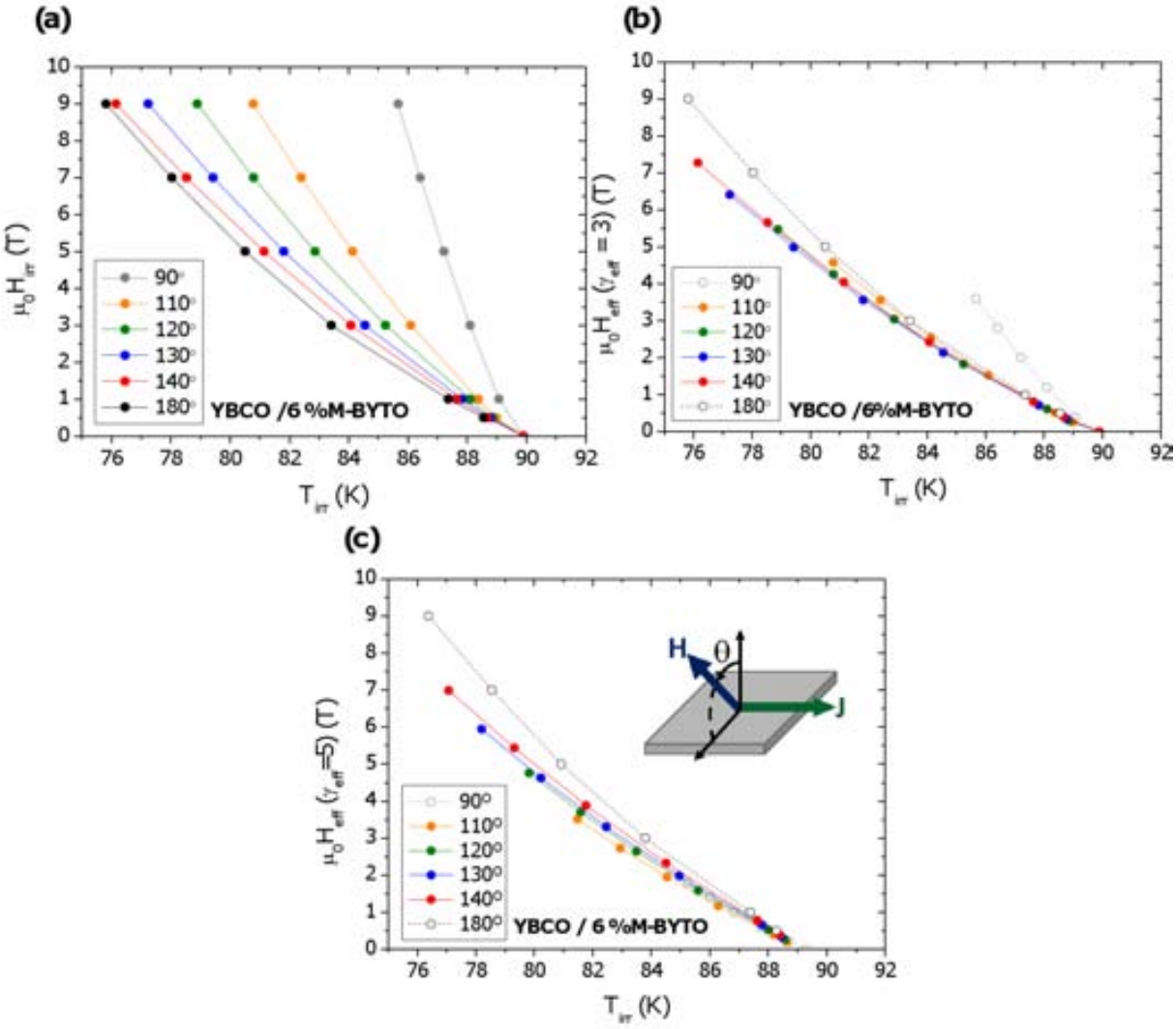

Figure 3.11.: (a) IL curves for different orientations of the $YBCO/6\%M-BYTO$ sample. **(b)** Isotropic collapse of a) with $\gamma_{eff} = 3$ following the Blatter scaling approach. **(c)** Non-isotropic collapse of (a) with $\gamma_{eff} = 5$.

The same analysis has been performed for the $YBCO/6\%M-BYTO$ sample. Again, $H_{irr}(T_{irr})$ curves are presented in Fig. 3.11$-a$ and collapsed in Fig. 3.11$-b$. In that case, the value of which collapses the curves of intermediate orientations is 3, much lower than the one obtained for the pristine $YBCO$ film. It can be observed in Fig. 3.11$-c$ the bad collapse obtained when considering the anisotropic parameter equal to 5. It is important to remark that the values of determined through this analysis are affected by the presence of all isotropic defects and these can vary from sample to sample. Thus, in order to differentiate the intrinsic $= \overline{m_c/m_{ab}} = {}_c/{}_{ab} = {}_{ab}/{}_c$ of the $YBCO$ (which will be analyzed in the next section) with respect to the experimental anisotropic parameter determined through these analysis, we are going to refer this last one as the effective anisotropic parameter, ${}_{eff}$.

By comparing the nanostrain values obtained for each sample and presented in Fig. 3.5, and the ${}_{eff}$ results determined from the Blatter scaling approach, we observe a single plot for the different concentrations of all series with different nanocomposites. Fig. 3.12 indicates that nanostrain is the parameter which controls the reduction of the effective anisotropy.

Thus, we have demonstrated that the pinning landscape present in $YBCO$ films differs strongly if secondary phases (nanoparticles) are spontaneously segregated during the growth process. These nanoparticles can be epitaxial or randomly oriented with respect to the $YBCO$ matrix but, we observed that randomly oriented nanoparticles (nanoparticles that present an incoherent interface) are the main responsible of local nanostrained regions founded in nanocomposites. On the other hand, this nanostrain reduces the effective anisotropy of the material, which depends on the interaction between vortices and defects.

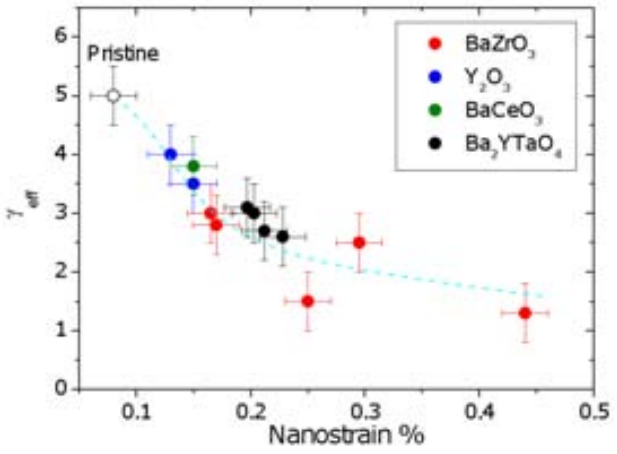

Figure 3.12.: γ_{eff} as a function of nanostrain.

3.4. Study of the upper critical field and intrinsic anisotropy

At this stage we could wonder if the lower $_{eff}$ values obtained for the nanocomposites through the study of the IL are derived from a modification of their intrinsic electronic properties, or if they are from the influence of the different vortex-pinning landscapes. Intrinsic anisotropy, , can be determined from the study of the angular dependence of the upper critical field, H_{c2}. This parameter is intrinsic from the material and thus, it is not influenced by any pinning contribution. To carry out this analysis, it is necessary to use ultra-high magnetic fields, $\mu_0 H_a > 10T$, since the value of H_{c2} can achieve several tens of Teslas near T_c. The study of H_{c2} has been performed through the evaluation of isothermal $\rho(H_a)$ curves at different orientations using a maximum applied magnetic field of $65T$ provided by a pulsed source in a high field installation. Details of measurement are given in sec. 2.3.2.3.

Fig. 3.13$-a$ displays several $\rho(H_a)$ curves measured at different temperatures at $H_a||c$ for $YBCO/15\%M-BYTO$. Grey lines indicate the criterion used to determine the value of H_{c2} as it is commented in sec. 2.3.2.3. In Fig. 3.13$-b$, H_{c2} is plotted as a function of the reduced temperature, $t_r = T/T_c$, for three different orientations: 180º ($H_a||c$), 135º and 90º ($H_a||ab$). As it is expected, due to the $YBCO$ anisotropy, $H_{c2}(90º) > H_{c2}(135º) > H_{c2}(180º)$ for all temperatures.

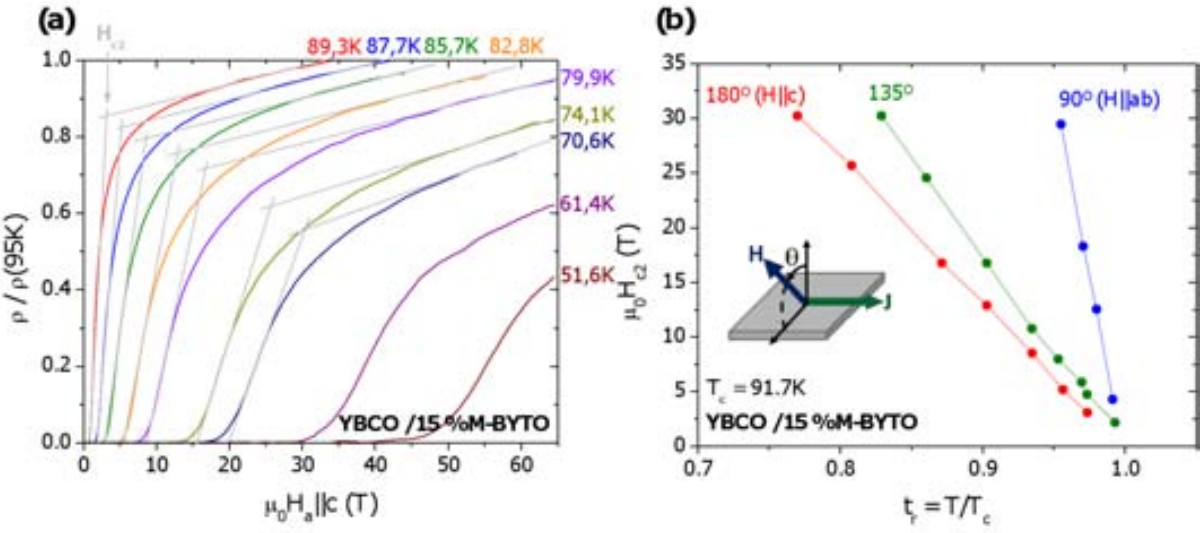

Figure 3.13.: **(a)** Normalized resitivity of $YBCO/15\%M-BYTO$ as a function of the magnetic field. Grey lines indicate the criterion used to determine the value of H_{c2}. **(b)** H_{c2} as a function of reduced temperature for $YBCO/15\%M-BYTO$ for different orientations.

By using the Blatter scaling approach, expression 3.1, we can collapse the obtained $H_{c2}(t_r)$ curves for the three studied orientations using the intrinsic anisotropic parameter, . It should be remarked that, in this case, since the measurement that we are performing is based on the transition normal-superconductor, the value of the anisotropic parameter must be the intrinsic one, , instead of $_{eff}$. Fig. 3.14 plots the obtained H_{c2} collapses for the three orientations for pristine, $6\%M-BYTO$ and $15\%M-BYTO$ samples. As it

is indicated in the plots, the value of which collapses the curves corresponds to 5.0, 5.0 and 5.4 respectively, which is in agreement with the intrinsic gamma of the $YBCO$ [131].

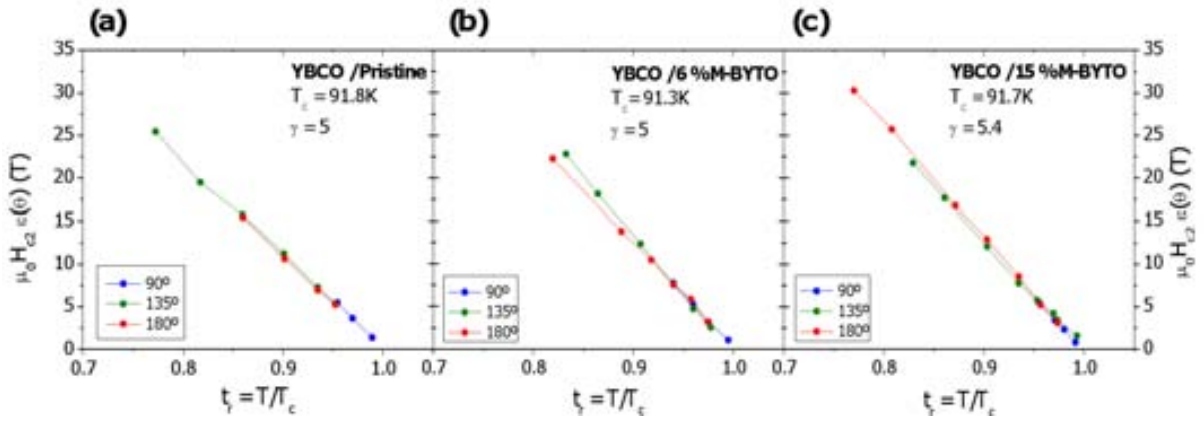

Figure 3.14.: H_{c2} collapse following the Blatter scaling approach as a function of the reduced temperature of **(a)** $YBCO/Pristine$ ($\gamma = 5$), **(b)** $YBCO/6\%M - BYTO$ ($\gamma = 5$) and **(c)** $YBCO/15\%M - BYTO$ ($\gamma = 5.4$).

Notice, that using a value of $= {}_{eff} = 3$ for the case of the $6\%M - BYTO$, which is the value obtained when colapsing the IL, the $H_{c2}(t_r)$ curves do not collapse, see Fig. 3.15. This clearly demonstrates that by the introduction of nanoparticles, the intrinsic mass anisotropy of the $YBCO$ is not modified. These results are in agreement with the results already reported by the group for the case of $BaZrO_3$ nanoparticles [121].

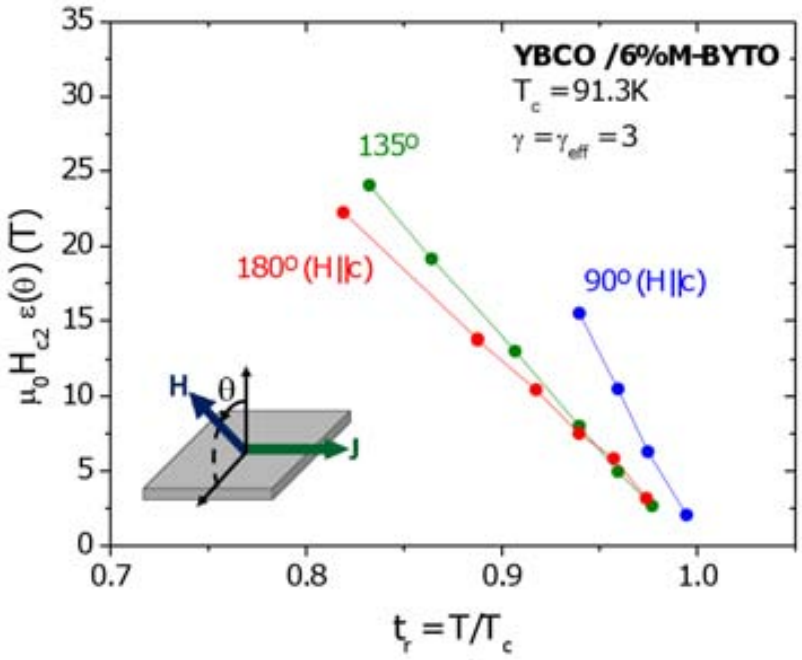

Figure 3.15.: Non-isotropic collapse of H_{c2} with $\gamma = \gamma_{eff} = 3$ for the $YBCO/6\%M - BYTO$ nanocomposite.

Using the obtained values of H_{c2}, we can ascertain if the nanocomposites show any

modification in the coherence lengths by using the following equations [13]:

$$\mu_0 H_{c2}(H_a||c) = \frac{0}{2 \quad ab} \tag{3.2}$$

$$\mu_0 H_{c2}(H_a||ab) = \frac{0}{2 \quad ab \quad c} \tag{3.3}$$

Fig. 3.16 plots the resulting values of the coherence lengths, $_{ab}$ and $_{c}$, along the different directions. As it is shown, in the three samples, the curve $_{ab}/$ corresponds to the curve $_{c}$ as expected from the isotropic collapse. We observe that the curves from different samples are practically equal indicating that the intrinsic properties are not modified significantly if secondary phases are segregated into the $YBCO$ films. Notice also that the results follow the trend descrived by expression 1.1 and the values of $_{ab}(T = 0K) = 1.7 \pm 0.1nm$ and $_{c}(T = 0K) = 0.32 \pm 0.04nm$ are in good agreement with the presented in Tab. 1.1.

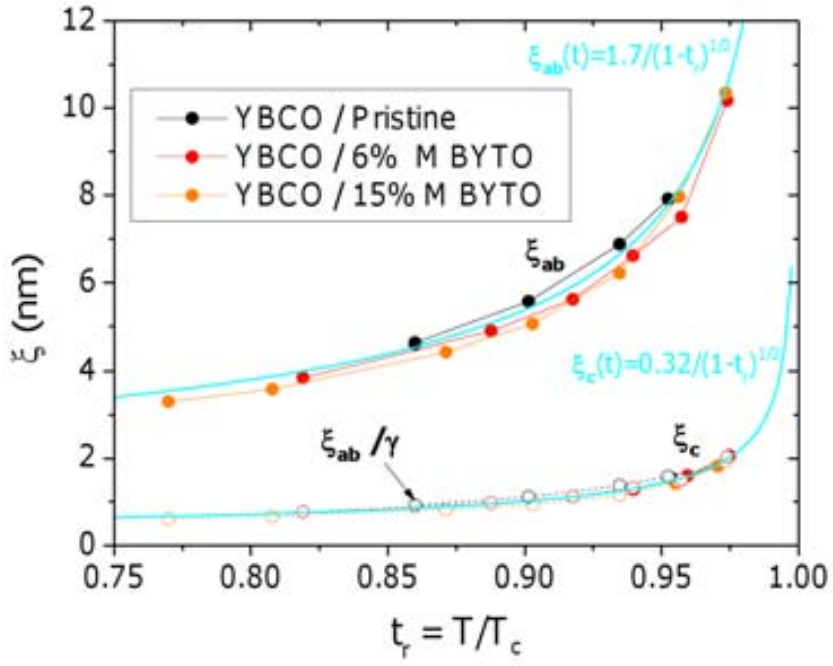

Figure 3.16.: Experimental coherence length along the *ab*-plane and *c*-axis as a function of the reduced temperature.

Therefore, we concluded that, although the interaction between vortices and the different defects reduce the effective anisotropy, $_{eff}$, in nanocomposites below the IL, the intrinsic mass anisotropy, , is not modified.

3.5. Study of Jc angular dependence

The anisotropic dependence of pinning centers can be determined from the analysis of J_c with respect to the applied magnetic field orientation: $J_c(H_a, T, \theta)$ measurements.

Furthermore, the use of the Blatter scaling approach, expression 3.1, allows separating isotropic and anisotropic pinning contributions defined in sec. 1.2.2 and the value of $_{eff}$.

Fig. 3.17 shows the $J_c(\theta)$ curves obtained for the five studied samples at $77K$ and $9T$, $5T$ and $1T$. As it was found in sec. 3.3 with the study of the irreversibility line, curves follow the angular behavior promoted by the effective anisotropy of the $YBCO$ and the presence of different anisotropic pinning contributions. In the case of $\mu_0 H_a = 9T$ (Fig. 3.17$-a$), the peaks at $\theta = 90^o$ and $\theta = 180^o$ are consequence of correlated defects present along these directions. As discussed in sec. 3.1, correlated defects along the ab-planes ($\theta = 90^o$) and c-axis ($\theta = 180^o$) are SFs and TBs respectively. Moreover, at $\theta = 90^o$, the intrinsic pinning contribution also plays an important role [69]. On the other hand, in the curves measured at $\mu_0 H_a = 5T$ and $1T$, Fig. 3.17$-b$ and Fig. 3.17$-c$ respectively, no remarkable peak at $\theta = 180^o$ is observed for any sample. This indicates that TBs are effective just at high fields, i.e. when vortices start to accommodate into them. Contrary, for $\theta = 90^o$, correlated pinning is still observed at $1T$.

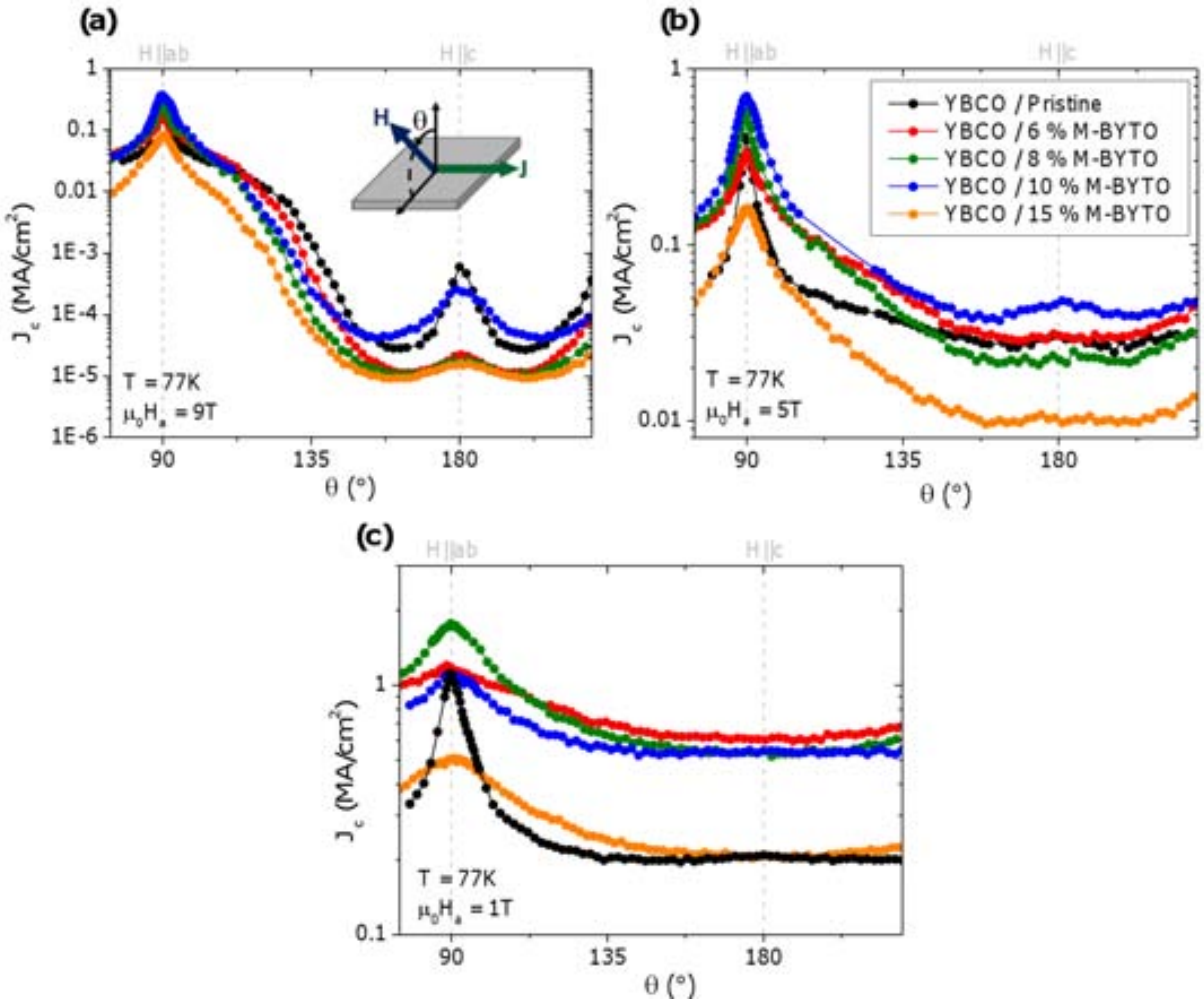

Figure 3.17.: $J_c(\theta)$ of the different samples at $77K$ and **(a)** $9T$, **(b)** $5T$ and **(c)** $1T$.

As we will comment in the next section, at the lowest plotted fields, i.e. $\mu_0 H_a = 5T$ and $1T$ (Fig. 3.17$-b$ and Fig. 3.17$-c$), an enhancement of the critical current density by

the addition of Ta salts is observed for all θ values. However, at $\mu_0 H_a = 9T$ (Fig. 3.17$-a$) the close presence of the IL strongly reduces J_c in all samples. On the other hand, it should be noticed that for the $YBCO/15\%M - BYTO$ sample, the values of $J_c(\theta)$ are below those obtained for the rest of nanocomposites. This reduction is associated to the large amount of $BYTO$ nanoparticles present in the $YBCO$ matrix, which leads to a reduced percolating critical current density. It has been also proved [132] that at high $BYTO$ loads ($> 10\%$), the nanoparticles tend to aggregate being much less e cient as pinning centers.

In order to separate the nature of the different pinning contribution regarding its anisotropy, we use again the Blatter scaling approach now in our J_c-measurements which also allows determining the value of $_{eff}$ [133, 134] as commented in sec. 3.3. Fig. 3.18 shows the collapsed $J_c(H_{eff})$ curves at $77K$ measured for the pristine sample derived from $J_c(\theta)$ measurements at different applied magnetic fields. The correspondent $H_a||ab$ and $H_a||c$ anisotropic peaks (which not follow the isotropic collapse) are indicated for $\mu_0 H_a = 9T$. The value of $_{eff}$ which collapses the $J_c(\theta)$ curves corresponds to $_{eff} = 5$ as expected from the results obtained in sec. 3.3. The cian curve corresponds to the isotropic contribution on the critical current density, J_c^{iso}.

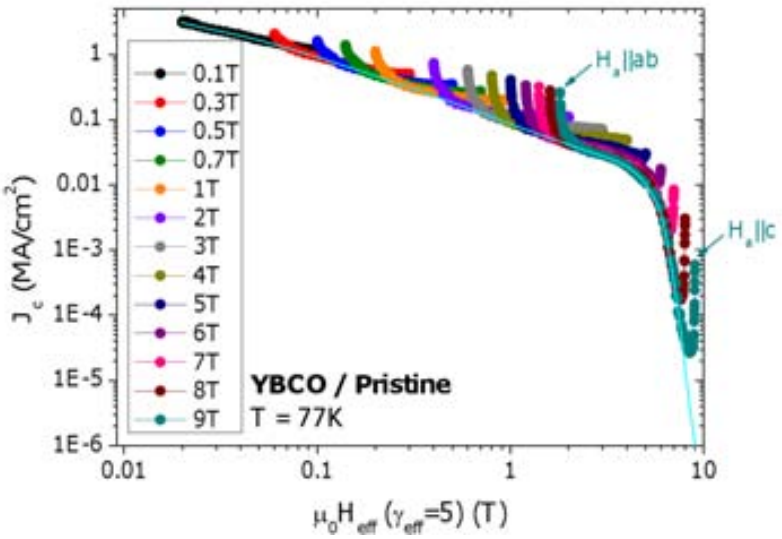

Figure 3.18.: Isotropic collapse with $\gamma_{eff} = 5$ of $J_c(\theta)$ for the $YBCO/Pristine$ sample at different magnetic fields.

The same analysis is performed for the case of the $YBCO/8\%M - BYTO$ nanocomposite. Fig. 3.19$-a$ displays the $J_c(H_{eff})$ collapse at $77K$ at different magnetic fields. In that case, a value of $_{eff} = 3$ is found, in agreement with the results obtained through the study of the irreversibility line (sec. 3.3). As observed in Fig. 3.19$-b$, the use of $\gamma_{eff} = 5$ does not give a good collapse of the $J_c(\theta)$ curves in the nanocomposites.

By the deconvolution of J_c^{iso} at each field, $J_c^{iso}(\theta)$ can be extracted and a separation of different pinning contributions can be obtained. This is displayed in Fig. 3.20 where the curves presented in Fig. 3.17 are now plotted together with the J_c^{iso} contribution, solid

lines. In a first approximation we adopted that:

$$J_c = J_c^{iso} + J_c^{aniso} \tag{3.4}$$

where J_c^{aniso} is the contribution on the critical current density derived from anisotropic defects. Therefore, the differences between the measured J_c and the J_c^{iso} corresponds to the J_c^{aniso} contribution which in the case of $\theta = 90^o$ corresponds to the intrinsic and SFs pinning, and in the case of $\theta = 180^o$ to the TBs pinning. In the case of Fig. 3.20$-a$ where the $9T$ field is studied, except at orientations near 90^o and 180^o, the contribution to J_c is mainly isotropic. Nevertheless, as commented above, at this field and temperature, no effect of nanoparticles is observed since we are very close to the IL.

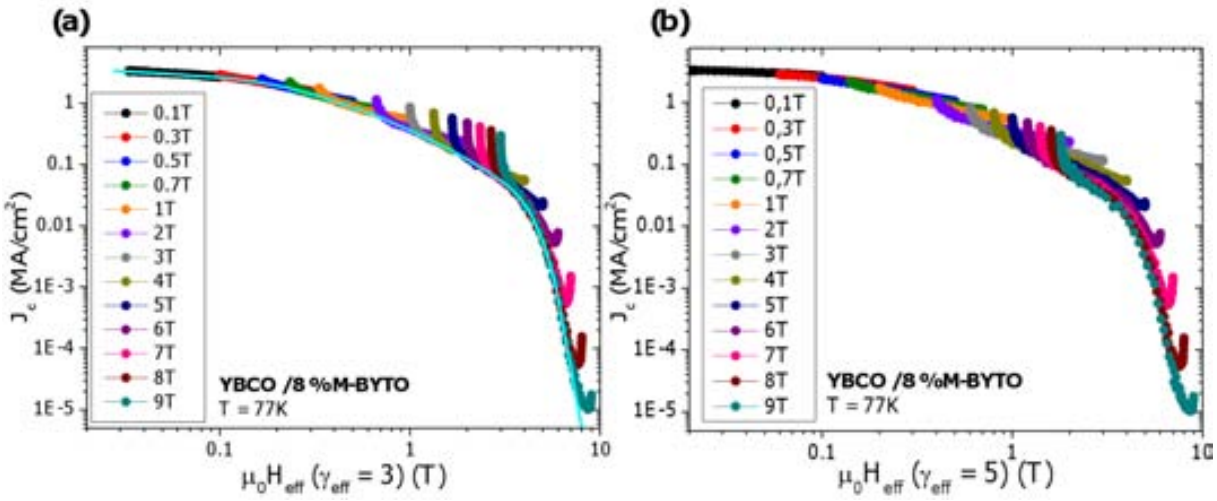

Figure 3.19.: **(a)** Isotropic collapse with $\gamma_{eff} = 3$ of $J_c(\theta)$ of the $YBCO/8\%M - BYTO$ sample at different magnetic fields. **(b)** Non-isotropic collase with $\gamma_{eff} = 5$ of the $YBCO/8\%M - BYTO$ sample.

Regarding the whole angular range at $5T$ and $1T$, Fig. 3.20$-b$ and Fig. 3.20$-c$ respectively, we demonstrate that the enhancement of $J_c(\theta)$ founded in nanocomposites (with an exception of the $YBCO/15\%M - BYTO$ as it has been commented before) is mainly, due to an enhancement of the isotropic pinning contribution. This support the scenario that nanocomposites present additional isotropic defects which contributes to the enhancement of J_c^{iso} and therefore to the overall enhancement of J_c [1]. The increase in J_c^{iso} results in a high improvement of the pinning performances of these materials which turns $CSD - YBCO/BYTO$ nanocomposites into very promising materials for power applications, where high isotropic critical current densities are needed.

Regarding the anisotropy of the material, we have demonstrated that the value of the effective anisotropy, $_{eff}$, is based on the anisotropy of the critical current densities reducing its value in the case of nanocomposites.

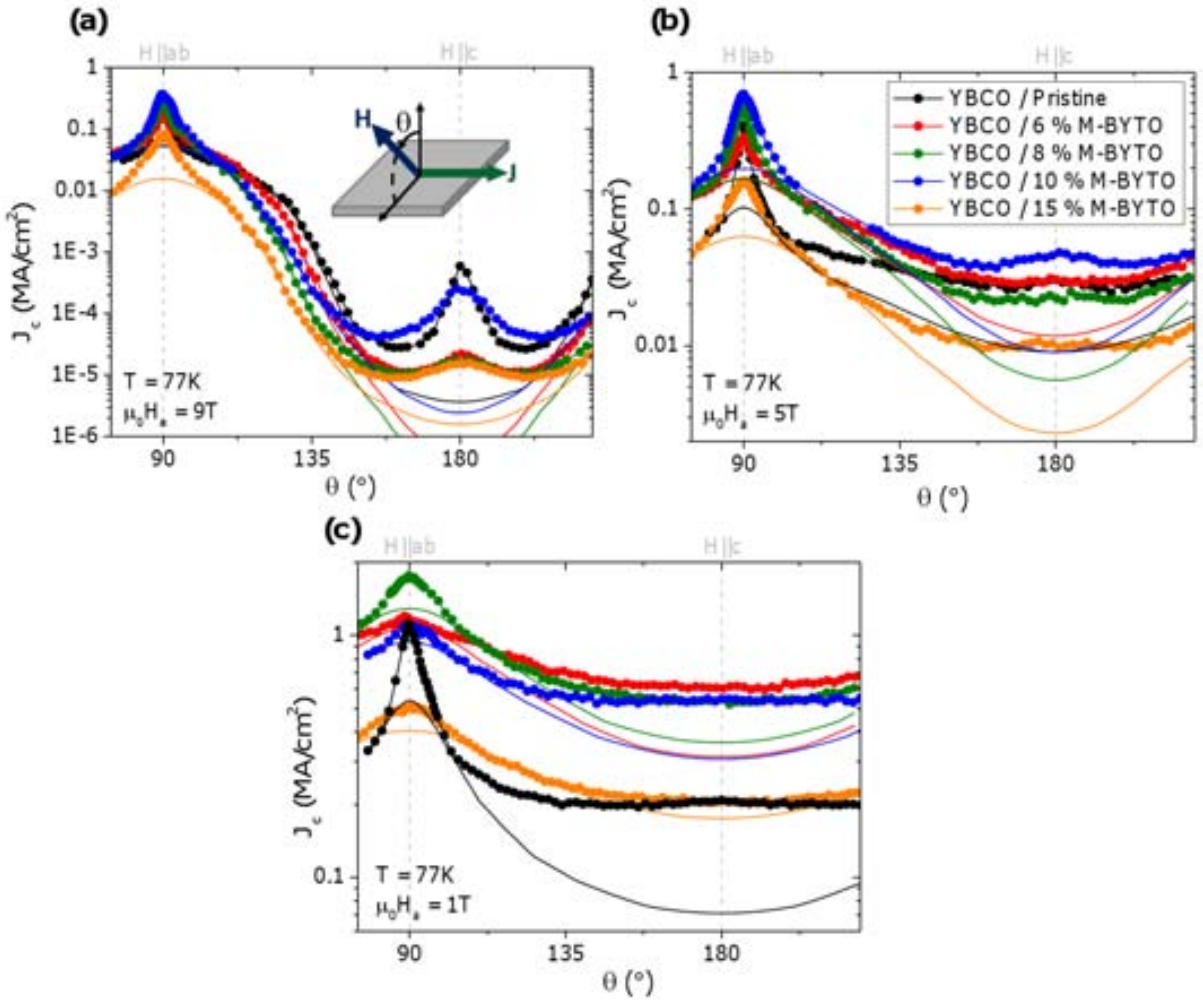

Figure 3.20.: $J_c(\theta)$and $J_c^{iso}(\theta)$ of the different samples at $77K$ and **(a)** $9T$ and **(b)** $5T$ and **(c)** $1T$.

3.6. Study of Jc with applied magnetic field parallel to the c-axis

A further analysis at regions where isotropic/anisotropic defects dominate can be performed by analyzing $J_c(H_a)$ curves at different temperatures for specific magnetic field orientations. In this section, and using the Blatter scaling approach and the temperature dependence of the different pinning centers, we are going to study the J_c contributions present along the c-axis at different regions of the $H_a - T$ phase diagram.

3.6.1. Magnetic field dependence of Jc(Ha||c)

Fig. 3.21 shows the $J_c(H_a)$ curves for several samples measured at $77K$ for $H_a||c$. It is well established that the $J_c(H_a)$ dependence of $YBCO$ thin films in a log-log plot shows three different regions [48,49,55,135–138]. At low fields there is a plateau of J_c associated with a single vortex pinning regime. At intermediate fields, vortex-vortex interactions

become relevant and a collective vortex motion is governed by a power law regime. Once the irreversibility field is approached, J_c drops very fast. In a first approach, the three different regions can be fitted with a single phenomenological equation [138–140] given by:

$$J_c = J_c^{sf} \left[1 + \frac{H_a}{H^+}\right]^{-} \left[1 - \frac{H_a}{H_{irr}}\right]^{2} \tag{3.5}$$

where J_c^{sf} is the self-field critical current density, $\quad$ is the exponent of the power law J_c behavior, H_{irr} corresponds to the irreversibility field and H^+ marks the transition form single-vortex pinning, dominated by the vortex-defect interactions, to the region dominated by vortex-vortex interactions.

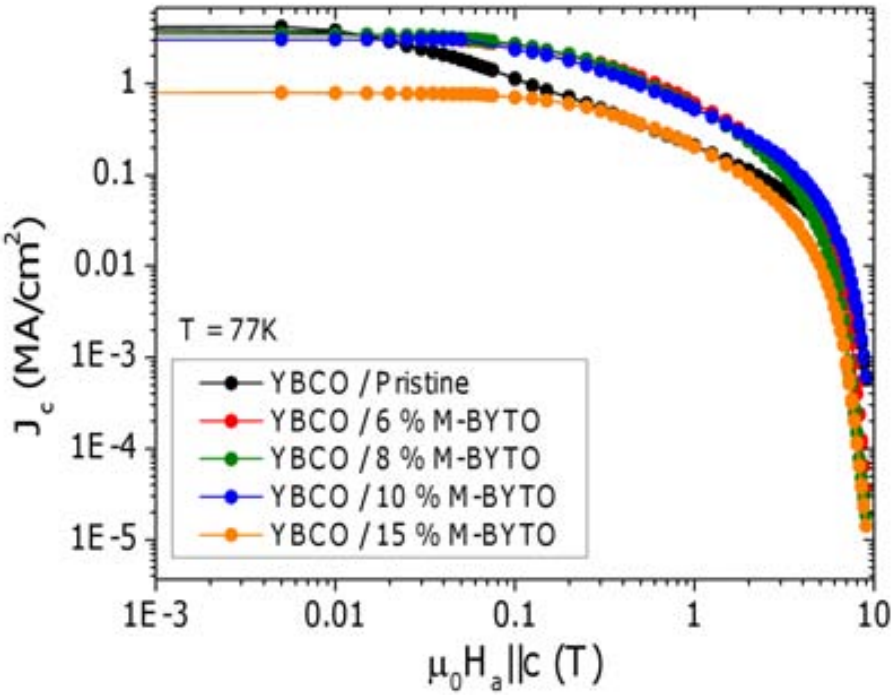

Figure 3.21.: $J_c(H_a)$ of the different studied samples at $77K$.

One of the first features that we observe by comparing the different $J_c(H_a)$ curves shown in Fig. 3.21 is that all samples present similar values of $\mu_0 H_{irr} \sim 9T$ while the values of H^+ are somewhat different. Fig. 3.22 plots the dependence of H^+ with the $\%M - BYTO$ concentration at $77K$. The criterion used to determine the value of H^+ is the magnetic field at which $J_c(H^+) = 0.6 J_c^{sf}$ since we observed that it is the best value that fits the expression 3.5. From Fig. 3.22 we observe that by increasing the amount of $BYTO$ nanoparticles, the crossover field (H^+) increases. This enhancement can be explained due to the increase of effective defects at $77K$ with the addition of $BYTO$ nanoparticles which shifts the vortex-defect interaction region to higher magnetic fields.

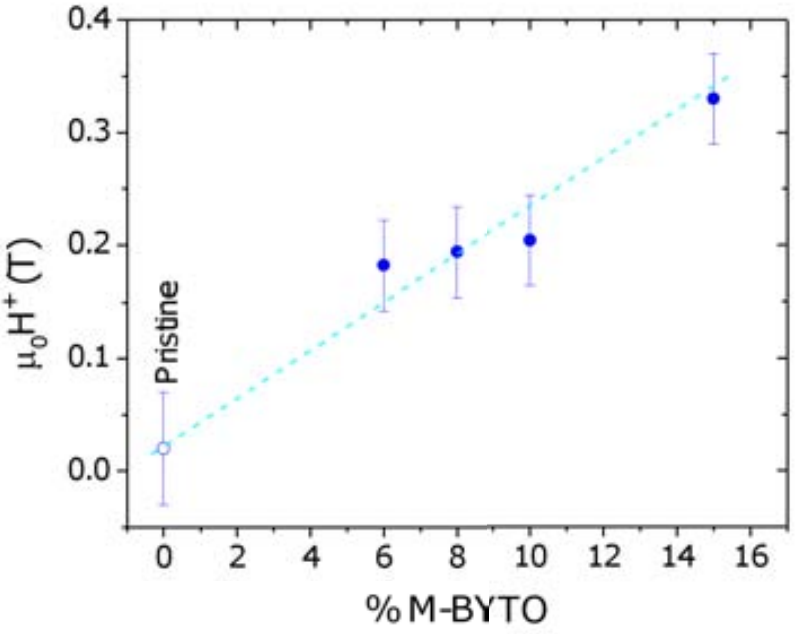

Figure 3.22.: H^+ as a function of $\%M - BYTO$

Using the isotropic/anisotropic contributions obtained from the Blatter scaling approach described in sec. 3.5, we study now their dependences with the magnetic field applied parallel to the c-axis. Fig. 3.23 shows the plots of the magnetic field dependence of the critical current density at $77K$ with its isotropic and anisotropic contributions obtained for the pristine film (Fig. 3.23$-a$) and for the $YBCO/8\%M-BYTO$ nanocomposite (Fig. 3.23$-b$). As it is observed, the incorporation of nanoparticles strongly increases the isotropic pinning contribution at high fields. The crossover between J_c^{iso} and J_c^{aniso} (above which $J_c^{iso} < J_c^{aniso}$) occurs at $\mu_0 H_a = 0.3T$ for the pristine sample, whereas for the nanocomposite the correspondent J_c^{iso} is higher than J_c^{aniso} until $\mu_0 H_a = 2T$.

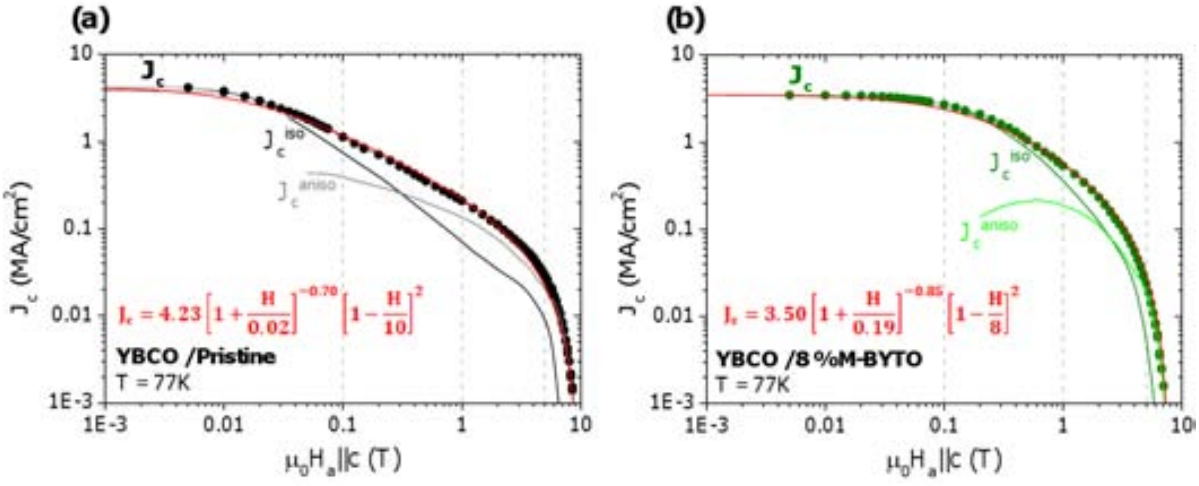

Figure 3.23.: $J_c(H_a)$ at $77K$ with their correspondent J_c^{iso} and J_c^{aniso} for **(a)** $YBCO/Pristine$ sample and **(b)** $YBCO/8\%M - BYTO$ nanocomposite. Red solid lines are fits of expression 3.5.

Red solid lines of Fig. 3.23 are fits of expression 3.5. The value of = 0.7 obtained for the pristine sample is in agreement with other $YBCO$ samples grown by chemical methods [138,141,142]. Concerning the obtained for the $YBCO/8\%M-BYTO$, a similar value of = 0.85 has been obtained.

Fig. 3.24 shows the weight of isotropic J_c (J_c^{iso}/J_c) for samples with different amount of $BYTO$, at different applied magnetic fields (vertical dashed lines in Fig. 3.23) and temperatures. It is clear that, at any field and temperature, the isotropic pinning contribution increases by introducing $BYTO$ nanoparticles in the $YBCO$ matrix. At low fields ($\mu_0 H_a = 0.1T$) J_c is mainly controlled by the isotropic defects; although the ratio J_c^{iso}/J_c for a sample without $BYTO$ nanoparticles is ~ 0.56 at $77K$ (Fig. 3.24$-a$), it increases to ~ 1 with the addition of $BYTO$ particles. At $1T$ and $77K$, where the contribution of anisotropic pinning starts to be important in the pristine sample, the ratio J_c^{iso}/J_c increases with the number of nanoparticles, being almost ~ 0.84 for the sample with $10\% - BYTO$. At high fields ($\mu_0 H_a = 5T$) the anisotropic pinning dominates in all samples although the contribution of J_c^{iso} can be slightly enhanced by the presence of secondary phases. These observations give again evidence that an isotropic pinning is induced in $CSD-YBCO$ nanocomposites. On the other hand, by comparing Fig. 3.24$-a$ and b, one can observe that the isotropic contribution is enhanced at low temperatures. In the next section, a deeply study of the temperature dependence of the critical current density is performed.

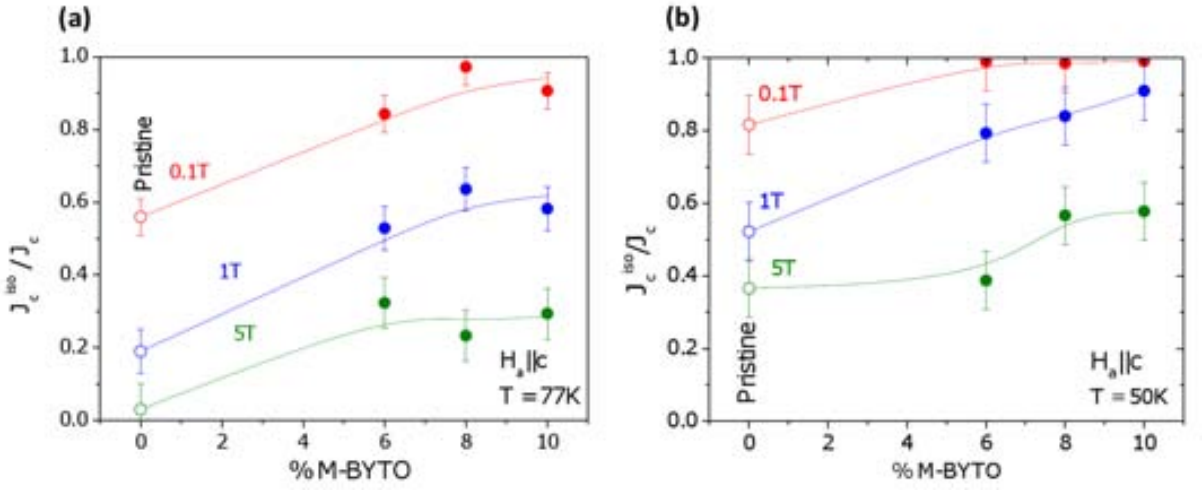

Figure 3.24.: J_c^{iso}/J_c at different magnetic fields as a function of $\%M - BYTO$ at **(a)** $77K$ and **(b)** $50K$.

3.6.2. Temperature dependence of $J_c(H_a||c)$

As we commented in sec. 1.2.2, pinning centers can be separated following different criterions. The criterion used in sec. 3.5 consisted of the separation of the pinning centers regarding its anisotropic behavior. Nevertheless, since isotropic defects involve many kind of defects (oxygen vacancies, nanoparticles...), in this section we are going to separate them depending on their strength (weak or strong isotropic pinning centers). Anisotropic

defects are always acting as strong pinning centers, whereas isotropic defects can be strong of weak depending on its temperature dependence [143–147].

In order to separate weak and strong isotropic contributions we use expressions 1.7 and 1.8 which gives the dependence of J_c^{iso} as a function of their different temperature behavior. By adjusting the parameters $J_c^{weak}(0)$, T_0, $J_c^{strong}(0)$ and T^* a breakdown of the different critical current density contributions can be obtained.

In Fig. 3.25 we plot the J_c values obtained at $7T$ and $0.5T$ at different temperatures for the case of the pristine sample. Dots represent the measured J_c data and the J_c isotropic/anisotropic contributions obtained from the Blatter scaling approach considering the assumption of expression 3.4. Orange and green lines are the fittings correspondent to the weak and strong contributions of J_c^{iso}, respectively. The red line is the sum of both contributions which adjust very well with the experimental J_c^{iso}. Blue line corresponds to the fitting of the strong pinning contribution, arising from anisotropic defects that again, it is well adjusted with the experimental $J_c^{aniso-strong}$. The black line, which fits the total value of J_c, is obtained from the sum of the fittings of the different critical current density contributions. Comparing Fig. 3.25$-a$ and Fig. 3.25$-b$, we observe that for the pristine sample the isotropic contribution is negligible at high temperatures since blue line overcomes the red one. As we will observe, the crossover J_c^{iso}, J_c^{aniso} (from which $J_c^{iso} < J_c^{aniso}$) occurs at lower temperatures for lower applied magnetic fields.

Concerning the characteristic energies obtained through these plots (T^* and T_0), they are between (in Kelvin units) $200 - 85K$ for the anisotropic-strong contribution, $80 - 60K$ for the isotropic-strong contribution and between $7 - 4K$ for the isotropic-weak contribution. These values are in agreement with already calculated values [144–146].

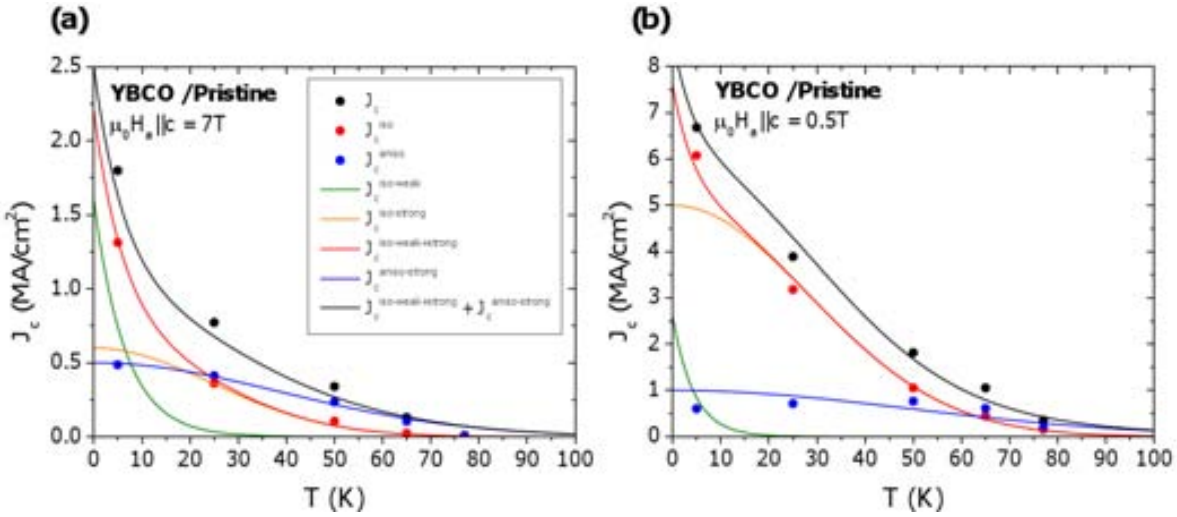

Figure 3.25.: $J_c(T)$ and different isotropic/anisotropic/strong/weak contributions of the $YBCO/Pristine$ sample at $77K$ and **(a)** $7T$ and **(b)** $0.5T$.

By performing the same analysis at different fields and temperatures, we can obtain a phase diagram where the different contributions can be plotted with respect to the total critical current density, J_c. This is shown in Fig. 3.26 where the contributions of $J_c^{iso-strong}$, $J_c^{aniso-strong}$ and $J_c^{iso-weak}$ to the total J_c are compared for the pristine sample

and the $8\%M-BYTO$. Different colors represent different ratios of these contributions. Regarding $J_c^{iso-strong}/J_c$ (Fig. 3.26$-a$ and b), the main difference between samples is that the nanocomposite presents much higher contribution than the pristine sample. This contribution dominates at intermediate temperatures $[15-45K]$ since at higher temperatures the anisotropic contribution mainly controls the J_c values (Fig. 3.26$-c$ and d). At very low temperatures the weak pinning contribution dominates (Fig. 3.26$-e$ and f) and no remarkable differences are obtained between samples. Concerning the $J_c^{aniso-strong}/J_c$ ratio, it is observed that for the pristine sample, the anisotropic contribution is extended at lower temperatures while for the nanocomposite, this contributions falls at much higher temperature ($\sim 60K$) due to the relevance of the isotropic-strong pinning centers. This analysis indicates that by the introduction of nanoparticles, no anisotropic or weak pinning centers are introduced, and that an additional isotropic-strong contribution is appearing controlling most of the H_a-T phase diagram.

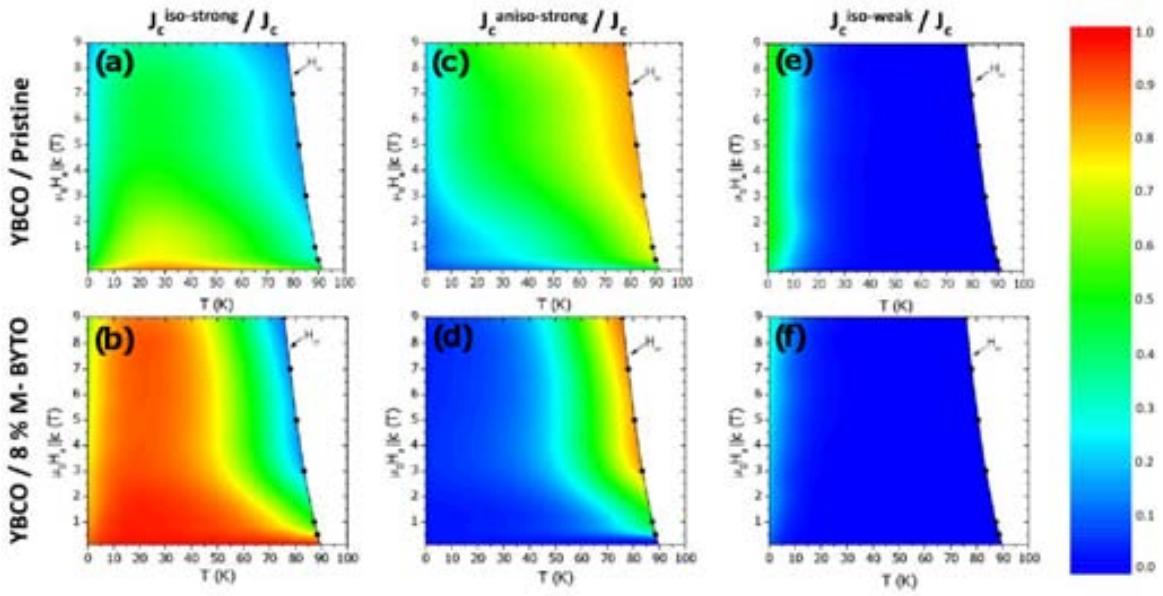

Figure 3.26.: $H-T$ maps for: $J_c^{iso-strong}/J_c$ for **(a)** $YBCO/Pristine$ sample and **(b)** $YBCO/8\%M-BYTO$; $J_c^{aniso-strong}/J_c$ for **(c)** $YBCO/Pristine$ sample and **(d)** $YBCO/15\%M-BYTO$; $J_c^{iso-weak}/J_c$ for **(e)** $YBCO/Pristine$ sample and **(f)** $YBCO/8\%M-BYTO$.

Comparing these results with the already reported for the $YBCO/10\%M-BZO$ [144,146] (Fig. 3.27), we observe an enhancement of the $J_c^{iso-strong}$ contribution in this last nanocomposite with respect to the $YBCO/8\%M-BYTO$. As we will further comment in the next section, this evidences that the isotropic new defects present in nanocomposites are highly present in the $10\%M-BZO$ nanocomposite.

Up to now we have demonstrated that the spontaneous segregation of secondary phases into the $YBCO$ produces nanostrained regions which arise from the formation of SFs. These SFs are promoted by the incoherent interface between the randomly oriented nanoparticles and the $YBCO$ matrix (Fig. 3.5). It has been proved that nanostrained regions are the main responsible of the reduction of the effective anisotropy, $_{eff}$

(Fig. 3.12). On the other hand, the presence of secondary phases allows an enhancement of the isotropic-strong contribution with respect to pristine samples (Fig. 3.26 and Fig. 3.27). In the next section we will further study the relationship between that nanostrained regions and the enhancement of J_c^{iso}/J_c observed in nanocomposites.

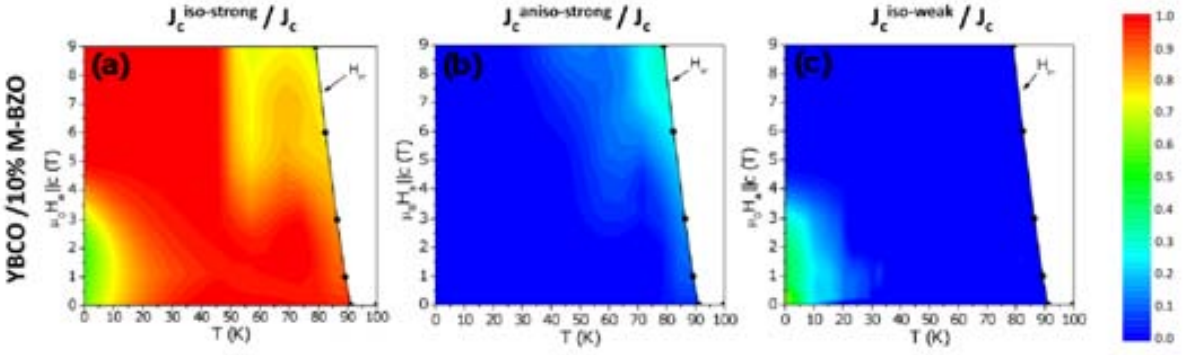

Figure 3.27.: $H-T$ maps of the different pinning contributions for the $YBCO/10\%M-BYTO$: **(a)** $J_c^{iso-strong}/J_c$ **(b)** $J_c^{aniso-strong}/J_c$ and **(c)** $J_c^{iso-weak}/J_c$.

3.7. Role of nanostrain in vortex pinning

A better way to analyze the enhancement of J_c^{iso}/J_c observed in nanocomposites is by plotting the pinning force and its isotropic/anisotropic contributions. The pinning force is defined as:

$$\overrightarrow{F_p} \quad \overrightarrow{F_L} \quad \overrightarrow{J} = \overrightarrow{J_c} \quad = \overrightarrow{J_c} \times \overrightarrow{B} \tag{3.6}$$

and F_p^{iso} and F_p^{aniso}, the correspondent pinning forces of the isotropic and anisotropic contributions, determined by using J_c^{iso} and J_c^{aniso} instead of the total J_c in expression 3.6. Results at $77K$ and $H_a||c$ are plotted for the case of the pristine sample, Fig. $3.28-a$, and for the $8\%M-BYTO$, Fig. $3.28-b$. As it was observed in Fig. 3.23 for J_c, the incorporation of nanoparticles enhances the isotropic contribution of the F_p.

By studding the contribution of the F_p^{iso} as a function of the nanostrain, we obtain a clear relation between these two parameters. This is plotted in Fig. $3.29-a$ where the maximum of F_p^{iso} ($F_p^{max\,iso}$), normalized by the maximum total pinning force (F_p^{max}) is plotted as a function of the nanostrain. For completeness, also different samples with different nanocomposites studied in the past by the group are plotted, too. Notice that the $YBCO/10\%M-BZO$ nanocomposite presented in Fig. 3.27, which presents the highest $J_c^{iso-strong}$ contribution of all studied samples, is the one that presents the highest nanostrain. This correlation demonstrates that nanostrained regions are the main responsible of the enhancement of J_c^{iso} and, in particular, of the enhancement of $J_c^{iso-strong}$.

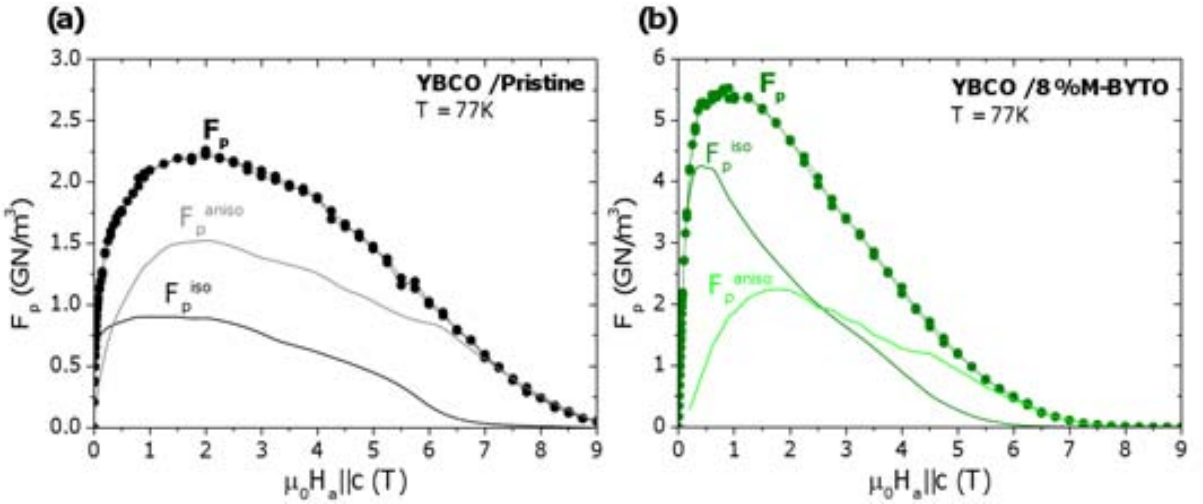

Figure 3.28.: $F_p(H_a)$ at $77K$ with their correspondent F_p^{iso} and F_p^{aniso} for **(a)** $YBCO/Pristine$ sample and **(b)** $YBCO/8\%M-BYTO$ nanocomposite.

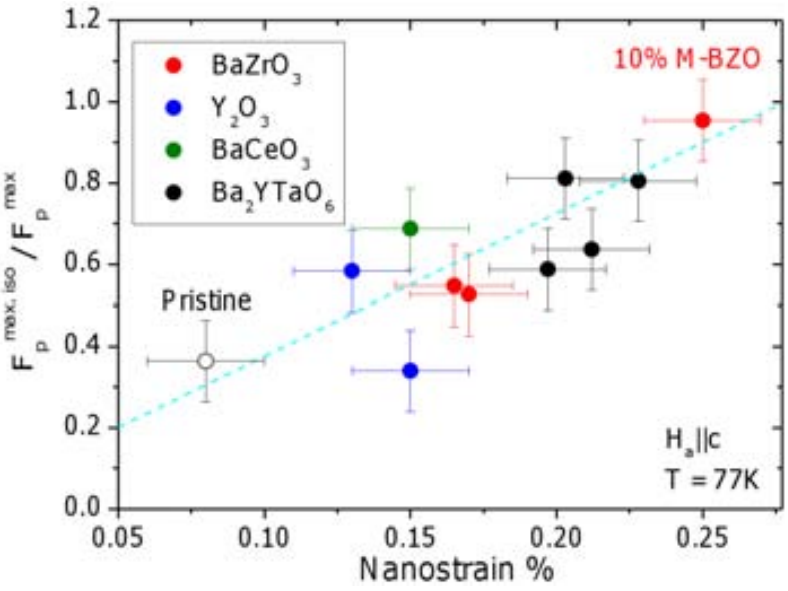

Figure 3.29.: Dependence of the normalized maximum isotropic pinning force of all nanocomposite series as a funtion of the nanostrain.

The existence of a direct influence between nanostrain and the suppression of the superconducting order parameter, which promotes pinning centers, is an unprecedent phenomenon in superconductivity. A new mechanism correlating the two phenomena [148], based on the bond-concentration pairing model, could eventually explain our experiments. This model stresses that a key role in the pairing mechanism should be attributed to the in-plane $Cu-O$ distances, because hole pairing in adjacent Cu position is made possible by the contraction of these bonds. The pair-breaking energy 2Δ is the difference gained by pair formation and the energy of two separated carriers at the bottom of the conduction

band:

$$2\Delta = 4\frac{(t_{CuO})^2}{U_C} - 8t_h \tag{3.7}$$

where t_{CuO} is the transfer integral between a d orbital (Cu) and a p orbital (O) in the presence of doped holes, U_C is the on-site Coulomb repulsion and $8t_h$ is the half-bandwith. The pairs are formed when the first term in the right-hand side of expression 3.7 overcomes the second one and so Δ is positive. Whereas Δ is known to be of the order of $50meV$ in $YBCO$, both terms of the right hand side of expression 3.7 are in the range of $1eV$. Here, t_{CuO} is very sensitive to the $Cu-O$ bond length ($t_{CuO} \propto 1/d^5_{CuO}$) and some elongation of $Cu-O$ ($\sim 1\%$ tensile strain) would quench the pair formation; that is, the second right term would overcome the first one in expression 3.7. This theory has successfully explained the weak-link behavior observed for low-angle ($< 10^o$) grain boundaries in HTS [88] taking into account the tensile strain associated with the dislocations [149,150], and justifies the detrimental effect of the grain-boundary tensile strain on J_c [151].

3.8. Role of twin boundaries in vortex pinning

As it has been commented in sec. 3.2, the structural defects present in $YBCO-CSD$ samples along the c-axis are mainly twin boundaries. However, in the case of nanocomposites, they interact with the already formed stacking faults and the final microstructure is the result of the different defects-interactions.

In this section we are going to study the role of twin boundaries on the vortex dynamics. The influence of TBs on vortex pinning has been a complex issue since different experiments reflect that twin planes can act as strong pinning centers [42–44,46] or channels for easy vortex flow [152,153] depending on the field, temperature or motion direction. In the case of the $YBCO-CSD$ samples studied in this thesis, twin boundaries lead to a rather complex behavior and actually, a crossover from vortex pinning to channeling is observed when the magnetic field and temperature are modified, in analogy with previous reports [154]. Due to the different TBs structure that $YBCO-CSD$ samples present when they interact with the already formed SFs, Fig. 3.6, different TB-vortex interactions will be originated.

In order to study these interactions, we are going to use three different systems: a pristine sample which presents coherent TBs along the whole thickness (Fig. 3.6$-a$), a $YBCO/10\%M-BYTO$ sample which presents a structure of non-coherent TBs along the c-axis (Fig. 3.6$-b$), and a third $YBCO$ sample consisting of a pristine $YBCO$ film grown on a Yttria Stabilized Zirconium oxide single crystal (YSZ) buffered with a CeO_2 layer of $20nm$ ($YBCO/CeO_2$ sample). To carry out the transport measurements, two different $30\mu m$ wide and $200\mu m$ long bridges with standard 4-poing geometry were patterned in each sample. One of them was oriented along the substrate edges ($B0$) and the other one was tilted 45^o ($B45$).

It is important to note that $YBCO$ films grown on LAO (pristine sample and $YBCO/10\%M-BYTO$) grow with a cube-on-cube epitaxial relationship whereas for

the $YBCO/CeO_2$ sample, due to the relative large lattice mismatch between $YBCO$ and CeO_2, the $YBCO$ layer will be rotated 45º in-plane relative to the [100] CeO/YSZ. Thus, TBs planes will be tilted 45º from the substrate edges for $YBCO$ films on LAO whereas they will be parallel (and perpendicular) to the edges for films grown on CeO/YSZ. Fig. 3.30 shows a schematic representation of the TBs domains in $B0$ and $B45$ for different magnetic fields orientations rotated an angle θ. Cylinders corresponds to vortices: in red are illustrated those vortices localized into the TBs and in orange the ones that cross the TBs for a point.

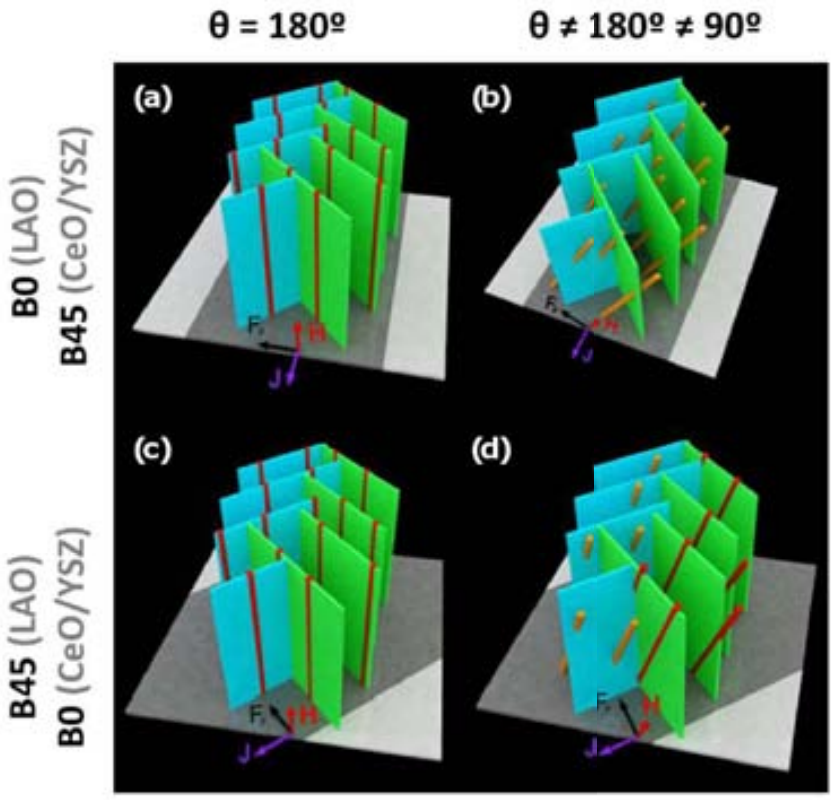

Figure 3.30.: Schematic representation of TBs with different magnetic field orientations rotated an angle θ. $B0$ and $B45$ configurations are indicated for samples containing LAO as a substrate ($YBCO/Pristine$ and $YBCO/10\%M-BYTO$) and for the $YBCO$ layer grown on CeO/YSZ.

3.8.1. Role of twin boundaries in YBCO/LAO pristine films

We will start with the studies performed in the $YBCO/Pristine$ sample which is grown on a LAO substrate and presents a large coherence of TBs along the c-axis. Fig. 3.31 shows several angular transport $J_c(\theta)$ curves measured at $9T$ and different temperatures. In configuration $B0$, during the $J_c(\theta)$ measurement, the magnetic field is rotated forming an angle of 45º with the TBs (Fig. 3.30$-b$) and thus, vortices are confined within the TBs planes just at $\theta = 180^{o}$ (Fig. 3.30$-a$). In the case of $B45$ however, for the whole $J_c(\theta)$ curve, vortices are rotating being always within one of the TBs family planes (red vortices in Fig. 3.30$-c$ and d).

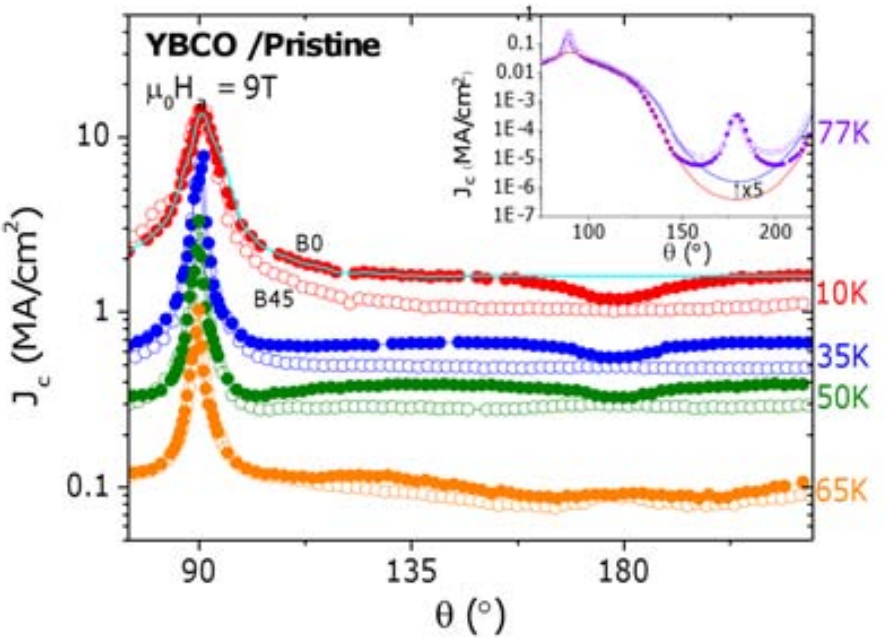

Figure 3.31.: $J_c(\theta)$ at $9T$ and different temperatures for the $YBCO/Pristine$ sample measured at different bridges, $B0$ full dots and $B45$ empty dots. Inset shows the curves obtained at $77K$ where the solid lines represents the isotropic contribution of the J_c.

As observed, different angular dependences are clearly obtained for the two configurations at temperatures $T < 65K$. In $B0$ (full dots), a suppression of J_c is observed when H_a is oriented along the c-axis of the $YBCO$, $\theta = 180^o$, which is associated to vortex channeling along the TB planes [125, 154]. On the contrary, in $B45$, vortices are confined to TBs through all the $J_c(\theta)$ curve and thus, channeling occurs at the whole angular orientations, except for $\theta \sim 90^o$ ($H_a||ab$), giving lower J_c values compared to those obtained in $B0$. At $\theta \sim 90^o$, these two curves coincide since intrinsic pinning blocks vortex channeling along TBs [154].

At higher temperatures ($65K$) TB planes generate directional vortex pinning instead of channeling and therefore, broad peaks are observed at $\theta = 180^o$ for both curves measured on $B0$ and $B45$. These peaks turn out to be more pronounced as we increase the temperature to $77K$ (black open and closed dots shown in the inset of Fig. 3.31). It should also be noted that at $77K$ and at intermediate θ values, $120^o < \theta < 170^o$, a higher J_c is obtained on $B45$ when vortices are rotated within a family of TBs and the Lorentz force is normal to them. In fact, in $J_c(\theta)$ measurements performed on $B45$, there is a family of TBs that contribute as isotropic pinning centers since vortices are rotated within the planes (Fig. 3.30$-d$) and thus, their pinning length does not depend on the magnetic field orientation. Therefore, the overall enhancement of $J_c(\theta)$ on $B45$ may occurs due to the additional isotropic J_c contribution associated to isotropic pinning within the TBs planes (blue line on the inset of Fig. 3.31) in comparison with $B0$, where this contribution does not exist (red line on the inset of Fig. 3.31). In particular, an increase of a factor 5 of this new isotropic contribution is obtained at $\theta = 180^o$ for the $B45$ bridge with respect to the $B0$.

Fig. 3.32 shows the effect of the magnetic field on the angular J_c behavior at $50K$ for

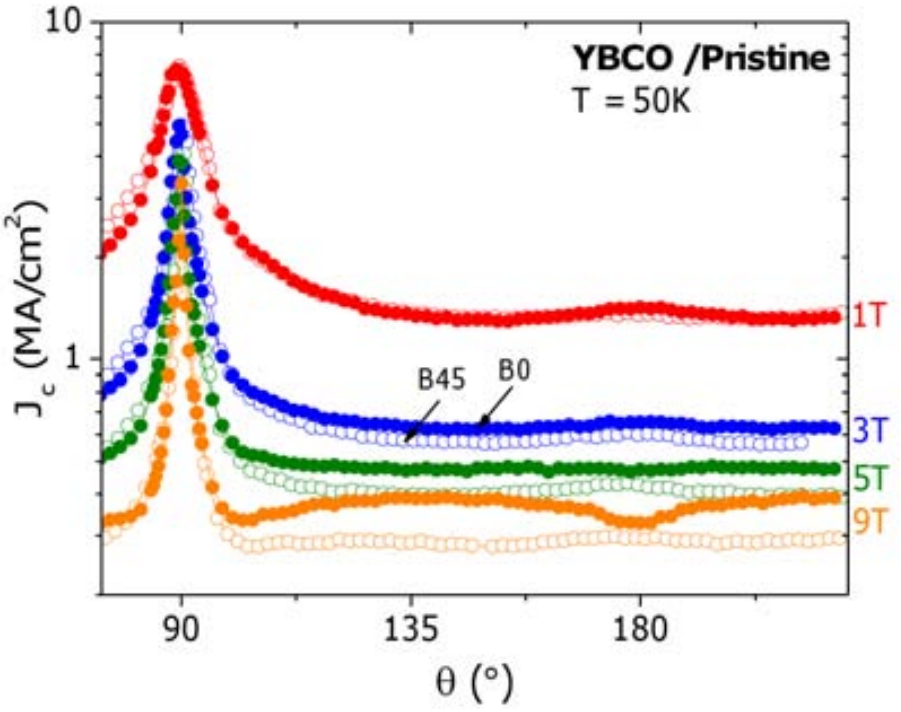

Figure 3.32.: $J_c(\theta)$ at $50K$ and different magnetic fields for the $YBCO/Pristine$ sample measured at different bridges: $B0$ full dots and $B45$ empty dots.

the pristine sample. It can be seen that as the magnetic field is decreased, the minimum at $\theta = 180^o$ is reduced and the difference between $J_c(\theta)$ measured on $B0$ and $B45$ diminishes. In fact, no difference between $B0$ and $B45$ (no effect of TBs plane geometry) is observed at $1T$.

With the aim to quantify the role of TB planes to vortex pinning/channeling for the pristine $YBCO/Pristine$ film, we have plotted in Fig. 3.33 a $\theta - T$ diagram with the contribution of TBs to the J_c for bridges $B0$ and $B45$ at $9T$; Fig. 3.33$-a$ and b, respectively. We have evaluated this contribution by considering the difference between $J_c(\theta)$ measured on $B0$ or $B45$ and the theoretical $J_c(\theta)$ curve that one would measure in the same sample without TBs (cian solid line shown in Fig. 3.31), normalized to the measured $J_c(\theta)$. To estimate this theoretical curve, we have assumed that on samples grown on LAO substrates with the $B0$ configuration, TBs planes just play a role for angles around $\theta = 180^o$ where vortices start to be oriented along the TB plane direction. With this assumption we have disregard the anisotropic pinning contribution of other c-axis oriented defects since we know that TBs are the ones that are mainly governing c-axis vortex pinning in $YBCO - CSD$ films [117].

It is clearly observed from the diagrams that the influence of TBs is confined within $160^o < \theta < 200^o$ when $J_c(\theta)$ is measured on $B0$. In this configuration, at $\theta = 180^o$, J_c can be reduced as much as 40% due to vortex channelling at low temperatures ($10K$) or increased a 98% at high temperatures ($77K$) due to TB correlated vortex pinning. A wider effect is observed when $J_c(\theta)$ is measured on $B45$. In this configuration J_c is reduced more than 30% due to vortex channelling for all θ values 10^o away from the

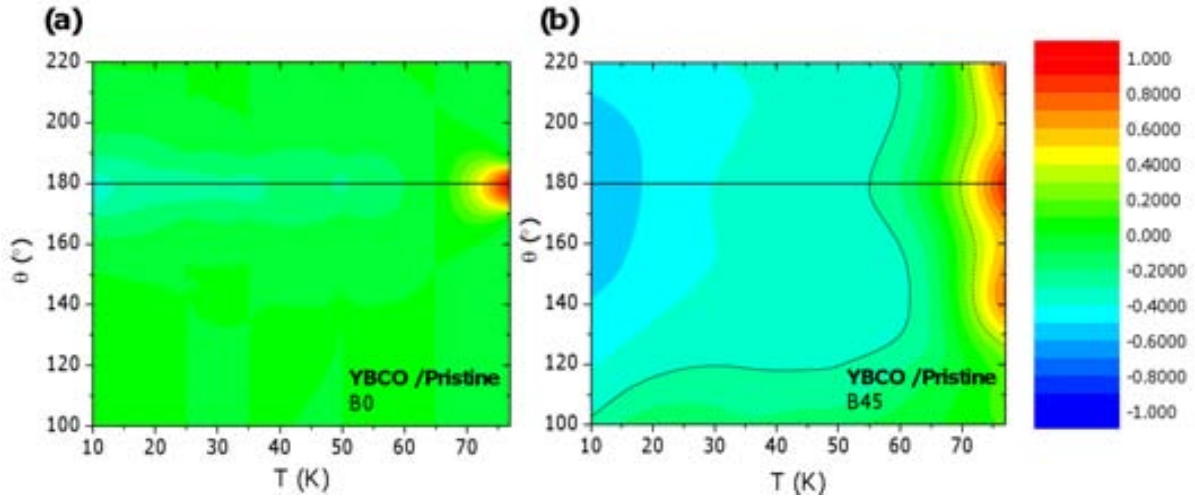

Figure 3.33.: $\theta - T$ maps of the contribution of the TBs to the critical current density in the pristine sample at **(a)** $B0$ bridge and **(b)** $B45$ bridge. Solid and dashed lines represents the 30% reduction/increase of J_c due to the TBs.

ab-peak ($100^o < \theta < 260^o$) at temperatures lower than $65K$ (a 30% J_c reduction is shown as a solid line in Fig. 3.33$-b$). On the contrary, J_c is increased more than 30% for $120^o < \theta < 240^o$ at $T > 70K$ (a 30% enhancement of J_c is shown as a dashed line in Fig. 3.33$-b$). At the maximum pinning/channelling configuration ($\theta = 180^o$) J_c increases a 98% (the same than for the $B0$ configuration) at $77K$ and diminish a 60% at $10K$ respectively.

3.8.2. Role of twin boundaries in YBCO/CeO_2 buffered films

It is clear therefore that depending on the current path orientation one can minimize the reduction of J_c at high fields due to vortex channelling at low temperatures or obtain the maximum pinning forces at higher temperatures. One way to change the current path orientation with respect to TBs planes, in a long length coated conductor where the direction of the current must always be along the direction of the tape, is by changing the substrate architecture which can be done by using specific buffer layers. This is the case of the second system used in this study: the $YBCO/CeO_2$ sample.

In Fig. 3.34 we show different $J_c(\theta)$ curves measured at $25K$ and $50K$ on $B0$ and $B45$ for the $YBCO/CeO_2$ sample where TBs planes grow parallel, and perpendicular, to the substrate edges. With this configuration, the bridge that keeps vortices within a family of TBs planes during the whole $J_c(\theta)$ curve is $B0$ and thus showing the lower $J_c(\theta)$ values due to vortex channelling. On the contrary, a channelling minima at $\theta = 180^o$ is observed for $B45$ when vortices are aligned with the TBs planes. Notice that therefore, the results obtained in the pristine sample for $B0$ are those obtained in the $YBCO/CeO_2$ for $B45$ and vice versa.

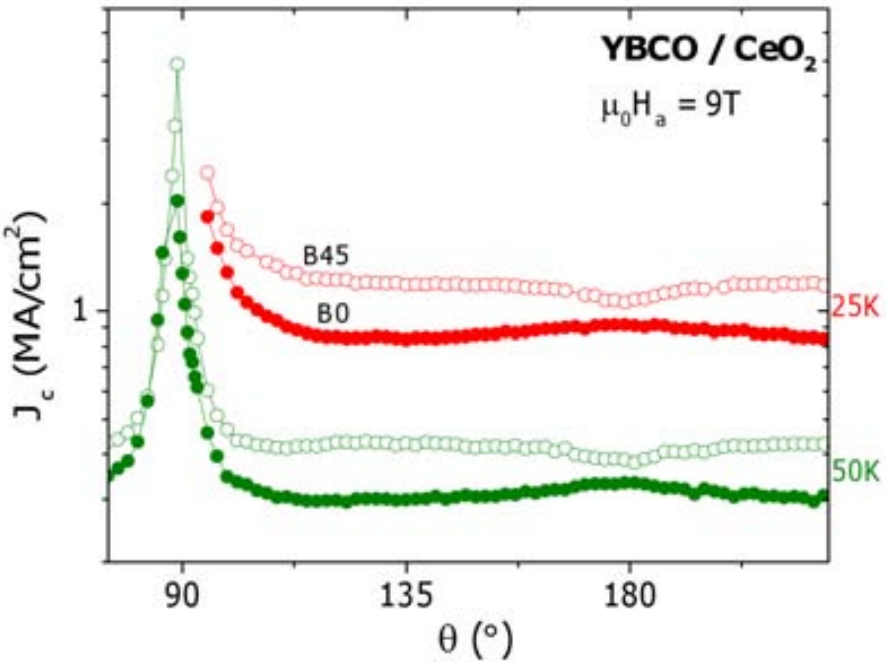

Figure 3.34.: $J_c(\theta)$ at $9T$ and $25K$ and $50K$ for the $YBCO/CeO_2$ sample measured at different bridges: $B0$ full dots and $B45$ empty dots.

3.8.3. Role of twin boundaries in YBCO nanocomposite films

In the case of nanocomposites, since they present a structure of non-coherent twin boundaries along the c-axis (Fig. 3.6$-b$), a different situation emerges. Fig. 3.35 shows

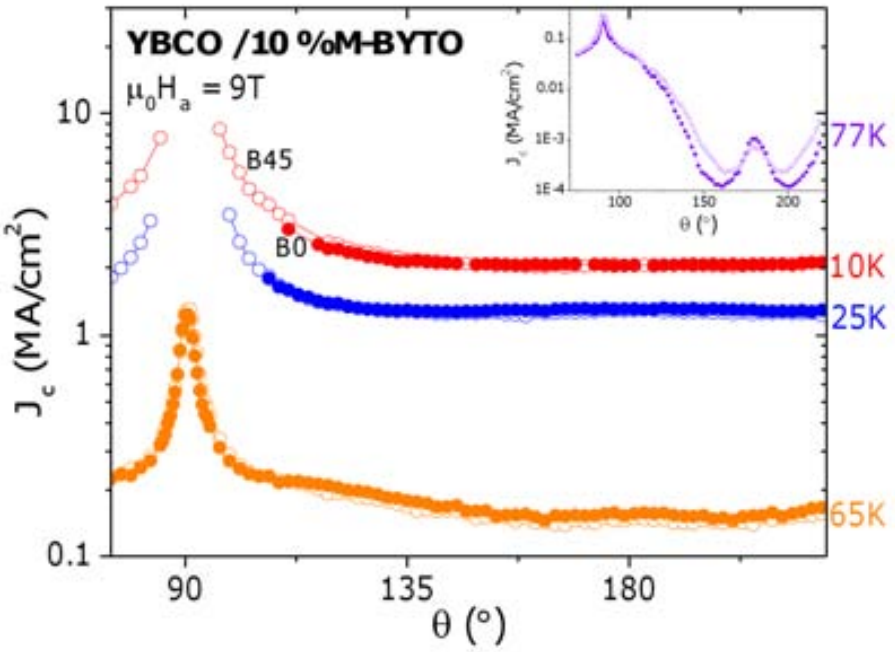

Figure 3.35.: $J_c(\theta)$ at $9T$ and different temperatures for the $YBCO/10\%M-BYTO$ sample measured at different bridges: $B0$ full dots and $B45$ empty dots.

the angular J_c dependence measured on $B0$ and $B45$ at $\mu_0 H_a = 9T$. Contrary to the situation observed in standard $YBCO$ films, no difference is obtained between $J_c(\theta)$ sweeps performed on $B0$ and $B45$ at $T \leq 65K$. These results give evidence that no effect of TB plane orientation is observed on $BYTO$ nanocomposites at low temperatures. Moreover, no channelling minimum is obtained at $\theta = 180^{o}$ on the measurement performed on $B0$ giving further evidence that vortex channelling along TB planes do not occur in $YBCO$ nanocomposites. These results can be explained considering the reduction of the TB coherence along the c-axis. The interaction of the high density of SFs in nanocomposites with the twin boundary planes was deeply studied in [125] where we found that SFs completely change the TBs length and distribution (see Fig. 3.6$-b$ and Fig. 3.7). In particular we found that the TBs coherence along the c-axis is broken reducing their length and spacing. This reduction of TBs coherence precludes vortex channelling along the planes.

Regarding the $J_c(\theta)$ behavior at high temperatures ($T = 77K$), we observe a clear difference between the two different $J_c(\theta)$ curves, with an overall enhancement of $J_c(\theta)$ at intermediate θ values, $120^{o} < \theta < 170^{o}$, on $B45$ as it occurs for the pristine sample (open and closed circles shown in Fig. 3.31). This means that while a reduction of the TBs vertical length precludes vortex channelling, vortex pinning due to TB planes at high temperatures is still effective due to the elasticity of the vortex that allows its accommodation along the non-coherent TBs.

Therefore, we have demonstrated that vortex pinning at high temperature is promoted by twin boundaries when $H_a||c$. Its effectiveness is not too much influenced by the TBs length along the c-axis since non-coherent TBs also act as pinning centers as we have demonstrated in the case of nanocomposites grown by CSD. However, vortex channeling at low temperatures is just observed when the TBs are coherent along the c-axis resulting in the no-observation of this effect in CSD-nanocomposites. On the other hand, as the orientation of the $YBCO$ crystallographic axis with respect to the current path can be controlled by using a suitable buffer layer, the effects of TBs will be also modified. This is observed by comparing the pristine $YBCO$ sample (grown on LAO) with a second pristine $YBCO$ sample grown over a CeO_2 buffer layer. In that second case, since a and b axis are rotated 45^{o} with respect to the the film grown on LAO, TBs are parallel (and perpendicular) to the substrate edges. Therefore, the $J_c(\theta)$ results obtained in the $YBCO/Pristine$ sample in a bridge patterned parallel to the substrate edges are the same than the obtained in the $YBCO/CeO_2$ sample with a bridge forming an angle of 45^{o} with the edges of the substrate and vice versa. In any case, when the vortex moves within the TB planes, an additional isotropic contribution arising from the TBs (which do not strongly depends on the the TB length) increase the critical current density in a wide $J_c(\theta)$ region.

3.9. Study of the magnetic flux relaxation

Tailoring the vortex pinning landscape of $YBCO$ is one of the major challenges towards their use in large scale applications. However, the effectiveness of pinning defects is ultimately limited by thermally activated flux-creep processes. Whereas the effect of

random point defects and correlated columnar effects in flux creep has been thoroughly studied in the past in HTS [55, 66, 73, 78–82, 142, 155], there is a need to increase our understanding about magnetic flux relaxation in nanocomposites with the presence of randomly distributed extended nanoparticles, which, as we have demonstrated, produce significant strong-isotropic pinning centers.

Magnetic relaxation of the critical current density has been measured in pristine, $YBCO/6\%M-BYTO$ and $YBCO/10\%M-BYTO$ samples over times of one hour (the $YBCO/15\%M-BYTO$ sample has not been considered due to the reduced J_c^{sf} arising from the nanoparticles aggregation [132]). An additional sample of $YBCO/10\%M-BZO$ has been used for comparison. By measuring the $J_c(t)$ dependence at a fixed field and temperature, we obtain the typical relaxation curves shown in (Fig. 3.36). By using expression 1.13 to fit the experimental data, we can determine the value of S at different applied magnetic fields and temperatures.

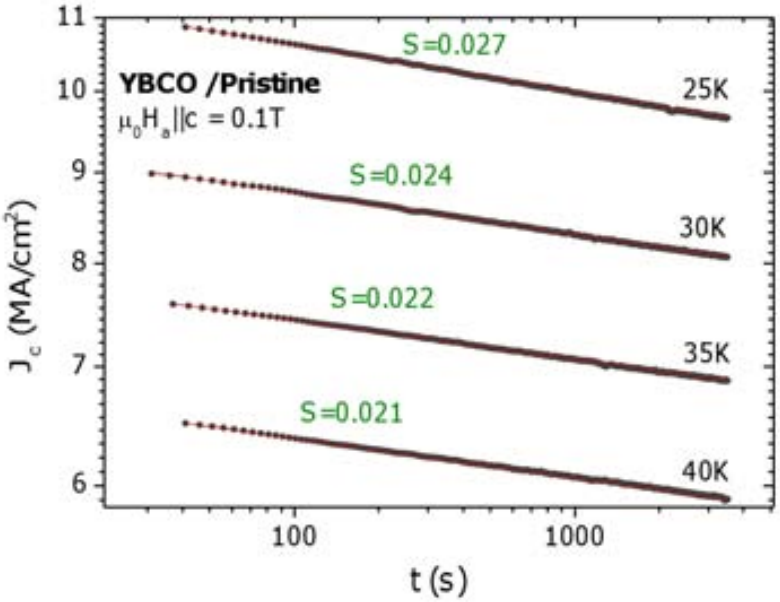

Figure 3.36.: Typical set of relaxation curves in $YBCO/Pristine$ at $\mu_0 H_a||c = 0.1T$.

Fig. 3.37 plots the relaxation results obtained for the five samples at four different applied magnetic fields. The main observation to be done by comparing the curves is that the plastic creep (see sec. 1.3) in the pristine sample appears at $10-20K$ below that of nanocomposites. The temperature transition from elastic to plastic creep, T^{cross}, is plotted in Fig. 3.38$-b$ at different applied magnetic fields, for the different samples. A common practical criterion to determine T^{cross} at each field corresponds to the position of maximum in a $S/T(T)$ plot as shown in Fig. 3.38$-a$ [156]. Therefore, from the data shown in Fig. 3.37 and Fig. 3.38$-b$, we can observe that by the introduction of secondary phases into the $YBCO$ matrix, the fast enhancement of the magnetic flux relaxation due to plastic creep is shifted at higher temperatures for a given value of applied magnetic field.

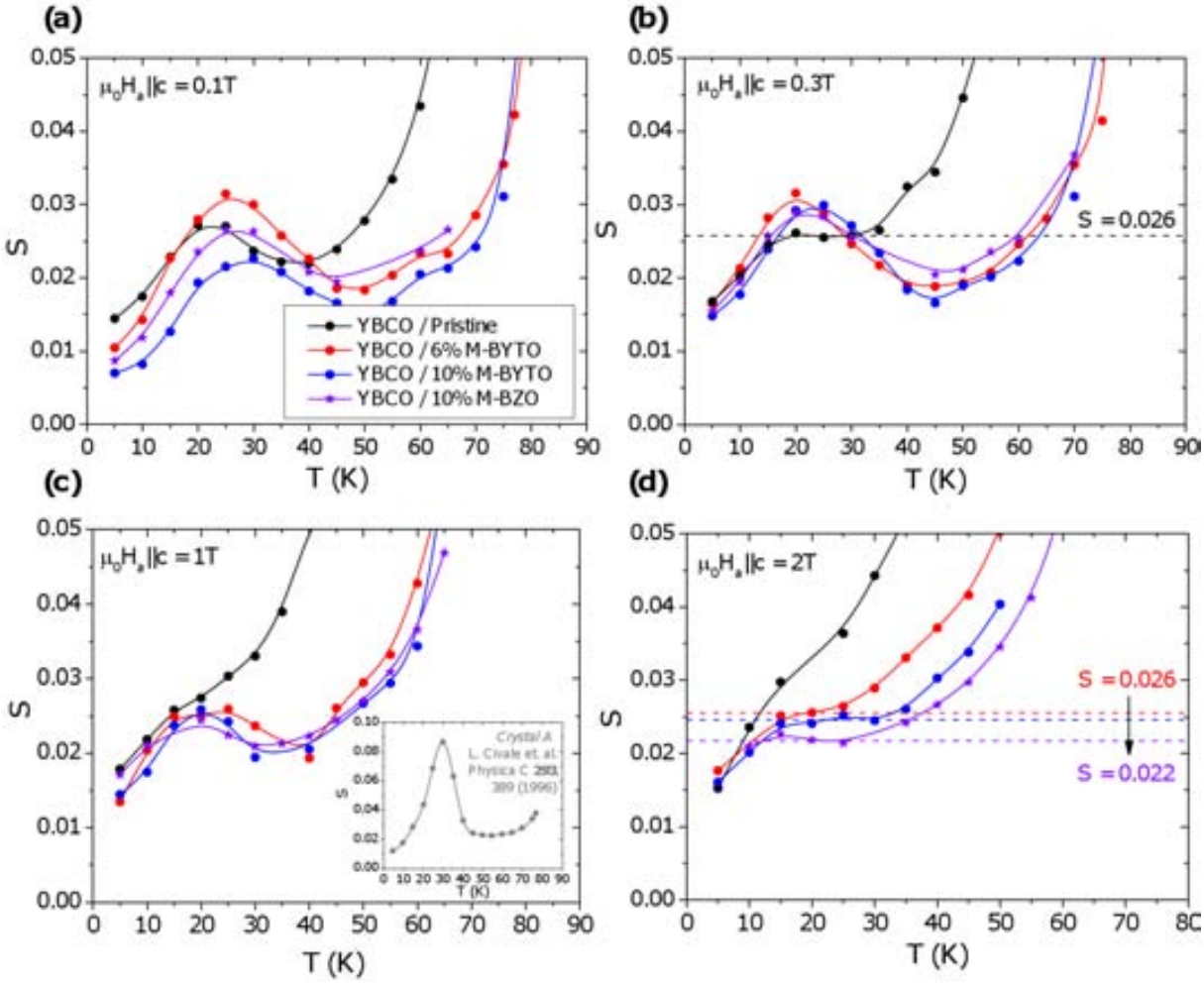

Figure 3.37.: Magnetic ux relaxation of different samples at **(a)** $0.1T$, **(b)** $0.3T$, **(c)** $1T$ and **(d)** $2T$. For comparison, also a BZO sample (violet-stars) is plotted. Also, data from [80] is plotted in c-inset. Dashed lines marks the obtained values of the characteristic vortex-glassy plateau.

Another feature to be commented is that at intermediate temperatures, where a plateau should be observed in agreement with the collective flux creep theory [78], a peak around $25K$ appears at fields of $0.1T$, $0.3T$ and $1T$. This peak has been related with the excitation of Double Kinks (DK) due to the presence of columnar defects like twin boundaries in our cases. Although nanocomposites present non-coherent TBs along the c-axis, they could be long enough to allow the formation of DK where just short lengths of the vortex are necessary [55]. Nevertheless, it is important to note that this peak is much smaller than the reported for $YBCO$ crystals and films with strong columnar defects [79–82] which it can arrives at values of $S = 0.09$ as it can be observed in Fig. 3.37$-c(inset)$ where the data of [80] is plotted.

As we commented in sec. 1.3, at fields above the matching where the DK excitation disappears, the correspondent plateau that arises from the glassy vortex dynamics resulting from random disorder, can be observed. This plateau is observed at $\mu_0 H_a = 0.3T$ in the pristine sample and at $\mu_0 H_a = 2T$ in nanocomposites (dashed lines in Fig. 3.37). In agreement with [78], the S values are found to be between 0.02 and 0.035. Notice that this plateau is achieved at high temperatures when $U_0 \lll \mu K_B T ln(t/t_{eff})$ and following

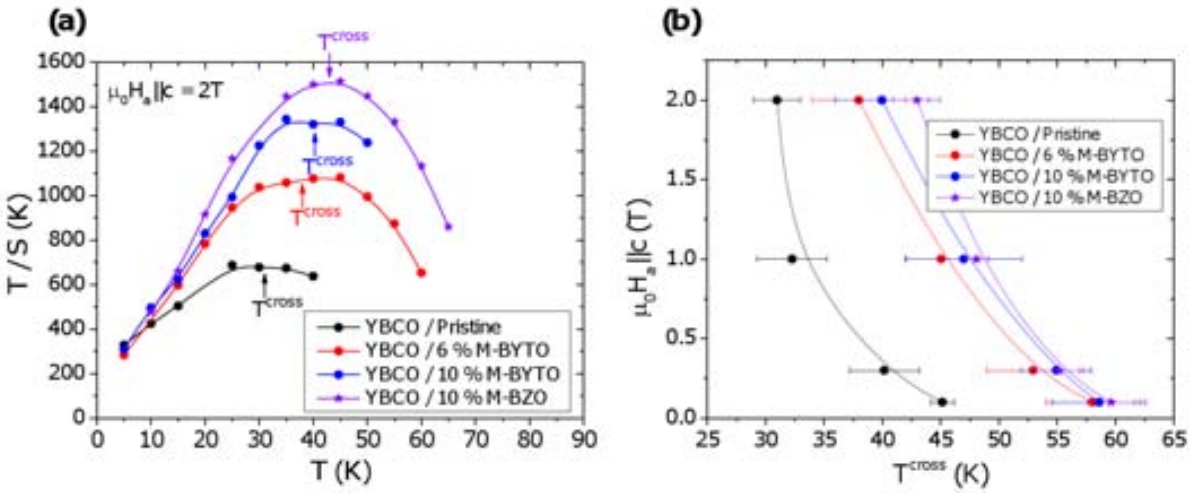

Figure 3.38.: **(a)** T/S representation as a function of temperature to determine the value of T^{cross}. **(b)** Elastic-Pastic transition, T^{cross}, at different magnetic fields and samples. For comparison, the $YBCO/10\%M-BZO$ sample (violet-stars) is also plotted.

expression 1.16, it implies a flux magnetization rate of $S = 1/\mu ln(t/t_{eff})$ (independent of U_0 and its temperature dependence).

It should be also noted that, especially at $\mu_0 H_a = 0.1T$ and $0.3T$ (Fig. 3.37$-a$ and b), between $40 - 55K$, nanocomposites present a S value below 0.02 and in particular, below the expected glassy behavior plotted in Fig. 3.37$-d$ as dashed lines. This result is in agreement with previous works where nanocomposites have been grown by chemical methods [142, 155].

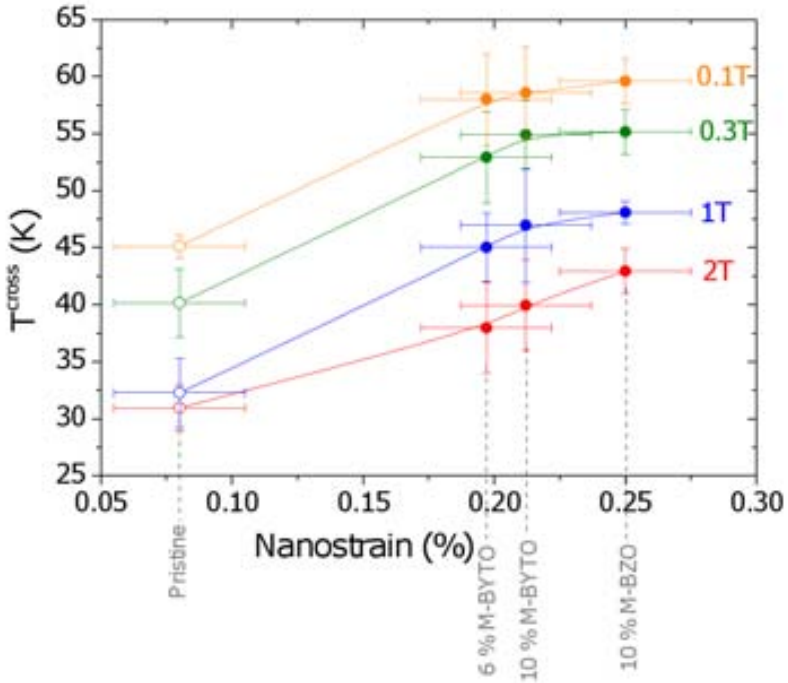

Figure 3.39.: Elastic-Pastic temperature transition, T^{cross}, as a function of nanostrain for different magnetic fields.

In order to explain the obtained results of $S(T)$ in nanocomposites, and in particular the shift of the elastic-plastic transition, Fig. 3.39 displays T^{cross} as a function of the nanostrain. As we have commented above, nanostrain (controlled by the introduction of nanoparticles) increases the isotropic-strong contribution of $J_c$and reduces the effective anisotropy of $YBCO$ nanocomposites. From the study of magnetic flux relaxation, we observe a clear relation between T^{cross} and nanostrain, demonstrating that nanostrained regions also avoid the reduction of J_c with time at high temperatures.

Thus, we have demonstrated that by the introduction of secondary phases into the $YBCO$ matrix, we are able to reduce the magnetic relaxation maintaining the elastic creep regime at higher temperatures. It results in an effective enhancement of the critical current density at high temperatures since in the plastic creep regime, thermal activation is very strong.

3.10. Conclusions

In this chapter, we have have analyzed the pinning properties of $YBCO$ nanocomposites grown by CSD and we have seen that the addition of nanoparticles is a very effective route to enhance the isotropic contribution of the critical current density in $YBCO$ films. This is reflected in the performance of the $J_c(\theta)$ curves and in the reduction of the effective anisotropy, $_{eff}$, from 5 to even values close to 2, by the introduction of $BYTO$ secondary phases. Nevertheless, by the study of the upper critical field, H_{c2}, we have demonstrated that the intrinsic properties of the $YBCO$ do not change in nanocomposites.

We have correlated the enhancement of the isotropic pinning contribution with an increase of nanostrained regions in the $YBCO$ matrix, which is promoted by the high density of stacking faults founded in nanocomposites. Stacking faults are formed in order to relive the strain produced at the interface of the $YBCO$ matrix and the incoherent nanoparticles. It has been demonstrated that nanoparticles which highly contribute to the formation of strained regions are those randomly oriented with the $YBCO$ matrix, since are those presenting a large incoherent interface.

By analyzing, the temperature dependence of the critical current density and its anisotropic and isotropic contributions (determined thought the Blatter scaling approach), we observe that strained regions in nanocomposites act as strong-isotropic pinning centers. This analysis allows us generating J_c phase diagrams which give information about the main pinning contributions present at each temperature and magnetic field conditions. These results strongly differs from nanocomposites grown by PLD where oriented nanorods along the c-axis does not generate isotropic-strong pinning centers. In contrast, nanoparticles in $YBCO - PLD$ samples highly increase the critical current density along the nanodots direction but have a minimum effect to the rest of orientations [32, 40, 115].

Natural defects, intrinsic to the $YBCO$ film, formed at different grown states, interact with artificially introduced nanoparticles. In particular, stacking faults, which appear in a previous growth state than the twin boundaries, change the size and distribution of TBs yielding to a new pinning landscape. The high density of SFs in the case of the nanocomposites avoids the formation of coherent twin boundaries along the c-axis. It

results in a TBs distribution with narrower domains and shorter lengths along the c-axis, typically $\sim 5nm$.

By transport measurements we have demonstrated that these non-coherent twin boundaries avoid channeling effects whereby the critical current density drops when the vortex is parallel to TB planes. These effects are only observed in $YBCO/Pristine$ samples at low temperatures ($T < 65K$) where coherent twin boundaries allows the slide of the vortex through the twin boundary plane. At high temperatures ($T > 65K$), pinning effects are observed due to the presence of TBs. At these temperatures, since elasticity allows an accommodation of the vortex into the broken twin boundaries, pinning is also founded in $BYTO$ nanocomposites.

Finally, magnetic relaxation measurements reveal that nanostrain induced in $YBCO-BYTO$ nanocomposites also promotes a shift of the elastic regime to higher temperatures, reducing relaxation effects at high temperatures.

In general, we have demonstrated that by the introduction of secondary phases, a new isotropic pinning mechanism is obtained due to the formation of strained regions into the $YBCO$ matrix. This new pinning centers, do not only reduce the effective anisotropy of the material, but increases the critical current density in a wide range of orientations. In addition, plastic-flux creep is shifted to higher temperatures in the presence of nanoparticles.

Therefore, a control of the isotropic contribution and thermal excitations can be obtained through the addition of randomly oriented nanoparticles into the $YBCO$ matrix, validating this low cost methodology for large scale applications.

4. YBCO thin films patterned with assymetric arrays

The possibility of directed transport in systems with a periodic spatially asymmetric potential energy landscape has been a fascinating topic for many years. Such scenario was considered by Feynman [157] using a ratchet to show how anisotropy never could lead to net motion in an equilibrium system. Since then, asymmetric sawtooth potentials are called ratchet potentials and, in general, a device with broken inversion symmetry is called a ratchet device. Therefore, the ratchet effect occurs when asymmetric potentials induce outward particle flowing under external fluctuations in the lack of any driving direct outward forces. As a result, ratchet systems can rectify an AC source in a DC one.

4.1. State of the art

Most of the ratchet studies performed on superconducting samples have been focused on vortex motion in conventional LTS, at fields below the matching field, where a single vortex moves on a nonsymmetrical pinning potential. In this kind of ratchet, for magnetic fields above the first matching field, interplay between external and internal vortices has been observed producing sign reversals by tuning the density of the vortex lattice [158].

In order to obtain these asymmetrical artificial pinning potentials, different methodologies and type of structures can be used [159]: One possibility is to pattern the sample with an array of antidots. De Souza Silva et.al. [160] and Wordenweber et.al. [10] observed ratchet effects when symmetrical antidots were distributed in a nonsymmetrical way. A different case was studied by Ooi et.al. [161] where using an array of asymmetrical antidots with a symmetrical distribution, they observed a similar effect.

Another way to induce asymmetric pinning centers is by patterning with ferromagnetic nanostructures, either over and above a superconducting film [158, 162–167]. In these cases, depending on the existence, or not, of a non-superconducting layer between the nanostructures and the superconductor, the magnetic orientation of the ferromagnetic nanostructures or the superconducting layer analyzed, different ratchet behaviors have been observed [159].

In another particular case, Plourde et.al. [168] decreased the thickness at some nanometric regions in a amorphous $MoGe$ film (weak-pinning superconductor). By doing so, they found an asymmetric motion of vortices which have to cross a surface barrier induced by the thickness modulation. They explained this effect not only taking account the change in the vortex line free energy (which depends on the sample thickness), but also considering the distortion of screening currents near the step edges due to current

crowding effects [169, 170]. Similar effects were also obtained by He et.al. [171] in Nb films.

Besides the ratchet systems commented above, a different type of ratchet system were theoretically proposed by [172], in which the ratchet effect is not directly originated for the interaction between vortices and asymmetric potentials. Instead, the asymmetric pinning potential is created by vortices which remain in asymmetrical structures and transfer the asymmetry to weakly pinned external vortices through their interaction. This kind of ratchet, which appears as a consequence of the long-range interaction between vortices, was called "collective interaction-driven ratchet".

As commented, most of ratchet studies have been performed in LTS where weak-natural pinning centers ensures the effecting of artificial defects. On the contrary, strong-intrinsic-pinning superconductors (as $YBCO$ thin films) present many natural pinning centers along the matrix, which are high enough to overcome to the Artificial Pinning Centers (APCs). Thus, strong APCs should be induced in order to be able to interfere on the vortex dynamics in this kind of systems.

4.2. Experimental ratchet effect in asymmetric pinning potentials

In this section, we will analyze different samples with asymmetric pinning configurations with the aim to observe and understand the ratchet effect in $YBCO$ 250nm-thick films. Two different methodologies are used to pattern asymmetric $APCs$, based on high resolution lithography techniques: Focused Ion Bean and Focused Electron Bean Lithography (FIB and $FEBL$, respectively). The physical interpretation of the obtained results will be presented in sec. 4.3.

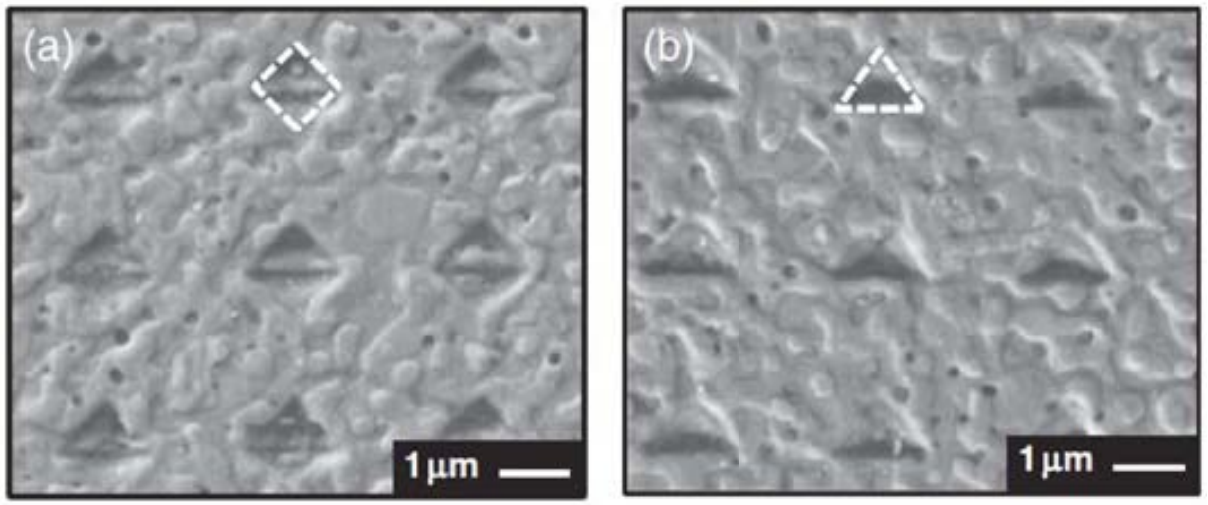

Figure 4.1.: SEM images of bridges patterned by FIB with **(a)** diamonds and **(b)** triangles.

4.2.1. Ratchet effect in FIB patterns

In order to evaluate the possibility to generate ratchet pinning centers in $YBCO$ films, we have studied vortex motion in $YBCO$ thin films containing symmetric (diamonds) and asymmetric (triangles) $APCs$ patterned with the FIB technique. These consist of blind-antidot arrays which are patterned with the desired geometry (diamonds and triangles in our case) at different transport bridges. We use the term of blind-antidots to refer at holes that do not perforate completely the superconducting film thus, vortices can be nucleated inside or outside the blind-antidots.

For this analysis, three different bridges of $100 \times 20\mu m$ are used: a bridge containing an array of $1\mu m$-lateral-side and $2.5\mu m$-apart diamonds (Fig. 4.1$-a$), another with triangles with the same side and separation (Fig. 4.1$-b$), and a third bridge kept without any patterning to be used as a reference (pristine bridge). Atomic Force Microscopy (AFM) was used to determine the depth of the blind-antidots patterned being $\sim 70nm$. The orientation of the arrays with respect to the bridge is displayed in Fig. 4.2 where also the applied magnetic field (H_a), the applied positive and negative current densities (J^+ or J^-, respectively), and the resulting Lorentz force (F_L) are indicated.

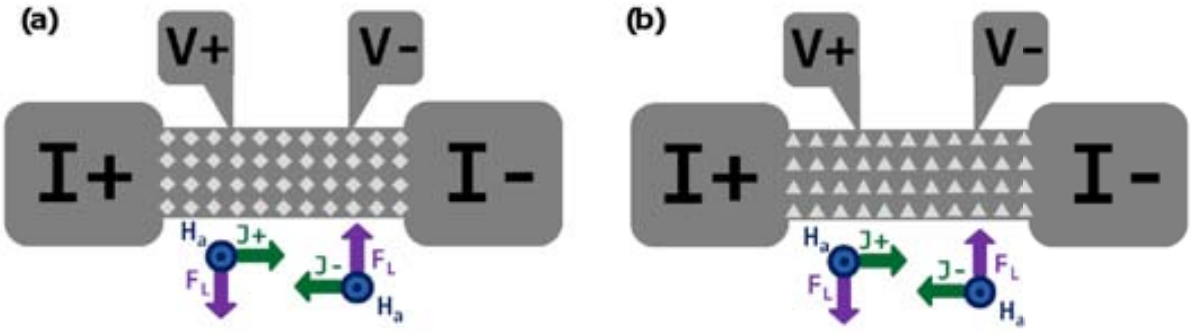

Figure 4.2.: Schemanic representantion of the 4-point configuration bridges in the **(a)** symmetrical (diamonds) and **(b)** assymetrical (triangles) systems.

It is important to note that, after the FIB etching, small reduction of T_c and no considerable variation in ΔT_c of the $YBCO$ film are obtained, as it is plotted in Fig. 4.3$-a$. On the other hand, J_c self field, i.e. J_c at $\mu_0 H_a = 0T$ (J_c^{sf}), is reduced around 30%. This reduction has been obtained considering the full cross-section of the bridge to calculate the value of J_c both, before and after the patterning (Fig. 4.3$-b$). The obtained reduction in J_c^{sf} is higher than the expected one associated to the final the cross-section, after the blind-antidots patterning (11%), provably as a consequence of the amorphization of part of the material surrounding the blind-antidots during the ion etching.

Concerning the FIB technique, and taking into account that we used low ion currents to perform the patterns, we assume that the effect of the Ga^+ implantation will not strongly modify the pinning properties of the material within the blind-antidots. In fact, in sec. 4.2.2 we will demonstrate that the possible implantation of these Ga^+ ions is not a crucial factor for the observation of the ratchet effect.

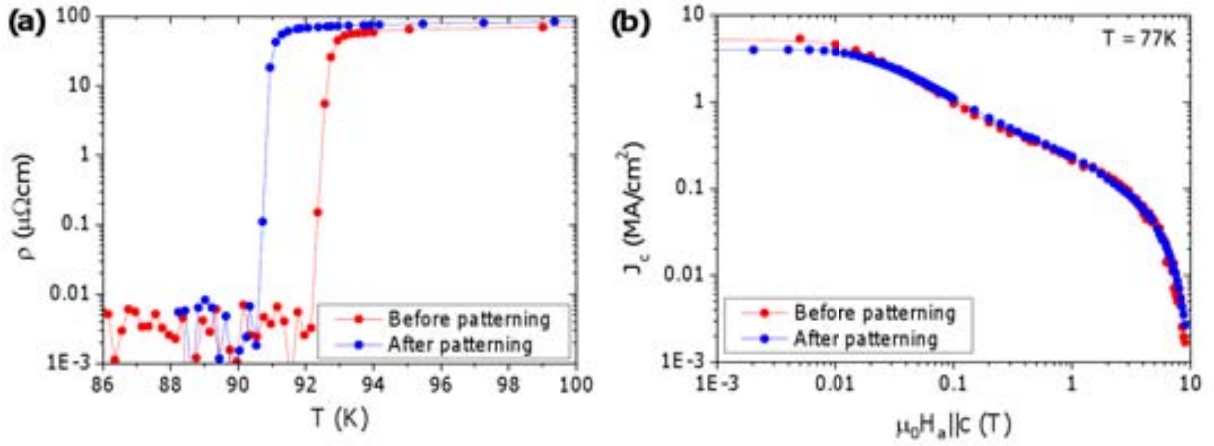

Figure 4.3.: (a) Comparison of the critical temperature before and after the patterning. **(b)** Comparison of the field dependence of the critical current density at $77K$ before and after the patterning.

The effect of blind-antidots geometry in the vortex dynamics has been analyzed by measuring the current-density-electric-field curves, $J(E)$, under positive, J^+, and negative, J^-, applied DC currents, for different applied magnetic fields perpendicular to the c-axis of the superconductor. By inverting the sign of the current, the sense of the Lorentz force is inverted ($F_L = J \times B$) and thus, voltage drops associated to vortex motion change their sign. Consequently, if blind-antidots are effective enough, different vortex motion should be obtained with symmetric or asymmetric pinning sites. These results are plotted in Fig. 4.4$-a$ where a comparison between the negative, J^-, and positive, J^+, branches of the $E(J)$ curves for bridges with triangles and diamonds at $0.02T$ and $65K$ are plotted (for a direct comparison, both J^+ and J^- are displayed in the same quadrant). A clear difference is observed in the $E(J)$ response by comparing the two systems: while in the bridge with symmetric pinning sites (diamonds) same curves are obtained by inverting the sign of the current, in the case of asymmetric pinning sites (triangles) a difference between the two polarities is observed.

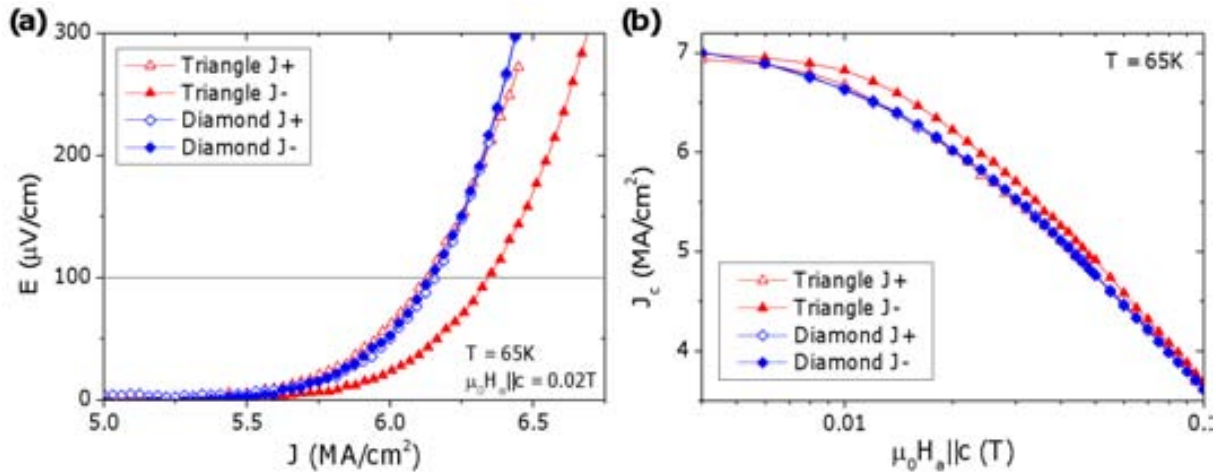

Figure 4.4.: (a) $E(J)$ curve at $0.02T$ and $65K$ for the symmetric and assymetric systems ($1\mu m$-lateral-side ; $2.5\mu m$-apart ; $70nm$-depth). **(b)** $J_c(H)$ at $65K$ for both systems.

Performing the same measurements at different applied magnetic fields, the field dependence of the critical current density under positive and negative external current, $J_c^+(H_a)$ and $J_c^-(H_a)$ respectively, is obtained. Fig. 4.4$-b$ shows the $J_c^+(H_a)$, $J_c^-(H_a)$ curves at $65K$ for the bridges with symmetric and asymmetric arrays. A criterion of $100\mu V/cm$ has been used to determine J_c in order to better observe the differences in $J_c(H_a)$. Note that the bridge with triangular blind-antidots exhibits a difference between $J_c^-(H_a)$ and $J_c^+(H_a)$ while the situation for the bridge with diamonds is somewhat different since the same $J_c(H_a)$ curves are observed when F_L is reversed. Overall, these results demonstrate that the asymmetric pinning potentials induce a preferential vortex motion in a certain sense. This effect, defined as "ratchet effect", is effective up to high magnetic fields ($\sim 0.1T$ at $65K$) and is clearly reflected as an asymmetric response of J_c.

Fig. 4.5 shows the differences in critical current density obtained with the two polarities of the current, i.e. $[J_c^+ - J_c^-]$ at $65K$ as a function of the applied magnetic field, for the three studied bridges. As already obseved in the $J_c(H_a)$ curves, the bridge patterned with triangles presents a clear difference between J_c^+ and J_c^- (ratchet effect) which shows a maximum around $0.15MA/cm^2$ at $0.02T$ and disappears at fields $\sim 0.1T$. On the contrary, no diferences on J_c^+ and J_c^- are observed for the bridge with simetric blind-antidots and for the pristine sample.

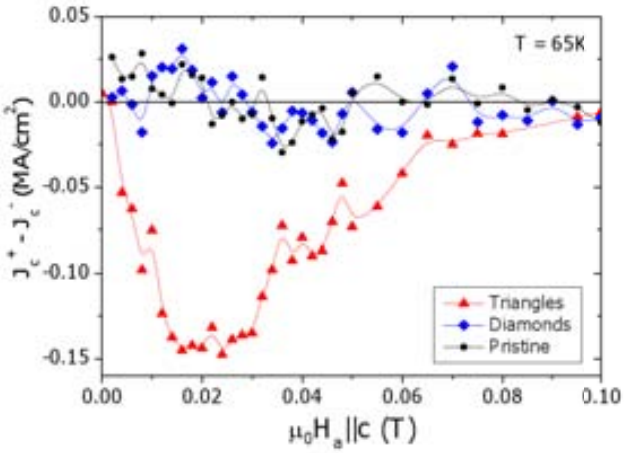

Figure 4.5.: Experimental $J_c^+ - J_c^-$ subtractions for symmetrical, asymmetrical ($1\mu m$-lateral-side ; $2.5\mu m$-apart ; $70nm$-depth) patterns. For comparison, subtractions on a pristine sample are plotted too.

Temperature / Magnetic Field dependence of the ratchet effect

In the following, an evaluation of applied magnetic field and temperature dependence of the ratchet effect is performed. In Fig. 4.6, $[J_c^+ - J_c^-]$ subtractions for the case of the asymmetric array (triangles) are displayed for three different temperatures: $77K$, $65K$ and $50K$. For comparison, subtractions obtained for the pristine system at $77K$ (where no-ratchet effect is observed) are plotted too. As expected, the sign of $[J_c^+ - J_c^-]$ obtained in the asymmetric array is reversed by inverting the sense of the applied magnetic field since Lorenz force is also inverted.

One of the most obvious features of Fig. 4.6 is that the value of $[J_c^+ - J_c^-]$ increases by decreasing the temperature indicating that the ratchet effect is maximized at low temperatures. Another remarkable issue disclosed from Fig. 4.6 is that the ratchet effect is extended to higher fields at lower temperatures.

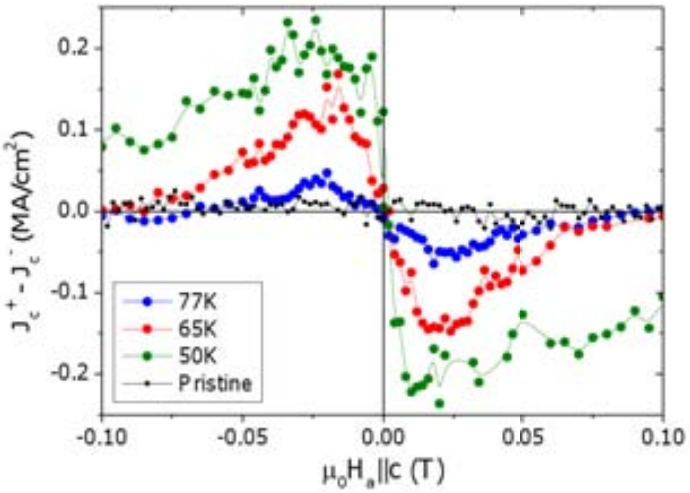

Figure 4.6.: Experimental ratchet effect for the asymmetric array ($1\mu m$-lateral-side ; $2.5\mu m$-apart ; $70nm$-depth) at different temperatures. For comparison, results obtained for the pristine sample at $77K$ are also plotted.

Geometrical factors relevant for the ratchet effect

In this section, we analyze the effect of the geometry of the asymmetric blind-antidots on the ratchet effect. To evaluate this geometry dependence, triangles of $1.7\mu m$-lateral-side were patterned into a different bridge with the same crosswise separation and depth

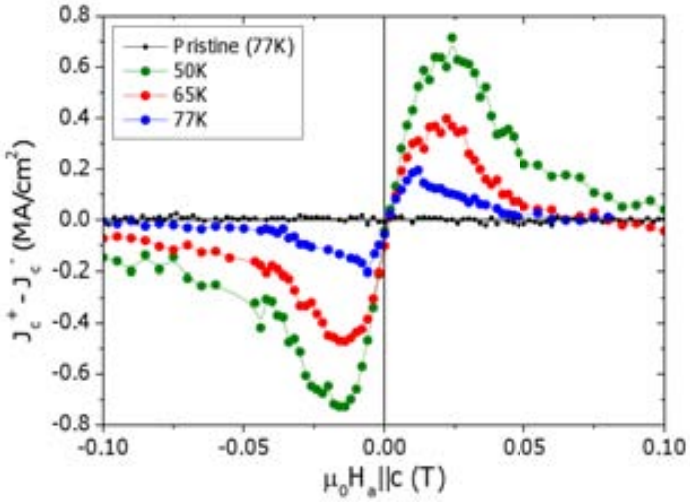

Figure 4.7.: Experimental ratchet effect for the asymmetric array ($1.7\mu m$-lateral-side ; $2.5\mu m$-apart ; $70nm$-depth). For comparison subtractions of the pristine sample are also displayed.

than the previous analyzed sample, $2.5\mu m$ and $70nm$ respectively, and using the same methodology (FIB) and conditions. $[J_c^+ - J_c^-]$ subtractions at $77K$, $65K$ and $50K$ were obtained by performing the analysis shown above (Fig. 4.7). Again, $[J_c^+ - J_c^-]$ subtractions of a pristine system at $77K$ are plotted for comparison.

As we observed in the previous sample, ratchet effect is maximized and extended to higher fields at lower temperatures. Nevertheless, comparing Fig. 4.6 and Fig. 4.7 one can clearly observe that the ratchet effect is inverted, i.e. the direction of preferential vortex motion is the opposite in this sample, giving an inversion in the $[J_c^+ - J_c^-]$ sign. In order to differentiate this ratchet effect to the previous one, we will define it as "direct ratchet effect" whereas the presented in sec. 4.2.1 will be referred as "reversal ratchet effect". From data shown in Fig. 4.6 and Fig. 4.7, we can conclude that the geometrical factors defining the asymmetric nanostructures, seem to determine the final sign of the ratchet effect. We will discuss in the following section the difference between these two ratchet effects.

4.2.2. Ratchet effect in FEBL patterns

At this point, we must evaluate the possible contribution of Ga^+ ions implantation near the FIB irradiated surface to the observed ratchet effect. To evaluate this contribution, a different technique has been used to perform the blind-antidots in our $YBCO$ film: the $FEBL$. Two different arrays are patterned in two different bridges following the procedure described in sec. 2.2.3. In this case, triangles are $3\mu m$-lateral-side and separated 5 and $7.3\mu m$ respectively with a depth of $70nm$, in bridges of $100 \times 30\mu m$ size.

Fig. 4.8 displays the $[J_c^+ - J_c^-]$ subtractions obtained for the two different cases at $77K$. It can be clearly observed that arrays created by $FEBL$ also present the ratchet effect. This result evidences that the possible implanted Ga^+ ions are not the key factor to produce the effect. Notice that, as it happened in the previous analyzed samples (patterned with FIB), by modifying the geometry of the triangles and/or the separation between them, an inversion of the ratchet effect is obtained.

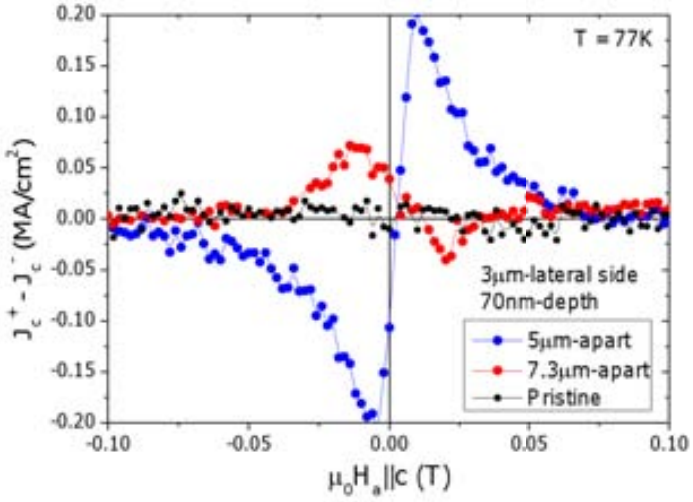

Figure 4.8.: Ratchet effect for arrays patterned by $FEBL$ at $77K$ ($3\mu m$-lateral-side ; $5/7.3\mu m$-apart ; $70nm$-depth). Again, pristine sample is used for comparison.

To sum up, we have demonstrated that a preference sense of the vortex motion in HTS films is possible by generating asymmetric potentials in our $YBCO$ thin films. We have observed that the effect can be obtained regardless of the etching technique used to perform the blind-antidots (FIB or $FEBL$).

4.3. Vortex motion in ratchet systems

In order to understand the dissipative mechanisms involved into the ratchet effect observed in our systems, we will consider two different populations of vortices: vortices located inside and outside the blind-antidots: internal and external vortices, respectively. Due to the reduction of the effective cross-section at areas located below the blind-antidots, current density will not be homogeneously distributed through the whole width of the bridge. Consequently, the critical current density would be firstly reached, at regions where the cross section is lower [169, 170], which one should expect that would be the regions located below the triangles (regions where we have reduced the cross-section). This would result in an initial movement of internal vortices while the external ones, remain pinned.

This argument clearly demonstrates the obtained results in the direct ratchet effect where $J_c^+ > J_c^-$ for positive applied magnetic fields. In this configuration, when we apply J_c^+, internal vortices must flow against the base of the triangles (scheme of Fig. 4.9$-a$). This motion require a larger F_L that the necessary to move vortices against the tilted edges of the triangles, when the polarity of the current is reversed (scheme of Fig. 4.9$-b$).

The situation for the reversal ratchet effect is somewhat different since in that case, the sign of the ratchet effect is reversed, which indicates that external vortices are the ones producing the observed effect. This can be explained if the current density at external positions is equal or higher than that at internal positions. If this is the case, external vortices may be the ones that initiate the motion. We have to consider here that, internal

vortices must overcome a potential barrier to start their movement [168] which arises, not only from the change of the vortex line free energy (due to thickness modulation inside the triangles), but also from the distorsion of screening currents near the step edges. Thus, if the Lorentz force generated in the internal vortices is not high enough, this vortices will be trapped into the triangles forming an asymmetric barrier (blue vortices in Fig. 4.9$-c$ and Fig. 4.9$-d$) that external vortices will have to overcome. In this situation, we will measure dissipation associated to the initial motion of external vortices which will feel the asymmetry of the pinning potential created by vortices trapped in non-symmetric triangles. It is important to note that the lattice vortex parameter at fields where we are observing the ratchet effect is $\sim 400nm$, which is lower than the side of triangles ($\sim 1\mu m$). Thus, there are at least 3 vortices into the triangles which can generate the asymmetric pinning potential. Consequently, when J^- is applied, external vortices must flow against a row of pinned internal vortices (scheme of Fig. 4.9$-d$) and therefore, $J_c^- > J_c^+$ in that last case.

Further evidence that in samples with reversal ratchet effect, asymmetric dissipation initiates from movement of external vortices can be obtained if we compare the $J_c^-(H_a)$ and $J_c^+(H_a)$ curves, measured for the sample with triangular and diamond blind-antidots (Fig. 4.4). We observe that $J_c^+(H_a)$ measured for the bridge with triangles coincides with the $J_c^-(H_a) = J_c^+(H_a)$ curves obtained in the sample with symmetric diamonds. On the contrary, $J_c^-(H_a)$ measured for the bridge with asymmetric triangles goes above those ones. In this configuration, external vortices must flow against a row of fixed vortices at the base of the triangles (scheme of Fig. 4.9$-d$) which require a larger F_L than that

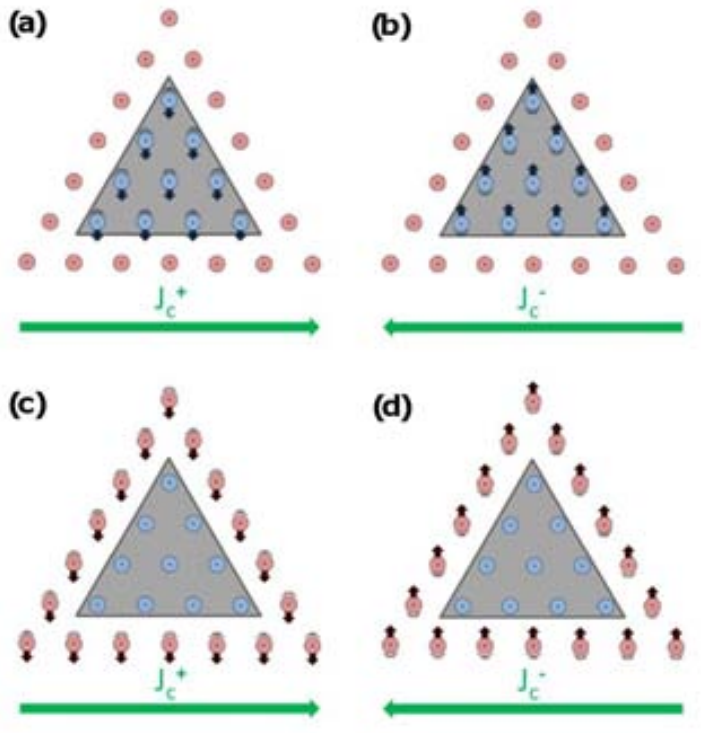

Figure 4.9.: Schematic representation of the vortex movement (**(a)** and **(b)** direct ratchet effect and **(c)** and **(d)** reversal ratchet effect). Green arrows indicate the two polarizations of the electrical current. Red and blue arrows indicate the movement of the vortices.

necessary to overcome vortices pinned at the tilted edges of the triangles (scheme of Fig. 4.9−*c*). In the last case, external vortices see a very similar pinning potential than that created by the fixed vortices in the diamonds and hence, very similar $J_c(H_a)$ curves are found. Therefore, we conclude that in this system, and in the range of H_a where we observe a difference between J_c^+ and J_c^-, the critical current density is determined by the motion of external vortices.

It is important to remark that, as we will see in sec. 4.3.3, in general, we are not modifying the pinning energy in the material by patterning the blind-antidots. However, due to the inhomogeneous distribution of current density, different Lorentz forces will be achieved at different parts of the film inducing direct or reversal rachet effects. We have also to consider that the influence of the potential barrier due to thickness modulation can also affect the final vortex motion in particular systems.

4.3.1. Evaluation of the field dependence on the ratchet effect

Concerning the response of the ratchet effect as a function of the applied magnetic field, a clear relation is obtained between the region where the effect is observed and the different regimes of the $J_c(H_a)$ curve, i.e. vortex-defect and vortex-vortex interaction regimes. As it has been commented in chapter 3, it is well established for $YBCO$ thin films that a $log - log$ $J_c(H_a)$ curve sets the scale for the transition from a low-field J_c plateau, associated with single-vortex pinning (vertical grey lines in Fig. 4.10), to a power-law region dominated by collective vortex-vortex interaction effects (horizontal grey lines in Fig. 4.10) [48, 49, 55, 135–138]. The crossover between these two regimes is associated with different temperature-dependent interactions where vortex-vortex interaction and vortex-defect interaction compete (squared grey lines in Fig. 4.10). By analyzing the $J_c(H_a)$ behavior at different temperatures for the bridge with triangular blind-antidots (Fig. 4.10), it is possible to establish a direct correlation between the fields at which the ratchet effect disappears (black-empty dots of Fig. 4.10) and the setting of the collective vortex pinning regime. For fields lower than the region where the vortex-vortex interaction is the dominant therm, the ratchet effect can be observed. At higher fields, the strong vortex-vortex interaction begins to inhibit the ratcheting motion in both, the direct and reversal ratchet systems. [172]. As observed in black-empty dots of Fig. 4.10, the vortex-vortex interaction starts at higher fields by decreasing the temperature in agreement with the wider range where the ratchet effect is observed by decreasing temperature (Fig. 4.6 and Fig. 4.7).

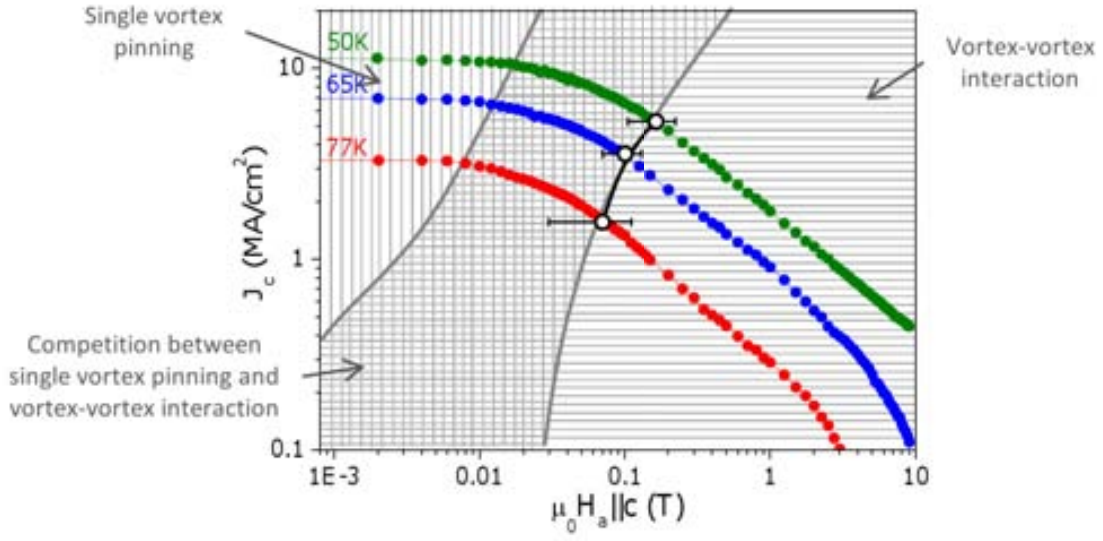

Figure 4.10.: $J_c(H_a)$ dependence of the sample with triangles patterned by FIB ($1\mu m$-lateral-side ; $2.5\mu m$-apart ; $70nm$-depth) at $77K$, $65K$ and $50K$. Black-empty dots indicate the region where the ratchet effect disappears which corresponds to the region where the vortex-vortex interaction becomes relevant in front of the vortex-defect interaction. Different interaction regimes are indicated as grey lines.

Further discussion about this dependence, and in particular differences on the magnetic field dependence between the direct ratchet effect and the reversal ratchet effect, will be performed in sec. 4.3.4.

4.3.2. Evaluation of the temperature dependence on the ratchet effect

Regarding the temperature dependence of the ratchet effect observed in Fig. 4.6 and Fig. 4.7, as we have commented before, the ratchet effect increases by decreasing temperature. Nevertheless, normalizing $[J_c^+ - J_c^-]$ subtractions by the values of $J_c^{\downarrow}(H_a)$, where $J_c^{\downarrow}(H_a)$ is $min[J_c^+(H_a), J_c^-(H_a)]$, we observe that the maximum value of $[J_c^+ - J_c^-]/J_c^{\downarrow}$ is nearly the same for all temperatures (Fig. 4.11). This can be understood if one considers that the increase of the $[J_c^+ - J_c^-]$ subtractions by decreasing the temperature, for a defined array, is due to an increase of J_c^{sf}. Thus, similar values on the normalized differences suggest that geometry is the key factor on the observed ratchet effect.

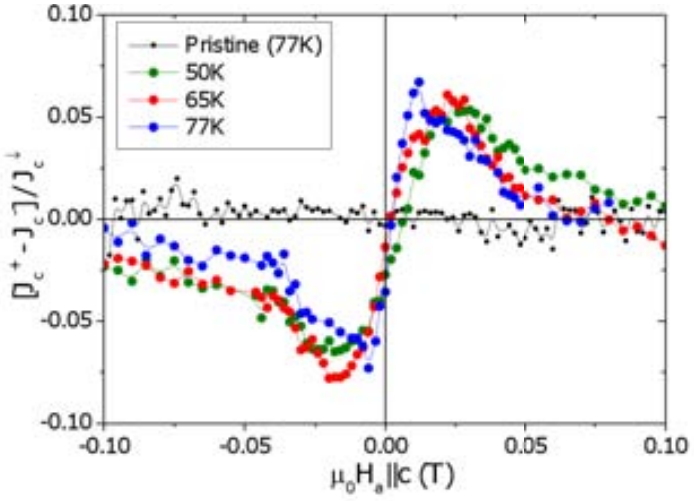

Figure 4.11.: Normalized $[J_c^+ - J_c^-]$ substractions of the direct ratchet effect obtained in Fig. 4.7.

4.3.3. Role of the patterned array geometry on the ratchet effect

In order to understand the role of the patterned geometry of blind-antidots on the preferential vortex motion, samples with different parameters on the triangular array have been prepared in bridges of $100 \times 20 - 40\mu m^2$ (the width of the bridges is modified in order to obtain in the final system between 4 and 10 rows of triangles in each bridge). The quality of all samples has been tested and compared with the results before the patterning. All samples present similar variations in T_c and ΔT_c than that shown in Fig. 4.3$-a$. As observed in samples discussed in sec. 4.2, the reduction of the critical current density at self field is higher than the reduction of the effective cross-section after the patterning in all these new patterned systems.

Separation between triangles is modified lengthwise (X *separation*) and crosswise (Y *separation*) between $0.7\mu m$ and $11\mu m$, triangular lateral side between 0.6 and $3\mu m$ and depth between 50 and $80nm$. Tab. 4.1 presents the different parameters of the used patterns where "X, Y *separations*" are the distance between triangles along the $X - Y$ directions, "X, Y *sides*" the lengths of the lateral sides of the triangle along the two respective directions, and "*Depth*" is the depth of the blind-antidot. The nomenclature of this configuration is displayed in Fig. 4.12 where lateral, top and front views are illustrated, together with the direction of the applied transport current. A "*Geometrical YZ Factor*", which will be used in the following to analyze the ratchet effect, is also indicated in Tab. 4.1.

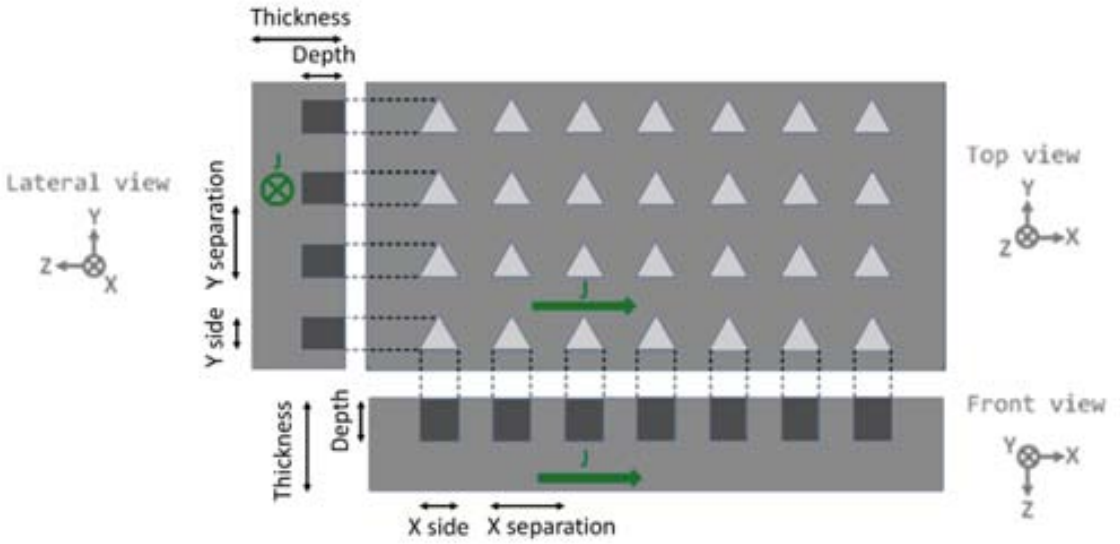

Figure 4.12.: Geometrical scheme of a bridge with a triangular array of blind-antidots and nomenclature of the parameters used to characterize the ratchet effect.

Etching process	**X separation** (μm)	**Y separation** (μm)	**X side** (μm)	**Y side** (μm)	**Depth** (nm)	**Geometrical YZ Factor** (%)
FIB	2.7	3.4	1.0	0.9	70	**7.4**
FEBL	11.0	11.0	3.0	2.6	80	**7.6**
FIB	2.7	3.2	1.0	0.9	70	**7.9**
FIB	2.5	2.5	1.0	0.9	70	**9.5**
FEBL	7.3	7.3	3.0	2.6	70	**9.9**
FIB	1.5	1.8	1.0	1.0	50	**11.1**
FIB	4.0	2.5	1.7	1.0	70	**11.2**
FIB	1.2	0.7	0.6	0.4	50	**11.9**
FIB	6.0	2.3	2.0	1.0	70	**12.2**
FIB	1.6	0.9	1.1	0.6	50	**13.3**
FEBL	5.0	5.0	3.0	2.5	70	**14.0**

Table 4.1.: Geometrical parameters of the different studied ratchet systems. Also the etching process is indicated.

The "*Geometrical YZ Factor*" corresponds to the relation between the maximum surface of the triangle on the YZ plane of Fig. 4.12 (lateral view), i.e. ["*Y side*" · "*Depth*"], and the cross-section of the bridge before the patterning, ["*Y separation*" · "*Thickness*"]. Notice that for this calculation, just one row of triangles is used although the same results would be obtained by considering the entire bridge. Therefore, the percentage of this ratio

(the "*Geometrical YZ Factor*") can be expressed as:

$$GeometricalYZFactor = \frac{[Yside][Depth]}{[Yseparation][Thickness]} \cdot 100 \tag{4.1}$$

Due to the reduction of $YBCO$ thickness below the patterned triangles, a redistribution of the current density is expected along the cross-section. As we will see, the redistribution of the current density not only depends on the thickness reduction but also on the parameters "*Y separation*" and "*Y side*". The "*Geometrical YZ Factor*" takes into account these 3 different parameters as observed in expression 4.1, and it will be relevant in the final observed ratchet effect.

Fig. 4.13 shows the "$Maximum[J_c^+ - J_{c-}]/J_c^{\downarrow}$" obtained at different temperatures for the whole set of analyzed samples, as a function of the "*Geometrical YZ Factor*". We observe that the relevance of the ratchet effect, i.e. the maximum value of $[J_c^+ - J_c^-]/J_c^{\downarrow}$ can be tuned by the patterned array. As a criterion, "$Maximum[J_c^+ - J_c^-]/J_c^{\downarrow}$" value is taken negative for the reversal ratchet effect and positive for the direct ratchet effect. One of the most obvious features of Fig. 4.13 is that all points obtained at different temperatures and from different patterning techniques, follow a single trend. It can be also clearly observed that, for high values of the "*Geometrical YZ Factor*" ($> 10\%$, high redistributions of current density), the direct ratchet effect is obtained, i.e. internal vortices are which start the measured dissipation. Within the studied range, when "*Geometrical YZ Factor*" is increased, the direct ratchet effect is enhanced. Regarding low modifications of the cross-section, ("*Geometrical YZ Factor*" $< 10\%$, i.e. low redistributions of current density), the reversal ratchet effect is obtained and again, experimental data indicates that it is more pronounced when "*Geometrical YZ Factor*" decreases. In that case however, a maximum should be reached because the reversal ratchet effect must disappear when "*Geometrical YZ Factor*" $= 0$.

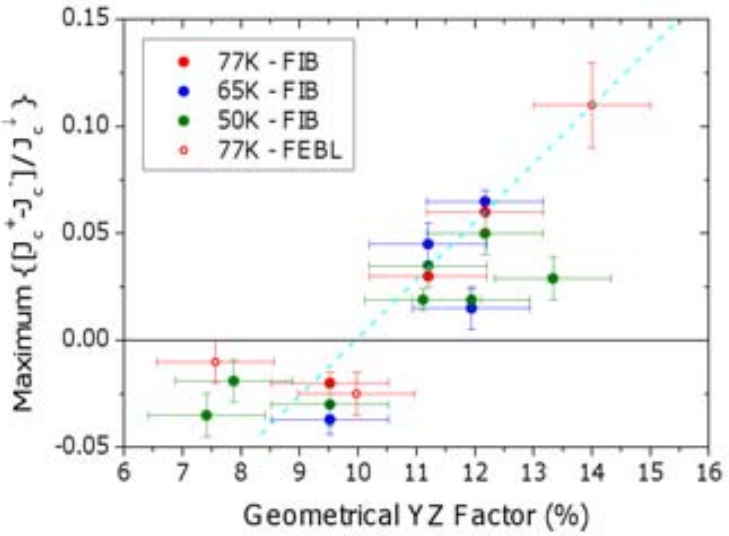

Figure 4.13.: Normalized maximum subtractions of the ratchet effect as a function of the "*Geometrical YZ Factor*". As a criterion, "$Maximum[J_c^+ - J_c^-]/J_c$" value is taken negative for the reversal ratchet effect and positive for the direct ratchet effect.

Therefore, we have demonstrated that the sign of the ratchet effect is controlled by the reduction of the effective superconducting cross section (which can be studied as a function of the "*Geometrical YZ Factor*"). On the other hand, we have also shown that, regardless of which population initializes its movement, the effect becomes unobservable at fields higher than the setting of the magnetic field region dominated by vortex-vortex interaction.

Theoretical simulation of vortices initiating the dissipation in the ratchet effect

Results shown in the last sections can be understood with a theoretical simulation performed in collaboration with the *Superconductivity Group* from *Universitat Autonoma de Barcelona* (*UAB*) presented below. The model used in this simulation cannot quantify the relevance of the ratchet effect, i.e. the "$Maximum[J_c^+ - J_c^-]/J_c^{\downarrow}$" but provides information about which population of vortices promotes the effect.

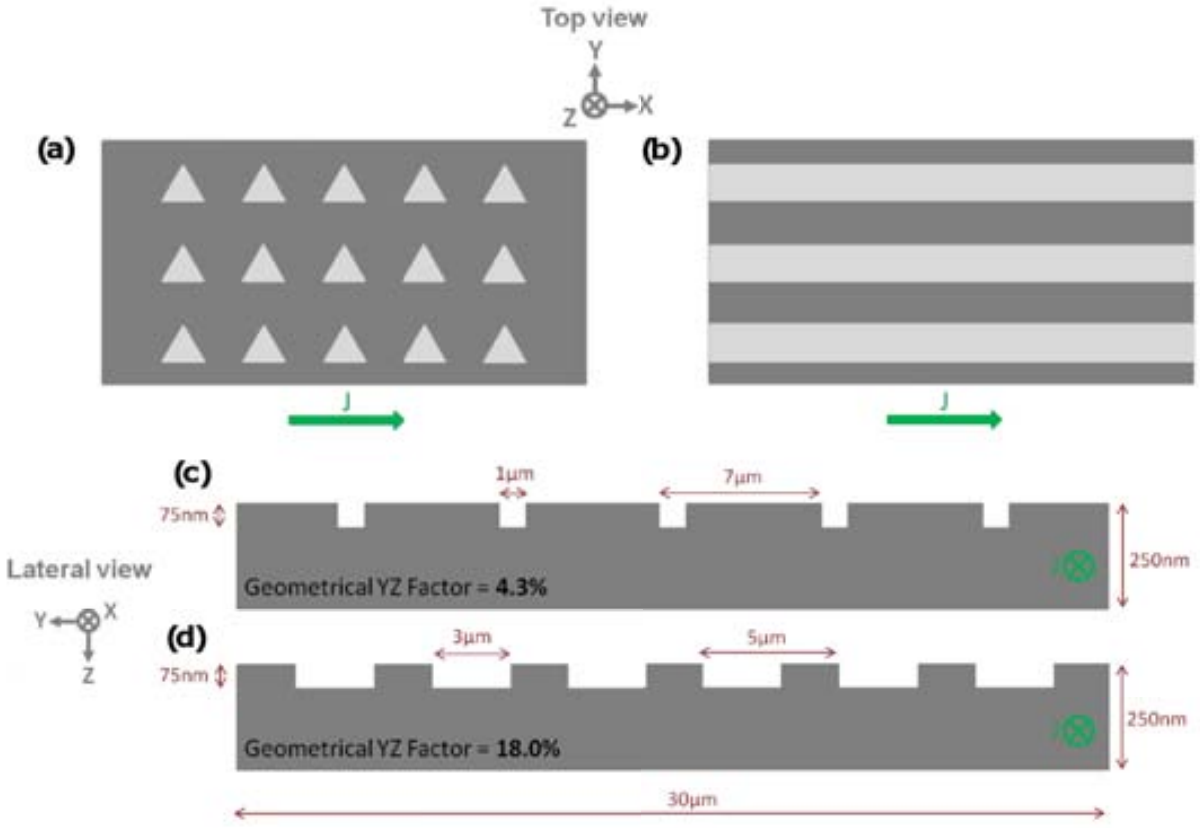

Figure 4.14.: Analogy between the **(a)** experimental system and **(b)** the simulated system. **(c)** and **(d)** show the crossections of two simulated systems used to evaluate vortex motion in different ratchet systems.

Since we have seen that the relevant parameter for the ratchet sign is the cross-section, we have simulated a bridge with different strips (Fig. 4.14$-a$) emulating the triangles (Fig. 4.14$-b$) with different "*Geometrical YZ Factors*", Fig. 4.14$-c$ and Fig. 4.14$-d$.

The width of these strips corresponds to the "Y *side*" of the triangles. To perform the simulations, same pinning energies are assumed below and between the triangles.

In a first approach, this last assumption is in agreement with our Bitter Decoration studies performed in a $YBCO$ 250nm-thick film where a triangle of 100μm-lateral side and 80nm-depth is patterned by $FEBL$. We have performed the decoration experiment at $4.2K$ and in the remanent state of the superconductor after a field cooled process at $3.3mT$. Results are displayed in Fig. 4.15. Since trapped vortices at the remanent state provide information about the pinning energy of the system, by determining the density of vortices at different areas, inside and outside the triangle, qualitative information about this energy can be obtained at the different positions. Experimentally, we have obtained a vortex density of about $0.75 vortices/\mu m^2$ at internal and external positions, revealing that, the thickness reduction inside the triangles, does not enhance, directly, the pinning energy.

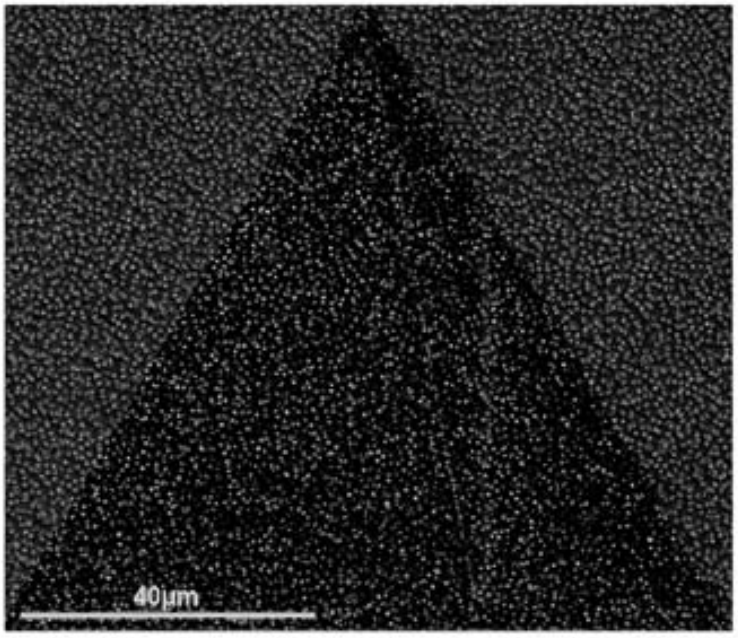

Figure 4.15.: Bitter Decoration SEM image on a $YBCO$ thin film in which a triangle of 80nm-depth that has been patterned by the $FEBL$ technique.

To perform the simulation we have choosen two different bridges of 30μm-width and 250nm-thick. The first one corresponds to a bridge with triangles separated 7μm, 1μm-"Y *side*" and 75nm-depth (Fig. 4.14$-c$). The second one corresponds to a bridge with triangles 5μm-apart, 3μm-"Y *side*" and 75nm-depth and (Fig. 4.14$-d$). By calculating the corresponding "*Geometrical* YZ *Factor*" we obtain 4.3% and 18.0% respectively, which correspond to the experimental systems where the dissipation is initialized by external and internal vortices, respectively.

For the simulation, we assume that the superconductor obeys the critical-state model with a field-dependent critical current density $J_c(H_{local})$, where H_{local} is the modulus of the local magnetic field. The developed model follows an iterative procedure used also in [173–175]. The cross-section is discretized in $N \times M$ infinitely long cells (in X direction)

of rectangular cross-section in the YZ plane, and it is assumed that the critical current density in each cell k, $J_{c,k}$, is uniform over the cell and with a value given by the Kim's critical-state model, equation4.2 [176].

$$J_{c,k}(H_{local}) = \frac{J_{c0}}{(1 + H_{local,k}/H_0)} \tag{4.2}$$

where J_{c0} and H_0 are constants and $H_{local,k}$ is the modulus of the local magnetic field at the center of the cell k. This dependence is chosen because it has been shown to fit well the $J_c(H_a)$ dependence measured in thin $YBCO$ films [173]. The iterative procedure starts by setting $J_{c,k} = J_{c0} = J_c(\mu_0 H_{local} = 0)$ for all k's. With this current density distribution, the new local magnetic field is calculated and a new set of $J_{c,k}$ is found using expression 4.2. In each iteration step, the transport $J_{c,k}$ is calculated for each cell and the iterative process is repeated until the difference between two consecutive evaluations of J_c is less than $10^{-6} J_{c0}$.

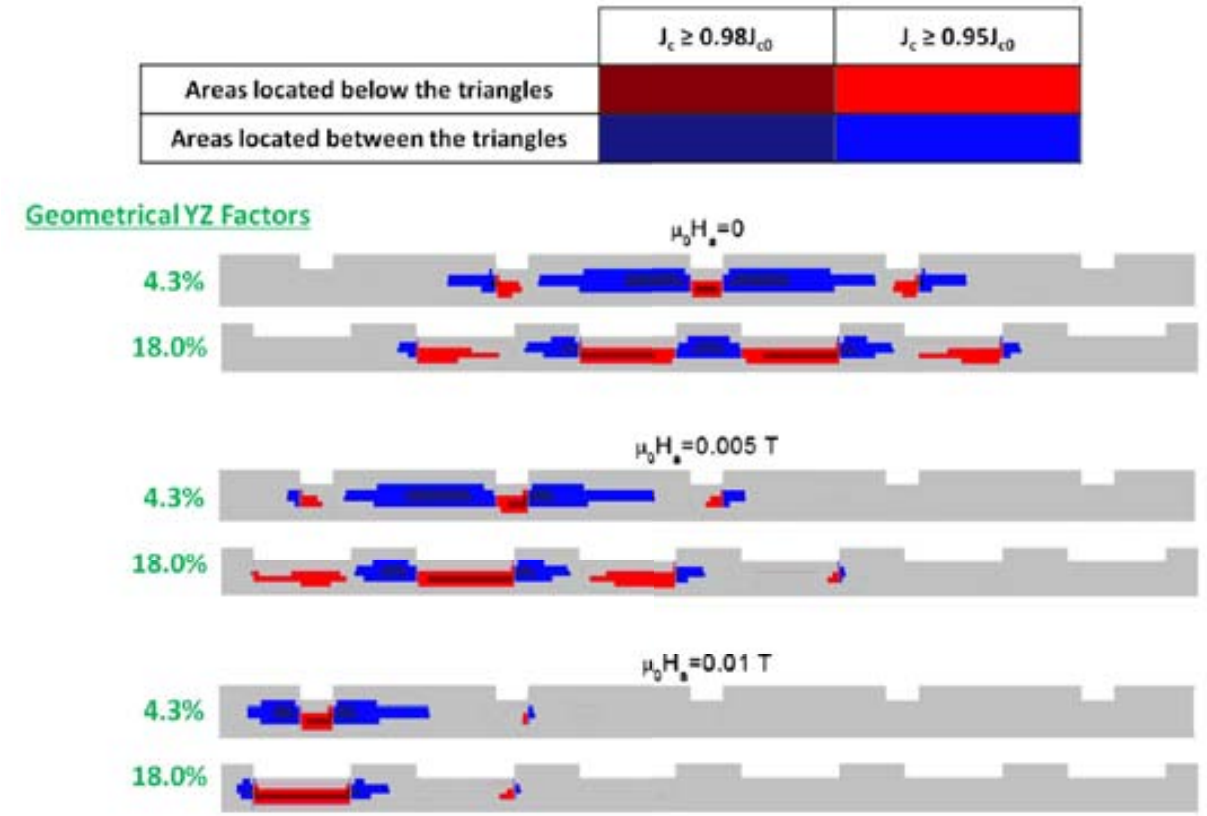

Figure 4.16.: Two simulated systems at different $\mu_0 H_a$ where the regions with the maximum critical current densities are indicated by different colors. As a criterion dark colors indicate the region where the critical current is higher than $0.98 J_c(\mu_0 H_{local} = 0)$ and light colors when $0.95 J_c(\mu_0 H_{local} = 0)$. Blue family colors correspond to the regions outside the stripes (triangles in the experimental case) and red family colors the regions down the stripes.

Fig. 4.16 plots the regions in the cross-section where a certain J_c is exceed, for different applied magnetic fields. In particular J_c values larger than $0.98 J_{c0}$ and $0.95 J_{c0}$ are

presented in different color-scheme. Red-family-color corresponds to the highest critical current densities located below the strips (triangles) and blue-family-color to the interstitial positions.

From the figures obtained with the simulations we observe that maximum critical current densities are located at different regions: below and between the triangles, depending on the sample geometry. As a first approximation, we assume that the system will start to dissipate in the regions where maximum J_c is achieved. It is important to note that this simulation emulates the critical current density profile before the system starts to dissipate. Therefore, it is reasonable to assume that a minimum increase of the current density will produce movement of vortices (dissipation) at the regions with the maximum J_c (regions where the current cannot further incrase its value). These regions are those marked in Fig. 4.16 with different colors, depending on the J_c criterion chosen. We have also to take into account that the dissipation that we will measure experimentally will also depend on the number of vortices that initialize the movement.

In the case of the direct ratchet effect, i.e. the 18% case, the maximum regions with highest critical current density are achieved, mainly, below the stripes (triangles), since the red-family-color is the dominant. This indicates that internal vortices would be the ones that will start the measured dissipation, producing a direct ratchet effect. In this case, the Lorentz force generated below the triangles must be higher enough to overcome the possible potential barrier generated due to the thickness modulation in the blind-antidots.

On the opposite, for the reversal ratchet effect, i.e. the case of 4.3%, the dominant color is the blue indicating that in this case, maximum critical current densities are located, mostly, between the stripes (triangles). Consequently, we expect that the main dissipation will start from external vortices providing a reversal ratchet effect.

Thus, with this theoretical simulation we can explain the different ratchet behaviors observed (direct or reversal) if we assume that we measure dissipation mainly associated to the regions where critical current density is achieved. Therefore, depending on the geometry of our system, either vortices located below or between the triangles will start to dissipate, giving us a tool to tune the direction of the ratchet effect.

4.3.4. Dynamic differences between direct and reversal ratchet effect: H_a and T dependences

After the analysis of the origin of the different ratchet systems, we will further study the dissipative process at regions where the ratchet effect is observed. We have demonstrated that the ratchet effect occurs just at fields where the vortex-vortex interaction is not dominant. However, it is still not clear which kind of interactions are governing the vortex dynamics in each kind of ratchet.

In order to fully understand these interactions, we now evaluate the dissipation in terms of electric field or voltage drop. We compare the two voltage drops arising from the two electrical polarities, obtained for a given value of the external current. To carry out this procedure, we set the maximum value of the critical current density obtained for the two polarities (J_c^+ in the example shown in Fig. 4.17), determined with a given criteria

of voltage drop ($V_{criterion}$). With this current value, we evaluate the obtained differences in dissipation comparig the curves J^+ and J^-, ΔV. A schematic representation of this procedure is illustrated in Fig. 4.17 where again, for a better comparison both, J^+ and J^-, are displayed in the same quadrant.

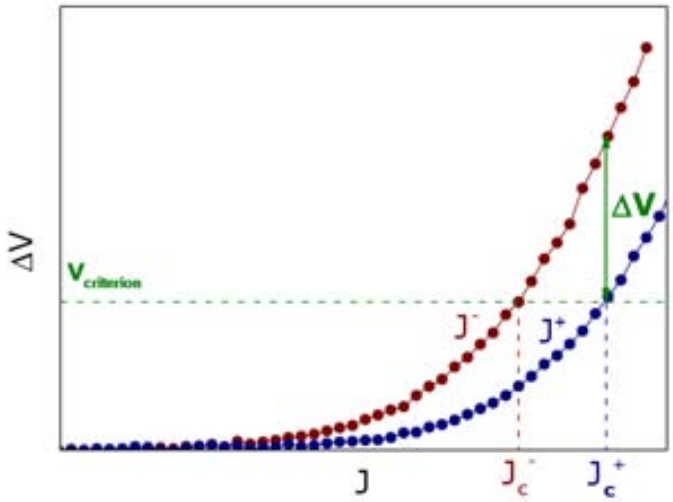

Figure 4.17.: Schematic representation of the methodology used to determine the final ΔV obtained in an asymmetric system. In this particular example, $J_c^+ > J_c^-$.

The obtained ΔV values can be related with the vortex net velocity through expresion 1.6 of chapter 1, which in terms of voltage is:

$$\frac{\Delta V}{d} = |\overrightarrow{B} \times \overrightarrow{\Delta v}| \tag{4.3}$$

where d is the bridge length, B is the local magnetic field and Δv is the vortex net velocity. Therefore, the study of ΔV would provide us information about the velocities that vortices have in different conditions.

Fig. 4.18 displays the value of ΔV at $77K$ as a function of the applied magnetic field for 4 different systems characterized by their "*Geometrical YZ Factor*". A $V_{criterion} = 5 \cdot 10^{-7}V$ has been used in this plot. Again, as a criterion, for positive applied magnetic fields, ΔV is chosen negative in the reversal ratchet effect (red dots) and positive in the direct ratchet effect (blue dots). As observed, a variation on the "*Geometrical YZFactor*" from 9.9 to 11.2, invert the ratchet effect which is in agreement with the data shown in Fig. 4.13.

As it is indicated with dashed lines, the value of the applied magnetic field at which the maximum ΔV is obtained, ΔV^{max}, is the same for systems that presents the same kind of ratchet (direct or reversal) regardless of its "*Geometrical YZ Factor*". It suggests that the mechanism that rules the vortex dynamics in each specific kind of ratchet must be always the same. Further analysis must be performed in order to better understand the factors controlling the vortex velocity in the different systems.

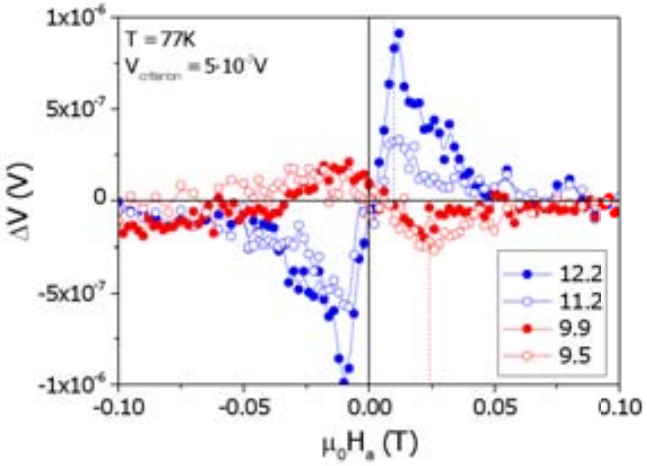

Figure 4.18.: ΔV at $77K$ as a function of the applied magnetic field for different samples characterized by their "*Geometrical YZ Factor*". A criterion of $5 \cdot 10^{-7} V$ has been chosen to determine the value of ΔV.

Fig. 4.19 plots the $J_c(H_a)$ curves obtained at different temperatures for a sample patterned with triangles (data also shown in Fig. 4.10). Besides the points where the ratchet effect vanish (which coincide with the setting of the collective vortex pinning regime) indicated as empty dots and discussed in sec. 4.3.1, the fields at which ΔV^{max} is reached are also displayed for the different kind of ratchet systems. Notice that, the field values at which the direct ratchet achieves its maximum effect, are lower than the obtained in the case of the reversal ratchet effect. In fact, in the case of the direct ratchet, these fields closely correspond to the fields where the single vortex pinning plateau ends. The situation for the reversal ratchet effect is somewhat different since these fields are located

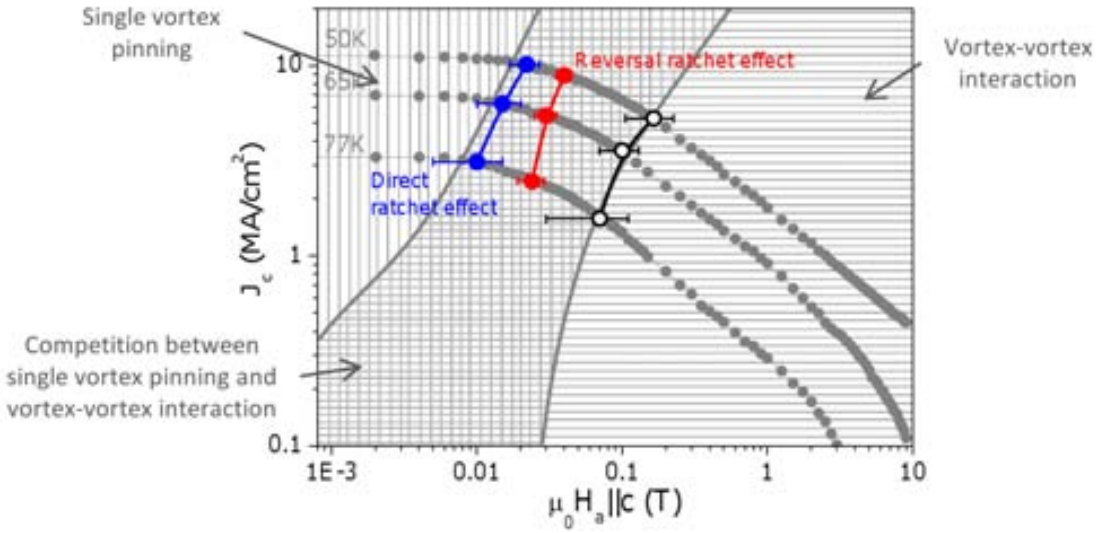

Figure 4.19.: $J_c(H_a)$ at different temperatures measured for a $YBCO$ film with triangular blind-antidots. The fields where the reversal ratchet effect and the direct ratchet effect achieve its maximum ΔV value are indicated (red and blue dots respectively). Also, fields where the ratchet effect (reversal or direct) disappears are indicated as a black dots.

in the region where the vortex-defect interaction strongly competes with the vortex-vortex interaction.

These observations suggest that the direct ratchet effect is mainly controlled by the interaction between vortices and the artificial asymmetric patterns. Notice that, in this case, when internal vortices start their movement, they feel the potential barrier associated to thickness reductions into the triangles [168]. When the vortex-vortex interaction starts to be present, the interaction between internal vortices with the asymmetric potential is reduced and the ratchet effect starts to diminish.

On the other hand, in the reversal ratchet effect, external vortices do not directly feel the asymmetric pinning potential induced inside the triangles. In this case, they observe an asymmetric potential due to their interaction with the internal vortices, which are confined into the triangles [172, 177]. Therefore, in this second case, vortex-vortex interactions are needed in order to observe the reversal ratchet effect.

4.4. Conclusions

In this chapter, we have seen that an asymmetric behavior of the vortex movement is possible by the creation of artificial asymmetric blind-antidots, triangles in our case. By transport measurements, we observed different values of the critical current density by inverting the polarity of the external electrical current. This effect is what it is called the ratchet effect.

FIB and $FEBL$ techniques allow us to generate effective artificial asymmetric nanostructures without damaging the superconducting properties. Both techniques, promote the ratchet effect indicating that the possible implantation of Ga^+ ions by using the FIB is not the key factor inducing this effect.

In order to explain the obtained behavior, we have divided the vortices in two populations: vortices located inside (internal) and outside (external) the triangles. As the superconducting cross-section is not the same along the width of the bridge due to the thickness modulation after the triangular patterns, the critical current density will be achieved at different positions with respect to the triangles. As a consequence, internal or external vortices can start the movement.

We have demonstrated how controlling the geometry of the patterned array, i.e. the lateral side of the triangles, their separation and depth, we can choose which vortices start to produce the measured dissipation. It has been observed how, for low reductions of the superconducting cross-section, the vortices that start the measured dissipation are the external ones. Consequently, due to the asymmetrical distribution of internal vortices, which are pinned into the triangles, external vortices observe these non-symmetric vortex-barriers generating therefore the reversal ratchet effect. In the opposite case, for high reductions of the superconducting cross-section, the vortices that start the movement will be the internal ones which feel a different barrier for the vortex movement arising from thickness modulations.

We have evaluated the temperature and magnetic field dependence of the two observed different ratchet systems. In the case of the direct ratchet, their effect starts to

decrease when the vortex-vortex interaction starts to be present, indicating that the interaction between vortices and defects associated to thickness variations, controls the effect. In the case of the reversal ratchet effect, since an interaction between both populations of vortices is needed, the effect is highly pronounced when vortex-defect and vortex-vortex interactions compete. In both cases, when the vortex-vortex interaction dominates, the effect disappears.

Therefore, we have demonstrated that an asymmetric motion of vortices is possible in a high temperature thin film by performing a patterning with asymmetrical blind-antidots. The regions where critical current density is achieved can be tunned by the geometry of the blind-antidots resulting in two different types of ratchet.

5. YBCO thin films patterned with Cobalt nanorods

Superconductivity and magnetism are two antagonic cooperative phenomena since Cooper pairs in a superconductor (SC) have opposite spin while in a ferromagnetic material (FM) spins are aligned [178]. In the SC/FM hybrids, an inhomogeneous magnetic field distribution produced by the ferromagnet can lead to a significant change in the properties of the superconducting layer like the critical temperature or the critical current density as a function of the applied magnetic field [179]. In this chapter, interaction between fields created by the ferromagnet and the superconductor are studied in $YBCO$ films with Co-nanorods with the aim to understand vortex dynamics in this particular hybrid SC/FM system.

5.1. State of the art

There has been extensive earlier work on the study of the interaction between SC/FM hybrids, most of them performed in LTS. Some of them are related with the proximity effect which occurs in layered ferromagnet-superconductor systems as presented in reference [179]. In other studies, the proximity effect is avoided by growing a thin protective insulating layer between the two materials, since this effect is present in lengths of the order of . In these cases, the study of the interaction between strays fields of the different materials (superconductor and ferromagnet) is the main goal.

One of the first studies in SC/FM hybrids were performed by Martin et. al. and Van Bael et. al. [6,180] where a $100nm$-thick Nb film was grown over an array of magnetic Ni dots. In that case, the stray fields generated by the dots, which were magnetized in-plane, gave rise to oscillations in the resistivity and/or magnetization versus the applied magnetic field, with period corresponding to one flux quantum per unit cell of magnetic dot lattice. In parallel, and using the same materials, Morgan and Ketterson [181] studied the J_c behavior as a function of the applied magnetic field. Oscillations in J_c were also observed, although in this case, non-asymmetric J_c vs field behavior was obtained since the magnetic field was applied out-of-plane and the FM stray fields were superposed to the applied field. The same effect was observed and analyzed by Scanning Hall Probe Microscopy by Van Bael et. al. [182]. Hysteresis in the critical current density and resistivity were also studied by Palau et. al. [183] and Visani et. al. [184] in the case of SC/FM nanocomposites and multilayers, respectively. Another interesting effect with out-of-plane magnetized dots was reported by Moschalkov and Lyuksyutov et. al. [185–191]. In these studies, FM-stray-fields were superposed to the applied magnetic field modifying the local magnetic

field and inducing superconductivity at applied magnetic fields where in the absence of magnetic dots could not be observed.

In this chapter we study the transport critical current density in SC/FM materials and SC/insulator hybrid systems with high temperature superconducting films. We observed that stray fields generated in both hybrid systems cause hysteretic behaviors on J_c as a function of the applied magnetic field (H_a). Results has enabled us to understand the contributions of different stray fields playing a role in the two hybrid systems. The magnetic history of the ferromagnet and the superconducting layer, and the temperature, are seen to be the key factors controlling the final SC behavior.

5.2. Patterning of ferromagnetic nanostructures

To perform this study, three different bridges were undertaken simultaneously in a $YBCO$ film grown by chemical solution deposition: a pristine bridge used as a reference ($YBCO/P$), and two patterned bridges with hybrid systems: superconductor/insulator and superconductor/ferromagnet. In the first case, we performed a bridge with an array of antidots (holes) that perforate completely the superconductor ($YBCO/A$, Fig. 5.1$-a$), and in the second case, we performed a bridge with the same antidot array filled with cobalt-nanorods ($YBCO/AR$, Fig. 5.1$-b$). With the aim to induce the highest contribution of the ferromagnetic stray field, generated by the nanorods, to the superconducting film, 125nm-thick films have been prepared (instead of the 250nm-films used in the rest of this thesis).

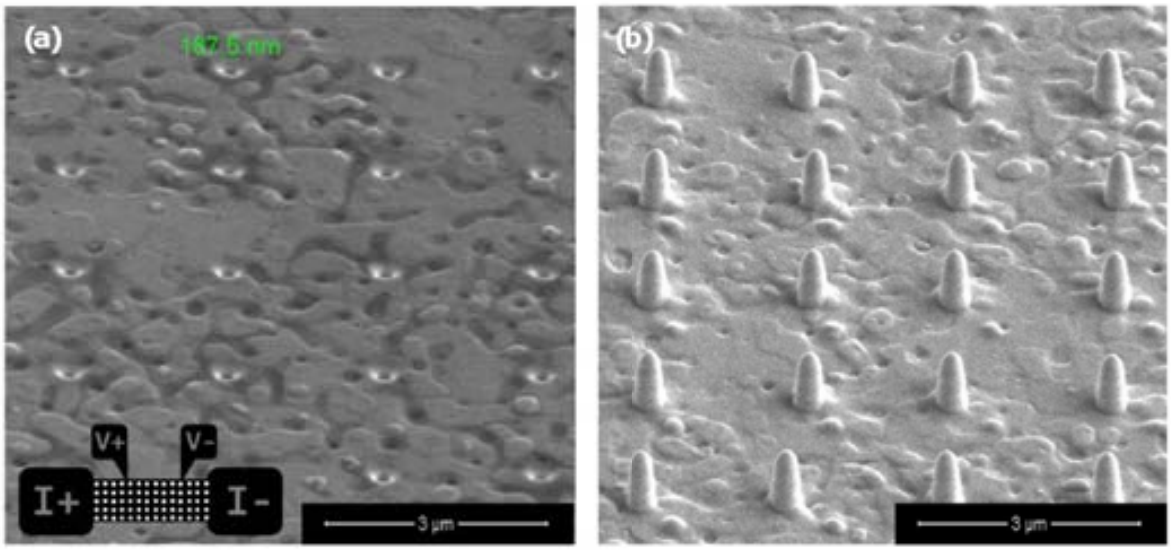

Figure 5.1.: 52º tilted SEM images of bridge patterned by **(a)** antidots and **(b)** antidots + Co-nanords. The detail of the figure shows the schematic representation of the location of the antidots and antidots + Co-nanorods in a bridge patterned with a 4-point measurement configuration.

The antidot array consists of holes of 200nm-diameter and about 315nm-depth (completely perforating the film and part of the substrate) with a period of 2μm. Co-nanorods

have 200nm-diameter and 500nm-length; therefore they are extended $\sim 190nm$ above and below the SC film. In order to pattern the antidots and grow the ferromagnetic nanostructures, the FIB and $FEBID$ techniques have been used, respectively (see sec. 2.2.2 and sec. 2.2.4), in collaboration with *Instituto de Nanociencia de Aragon* (INA).

With the aim of quantify the damage on the $YBCO$ film produced during the patterning processes, T_c and J_c measurements have been performed before and after the patterning. A reduction of $\sim 5K$ on the critical temperature in both systems and about $1K$ on ΔT_c in the $YBCO/AR$ system, are obtained due to the patterning, Fig. 5.2$-a$. Regarding the critical current density, a reduction larger than 70% on the self-field J_c, J_c^{sf} is obtained in the $YBCO/A$ system and around 90% in the $YBCO/AR$, Fig. 5.2$-b$. This reduction is higher than the expected according to the reduced cross-section (determined considering the presence of antidots), which should decrease J_c^{sf} a 10%. The geometrical factors used to calculate the J_c after the patterning were considering the entire cross-section of the bridge. As already discussed in the previous chapter, with the results obtained on the ratchet systems, a higher reduction of the cross-section than the expected due to the cross-section reduction, may be attributed to the amorphization of the material surrounding the antidots. This happens during the ion beam etching in both systems, and in the case of the $YBCO/AR$ system, due to the the additional growth of Co-nanorods which could also deteriorate the superconducting properties. In these cases, a degradation of a layer of about $\sim 750nm$ around the antidots would explain the obtained J_c^{sf} values as observed in the $YBCO/A$ system in Fig. 5.2$-b$.

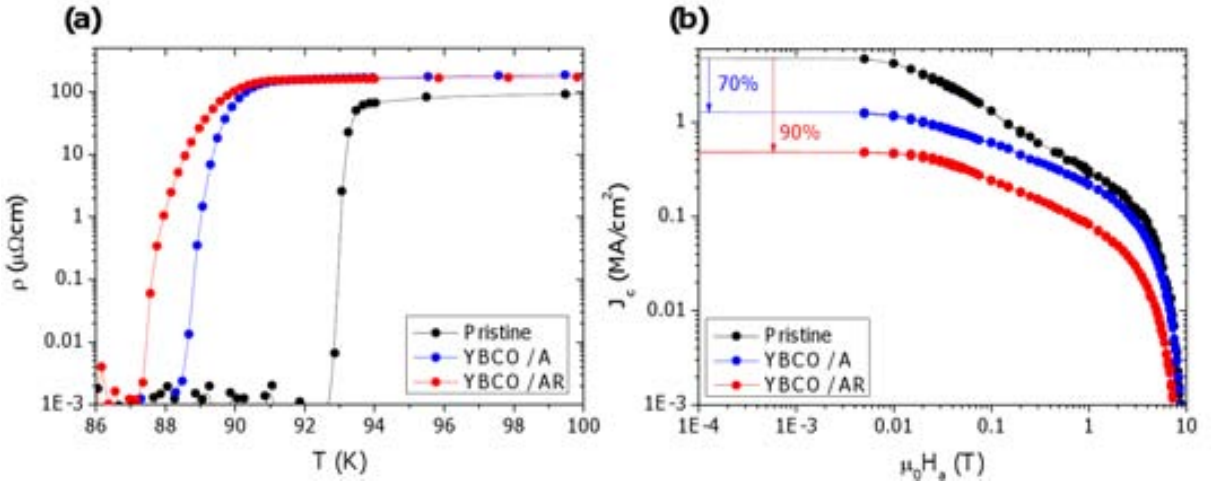

Figure 5.2.: Comparison of the **(a)** T_c and **(b)** $J_c(H_a)$ **(b)** for the different studied systems.

5.3. Magnetic characterization of one single Co-nanorod

In order to characterize the FM-nanostructures, we have measured the magnetization of one single Co-nanorod by Magneto Optical Kerr Effect ($MOKE$) in collaboration with Ikerbasque foundation. Measurements are performed at room temperature, with an applied magnetic field parallel to the ab-plane of the superconductor ($H_a||ab$), Fig. 5.3.

Since the Curie temperature (temperature at which ferromagnetism disappears) in cobalt, T_{Curie}^{Co}, is above $1000K$, we suppose the same contribution of the nanorods for $T < 300K$.

Results show that the saturating magnetic field of the ferromagnetic nanords (H_{sat}^{FM}) measured with $H_a||ab$ is $\sim 0.1T$, Fig. 5.3. Although this magnetic field orientation does not corresponds to the direction in which we have performed all the experiments in the hybrid systems ($H_a||c$-axis of the $YBCO$), this measurements give us a maximum value of H_{sat}^{FM}, since we would expect that $H_a||c$ is the easy magnetization axis, considering the aspect ratio of the nanorods ($AR = Rod\ Length/Rod\ Diameter = 2.5$). Thus, in a first approximation, we can consider that $H_{sat}^{FM}(H_a||c) \leq H_{sat}^{FM}(H_a||ab) \sim 0.1T$.

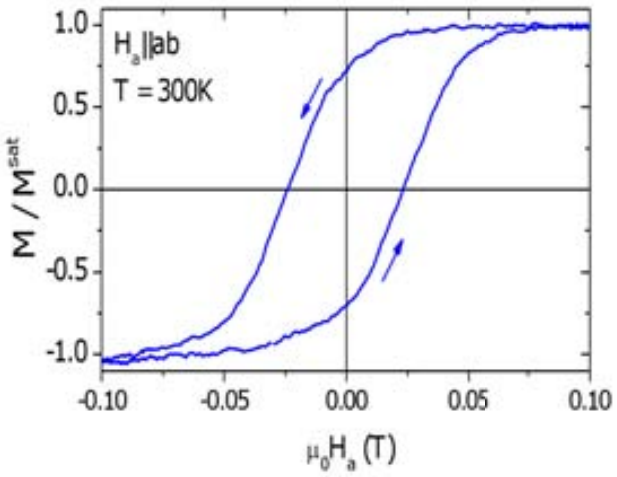

Figure 5.3.: Magnetic-loop of one single nanorod obtained by $MOKE$ with $H_a||ab$ and $T = 300K$.

5.4. Hysteretic effect on the irreversibility line of hybrid systems

The first study performed on the hybrid systems ($YBCO/A$ and $YBCO/AR$) consists of the analysis of the irreversibility line, IL, by applying low magnetic fields parallel to the c-axis. Before starting each measurement, systems were magnetized at different magnetic fields ($\mu_0 H_{mag} = \pm 0.2T$, $\pm 0.1T$, $\pm 0.075T$ and $\pm 0.05T$) at $T > T_c$. Consequently, just Co-nanorods were magnetized while the superconductor, in both systems, was in the normal state. In order to avoid large contributions of the remanent magnetic field arising from the superconducting coil, just $\mu_0 H_a \leq 0.2T$ will be studied in this chapter.

For each positive magnetization, the procedure to determine the IL is what follows:

i) Magnetize the system at $(+)\mu_0 H_{mag}$ and $T = 100K$ ($T > T_c$).

ii) Decrease the applied magnetic field from $(+)\mu_0 H_{mag}$ to $\mu_0 H_a = 0.02T$ at $T = 100K$ (just T_{irr} measurements between $0.02T$ and $-0.02T$ were performed).

iii) At $\mu_0 H_a = 0.02T$, decrease the temperature from $100K$ to $85K$ while resistivity measurements, $\rho(T)$, are carried out.

iv) At $\mu_0 H_a = 0.02T$, increase the temperature from $85K$ to $100K$ and decrease the magnetic field from $\mu_0 H_a = 0.02T$ to $0.015T$.

Procedures iii) and iv) are repeated at different $\mu_0 H_a$ until $\mu_0 H_a = -0.02T$ (descending sweep). After that, IL studies are performed with negative magnetizations of Co-nanorods, i.e.:

v) Magnetize the system at $(-)\mu_0 H_{mag}$ and $T = 100K$ $(T > T_c)$.

vi) Increase the applied magnetic field from $(-)\mu_0 H_{mag}$ to $\mu_0 H_a = -0.02T$ at $T = 100K$.

vii) At $\mu_0 H_a = -0.02T$, decrease the temperature from $100K$ to $85K$ while resistivity measurements, $\rho(T)$, are performed.

viii) At $\mu_0 H_a = -0.02T$, increase the temperature from $85K$ to $100K$ and increase the magnetic field from $\mu_0 H_a = -0.02T$ to $-0.015T$.

Again, procedures vii) and viii) are repeated at different $\mu_0 H_a$ until $\mu_0 H_a = 0.02T$ (ascending sweep).

Fig. 5.4 plots some of the $\rho(T)$ curves obtained after $\mu_0 H_{mag} = 0.1T$ for the $YBCO/AR$ system. The criterion used to determine the irreversibility line, in this particular analysis, is $\rho(T_{irr})/\rho(95K) = 0.01$. From the $\rho(T)$ curves obtained at different fields, we find that the highest irreversibility temperature (T_{irr}) is obtained at $\mu_0 H_a = 2mT$ whereas in a superconducting system, the maximum T_{irr} should be obtained at zero applied magnetic field. Thus, this measurement demonstrates that in this hybrid system, an additional return magnetic field ($\mu_0 H_r \sim 2mT$), which compensates the applied magnetic field H_a, is present.

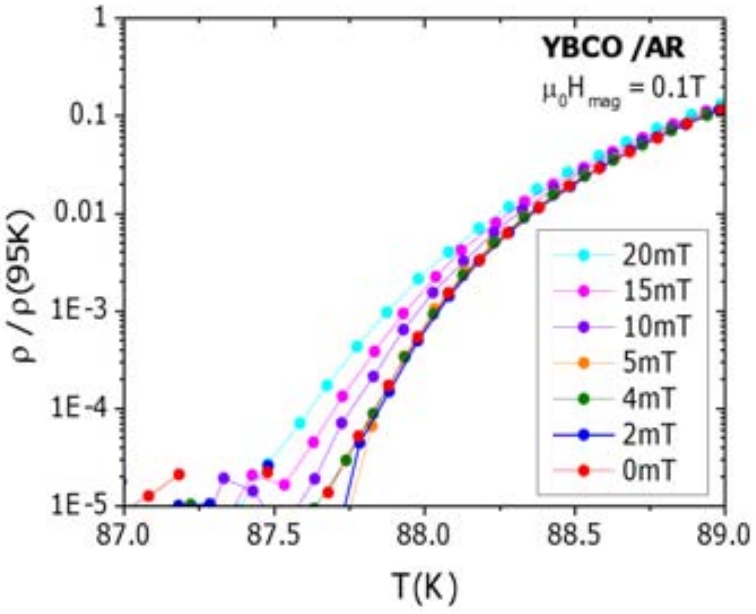

Figure 5.4.: Experimental $\rho(T)$ measurements of the $YBCO/AR$ system when $\mu_0 H_{mag} = 0.1T$; for clarity just fields during the descending sweep $0.2T - 0T$ are plotted.

The presence of a return magnetic field is better observed in Fig. 5.5 for the particular case of $\mu_0 H_{mag} = \pm 0.1T$ where we have plotted the irreversibility line measured during the

ascending and descending sweeps in both systems. To better compare the two systems, the irreversibility field, H_{irr}, have been plotted as a function of the reduced temperature, $t_{irr} = T/T_c$. In the $YBCO/AR$ system, a clear hysteresis is observed which is associated to the presence of a finite magnetic field, $\mu_0 H_r \sim 2mT$, which compensates H_a. On the other case, in the $YBCO/A$ system, the IL is completely reversible, with a maximum T_{irr} at $\mu_0 H_a = 0T$ indicating that $\mu_0 H_r = 0T$.

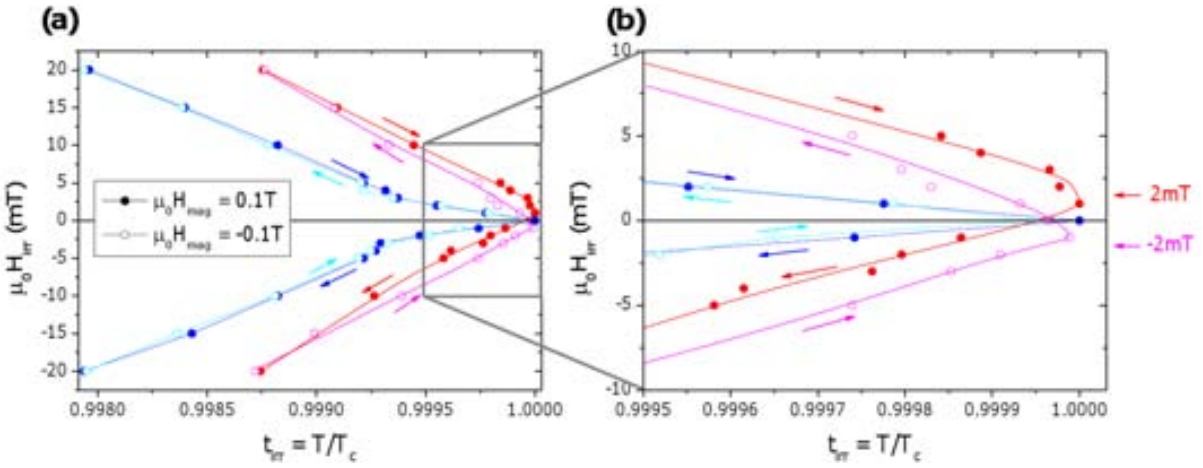

Figure 5.5.: (a) Experimental results of the irreversibility line measured during ascending and descending sweeps of the applied magnetic field, for the $YBCO/A$ and $YBCO/AR$ systems (blue and red dots respectively) after magnetizing them at $0.1T$. Arrows indicate the sweep sense. A zoom in **(b)** is plotted for clarity.

At this stage, we could wonder about which are, in general, the different magnetic field contributions to the local magnetic field (H_{local}) within the transport bridge. In one hand, it is well known that in a superconducting film with strong intrinsic pinning centers, like our $YBCO$ thin films, return magnetic fields are generated at the edges of the film arising from demagnetizing effects [58, 59]. Furthermore, in the case of a $YBCO$ thin film with an array of antidots, demagnetizing effects will also generate return magnetic fields at the edges of the antidots [192] which will depend on the magnetic history of the material (further discussion about this contribution will be commented in the next section). We are going to refer to this magnetic field contribution as H_r^{SC}. Thus, the local magnetic field for the $YBCO/A$ system will be expressed as:

$$H_{local}^{YBCO\ A} = H_a + H_r^{SC} \tag{5.1}$$

On the other hand, in the case of the $YBCO/AR$ system, the additional presence of a ferromagnetic material originates a return magnetic field which will depend on the nanorod magnetization, we will refer to this contribution as H_r^{FM}. Consequently, the local magnetic field for the $YBCO/AR$ system will be:

$$H_{local}^{YBCO\ AR} = H_a + H_r^{SC} + H_r^{FM} \tag{5.2}$$

It is worth noting at the outset that, in our T_{irr} measurements, the superconductor is in the vortex-liquid state and therefore, its magnetic behavior is completely reversible since it does not trap any magnetic field. Therefore, in this kind of measurements, $\mu_0 H_r^{SC} = 0T$ and a return magnetic field contribution will be just present in the $YBCO/AR$ system. In this system, the return field associated to Co-nanorods, H_r^{FM}, generates the obtained hysteresis observed in Fig. 5.5.

Fig. 5.6 displays the applied magnetic field that compensates the applied magnetic field giving $\mu_0 H_{local}^{YBCO\ A}$ and $\mu_0 H_{local}^{YBCO\ AR} = 0T$, i.e. H_r when the maximum T_{irr} is obtained in the IL measurements, as a function of H_{mag}, for $YBCO/A$ and $YBCO/AR$ systems. In other words, using equations 5.1 and 5.2, we determine $H_r(H_{mag})$ where $\mu_0 H_r = \mu_0 H_r^{SC} = 0T$ for $YBCO/A$ system and $\mu_0 H_r = \mu_0 H_r^{SC} + \mu_0 H_r^{FM} = \mu_0 H_r^{FM}$ for $YBCO/AR$.

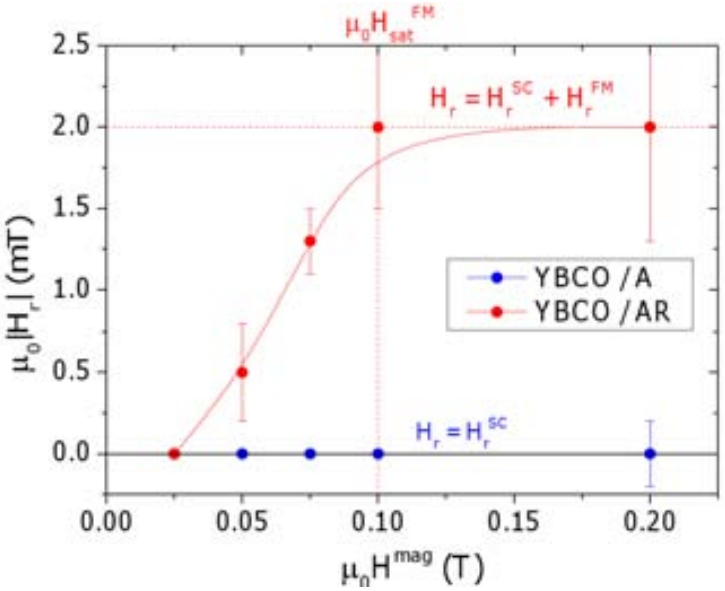

Figure 5.6.: Total return field when $\mu_0 H_{local} = 0$ as a function of H_{mag}.

From Fig. 5.6 we can see that H_r^{FM} increases by increasing the value of H_{mag} at low fields and it saturates at $\mu_0 H_{mag} \sim 0.1T$. This value is in agreement with the value of H_{sat}^{FM} determined by $MOKE$ measurements. For H_{mag} H_{sat}^{FM}, the same H_r^{FM} values are obtained since the nanorods are magnetically saturated.

Results confirm that the IL in our $YBCO/AR$ system is modulated by the return magnetic field generated by the Co-nanorod, H_r^{FM}, which depends on the value of H_{mag}. In contrast, since the magnetic behavior of the SC is completely reversible during the measurement of the IL, the value of H_{irr} in the $YBCO/A$ system depends only on the applied magnetic field since $\mu_0 H_r^{SC} = 0T$.

5.5. Hysteretic effect on Jc of hybrid systems

In this section, we are going to study the influence of the return magnetic fields present in our hybrid systems, H_r^{SC} and H_r^{FM}, on the critical current density behavior

(i.e. within the vortex-solid state). It is important to note that, in this regime, the magnetic behavior of the superconducting film is non-reversible (i.e. it follows a magnetic hysteretic loop) resulting on the presence of demagnetizing effects at the antidot edges and consequently, $\mu_0 H_r^{SC} \neq 0T$. We will firstly evaluate the effect of the H_r^{SC} by studying the $YBCO/A$ system and secondly, we will analyze the additional contribution of H_r^{FM} by studying the $YBCO/AR$ system.

The procedure followed to determine the J_c dependence on H_r^{SC} and H_r^{FM} consists of:

i) Cooling the sample from $100K$ to $65K$ in a Zero Field Cool (ZFC) process.

ii) Magnetize the systems at $0.1T$.

iii) Decrease the applied magnetic field from $\mu_0 H_a = 0.1T$ to $\mu_0 H_a = -0.1T$ while J_c transport measurements are performed (descending sweep). Blue curves of Fig. 5.7 plot schematic representations of the magnetic moment induced in the SC film (Fig. 5.7$-a$) and the FM nanorods (Fig. 5.7$-b$) during the J_c measurements.

iv) Increase the applied magnetic field from $\mu_0 H_a = -0.1T$ to $\mu_0 H_a = 0.1T$ while J_c transport measurements are carried out (ascending sweep). Again, red curves plotted in Fig. 5.7 display the magnetic moment induced in the SC film and the FM nanorods while J_c is measured during the ascending sweep.

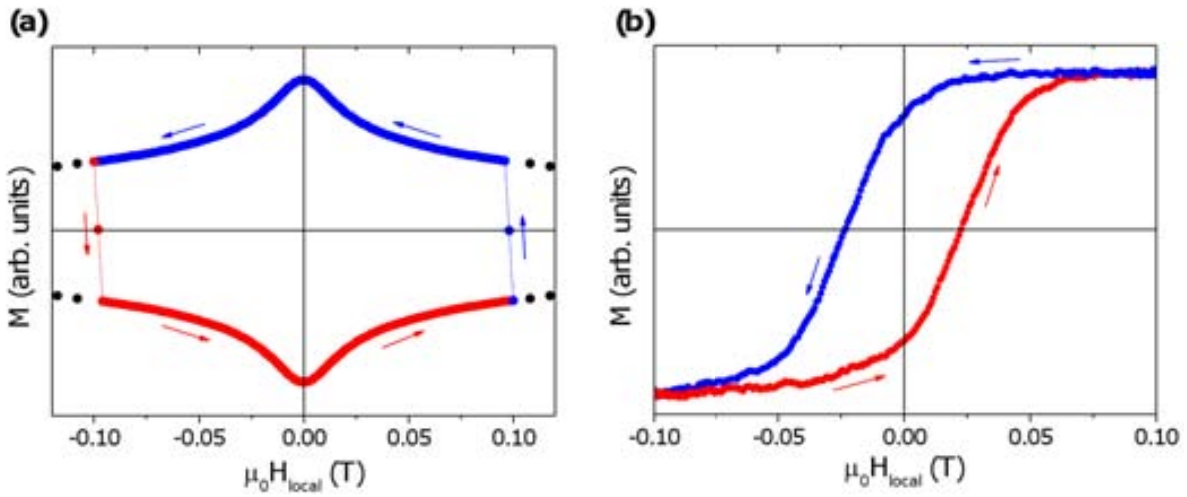

Figure 5.7.: Schematic representation of the magnetic hysteretic loops obtained for **(a)** the superconductor and **(b)** the ferromagnet, by performing the study of the $J_c(H_a)$ hysteretic behavior.

Analysis of the YBCO/A hybrid system

In the case of the $YBCO/A$ system, H_r^{SC} will be analyzed by measuring J_c as a function of the applied magnetic field parallel to the c-axis, following the procedure described above. The obtained J_c results, normalized by J_c measured at $\mu_0 H_a = 0T$ after a ZFC process (J_c^{ZFC}), are plotted in Fig. 5.8$-b$. For comparison, results obtained for a pristine system ($YBCO/P$), are also displayed in Fig. 5.8$-a$. As it is clearly observed, $YBCO/A$ system presents an hysteretic behavior of J_c non-present in the $YBCO/P$ case, indicating that the antidots are at the origin of this non-reversible behavior.

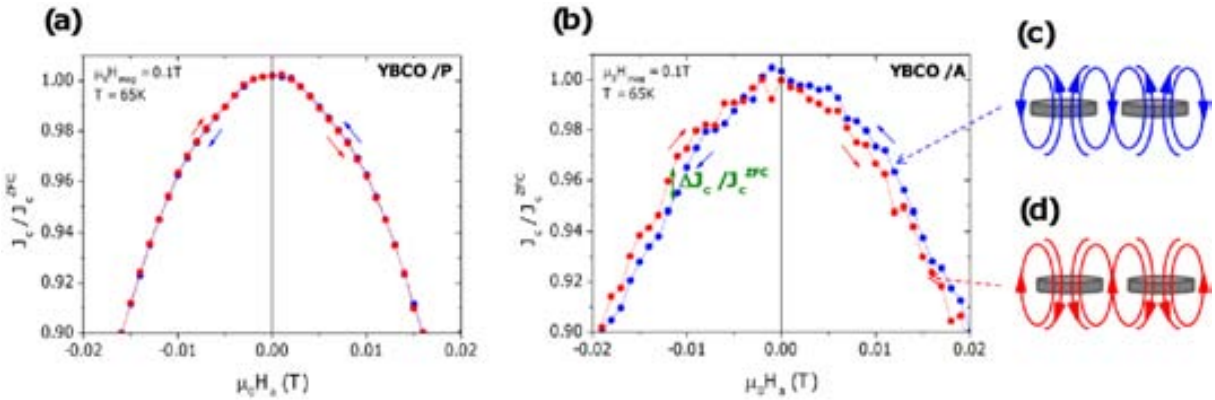

Figure 5.8.: $J_c(H_a)$ transport measurements for **(a)** $YBCO/P$ system and **(b)** $YBCO/A$ system after magnetizing the samples at $0.1T$. **(c)** and **(d)** show an schematic representation of H_r^{SC} at the regions where the superconductor starts to dissipate for the descending (blue) and ascending (red) J_c sweeps respectively. The sense of H_r^{SC} is indicated by arrows.

The $J_c(H_a)$ hysteretic behavior observed in the $YBCO/A$ system can be explained through the differences of H_{local} associated to the presence of trapped magnetic fields within the superconductor, generated due to the presence of antidots. The distortions in the internal magnetic field in a bridge with antidots have been evaluated by performing a simulation in collaboration with the *Superconductivity Group* from *Universitat Autonoma de Barcelona* (*UAB*). Details of the theoretical analysis performed in the simulation are explained in Appendix A.

We have emulated our experimental system considering an infinite strip of width W with an array of 4-squared-antidots of side ahole. Fig. 5.9$-a$ and Fig. 5.9$-b$ displays the contour maps of the local magnetic field (in the lack of electrical transport current) for a given H_a during an ascending[1] and desdending sweeps described in sec. 5.5, respectively. If after considering the field profiles obtained in Fig. 5.9$-a$ and b, we introduced an external transport current, the local magnetic field contour maps are modified resulting in the field distribution plotted in Fig. 5.9$-c$ and d. With the magnetic simulations we observe clear differences between Fig. 5.9$-c$ and d (i.e. between the local field distribution obtained in the ascending and descending branches of $J_c(H_a)$ sweeps). Thus, the values of H_{local} at the regions where the superconductor will transist (regions between antidots, black-crosses in Fig. 5.10$-a$) are different by increasing or decreasing H_a, resulting in the obtained hysteretic behavior of $J_c(H_a)$.

A similar behavior was studied by Bartolome et.al. [192] where a superconducting thin film with a square array of antidots was compared with a granular system like a $YBCO$ coated conductor [48]. Fig. 5.10$-a$ shows how this analogy whould be applied in our system, where white-dots correspond to antidots and orange-circumferences to equivalent grains of radius R_{grain}. In Fig. 5.10$-b$ is shown the local magnetic field profile trapped within two saturated grains for a value of H_a (i.e. after saturating at $H_{mag} \quad 2H^*$ and decreasing the field to $H_a << H_{mag}$) (see sec. 1.2.3). It is observed that the edges of the grains present a negative return magnetic field component, H_r^{grain}, which will

[1]The ascending sweep considered in the simulation starts from a ZFC, instead of the described in the experiment which starts from negative magnetization.

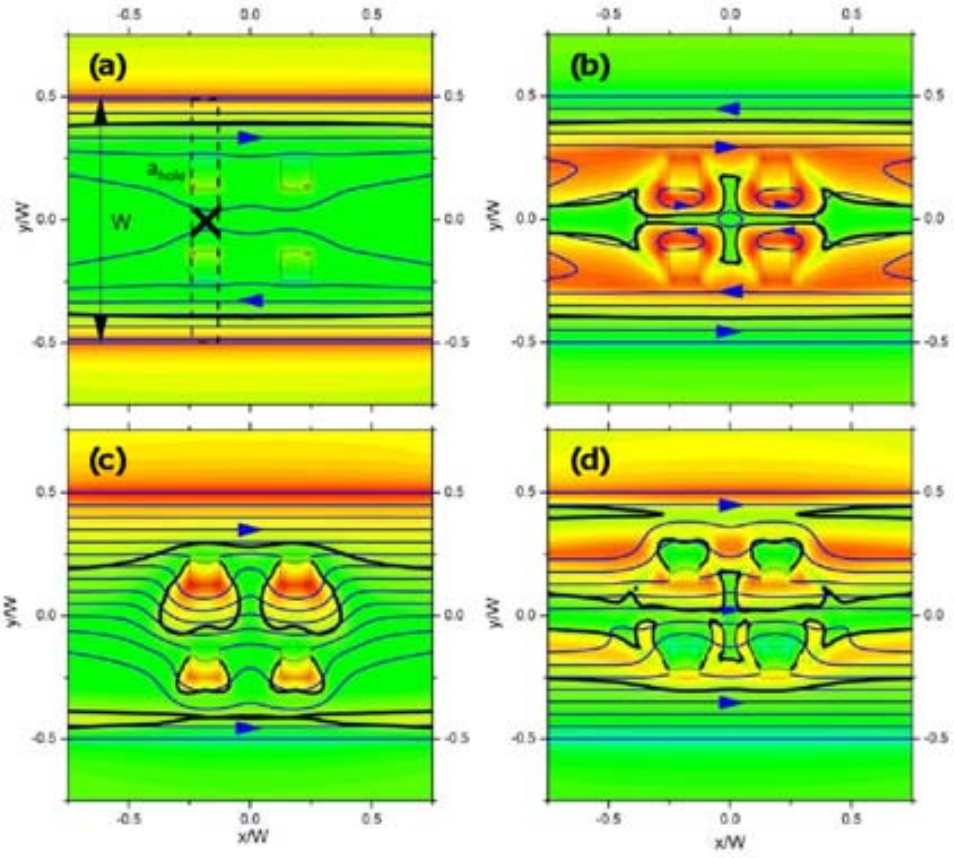

Figure 5.9.: Out-of-plane magnetic field H_{local} (color), and current stream lines (blue lines, arrows indicate direction of current) induced in a thin straight superconducting strip of uniform thickness t_s, width W and constant critical current J_c. The strip presents four symmetrical square antidots of side a_{hole}. It is subjected to a uniform perpendicular positive magnetic field, $H_a < H^*$ applied during **(a)** an ascending sweep afther a ZFC process and **(b)** a descending case. **(c)** and **(d)** represents the magnetic field profiles of (a) and (b), respectively, after aplying a longitudinal tranport current. [H_{local} ranges from its minimum (blue) through 0 (green) and up to its maximum (red), with the thick black lines separating the regions with $H_{local} < H_a$ from these with $H_{local} > H_a$].

reduce the local magnetic field. As a first approximation we consider that this return magnetic field will be the one generated at the regions marked with black-crosses in figure Fig. 5.10$-a$, which are the regions where the superconductor will dissipate in the presence of an external electrical current (regions with smaller cross-section) thus, at these regions, we will assume that the return magnetic field is $2H_r^{grain}$.

Therefore, in a first approximation, the resulting return magnetic field arising from trapped magnetic fields within the grains, and in particular at the points marked with black-crosses, will be $H_r^{SC} = 2H_r^{grain}$. Obviously, this field will depend on the magnetic history performed on the superconducting film and temperature. Fig. 5.8$-c$ and d show the sign of the trapped magnetic field and the associated H_r^{SC}, (which give a hysteretic J_c behavior shown in Fig. 5.8$-b$) for the descending and ascending J_c sweeps respectively.

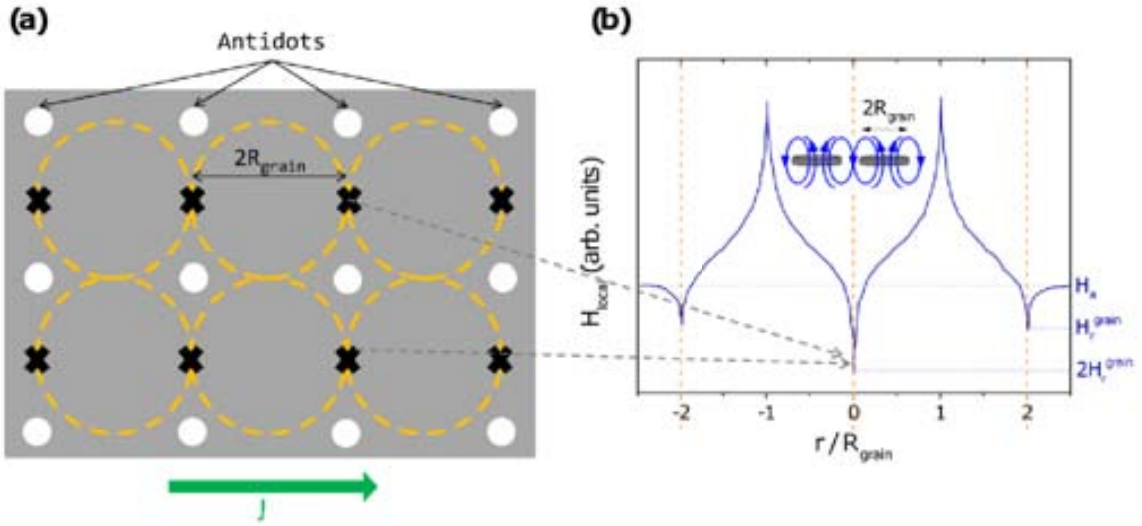

Figure 5.10.: **(a)** Schematic representation of the hybrid systems where antidots are indicated by white dots. Orange-circumferences emulate the grains used for the calculation of H_r^{SC}. Black-crosses indicate the regions where the superconductor will dissipate under the application of an external transport current. **(b)** Local magnetic field profile of two consecutive grains when $H_a \ll H_{mag}$.

Analysis of the YBCO/AR hybrid system

Applying the same methodology followed in the previous section, the analysis of the return magnetic fields present in the $YBCO/AR$ system is performed in this section. Hysteretic $J_c(H_a)$ curve is plotted in Fig. 5.11$-a$ for $YBCO/AR$ system. We clearly observe in this case a larger hysteresis compared with the one obtained in the $YBCO/A$ system (Fig. 5.8$-b$).

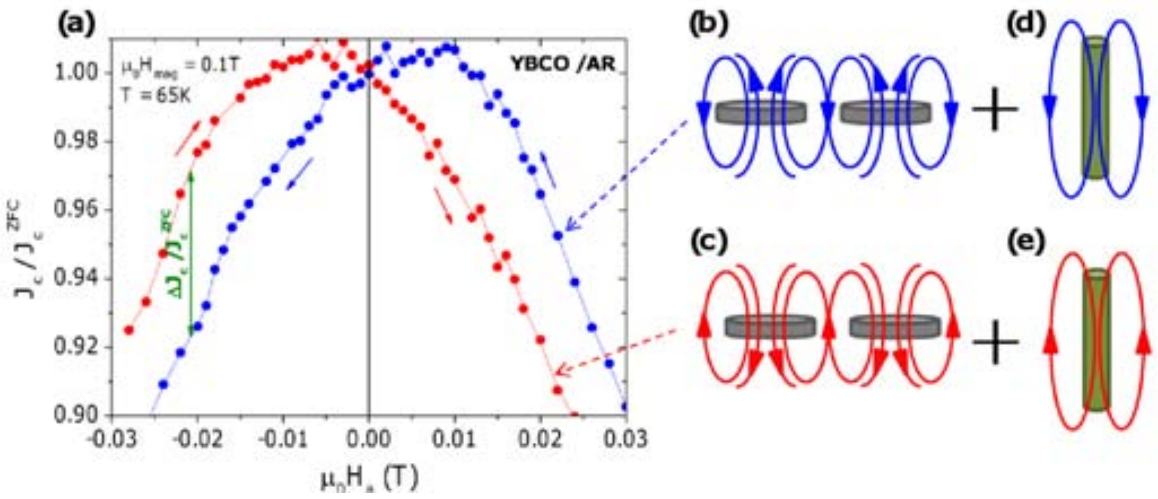

Figure 5.11.: $J_c(H_a)$ measurements for **(a)** $YBCO/AR$ system after magnetizing the sample at $0.1T$. **(b)** and **(c)** are schematic representations of H_r^{SC} for the descending (blue) and ascending (red) magnetic sweeps, respectively. **(d)** and **(e)** are the schemes of H_r^{FM} in each case.

Since in the $YBCO/AR$ system, there are antidots in addition to the Co-nanorods,

we will also have the contribution of H_r^{SC} on the hysteretic behavior of J_c as schematically shown in Fig. 5.11$-b$ and Fig. 5.11$-c$. Moreover, in the $YBCO/AR$ system, an additional non-reversible contribution arises from the stray field generated by Co-nanorods, H_r^{FM} as it is shown in the schematic representation of Fig. 5.11$-d$ and Fig. 5.11$-e$. This contribution has the same sign that H_r^{SC} for fields lower (in absolute value) than H_{coher}, where H_{coher} is the cohercitive magnetic field of the ferromagnet.

On the whole, these results reflect that the local magnetic field, $H_{local}^{FM} = H_a + H_r^{SC} + H_r^{FM}$, in the $YBCO/AR$ system is modified due to the presence of antidots and Co-nanorods. Thus, since H_r^{FM} is just present in the $YBCO/AR$ system, we observe that the hysteresis in J_c in this hybrid is larger than that obtained in the $YBCO/A$ system. As a first approximation, to analyse the $YBCO/AR$ system we will consider that the local magnetic field of Co-nanorods is not affected by the return magnetic fields induced at the edges of the antidots, H_r^{SC}.

5.6. Return magnetic fields of hybrid systems

With the aim to understand the influence of the different return magnetic field contributions (H_r^{SC} and H_r^{FM}) to the local field, an analysis on the differences of the critical current density as a function of the applied, H_a, performing different magnetic sweeps, have been done.

5.6.1. Hysteretic J_c behavior as a function of H_{mag}

The first study consists of the evaluation of the J_c differences during the ascending and descending sweeps of H_a, $\Delta J_c(H_a)$. Two different magnetized fields (maximum applied fields) will be used: $\mu_0 H_{mag} = 0.1T$ and $0.05T$.

Fig. 5.12 shows the normalized hysteresis, $\Delta J_c/J_c^{ZFC}$, obtained at $65K$ for the cases of a) $YBCO/A$ and b) $YBCO/AR$. In the $YBCO/AR$ case, Co-nanorods have been demagnetized at $T > T_c$ by sweeping the magnetic field from $9T$ to $0T$ in an oscillating mode of the superconducting coil, allowing to remove the remanent magnetic field arising from the nanorods and the superconducting coil itself [193].

The first feature than can be clearly observed is that the normalized hysteresis obtained for the $YBCO/AR$ system is 4-5 times higher than that obtained for the $YBCO/A$ system, for both values of H_{mag} (see Fig. 5.12). Furthermore, in the case of the $YBCO/A$ system (Fig. 5.12$-a$), the maximum difference of J_c is the same regardless the value of H_{mag}. A different situation emerges in the case of the $YBCO/AR$ system where the maximum hysteresis obtained with $\mu_0 H_{mag} = 0.1T$ is larger than for $\mu_0 H_{mag} = 0.05T$ (Fig. 5.12$-b$). To understand these features, we need to evaluate the effect of the different return fields mentioned before.

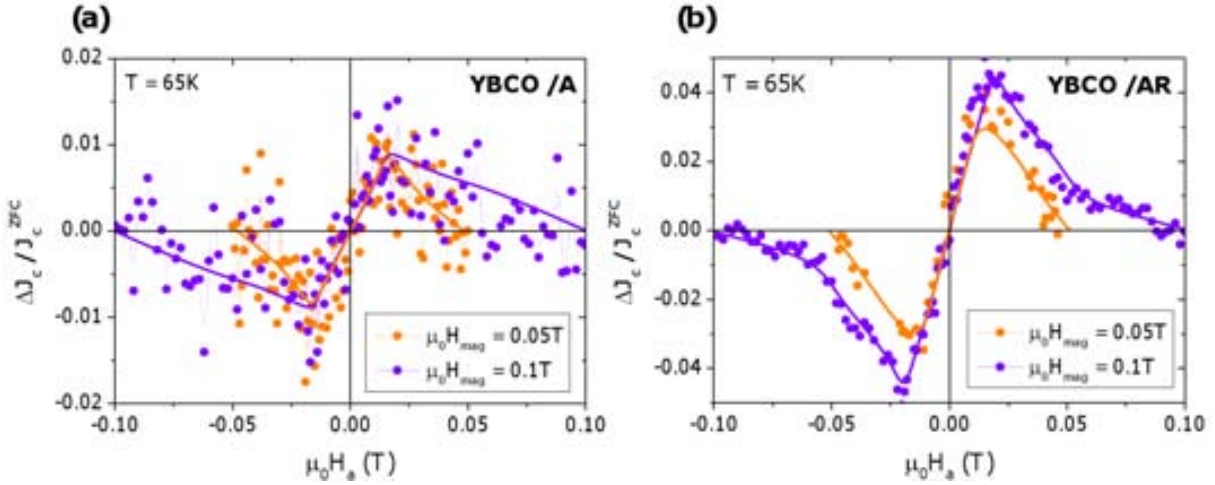

Figure 5.12.: J_c normalized hysteresis obtained as a function of applied magnetic field for **(a)** $YBCO/A$ system and **(b)** $YBCO/AR$ system. Orange dots correspond to the data obtained when $\mu_0 H_{mag} = 0.05T$ and violet dots for $\mu_0 H_{mag} = 0.1T$.

In collaboration with the *Superconductivity Group* from *Universitat Autonoma de Barcelona* (UAB), and with the aim to quantify, in a first approximation, the value H_r^{SC}, we have calculated the return magnetic field derived from a saturated cylinder, in order to emulate the magnetic grains composing our systems, see Fig. 5.10$-a$. We have considered cylinders of different aspect ratios R_{grain}/t_s, where R_{grain} corresponds to the cylinder radius and t_s the cylinder thickness. According to these calculations, H_r^{SC} at the black-crosses of Fig. 5.10$-a$ (edges of the cylinders) can be determined by [194]:

$$\mu_0 H_r^{SC} = 2\mu_0 H_r^{grain} = 2\left\{-\frac{3M^{grain}(H_{local},T)}{R_{grain}} x t_s\right\} \tag{5.3}$$

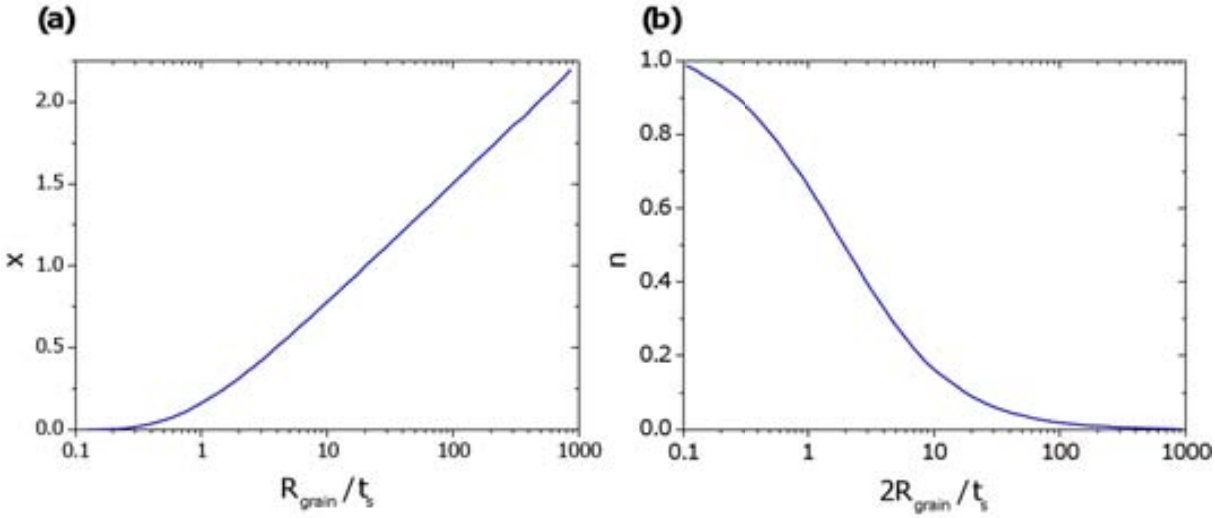

Figure 5.13.: Numerically calculated dimensionless factors x and n as a function of the ratio R_{grain}/t and $2R_{grain}/t$ respectively.

where M^{grain} is the magnetic moment of one single grain and x is a numerically calculated dimensionless factor depending on the ratio R_{grain}/t_s (Fig. 5.13$-a$). The factor $(3M^{grain}(H_{local},T))/R_{grain}$ corresponds to the critical current density of a single grain (see expression 1.9), which for our calculations is supposed to be the same than that obtained in a non-granular sample. The sign (–) indicates that the return magnetic field has opposite sign that of the trapped magnetic moment in the sample (see figures Fig. 5.8$-c$ and Fig. 5.8$-d$).

Additionally, by using a numerical simulation based on energy minimization in the Bean critical state model, we have also calculated the full penetration field, H^*, for cylinders of different aspect ratios, R_{grain}/t_s [195]. Results for any value of $2R_{grain}/t_s$ can be expressed as:

$$\mu_0 H^* = J_c^{sf}(T) n R_{grain} \tag{5.4}$$

where again n is a numerically calculated dimensionless factor depending on the ratio $2R_{grain}/t_s$ shown in figure Fig. 5.13$-b$, and J_c^{sf} is the self field critical current density of a single grain, again assumed to be the same than that obtained in a non-granular sample.

From equation 5.3, we can observe that the maximum H_r^{SC} will be achieved when $\mu_0 H_{local} = 0T$ since $M^{grain}(H_{local},T)$ will be maximum. Thus, considering the critical current density of the sample at zero applied field and $65K$, $J_c^{sf}(T=65K) = 3.02MA/cm^2$, and using the values of $R_{grain} = 1\mu m$, $t_s = 0.125\mu m$ ($x = 0.73$ and $n = 0.11$), we obtain that the maximum H_r^{SC} is $\mu_0 H_r^{SC}$ $7mT$ and $\mu_0 H^*$ $4mT$.

At this point, we are able to understand the hysteretic results obtained for the $YBCO/A$ system, Fig. 5.12$-a$. As it has been explained in sec. 1.2.3, type-II superconductors are saturated if the maximum local magnetic field is larger than $2H^*$. The value obtained at $65K$ of $2\mu_0 H^*$ $8mT$, is much lower than the two values of $\mu_0 H_{mag}$ used during our experiment. Consequently, at $\mu_0 H_{mag} = 0.05T$, the $YBCO/A$ system is already saturated providing the same hysteresis than that obtained at $\mu_0 H_{mag} = 0.1T$. Due to the limitations of the superconducting coil used for these measurements, where the minimum field step is $1mT$, studies at $65K$ and $H_{mag} < 2H^*$ have not been performed. As can be disclosed from expression 5.4, H^* will increase by decreasing the temperature nevertheless, as we will see in sec. 5.6.3, the hysteretic effect in these hybrid systems is very di cult to analyze at lower temperatures.

On the other hand, with the aim of quantifying the value of H_r^{FM} as a function of H_a, we will use the results obtained in sec. 5.4, where the IL was studied. In that analysis, we found that the saturated return magnetic field given by Co-nanorods was $\mu_0 H_r^{FM} = -2mT$ (Fig. 5.6). Regarding the shape of the magnetic loop, we will use the loop measured by $MOKE$ for one single Co-nanorod (Fig. 5.3).

From the data shown in, Fig. 5.12$-b$, we observe that the maximum J_c hysteresis obtained with $\mu_0 H_{mag} = 0.1T$ is larger than that for $\mu_0 H_{mag} = 0.05T$. These results are in agreement with the values of $H_r(H_a)$ obtained in Fig. 5.6, where we observe that Co-nanorods are not saturated at $0.05T$. Notice that we have considered that the contribution of H_r^{SC} is saturated at $\mu_0 H_{mag} = 0.05T$. This assumption is reasonable considering that,

since $J_c(H_a, T)$ for $YBCO/A$ system is higher than that obtained for the $YBCO/AR$, see Fig. 5.2$-b$, the values of H_r^{SC} and H^* provided for the $YBCO/A$ are upper limits for $YBCO/AR$.

5.6.2. Hysteretic J_c behavior as a function of the initial magnetic state

With the purpose of fully understanding the contributions of the different return magnetic fields present in our systems, H_r^{SC} and H_r^{FM}, an additional experiment will be performed with a different $J_c(H_a)$ sweep. In these analysis, we will compare the J_c results obtained after three different sweeps of H_a following this procedure:

i) Cooling the sample from $100K$ to $65K$ in a Zero Field Cool (ZFC) process.

ii) Magnetize the systems at $-0.1T$.

iii) Increase the applied magnetic field from $\mu_0 H_a = -0.1T$ to $\mu_0 H_a = 0T$.

iv) Increase the applied magnetic field from $\mu_0 H_a = 0T$ to $\mu_0 H_a = 0.1T$ while J_c measurements are performed (sweep (1)). Red curves of Fig. 5.14 plot the magnetization associated to the SC (Fig. 5.14$-a$) and the FM nanorods (Fig. 5.14$-b$) by following this sweep.

v) Decrease the applied magnetic field from $\mu_0 H_a = 0.1T$ to $\mu_0 H_a = 0T$ while J_c measurements are performed (sweep (2)). Again, blue curves of Fig. 5.14 plot the magnetization of the SC and FM nanorods during this sweep.

vi) Increase again the applied magnetic field from $\mu_0 H_a = 0T$ to $\mu_0 H_a = 0.1T$ while J_c measurements are performed (sweep (3)); green curve on the magnetic profiles of Fig. 5.14).

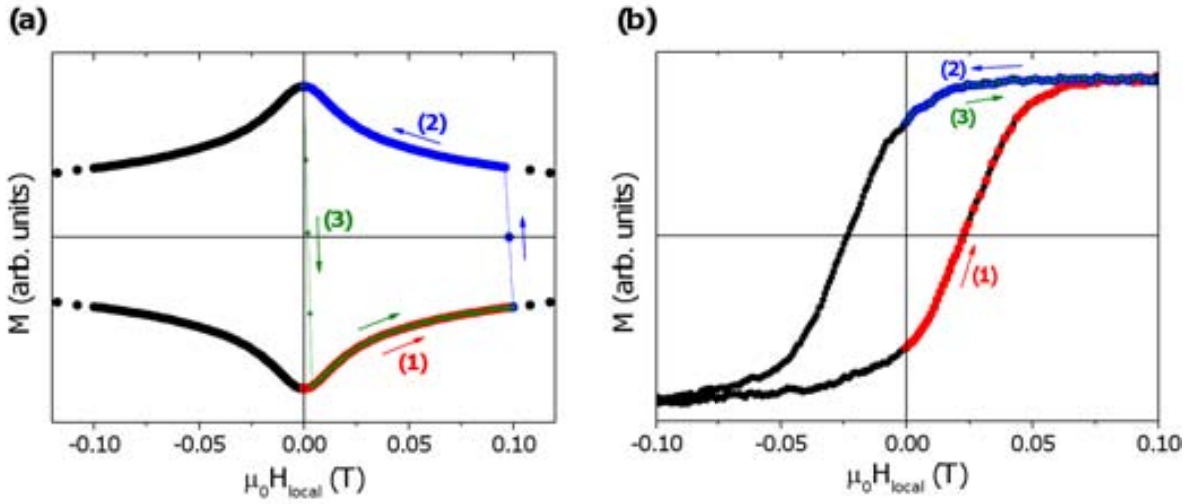

Figure 5.14.: Schematic representation of the magnetic hysteretic loops obtained for **(a)** the superconductor and **(b)** the ferromagnetic nanorods, by performing different $J_c(H_a)$ sweeps.

Analysis of the YBCO/A hybrid system

The H_r^{SC} behavior will be studied by comparing the critical current densities determined during different sweeps: $J_c^{(1)}$, $J_c^{(2)}$ and $J_c^{(3)}$, which correspond to the J_c values obtained during (1), (2) and (3) sweeps, respectively. Normalized J_c-subtractions, that correspond to $\Delta J_c^{(2)-(1)}/J_c^{ZFC} = [J_c^{(2)} - J_c^{(1)}]/J_c^{ZFC}$ and $\Delta J_c^{(3)-(1)}/J_c^{ZFC} = [J_c^{(3)} - J_c^{(1)}]/J_c^{ZFC}$, will be also analyzed.

Fig. 5.15$-a$ plots the obtained $J_c(H_a)$ dependences where red, blue and green curves correspond to sweeps (1), (2) and (3), respectively. $\Delta J_c/J_c^{ZFC}$ subtractions are plotted in Fig. 5.15$-b$, where lines are a guide for the eye. Blue curve of Fig. 5.15$-b$ is the same than violet curve shown in Fig. 5.12$-a$, since the data corresponds to the same $J_c(H_a)$ sweeps.

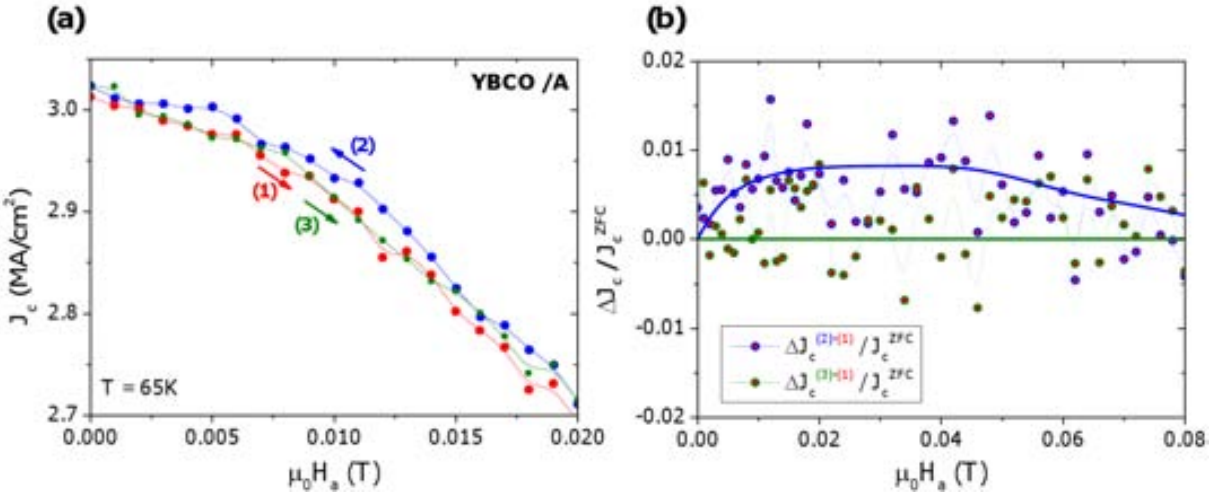

Figure 5.15.: (a) Transport J_c measurements obtained for the $YBCO/A$ system as a function of H_a performing the three different sweeps described in the text: Sweep (1) red curve, (2) blue curve and (3) red curve. **(b)** Normalized differences of J_c for sweeps (2) and (3) with respect to (1).

From the J_c-subtractions we observe that no hysteresis is obtained by performing the sweeps (3) and (1), whereas a maximum hysteresis of $\Delta J_c/J_c^{ZFC} \sim 0.01$ is observed by comparing sweeps (2) and (1). To better understand the origin of this hysteresis, we are going to evaluate the value of H_r^{SC} through expression 5.3. As a first approximation, we will assume that the field dependence of $M^{grain}(H_{local}, T = 65K) = M^{grain}(H_a, T = 65K)$. With this assumption, we have determined the values of $H_r^{SC}(H_a)$ (Fig. 5.16$-a$) and the correspondent local magnetic field, $H_{local}^{YBCO\ A} = H_a + H_r^{SC}$, (Fig. 5.16$-b$) at the edges of the grains (see Fig. 5.10$-a$) for the different field sweeps. Moreover, we have also determined the differences of the absolute value of the local magnetic field as a function of the applied field (Fig. 5.16$-c$) for sweeps (2)-(1) and (3)-(1). All these calculations have been performed for the case of $\mu_0 H_{mag} = -0.1T$.

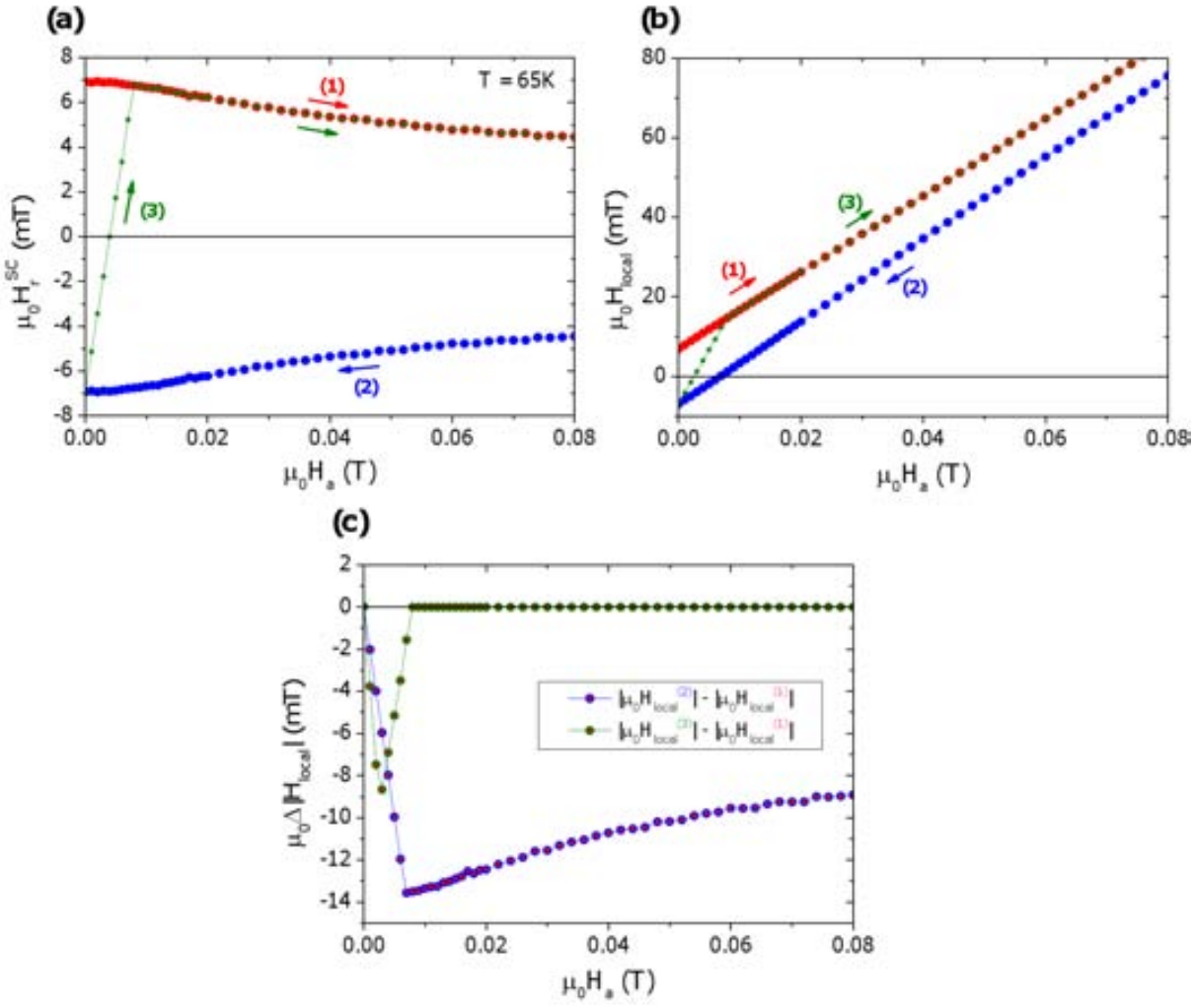

Figure 5.16.: **(a)** Estimated value of H_r^{SC} at the edges of the antidots as a function of H_a for the three different sweeps indicated in the text. **(b)** Calculated H_{local} at the black-crosses of Fig. 5.10$-a$, as a function of H_a for the three different sweeps. **(c)** Differences on the local magnetic field by comparing sweeps (2) and (3) with respect to (1).

We observe that the experimental data obtained for the J_c hysteresis in Fig. 5.15$-b$ is in agreement with the modification of the local magnetic field due to the contribution of H_r^{SC} (shown in Fig. 5.16$-c$). In the case of the green curves (comparison between sweeps (3) and (1)), we observe that $\Delta J_c/J_c^{ZFC}$ 0 (green-red dots in Fig. 5.15$-b$) in agreement with a very small difference between local fields (green-red dots in Fig. 5.16$-c$). On the contrary, a larger difference is observed in $\Delta J_c/J_c^{ZFC}$ comparing sweeps (2) and (1) (blue-red dots in Fig. 5.15$-b$) because in this case, a notable difference is obtained on the local magnetic field between different sweeps (blue-red dots in Fig. 5.16$-c$).

Thus, we have shown that the hysteresis obtained in the J_c measurements are correlated with variations in the local magnetic field originated by H_r^{SC} in the presence of antidots. The, analysis of the temperature dependence of H_r^{SC} will be discussed in sec. 5.6.3.

Analysis of the YBCO/AR hybrid system

Following the same procedure than that used in the last section for the $YBCO/A$ hybrid, the behavior of the critical current density is also studied in the case of $YBCO/AR$ system. Fig. 5.17$-a$ plots the J_c values by performing the three different magnetic field sweeps described above. Again, red dots correspond to sweep (1), blue dots to sweep (2) and green to sweep (3). Also, subtractions between different sweeps are performed and plotted in Fig. 5.17$-b$ where blue-red dots correspond to $\Delta J_c^{(2)-(1)}/J_c^{ZFC}$ and green-red dots to $\Delta J_c^{(3)-(1)}/J_c^{ZFC}$.

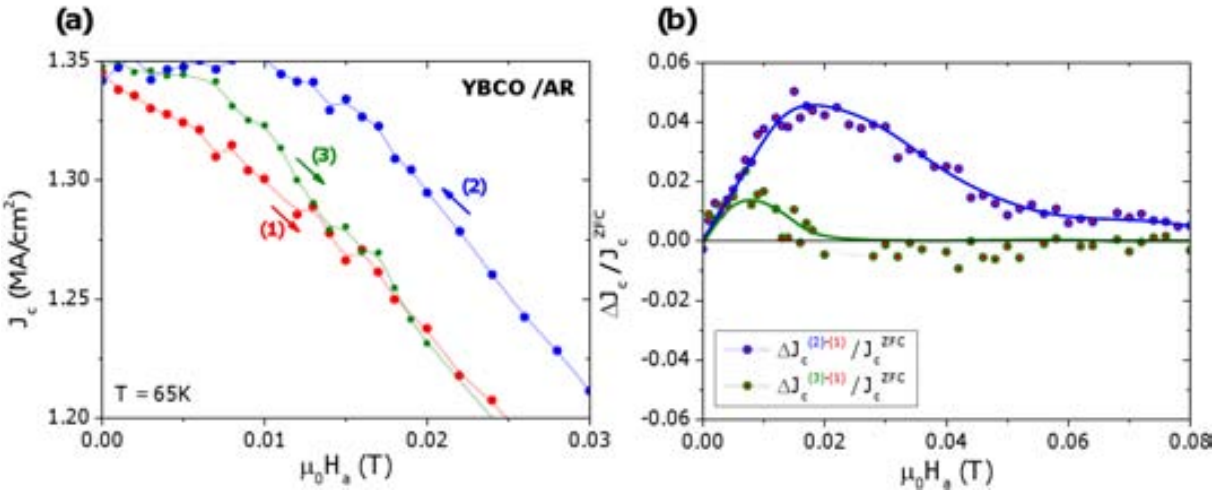

Figure 5.17.: (a) Transport J_c measurements obtained for the $YBCO/AR$ system as a function of H_a. **(b)** Normalized differences in J_c for the sweeps (2) and (3) with respect to (1).

As observed, the hysteresis in the $YBCO/AR$ system is 4-5 times larger than that obtained in $YBCO/A$ due to the contribution of Co-nanorods, as we has already been commented in Fig. 5.12. By comparing sweeps (3) and (1), in this case a clear hysteresis is observed at low fields, contrary to what happened in the $YBCO/A$ system. This hysteresis is associated then to the presence of Co-nanorods.

In order to analyze the hysteretic behavior obtained on this hybrid systems, a similar procedure than the one developed in the $YBCO/A$ case is performed, now considering the presence of FM nanostructures. Since we have the same array of antidots filled by Co-nanorods, we consider that the contribution of H_r^{SC} is the same than the one obtained for the $YBCO/A$ system (plotted in Fig. 5.16$-a$).

Regarding the contribution of Co-nanorods, we have plotted in Fig. 5.18$-a$ the values of $H_r^{FM}(H_a)$ obtained by performing the different sweeps and considering the hysteretic loop of the rods (Fig. 5.3). In Fig. 5.18$-b$, we plot the total return magnetic field as the sum of H_r^{SC} and H_r^{FM}, determined at the black-crosses of Fig. 5.10$-a$. H_{local} at this positions is plotted in Fig. 5.18$-c$ and the differences between the local magnetic fields during different sweeps in Fig. 5.18$-d$.

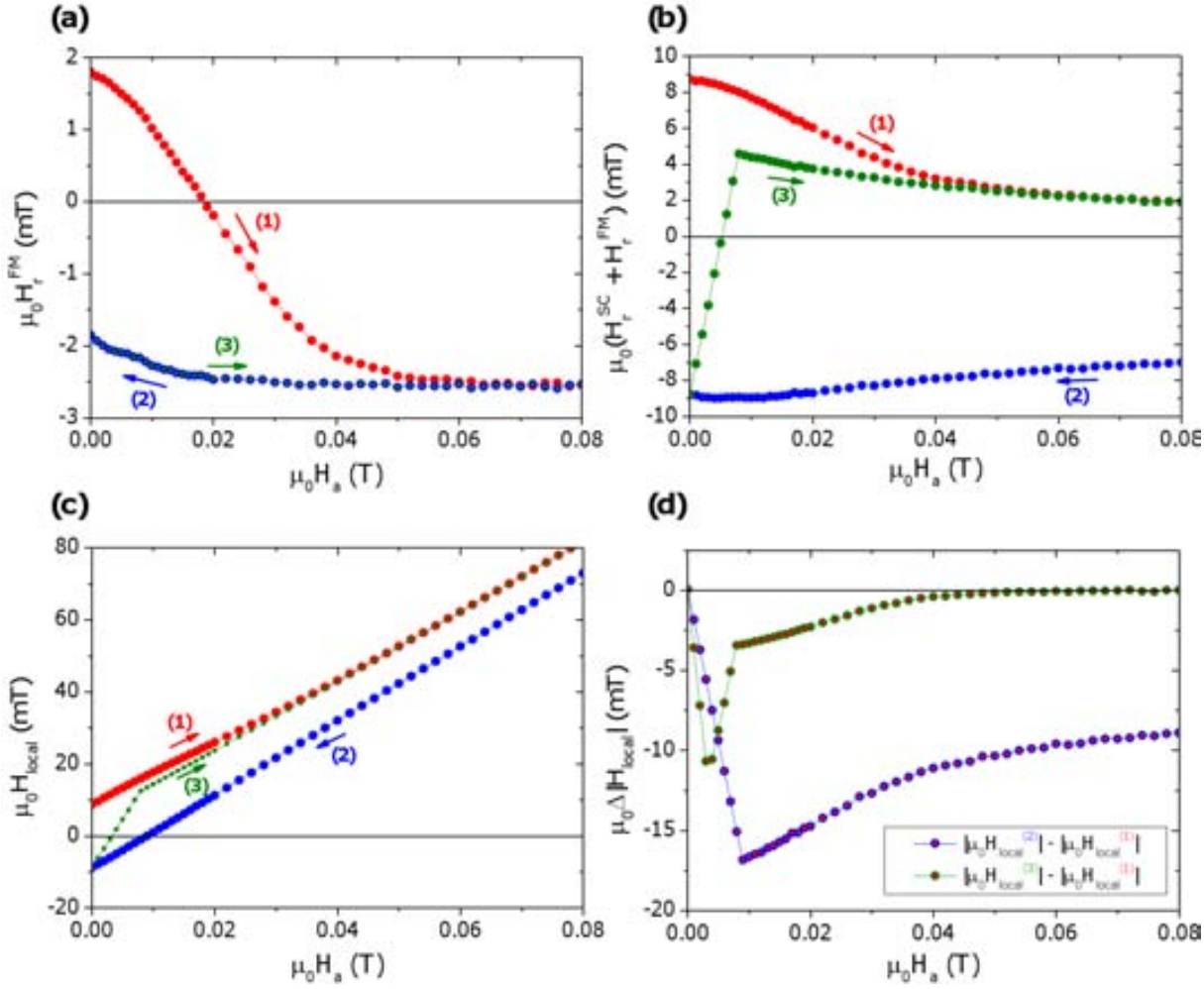

Figure 5.18.: **(a)** Estimate value of H_r^{FM} as a function of H_a during the three different studied sweeps. **(b)** Estimation of the total return field, $H_r^{SC}+H_r^{FM}$ at the black-crosses of Fig. 5.10$-a$ as a function of H_a. **(c)** H_{local} as a function of H_a. **(d)** Differences on the local magnetic field by comparing the sweeps (2) and (3) with respect to (1).

By comparing the field dependence of the differences in H_{local} obtained by performing the different sweeps (Fig. 5.18$-d$), we observe that again they are in agreement with the $\Delta J_c/J_c^{ZFC}$ behavior obtained in Fig. 5.17$-b$.

Fom the estimated values obtained for the different contributions of the return field, we observe that the additional contribution of the Co-nanorods increases the return magnetic field at the regions where our superconductor dissipates. In the comparison between sweeps (3) and (1) we observe that the contribution of H_r^{SC} is not su cient to produce an observed hysteresis in J_c (green-red dots of Fig. 5.15$-b$). Whereas, with the additional contribution of H_r^{FM} a much higher variation of H_{local} is obtained (green-red dots of figure Fig. 5.18$-d$) producing a notable J_c hysteresis (green-red dots of Fig. 5.17$-b$).

Up to now, we have demonstrated that the differences in J_c for a given value of H_a, are due to the existence of a non-reversible return magnetic field within the superconducting film. In our hybrid systems ($YBCO/A$ and $YBCO/AR$), this return magnetic field arises from the presence of demagnetizing effects at the edges of the antidots, H_r^{SC}, and the

stray fields arising from ferromagnetic Co-nanorods, H_r^{FM}. As we have discussed above, both return fields can be controlled by the magnetized fields, H_{mag}, and the magnetic history performed in the systems. In the next section we will analyze how the return magnetic fields are affected by the temperature.

5.6.3. Hysteretic J_c behavior as a function of temperature

In this section we are going to study the dependence of the two return magnetic fields present in our systems, H_r^{SC} and H_r^{FM}. We will perform an analysis at $77K$, $65K$ and $50K$. In particular, we are going to analyze the critical current density measured during sweeps (1) and (2) described in the previous section.

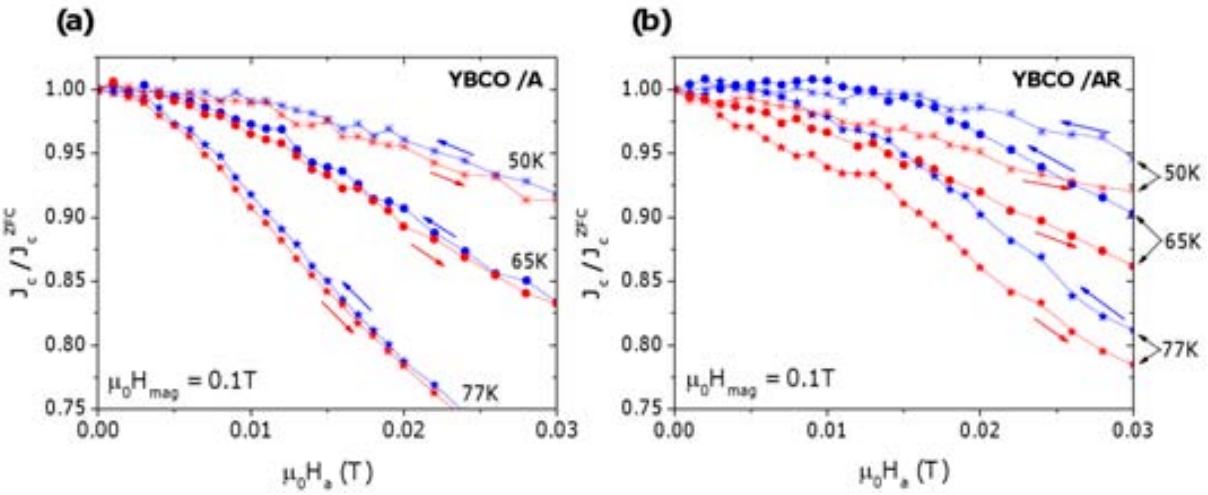

Figure 5.19.: Experimental J_c measurements as a function of H_a at different temperatures during sweeps (1) and (2) for **(a)** $YBCO/A$ and **(b)** $YBCO/AR$ systems.

Fig. 5.19 plots the normalized J_c/J_c^{ZFC} measured during these sweeps at the different temperatures. As we observed in the previous analysis performed at $65K$, we observe that the J_c-hysteresis in $YBCO/AR$ system is 4-5 times larger than in the case of the $YBCO/A$ for all temperatures. This fact is better observed in Fig. 5.20 where normalized $\Delta J_c/J_c^{ZFC}$ hystereses are plotted as a function of the applied magnetic field for the three studied temperatures.

One interesting effect that can be disclosed from Fig. 5.20, is that the maximum value of $\Delta J_c^{(2)-(1)}/J_c^{ZFC}$ is approximately the same in each system regardless its temperature. However, regarding expression 5.3, one would expect that the hysteretic behavior in J_c should increase due to the enhancement of H_r^{SC} by decreasing the temperature (since $M^{grain}(H_{local}, T)$ increases at low temperatures). The expected enhancement of H_r^{SC} is illustrated in Fig. 5.21 where the variation of the local magnetic field during the different sweeps, calculated following the methodology described in the previous section, is shown. Regarding the magnetic behavior of Co-nanorods, since $T_{Curie}^{Co} > 1000K$, we assume the same H_r^{FM} than that plotted in Fig. 5.18$-a$ for all temperatures. Therefore, differences in ΔH_{local} at different temperatures are originated by differences in H_r^{SC} since H_a and H_r^{FM} are temperature independent.

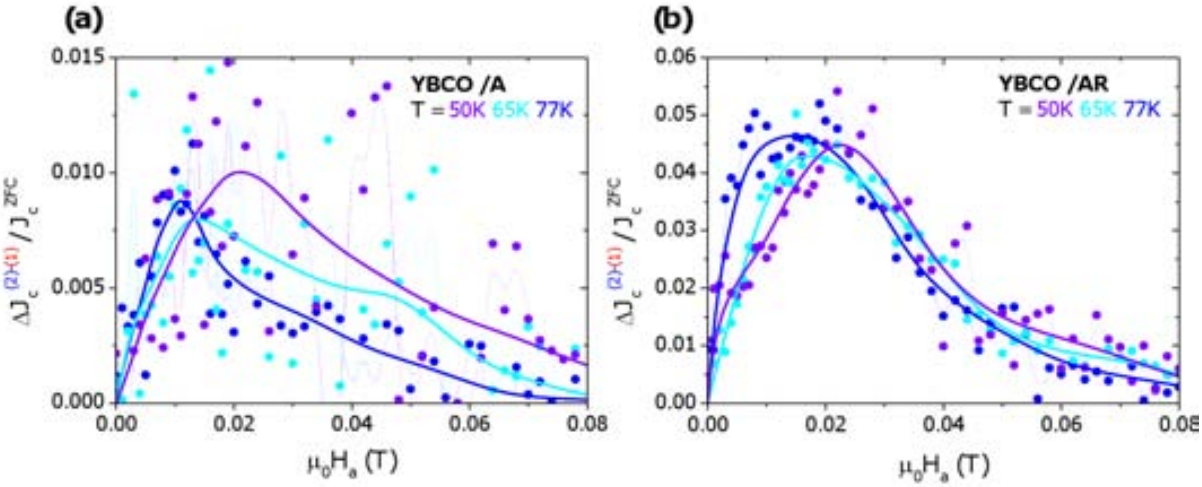

Figure 5.20.: Normalized differences of J_c as a function of H_a for sweeps (2)-(1) at different temperatures for **(a)** $YBCO/A$ and **(b)** $YBCO/AR$ systems.

Here, we can observe that by reducing the temperature, the variations in H_{local} increase, which should promote, at the outset, an enhancement of the normalized $\Delta J_c / J_c^{ZFC}$ hysteresis. Nevertheless, it is important to be noted that J_c has a smoother magnetic field dependence as temperature is reduced, as it can be observed in Fig. 5.19$-a$, where the slope of $J_c(H_a)$ curve for $\mu_0 H_a > 0.01T$ at $77K$ is 7 times larger than that obtained at $50K$. It means that small variations in H_{local} will strongly modify J_c at $77K$ than at $50K$. Thus, it is expected that the J_c hysteretic behavior, due to the presence of return magnetic fields, will be reduced and probably tend to vanish at much lower temperatures.

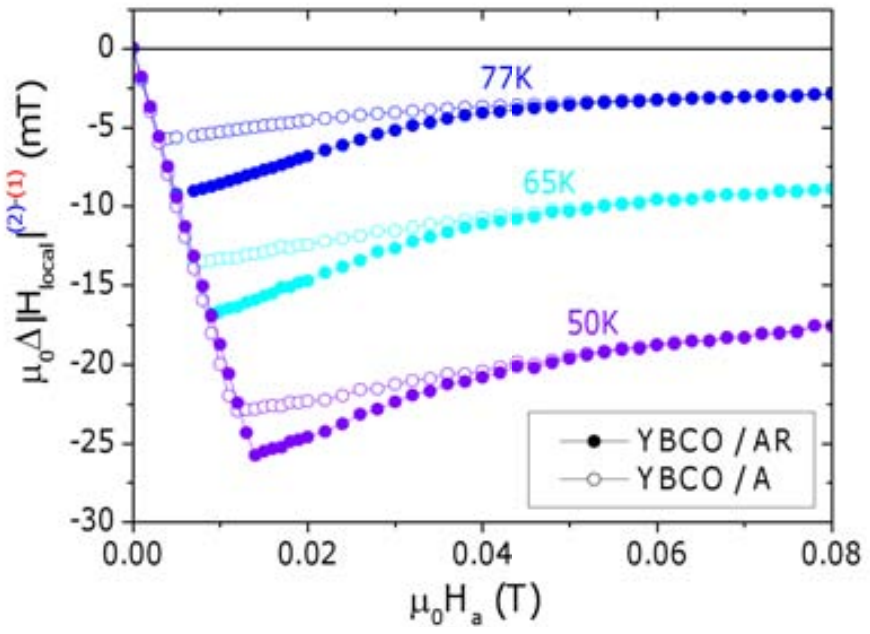

Figure 5.21.: Estimated differences in H_{local} as a function of H_a for sweeps (2)-(1) at different temperatures.

5.7. Conclusions

In this chapter, we have studied two model hybrid systems based on a $YBCO$ thin film with an array of antidots. In one of them, the antidots are kept empty ($YBCO/A$ system) while in the second, we have grown a ferromagnetic cobalt nanorods into the antidots ($YBCO/AR$ system) in order to study the interaction between the stray field generated by the ferromagnet and the superconductor.

As we have demonstrated, three different magnetic contributions are present within the superconducting film and in particular, in the regions where the superconductor starts to dissipate under the application of a external electrical current: the applied magnetic field, H_a, the return magnetic field generated at the edges of the antidots due to demagnetizing factors, H_r^{SC}, and the return magnetic field generated by the strays fields of the ferromagnetic nanords, H_r^{FM}. We have found that the H_r^{SC} contribution is not present in the analysis performed above the irreversibility line, IL, (vortex-liquid state) due to the absence of trapped magnetic fields when the superconductor is magnetically cycled. On the contrary, in the analysis performed on the vortex-solid state (below IL), we observed that magnetic flux lines are trapped within the superconductor generating return magnetic fields at the edges of the antidots and thus $H_r^{SC} \neq 0$.

The first study that we have performed consists of the analysis of the IL by performing different magnetic field sweeps. Results confirm that the contribution of H_r^{FM} at the $YBCO/AR$ system generates a hysteretic behavior of the IL while the $YBCO/A$ system is completely reversible. Furthermore, this analysis allows obtaining information about the saturated value of H_r^{FM}, and the field needed to saturate the magnetic nanorods.

The second analysis consists of the study of the hybrid systems in the vortex-solid state (analysis of the critical current density behavior). As we have demonstrated, due to the presence of non-reversible H_r^{SC}, the $YBCO/A$ system presents an hysteretic behavior of $J_c(H_a)$. However, this hysteresis is larger in the case of the $YBCO/AR$ case due to the additional contribution of H_r^{FM}.

In order to understand the characteristics of H_r^{SC} and H_r^{FM}, we have performed a serial of J_c measurements, considering different H_a sweeps, which allowed us to understand their contributions within the superconductor. In particular, we first demonstrated that the return magnetic field H_r^{SC} is saturated when the magnetization trapped within the superconductor saturates. We observe that since the saturating magnetic field of the superconductor is much lower than that resulting from the ferromagnet, the hysteresis in J_c for the $YBCO/AR$ system is observed in a wider range of H_a. Secondly, we have shown that depending on the sweeps performed, we can have situations in which variations in H_r^{SC} are not enough to produce a J_c hysteresis while with the addition of H_r^{FM} a clearly J_c hysteresis is observed.

Finally, we have analyzed the interaction of the return magnetic fields with the superconductor as a function of temperature. Since the Curie temperature of cobalt is larger than $1000K$, we suppose H_r^{FM} constant in the whole studied range. The situation for the H_r^{SC} is somewhat different since trapped magnetic fields into the superconductor, and therefore their return magnetic fields, increase by decreasing temperature. According to this, larger J_c hysteresis would be expected at lower temperatures. However, due to

the lower dependence of $J_c(H_a)$ when temperature is reduced, similar hysteretic values are obtained. These studies suggest that, at low enough temperatures, hysteretic effects should not be observed.

To sum up, we have demonstrated that by the antidots patterning in $YBCO$ thin films, an hysteretic behavior on the J_c can be obtained. The additional deposition of a ferromagnetic material into this antidots allows an enhancement of this hysteresis and furthermore, a non-reversible behavior of T_{irr} vs H_a. Therefore, these hybrid systems enables us to modulate the local fields within the superconductor tuning contribution of the return fields associated to the ferromagnetic nanorods and the superconductor itself, enviasing new potential devices.

General conclusions

In this work we have presented a complete study of vortex pinning and dynamics in artificially nanostructured $YBa_2Cu_3O_{7-x}$ ($YBCO$) thin films grown by chemical solution deposition (CSD). This methodology allows low cost, high performance and long tapes becoming much more attractive in large scale applications.

Our artificial framework involves spontaneous segregated secondary phases during the growth process, and asymmetric/ferromagnetic nanostructures. The formers consist of non-superconducting nanoparticles, which generate a new pinning landscape resulting from the interaction with the superconducting matrix. The latest are artificial nanostructures generated after sample growth, which allows controlling vortex motion.

We have used one of the main characteristics techniques to study interaction between vortices and defects by means of electrical transport measurements as a function of temperature, applied magnetic field and magnetic field orientation; $J_c(H_a, T, \theta)$ measurements. As superconductors are able to carry high electrical currents, there is a need to confine the applied electrical current in bridges with relative low cross-section ($\sim 1\mu m^2$) and the use of low electrical resistance contacts ($\sim 10\mu cm^2$ at $76K$).

The first study of this work is presented in chapter 3 where we have carried out a thoughtful analysis of the interaction between vortices and defects emerging from the presence of Ba_2YTaO_6 ($BYTO$) nanoparticles. As it was demonstrated, the main defects in $YBCO - CSD$ are stacking faults (SFs) and twin boundaries (TBs). Nevertheless, their size, shape and distribution are highly modified when $BYTO$ secondary phases are introduced into the $YBCO$ matrix.

As different defects appear in our systems, there is a need to separate the different pinning contributions. For example, by means of the Blatter scaling approach, one can separate these contributions regarding their anisotropic behavior. Consequently, it is found that one of the main effects of this new pinning landscape emerging in $YBCO{-}CSD$ nanocomposites, is the enhancement of the isotropic contribution of the critical current density. This is reflected in the performance of the $J_c(\theta)$ curves and in the reduction of the effective anisotropy ($_{eff}$) from 5 to even values close to 2. Still, through the study of the upper critical field (H_{c2}) by using high pulsed magnetic fields, we have shown that the intrinsic properties of $YBCO$ are not modified.

The main parameter which controls this $_{eff}$ reduction is the nanostrain, which arises from local atomic displacements due to the high density of SFs founded in CSD nanocomposites. It has been demonstrated that the nanoparticles which highly contribute to the formation of nanostrained regions are those randomly oriented within the $YBCO$ matrix, i.e. those show an incoherent interface with the $YBCO$ matrix.

By determining the angular dependence of J_c components, and analyzing the temperature dependence of the critical current density, we have demonstrated that these

nanostrained regions act as strong-isotropic pinning centers which govern most of the $H-T$ phase diagram.

One of the other consequences of the different pinning landscape of nanocomposites, is the modification of the TB distribution. The high density of planar defects in the $YBCO/BYTO$ films, avoids the formation of large twin domains, and coherent twin boundaries along the c-axis. It results in the none observation of channeling effect whereby the critical current density drops when the vortex is parallel to the TB planes. These effects are only observed in pristine $YBCO$ films at low temperatures ($T < 65K$) where TBs allows the slide of the vortex through the TB plane. On the contrary, at high enough temperatures ($T > 65K$), some TB pinning effects are observed in nanocomposites when the applied magnetic field is parallel to the TBs. In these cases, the elasticity of the vortex affords their accommodation into the broken TBs.

In this chapter, magnetic relaxation measurements have been also performed in $YBCO$ nanocomposites revealing that the transition from elastic creep regime to plastic creep regime is shifted to higher temperatures for a given applied magnetic field (H_a), with respect to a pristine sample.

In chapter 4 we have seen that an asymmetric motion of vortices is possible by patterning asymmetric nanostructures (triangles). In our case, blind-antidots, i.e. holes that do not perforate completely the superconducting layer, are patterned into the superconducting bridge generating a preferential sense for the vortex movement (ratchet effect).

Focused Ion Beam (FIB) and Focused Electron Beam Lithography ($FEBL$) are the two different techniques used in order to fabricate these asymmetric pinning potentials. It reveals that the possible implantation of Ga^+ ions by using the FIB is not the key factor of this effect.

In order to explain the obtained ratchet effect, we have divided the vortices in two different populations: vortices located inside (internal) and outside (external) the triangles. As a function of where the critical current density is firstly achieved, internal or external vortices will start their motion. As we have demonstrated, the election of which population of vortices starts to dissipate can be controlled by the geometry of the patterned array, i.e. by the reduction of the superconducting cross-section.

For low reductions of superconducting cross-section, the vortices which generate the experimental ratchet effect are the external ones. In that case, the dissipation is initialized, mainly, by external vortices while internals remain enclosed into the triangles due to the thickness modulation barrier, generating therefore an asymmetrical barrier for the movement of external vortices. In the case of high reductions of superconducting cross-section, the critical current density is achieved mainly at positions located below the triangles, resulting in the direct ratchet effect induced by internal vortices. In that case, the asymmetric barrier that these vortices feel is generated by thickness modulations and the distortion of screening currents near the step edges.

Due to the different mechanisms involving the two types of ratchets (direct or reversal), the applied magnetic field at which these effects are maximized differs one from each other. In the reversal ratchet effect, since both interactions are needed (vortex-defect for internal vortices which interact with the asymmetric blind-antidot, and vortex-vortex between the internal and the external vortices), the effect is maximized when these two

regimes compete. In the case of the direct ratchet effect, since the effect is promoted by the direct interaction between vortices and the triangles, when vortex-vortex interaction starts to be present, the effect vanishes. Nevertheless, it is important to note that in both cases, the effect is completely lost when vortex-vortex interaction strongly dominates.

In chapter 5, we have studied two model hybrid systems which generate a hysteretic behavior on the critical current density as a function of the applied magnetic field. Both of them are based on a $YBCO$ thin film with an array of antidots (holes that in that case, perforate completely the superconducting layer and even part of the substrate). However, one of them is filled with Co-nanorods using the Focused Electron Beam Induced Deposition ($FEBID$) technique.

The first analysis performed in order to study the hysteresis in our hybrid systems, is the investigation of the irreversibility line (IL). Since above the IL the superconductor does not trap any magnetic field, the return magnetic field at the edges of the antidots is equal to zero in the superconductor/insulating hybrid system. It results in the reversible behavior of the irreversibility temperature (T_{irr}). In contrast, in the superconductor/ferromagnetic system, since an hysteretic element is present (the Co-nanorod) its hysteretic stray field influences the local magnetic field into the superconductor generating a non-reversible $T_{irr}(H_a)$ behavior.

The second study consists of the analysis of the hysteretic behavior below the IL, i.e. the hysteresis on J_c. It has been demonstrated that, in our hybrid systems, this hysteresis arises in one part, from the presence of return magnetic fields at the edges of the antidots. This result is in agreement with theoretical simulations performed in collaboration with the *Superconductivity Group* from *Universitat Autonoma de Barcelona*. It demonstrates a hysteretic behavior on the local magnetic field between the antidots when the applied magnetic field is cycled. Furthermore, on the hybrid superconductor/ferromagnetic system, the hysteretic behavior is enhanced due to the additional presence of a non-reversible magnetic material which stray field affects the local magnetic field of the superconductor.

In order to clearly understand the two return magnetic field contributions arising from the superconductor and the ferromagnet, different experiments have been performed. All of them demonstrate that the value of the critical current density, can be tuned by magnetizing the sample at different applied magnetic fields or by cycling magnetically or systems.

Finally, we have studied the temperature behavior of our hybrid systems. Since the J_c has a lower dependence with H_a when the temperature is reduced, the differences on the local magnetic field are not observable at low temperatures.

Overall, we have demonstrated that by the nanostructuration of the $YBCO$, a control of the pinning and dynamic properties is possible. In particular through the introduction of $BYTO$ secondary phases, a tune of the isotropic pinning contribution and thermal excitations are obtained. On the other hand, the creation of asymmetric pinning potentials allows generating a preferential vortex motion sense. Finally, the creation of an array of antidots and the growth of ferromagnetic nanostructures, generates a controlled hysteretic behavior on the critical current density as a function of the applied magnetic field.

This work enriches the knowledge of $YBCO$ films grown by CSD and helps in the

definition of strategies to make us of this material either in high power applications (coated conductors) or for specific electronic devices where vortex guiding is a requirement.

A. Analytical simulation of the hysteretic $J_c(H_a)$ in a strip with antidots

The analytical calculation presented in Fig. 5.9 (plotted again in Fig. A.2 in this appendix) has been performed with the aim to study the effects of the antidots on the J_c behavior and confirm the presence of H_r^{SC}. It has been carried out in collaboration with the *Superconductivity Group* from the *Universitat Autonoma de Barcelona* (UAB) [196].

The simulated system consists of a superconducting thin film of uniform thickness t_s much smaller than the shortest perpendicular dimensions called as W, $t_s << W$, is placed at Z between $+t_s/2$ and $-t_s/2$ (with the c-axis parallel to the z-axis). Four squares of side ahole are also placed in the middle of the stripe playing the role of the antidots (Fig. A.1).

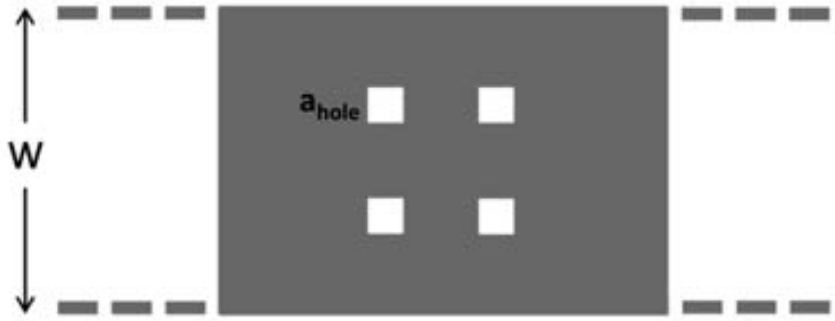

Figure A.1.: Schematic representation of the infinitely strip of width W used in our simulation. Holes of square a_{hole} are placed at the center of the strip.

Due to the small value of the ratio t_s/W, it is allowed to use the thickness-averaged current density instead of the volume critical current density, i.e. reducing a $3-D$ problem to a $2-D$ one. Therefore, it can be defined the $2-D$-critical current density as:

$$\overrightarrow{K}(x,y) \quad \int_{-t_s\ 2}^{+t_s\ 2} \overrightarrow{J}(x,y,z)dz \tag{A.1}$$

However, by considering a constant critical current density along the z direction it is found: $\overrightarrow{K}(x,y) \quad \overrightarrow{J}(x,y,0)t_s$.

In order to determine the sheet current $\overrightarrow{K}$ distribution that induces the internal magnetic fields in the sample, i.e. H_r^{SC} at the edges of the antidots, the condition of the continuity equation $\overrightarrow{\nabla} \cdot \overrightarrow{K} = 0$ is used. It indicates that a scalar sheet function $g = g(x, y)$ should exist with the condition of:

$$\overrightarrow{K}(\overrightarrow{r}) = \overrightarrow{\nabla} \times [g(\overrightarrow{r})\overrightarrow{z}] = -\overrightarrow{z} \times \overrightarrow{\nabla} g(\overrightarrow{r}) \tag{A.2}$$

where $\overrightarrow{\nabla} = (\partial / \partial x)\overrightarrow{x} + (\partial / \partial y)\overrightarrow{y}$ is the $2-D$ nabla operator and $\overrightarrow{r} = x\overrightarrow{x} + y\overrightarrow{y}$ is the in plane vector position and $\overrightarrow{x}, \overrightarrow{y}$ and $\overrightarrow{z}$ are the unit vectors along the x, y and z axis respectively.

It is worth to mention that $g(\overrightarrow{r})$ is constant at regions where $\overrightarrow{K}(\overrightarrow{r}) = 0$, which includes the exterior of the superconductor Moreover, the origin of this function is of no physical meaning and can be chosen. Nevertheless, two of the most important properties of the sheet function are:

The constant $g(\overrightarrow{r})$ lines correspond to the current streamlines.

The difference in $g(\overrightarrow{r})$ between two points within the sample plane equals the net current crossing any line connecting both points.

Therefore, the determination of the $g(\overrightarrow{r})$ function is the purpose of these studies which is solved from the minimization of the Gibbs free energy of the sample. The total magnetic energy E_m of the thin plate can be expressed in terms of the $g(\overrightarrow{r})$ function and its gradient. In this case:

$$E_m = E_{int} + E_{ext} \tag{A.3}$$

where

$$E_{int} = \frac{1}{2}\int_S \overrightarrow{K}(r)\overrightarrow{A_K}(r)dS = \frac{\mu_0}{8}\int_S\int_S \frac{\overrightarrow{\nabla} g(\overrightarrow{r})\,\overrightarrow{\nabla} g(\overrightarrow{r})}{|\overrightarrow{r} - \overrightarrow{r}|}dSdS \tag{A.4}$$

is the internal magnetic energy, that accounts for the interaction between induced currents and the stray fields created by themselves, and

$$E_{ext} = \int_S \overrightarrow{K}(\overrightarrow{r})\overrightarrow{A_a}(\overrightarrow{r})dS = \mu_0 H_a \int_S g(\overrightarrow{r})dS - \oint_S g(\overrightarrow{r})\overrightarrow{A_a}d\overrightarrow{l} \tag{A.5}$$

is the contribution of the applied magnetic fields. The second term of the expression A.5 corresponds to the surface where the currents enter and leave the sample. However, as the

interested results are situated in the middle of the sample where the antidots are located, this term is neglected.

In order to study the gradient of the function $g(\overrightarrow{r})$, i.e. the energy, in the different parts of the sample, it is divided in $N \times M$ squares and the vertex, or nodes, of this squares is where the function is defined. At a given conditions of applied magnetic field and critical current, the model applies the same variation of g in each node separately and finds the new energy for each case. The state in which a node provides the minimum energy is saved and the procedure is repeated in each node with this new initial state. The iteration finish when the energy of each node-variation is positive, i.e. larger than the energy of the previous state. The reason for use as the initial state of each iteration the state in which one node minimizes the energy of the whole system until no more reductions are possible is in order to obtain the absolute minimum energy state instead of a relative minimum energy state at the end of the procedure.

It should be noted that the minimization of the energy has to obey the following constrain in agreement with the definition of $g(\overrightarrow{r})$:

$$|\overrightarrow{K}(\overrightarrow{r})| = |\overrightarrow{\ }g(\overrightarrow{r})| \leq K_c \quad J_c t_s \tag{A.6}$$

When for each condition the energy is minimized, the function $g(\overrightarrow{r})$ is obtained and therefore the current streamlines and the magnetic field profile are achieved.

Fig. A.2 shows the out of plane magnetic field (color) and the current stream lines (blue arrows) for the same applied magnetic field, H_a, under different situations: Fig. A.2$-a$ corresponds to a uniform perpendicular positive magnetic field $H_a < H^*$ applied after a ZFC process. Fig. A.2$-c$ corresponds to the same situation after the application of an external transport electrical current parallel to the x-axis of the scheme. The region marked with a black-cross and framed with black-dashed-line, is the first to saturate at $J = J_c$ together with its symmetric counterpart by the right holes. Fig. A.2$-b$ and Fig. A.2$-d$ displays the same than Fig. A.2$-a$ and Fig. A.2$-c$ respectively but when the field is increased up to a large value of $H = H^*$ and then decreased to the same H_a (in the case of figure Fig. A.2$-d$, the same longitudinal transport electrical current is fed into the strip after H_a is reached). As we can observe, the region framed with black-dashed-line presents different local magnetic fields if we compare figures Fig. A.2$-a$ with Fig. A.2$-c$ and Fig. A.2$-b$ and Fig. A.2$-d$. It demonstrates the hysteretic behavior of J_c obtained in our real $YBCO/A$ system.

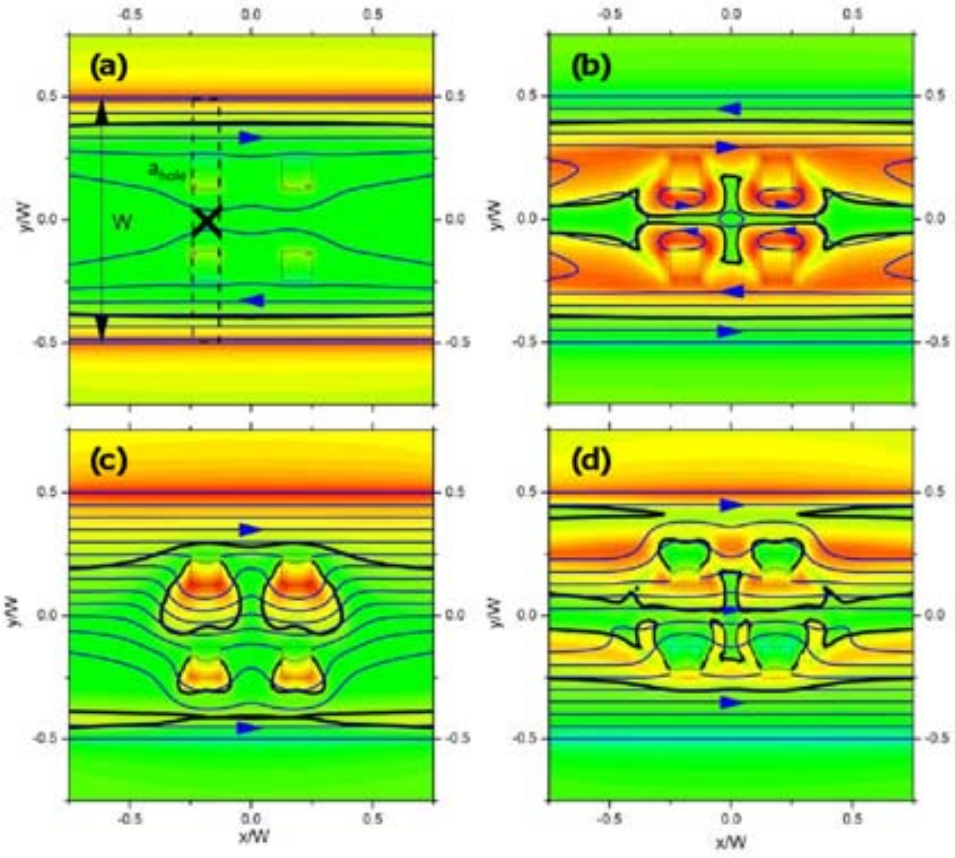

Figure A.2.: Out-of-plane magnetic field H_{local} (color), and current stream lines (blue lines, arrows indicate direction of current) induced in a thin straight superconducting strip of uniform thickness t_s, width W and constant critical current J_c. The strip presents four symmetrical square antidots of side a_{hole}. It is subjected to a uniform perpendicular positive magnetic field, $H_a < H^*$ applied during **(a)** an ascending sweep afther a ZFC process and **(b)** a descending case. **(c)** and **(d)** represents the magnetic field profiles of (a) and (b), respectively, after aplying a longitudinal tranport current. [H_{local} ranges from its minimum (blue) through 0 (green) and up to its maximum (red), with the thick black lines separating the regions with $H_{local} < H_a$ from these with $H_{local} > H_a$].

Bibliography

[1] J. Gutierrez, A. Llordes, J. Gazquez, M. Gibert, N. Roma, S. Ricart, A. Pomar, F. Sandiumenge, N. Mestres, T. Puig, and X. Obradors. Strong isotropic flux pinning in solution-derived $YBa_2Cu_3O_{7-x}$ nanocomposites superconductor films. *Nature Materials*, **6**: 367, (2007).

[2] A. Maeda, Y. Inoue, H. Kitano, S. Savelev, S. Okayasu, I. Tsukada, and F. Nori. Nanoscale friction: Kinetic friction of magnetic flux quanta and charge density waves. *Physical Review Letters*, **94**: 077001, (2005).

[3] S. Savel'ev and F. Nori. Experimentally realizable devices for controlling the motion of magnetic flux quanta in anisotropic superconductors. *Nature Materials*, **1**: 179, (2002).

[4] M. Baert, V. Metlushko, R. Jonckheere, V. Moshchalkov, and Y. Bruynseraede. Composite flux-line lattices stabilized in superconducting films by a regular array of artificial defects. *Physical Review Letters*, **74**: 3269, (1995).

[5] K. Harada, O. Kamimura, H. Kasai, T. Matsuda, A. Tonomura, and V.V. Moshchalkov. Direct observation of vortex dynamics in superconducting films with regular arrays of defects. *Science*, **274**: 1167, (1996).

[6] J.I. Martin, M. Velez, J. Nogues, and I.K. Schuller. Flux pinning in a superconductor by an array of submicrometer magnetic dots. *Physical Review Letters*, **79**: 1929, (1997).

[7] V.V. Moschalkov, M. Baert, V.V. Metlushko, E. Rosseel, M.J. Van Bael, K. Temst, Y. Bruynseraede, and R. Jonckheere. Pinning by an antidot lattice: The problem of the optimum antidot size. *Physical Review B*, **57**: 3615, (1998).

[8] M. Velez, J.I. Martin, J.E. Villegas, A. Hoffmann, E.M. Gonzalez, J.L. Vicent, and Ivan K. Schuller. Superconducting vortex pinning with artificial magnetic nanostructures. *Journal of Magnetism and Magnetic Materials*, **320**: 2547, (2008).

[9] I. Swiecicki, C. Ulysse, T. Wolf, R. Bernard, N. Bergeal, J. Briatico, G. Faini, J. Lesueur, and Javier E. Villegas. Strong field-matching effects in superconducting $YBa_2Cu_3O_{7-x}$ films with vortex energy landscapes engineered via masked ion irradiation. *Physical Review B*, **85**: 224502, (2012).

[10] R. Wordenweber, P. Dymashevski, and V. Misko. Guidance of vortices and the vortex ratchet effect in high-T_c superconducting thin films obtained by arrangement of antidots. *Physical Review B*, **69**: 184504, (2004).

[11] J. Bardeen, L.N. Cooper, and J.R. Schrieffer. Theory of superconductivity. *Physical Review*, **108**: 1175, (1957).

[12] J.R. Waldram. *Superconductivity of Metals and Cuprates.* Institut of Physics Publishing, London, (1996).

[13] G. Blatter, M.V. Feigelman, V.B. Geshkenbein, A.I. Larkin, and V.M. Vinokur. Vortices in high-temperature superconductors. *Review of Modern Physics*, **66**: 1125, (1994).

[14] H.F. Hess, R.B. Robinson, R.C. Dynes, J.M. Valles, and Waszczak. Scanning-Tunneling-Microscope observation of the Abrikosov flux lattice in the density of states near and inside a fluxoid. *Physical Review Letters*, **62**: 214, (1989).

[15] J.G. Bednorz and K.A. Muller. Possible high T_c superconductivity in the Ba-La-Cu-O system. *Zeitschrift fur Physik B, Condensed Matter*, **64**: 189, (1986).

[16] V. Breit, P. Schweiss, R. Hauff, H. Wuhl, H. Claus, H. Rietschel, A. Erb, and G. Muller-Vogt. Evidence for chain superconductivity in near-stoichiometric $YBa_2Cu_3O_x$ single crystals. *Physical Review B*, **52**: R15727, (1995).

[17] D. Larbalestier, A. Gurevich, D. Matthew Feldmann, and A. Polyanskii. High-T_c superconducting materials for electric power applications. *Nature*, **414**: 368, (2001).

[18] G. Blatter, V.B. Geshkenbein, and A.I. Larkin. From isotropic to anisotropic superconductors: A scaling approach. *Physical Review Letters*, **68**: 875, (1992).

[19] F. Bouquet, C. Marcenat, E. Steep, R. Calemczuk, W.K. Kwok, U. Welp, G.W. Crabtree, R.A. Fisher, N.E. Phillips, and A. Schilling. An unusual phase transition to a second liquid vortex phase in the superconductor $YBa_2Cu_3O_7$. *Nature*, **411**: 448, (2001).

[20] M.P. A. Fisher. Vortex-glass superconductivity: A possible new phase in bulk high-T_c oxides. *Physical Review Letters*, **62**: 1415, (1989).

[21] D.S. Fisher, M.P.A. Fisher, and D.A. Huse. Thermal fluctuations, quenched disorder, phase transitions, and transport in type-II superconductors. *Physical Review B*, **43**: 130, (1991).

[22] D.R. Nelson and V. Vinokur. Boson localization and pinning by correlated disorder in high-temperature superconductors. *Physical Review Letters*, **68**: 2398, (1992).

[23] D.R. Nelson and V.M. Vinokur. Boson localization and correlated pinning of superconducting vortex arrays. *Physical Review B*, **48**: 13060, (1993).

[24] J. Figueras. *Defects and the vortex liquid state in superconducting textured* $YBa_2Cu_3O_{7-x}$. PhD thesis, Universitat Autonoma de Barcelona, (2003).

[25] M. Tinkham. *Introduction to Superconductivity.* McGraw-Hill, Singapore, (1996).

[26] H. Ullmaier. *Irreversible Properties of Type II Superconductors.* New York: Springer-Verlag, (1975).

[27] R.P. Huebener. *Magnetic Flux Structures in Superconductors.* Berlin, Germany: Springer-Verlag, (1979).

[28] B.D. Josephson. Potential differences in the mixed state of type II superconductors. *Physics Letters*, **16**: 242, (1965).

[29] L. Civale. Vortex pinning and creep in high-temperature superconductors with columnar defects. *Superconductor Science and Technology*, **10**: A11, (1997).

[30] B. Dam, J.M. Huijbregtse, and J.H. Rector. Strong pinning linear defects formed at the coherent growth transition of pulsed-laser deposited $YBa_2Cu_3O_{7-x}$ films. *Physical Review B*, **65**: 064528, (2002).

[31] J.L. Macmanus-Driscoll, S.R. Foltyn, Q.X. Jia, H. Wang, A. Serquis, L. Civale, B. Maiorov, M.E. Hawley, M.P. Maley, and D.E. Peterson. Strongly enhanced current densities in superconducting coated conductors of $YBa_2Cu_3O_{7-x}$+$BaZrO_3$. *Nature Materials*, **3**: 439, (2004).

[32] Y. Yamada, K. Takahashi, H. Kobayashi, M. Konishi, T. Watanabe, A. Ibi, T. Muroga, S. Miyata, T. Kato, T. Hirayama, and Y. Shiohara. Epitaxial nanostructure and defects effective for pinning in $Y(RE)Ba_2Cu_3O_{7-x}$ coated conductors. *Applied Physics Letters*, **87**: 132502, (2005).

[33] A. Goyal, S. Kang, K.J. Leonard, P.M. Martin, A.A. Gapud, M. Varela, M. Paranthaman, A.O. Ijaduola, E.D. Specht, J.R. Thompson, D.K. Christen, S.J. Pennycook, and F.A. List. Irradiation-free, columnar defects comprised of self-assembled nanodots and nanorods resultin in strongly enhanced flux-pinning in $YBa_2Cu_3O_{7-x}$ films. *Superconductor Science and Technology*, **18**: 1533, (2005).

[34] C.V. Varanasi, P.N. Barnes, J. Burke, L. Brunke, I. Maartense, T.J. Haugan, E.A. Stinzianni, K.A. Dunn, and P. Haldar. Flux pinning enhancement in $YBa_2Cu_3O_{7-x}$ with $BaSnO_3$ nanoparticles. *Superconductor Science and Tecnology*, **19**: L37, (2006).

[35] P. Mele, K. Matsumoto, T. Horide, O. Miura, A. Ichinose, M. Mukaida, Y. Yoshida, and S. Horii. Tuning of the critical current in $YBa_2Cu_3O_{7-x}$ thin films by controlling the size and density of Y_2O_3 nanoislands on annealed $SrTiO_2$. *Superconductor Science and Technology*, **19**: 44, (2006).

[36] P. Mele, K. Matsumoto, T. Horide, A. Ichinose, M. Mukaida, Y. Yoshida, and S. Horii. Enhanced high-field performance in PLD films fabricated by ablation of YSZ-added $YBa_2Cu_3O_{7-x}$ target. *Superconductor Science and Technology*, **20**: 244, (2007).

[37] M. Peurla, H. Huhtinen, M.A. Shakhov, K. Traito, Y.P. Stepanov, M. Safonchik, P. Paturi, Y.Y. Tse, R. Palai, and R. Laiho. Effects of nanocrystalline target and columnar defects on flux pinning in pure $BaZrO_3$-doped $YBa_2Cu_3O_{6+x}$ films in fields up to 30T. *Physical Review B*, **75**: 184524, (2007).

[38] C.V. Varanasi, J. Burke, L. Brunke, H. Wang, M. Sumption, and P.N. Barnes. Enhancement and angular dependence of transport critical current density in pulsed laser deposited $YBa_2Cu_3O_7$+$BaSnO_3$ films in applied magnetic fields. *Journal of Applied Physics*, **102**: 063909, (2007).

[39] S.H. Wee, A. Goyal, J. Li, Y.L. Zuev, S. Cook, and L. Heatherly. The incorporation of nanoscale columnar defects comprised of self-assembled $BaZrO_3$ nanodots to improve the flux pinning and critical current density of $NdBa_2Cu_3O_{7-x}$ films grown on RABiTS. *Superconductor Science and Technology*, **20**: 789, (2007).

[40] P. Mele, K. Matsumoto, T. Horide, A. Ichinose, M. Mukaida, Y. Yoshida, S. Horii, and R. Kita. Ultra-high flux pinning properties of $BaMO_3$-doped $YBa_2Cu_3O_{7-x}$ thin films (M=Zr,Sn). *Superconductor Science and Technology*, **21**: 032002, (2008).

[41] X. Wang, A. Dibos, and J.Z. Wu. Weakening thickness dependence of critical current density in $YBa_2Cu_3O_{7-x}$ films using nanotube pore insertion. *Physical Review B*, **77**: 144525, (2008).

[42] J.Z. Liu, Y.X. Jia, R.N. Shelton, and M.J. Fluss. In-plane anisotropy of the interaction between vortex and twin boundary in $YBa_2Cu_3O_7$ single crystals. *Physical Review Letters*, **66**: 1354, (1991).

[43] G. Blatter, J. Rhyner, and V.M. Vinokur. Vortex pinning by twin boundaries in copper oxide superconductors. *Physical Review B*, **43**: 7826, (1991).

[44] H. Safar, J.Y. Coulter, M.P. Maley, S. Foltyn, P. Arendt, X.D. Wu, and J.O. Willis. Anisotropy and Lorentz-force dependene of the critical currents in $YBa_2Cu_3O_{7-x}$ thick films deposited on nickel-alloy substrates. *Physical Review B*, **52**: R9875, (1995).

[45] A. Diaz, L. Mechin, P. Berghuis, and J.E. Evetts. Evidence for vortex pinning by dislocations in $YBa_2Cu_3O_{7-x}$ low-angle grain boundaries. *Physical Review Letters*, **80**: 3855, (1998).

[46] H. Yamasaki, Y. Nakagawa, A. Sawa, H. Obara, and K. Develos. Flux pinning effects of twin boundaries studied with unidirectionally twined YBCO films. *Physica C*, **372**: 1885, (2002).

[47] J.M. Huijbregtse, F.C. Klaassen, A. Szepielow, J.H. Rector, B. Dam, R. Griessen, B.J. Kooi, and J.Th.M. de Hosson. Vortex pinning by natural defects in thin films of $YBa_2Cu_3O_{7-x}$. *Superconductor Science and Technology*, **15**: 395, (2002).

[48] A. Palau, T. Puig, J. Gutierrez, X. Obradors, and F. de la Cruz. Pinning regimes of grain boundary vortices in $YBa_2Cu_3O_{7-x}$ coated conductors. *Physical Review B*, **73**: 132508, (2006).

[49] S.R. Foltyn, L. Civale, J.L. Macmanus-Driscoll, Q.X. Jia, B. Maiorov, H. Wang, and M. Maley. Materials science challenges for high-temperature superconducting wire. *Nature Materials*, **6**: 631, (2007).

[50] J. Gutierrez, B. Maiorov, T. Puig, J. Gazquez, N. Roma, H. Wang, F. Sandiumenge, and X. Obradors. The role of stacking faults in the critical current density of mod films through a thickness dependence study. *Superconductor Science and Technology*, **22**: 015022, (2009).

[51] H. Yamasaki, K. Ohki, I. Yamaguchi, M. Sohma, W. Kondo, H. Matsui, T. Manabe, and T. Kumagai. Strong flux pinning due to dislocations associated with stacking faults in $YBa_2Cu_3O_{7-x}$ thin films prepared by fluorine-free metal organic deposition. *Superconductor Science and Technology*, **23**: 105004, (2010).

[52] V.F. Solovyov, H.J. Wiesmann, L. Wu, Q. Li, L.D. Cooley, M. Suenaga, B. Maiorov, and L. Civale. High critical currents by isotropic magnetic-flux-pinning centres in a 3μm-thick $YBa_2Cu_3O_7$ superconducting coated conductor. *Superconductor Science and Technology*, **20**: L20, (2007).

[53] P. Mele, K. Matsumoto, T. Horide, A. Ichinose, M. Mukaida, Y. Yoshida, and S. Horii. Insertion of nanoparticulate artificial centres in $YBa_2Cu_3O_{7-x}$ films by laser ablation of a Y_2O_3-surface modified target. *Superconductor Science and Technology*, **20**: 616, (2007).

[54] P. Mele, K. Matsumoto, T. Horide, A. Ichinose, M. Mukaida, Y. Yoshida, S. Horii, and R. Kita. Incorporation of double artificial pinning centers in $YBa_2Cu_3O_{7-x}$ films. *Superconductor Science and Technology*, **21**: 015019, (2008).

[55] B. Maiorov, S.A. Baily, H. Zhou, O. Ogurlu, J.A. Kennison, P.C. Dowden, T.G. Holesinger, S.R. Foltyn, and L. Cival. Synergetic combination of different types of defect to optimize pinning landscape using $BaZrO_3$-doped $YBa_2Cu_3O_7$. *Nature Materials*, **8**: 398, (2009).

[56] T. Puig and X. Obradors. Anisotropic vortex plasticity in the liquid state of $YBa_2Cu_3O_7$: Evidence for quenched c-axis vortex correlation length. *Physical Review Letters*, **84**: 1571, (2000).

[57] C.P. Bean. Magnetization of hard superconductors. *Physical Review Letters*, **8**: 250, (1962).

[58] D.X. Chen, C. Prados, E. Pardo, A. Sanchez, and A. Hernando. Transverse demagnetizing factors of long rectangular bars: I. analytical expressions for extreme values of susceptibility. *Journal of Applied Physics*, **91**: 5254, (2002).

[59] E. Pardo, A. Sanchez, and D.X. Chen. Transverse demagnetizing factors of long rectangular bars: II. numerical calculations for arbitrary susceptibility. *Journal of Applied Physics*, **91**: 5260, (2002).

[60] C.P. Bean. Magnetization of high-field superconductors. *Reviews of Modern Physics*, **36**: 31, (1964).

[61] D. X. Chen and R. B. Goldfarb. Kim model for magnetization of type-II superconductors. *Journal of Applied Physics*, **66**: 2489, (1989).

[62] A. Sanchez and C. Navau. Critical-current density from magnetization loops of finite high-T_c superconductors. *Superconductor Science and Technology*, **14**: 444, (2001).

[63] D.R. Nelson. Vortex entanglement in high-T_c superconductors. *Physical Review Letters*, **60**: 1973, (1988).

[64] P. Anderson. Theory of flux creep in hard superconductors. *Physical Review Letters*, **9**: 309, (1962).

[65] A.P. Malozemoff. Flux creep in high temperature superconductors. *Physica C*, **185**: 264, (1991).

[66] J.R. Thompson, Yang Ren Sun, L. Civale, A.P. Malozemoff, M.W. McElfresh, A.D. Marwick, and F. Holtzberg. Effect of flux creep on the temperature dependence of the current density in Y-Ba-Cu-O crystals. *Physical Review B*, **47**: 14440, (1993).

[67] E.H. Brandt. Susceptibility of superconductor disks and rings with and without flux creep. *Physical Review B*, **55**: 14513, (1997).

[68] M. Feigelman, V. Geshkenbein, A. Larkin, and V. Vinokur. Theory of collective flux creep. *Physical Review Letters*, **63**: 2303, (1989).

[69] L. Civale, B. Maiorov, J.L. MacManus-Driscoll, H. Wang, T.G. Holesinger, S.R. Foltyn, A. Serquis, and P.N. Arendt. Identification of intrinsic ab-plane pinning in $YBa_2Cu_3O_7$ thin films and coated conductors. *IEEE Transactions on Applied Superconductivity*, **15**: 2808, (2005).

[70] M. Dhalle. *Handbook of superconducting materials, Vol. 2: Characterization, Applications and Cryogenics*. Institute of Physics, Publishing Bristol and Philadelphia, 2003.

[71] P.W. Anderson and Y.B. Kim. Hard superconductivity: Theory of the motion of Abrikosov flux lines. *Reviews of Modern Physics*, **36**: 39, (1964).

[72] J.R. Thompson, Y.R. Sun, and F. Holtzberg. Long-term nonlogarithmic magnetic relaxation in single-crystal $YBa_2Cu_3O_7$ superconductors. *Physical Review B*, **44**: 458, (1991).

[73] L. Civale, L. Krusin-Elbaum, J.R. Thompson, R. Wheeler, A.D. Marwick, M.A. Kirk, Y.R. Sun, F. Holtzberg, and C. Feild. Reducing vortex motion in $YBa_2Cu_3O_7$ crystals with splay columnar defects. *Physical Review B*, **50**: 4102, (1994).

[74] G. Blatter, V.B. Geshkenbein, and V.M. Vinokur. Quantum collective creep. *Physical Review Letters*, **66**: 3297, (1991).

[75] L. Fruchter, A.P. Malozemoff, I.A. Campbell, J. Sanchez, M. Konczykowski, R. Griessen, and F. Holtzberg. Low-temperature magnetic relaxation in $YBa_2Cu_3O_{7-x}$: Evidence for quantum tunneling of vortices. *Physical Review B*, **43**: 8709, (1991).

[76] R. Griessen, J.G. Lensink, and H.G. Schnack. Thermally activated flux-motion and quantum tunneling of vortices in high-T_c superconductors. *Physica C*, **185**: 337, (1991).

[77] A.C. Mota, G. Juri, P. Visani, A. Pollini, T. Teruzzi, K. Aupke, and B. Hilti. Flux motion by quantum tunneling. *Physica C*, **185**: 343, (1991).

[78] A.P. Malozemoff and M.P.A. Fisher. Universality in the current decay and flux creep of Y-Ba-Cu-O high-temperature superconductors. *Physical Review B*, **42**: 6784, (1990).

[79] L. Krusin-Elbaum, L. Civale, J.R. Thompson, and C. Feild. Accomodation of vortices to columnar defects: Evidence for large entropic reduction of vortex localization. *Physical Review B*, **53**: 11744, (1996).

[80] L. Civale, G. Pasquini, P. Levy, G. Nieva, D. Casa, and H. Lanza. Time relaxation of persistent currents in $YBa_2Cu_3O_{7-x}$ crystals with columnar defects. *Physica C*, **263**: 389, (1996).

[81] J.R. Thompson, L. Krusin-Elbaum, L. Civale, G. Blatter, and C. Feild. Superfast vortex creep in $YBa_2Cu_3O_{7-x}$ crystals with columnar defects: evidence for variable-range vortex hopping. *Physical Review Letters*, **78**: 3181, (1997).

[82] D. Niebieskikwiat, L. Civale, C.A. Balseiro, and G. Nieva. Nonglassy relaxation by double kinks in $YBa_2Cu_3O_{7-x}$ with columnar defects. *Physical Review B*, **61**: 7135, (2000).

[83] M.V. Feigel'man and V.M. Vinokur. Thermal fluctuations of vortex lines, pinning, and creep in high-T_c superconductors. *Physical Review B*, **41**: 8986, (1990).

[84] L. Civale, L. Krusin-Elbaum, J.R. Thompson, and F. Holtzberg. Collective creep of vortex bundles in $YBa_2Cu_3O_7$ crystals. *Physical Review B*, **50**: 7188, (1994).

[85] J.R. Thompson, Y.R. Sun, D.K. Christen, L. Civale, A.D. Marwick, and F. Holtzberg. Observed regimes of collective flux creep in proton-irradiated, single crystal Y-Ba-Cu-O: Dependence on current density. *Physical Review B*, **49**: 13287, (1994).

[86] D. Dimos, P. Chaudhari, J. Mannhart, and F. LeGoues. Orientation dependence of grain-boundary critical currents in $YBa_2Cu_3O_{7-x}$ bicrystals. *Physical Review Letters*, **61**: 219, (1988).

[87] D. Dimos, P. Chaudhari, and J. Mannhart. Superconducting transport properties of grain boundaries in $YBa_2Cu_3O_7$ bicrystals. *Physical Review B*, **41**: 4038, (1990).

[88] H. Hilgenkamp and J. Mannhart. Grain boundaries in high-T_c superconductors. *Reviews of Modern Physics*, **74**: 485, (2002).

[89] B.A. Joyce. Molecular beam epitaxy. *Reports on Progress in Physics*, **48**: 1637, (1985).

[90] R. Eason. *Pulsed Laser Deposition of Thin Films. Applications-LED growh of Functional Materials*. John Wiley and Sons inc. Publication, (2007).

[91] E. Kuphal. Liquid phase epitaxy. *Applied Physics A. Solid and Surfaces*, **52**: 380, (1991).

[92] H. Yamane, H. Masumoto, T. Hirai, H. Iwasaki, K. Watanabe, N. Kobayashi, and Y. Muto. Y-Ba-Cu-O superconduction films prepared on $SrTiO_3$ substrates by chemical vapor deposition. *Applied Physics Letters*, **53**: 1948, (1988).

[93] X. Obradors, T. Puig, A. Pomar, F. Sandiumenge, S. Piñol, N. Mestres, O. Castaño, M. Coll, A. Cavallaro, A. Palau, J. Gazquez, J.C. Gonzalez, J. Gutierrez, N. Roma, S. Ricart, J.M. Moreto, M.D. Rossell, and G.van Tendeloo. Chemical solution deposition: a path towards low cost coated conductors. *Superconductor Science and Technology*, **17**: 1055, (2004).

[94] X. Obradors, T. Puig, S. Ricart, M. Coll, J. Gazquez, A. Palau, and X. Granados. Growth, nanostructure and vortex pinning in superconducting $YBa_2Cu_3O_{7-x}$ thin films based on trifluoroacetate solutions. *Superconductor Science and Technology*, **25**: 123001, (2012).

[95] A. Gupta, R. Jagannathan, E.I. Cooper, E.A. Giess, J.I. Landman, and B.W. Hussey. Superconducing oxide films with high transition temperature prepared from metal trifluoroacetate precursors. *Applied Physics Letters*, **52**: 2077, (1988).

[96] A. Llordes, K. Zalamova, S. Ricart, A. Palau, A. Pomar, T. Puig, A. Hardy, M.K. Van Bael, and X. Obradors. Evolution of metal-trifluoroacetate precursors in the

thermal decomposition toward high-performance $YBa_2Cu_3O_{7-x}$ superconducting films. *Chemistry of Materials*, **22**: 1686, (2010).

[97] E.D. Specht, C.J. Sparks, A.G. Dhere, J. Brynestad, O.B. Cavin, D.M. Kroeger, and H.A. Oye. Effect of oxygen pressure on the orthorombic-tetragonal transition in the high-temperature superconductor $YBa_2Cu_3O_x$. *Physical Review B*, **37**: 7426, (1988).

[98] C.J. Jou and J. Washburn. Formation of coherent twins in $YBa_2Cu_3O_{7-x}$ superconductors. *Journal of Materials Research*, **4**: 795, (1989).

[99] I. Takashi and S. Okazaki. Pushing the limits of lithography. *Nature - insight review articles*, **406**: 1027, (2000).

[100] R.F. Luccas. *Estudio Energetico de Redes de Vortices Nanoestructuradas en $YBa_2Cu_3O_{7-x}$ mediante Decoracion Magnetica*. PhD thesis, Universitat Autonoma de Barcelona, (2011).

[101] R.F.W. Pease. Electron beam lithography. *Contemporary Physics*, **22**: 265, (1981).

[102] C. Vieu, F. Carcenac, A. PÃ©pin, Y. Chen, M. Mejias, A. Lebib, L. Manin-Ferlazzo, L. Couraud, and H. Launois. Electron beam lithography: resolution limits and applications. *Applied Surface Science*, **164**: 111, (2000).

[103] W.F. van Dorp and C.W. Hagen. A critical literature review of focused electron beam induced deposition. *Journal of Applied Physics*, **104**: 081301, (2008).

[104] I. Utke, P. Hoffmann, and J. Melngailis. Gas-assisted focused electron beam and ion beam processing and fabrication. *Journal of Vacuum Science and Technology B*, **26**: 1197, (2008).

[105] W.F. van Dorp, B. van Someren, C.W. Hagen, and P. Kruit. Approaching the resolution limit of nanometer-scale electron beam-induced deposition. *NanoLetters*, **5**: 1303, (2005).

[106] A. Llordes. *Superconducting nanocomposite films grown by chemical solution deposition: synthesis, microstructure and properties*. PhD thesis, Universitat Autonoma de Barcelona, (2010).

[107] R. Guzman. *In-depth investigation of the origin, evolution and interaction of structural defects in YBCO nanocomposite thin films*. PhD thesis, Universitat Autonoma de Barcelona, (2013).

[108] Y. Yeshurun, A.P. Malozemoff, and A. Shaulov. Magnetic relaxation in high-temperature superconductors. *Reviews of Modern Physics*, **68**: 911, (1996).

[109] J.W. Ekin, T.M. Larson, N.F. Bergren, A.J. Nelson, A.B. Swartzlander, L.L. Kazmerski, A.J. Panson, and B.A. Blankenship. High T_c superconductor/noble-metal contacts with surface resistivities in the 10x10cm^2 range. *Applied Physics Letters*, **52**: 1819, (1988).

[110] P.J. Hirst and R.G. Humphreys. *Handbook of superconducting materials, Vol. 1: Superconductivity, Materials and Processes*. Institute of Physics, Publishing Bristol and Philadelphia, 2003.

[111] J.Z. Sun, C.B. Eom, B. Lairson, J.C. Bravman, and T.H. Geballe. Magnetic relaxation, current-voltage characteristics, and possible dissipation mechanisms for high-T_c superconducting thin films of Y-Ba-Cu-O. *Physical Review B*, **43**: 3002, (1991).

[112] W. Gong, H. Li, Z. Zhao, and J. Chen. Ultrafine particles of Fe, Co and Ni ferromagnetic metals. *Journal of Applied Physics*, **69**: 5119, (1991).

[113] U. Essmann and H. Trauble. The direct observation of individual flux lines in type ii superconductors. *Physics Letters*, **8**: 526, (1967).

[114] Y. Fasano, M. Menghini, F. de la Cruz, and G. Nieva. Weak interaction and matching conditions for replicas of vortex lattices. *Physical Review B*, **62**: 15183, (2000).

[115] S. Kang, A. Goyal, J. Li, A.A. Gapud, L. Thompson J.R. Martin, P.M. Heatherly, D.K. Christen, F.A. List, M. Paranthaman, and D.F. Lee. High-performance high-T_c superconducting wires. *Science*, **311**: 1911, (2006).

[116] T.G.N. Babu and J. Koshy. Ba_2GdTaO_6 a ceramic substrate for $YBa_2Cu_3O_{7-x}$ films. *Materials Letters*, **33**: 7, (1997).

[117] J. Gazquez, M. Coll, N. Roma, F. Sandiumenge, T. Puig, and X. Obradors. Structural defects in trifluoroacetate derived $YBa_2Cu_3O_7$ thin films. *Superconductor Science and Technology*, **25**: 065009, (2012).

[118] H.W. Zandbergen, R. Gronsky, K. Wang, and G. Thomas. Structure of CuO_2 double layers in superconducting $YBa_2Cu_3O_7$. *Letters to Nature*, **331**: 596, (1988).

[119] K. Char, M. Lee, R.W. Barton, A.F. Marshall, I. Bozovic, R.H. Hammond, M.R. Beasley, T.H. Geballe, and A. Kapitulnik. Properties of Y-Ba-Cu-O thin films with ordered defect structure: $Y_2Ba_4Cu_8O_{20-x}$. *Physical Review B*, **38**: 384, 1988.

[120] J. Narayan, V.N. Shukla, S.J. Lukasiewicz, N. Biunno, R. Singh, A.F. Schreiner, and S.J. Pennycook. Microstructure and properties of $YBa_2Cu_3O_{7-x}$ superconductors with transitions at 90 and near 290K. *Applied Physics Letters*, **51**: 940, (1987).

[121] A. Llordes, A. Palau, J. Gazquez, M. Coll, R. Vlad, J. Pomar, A. Arbiol, R. Guzman, S. Ye, V. Rouco, F. Sandiumenge, S. Ricart, T. Puig, M. Varela, D. Chateigner, J. Vanacken, J. Gutierrez, V. Moshchalkov, G. Deutscher, C. Magen, and X. Obradors. Nanoscale strain-induced pair suppresion as a vortex-pinning mechanism in high-temperature superconductors. *Nature Materials*, **11**: 329, (2012).

[122] G.K. Williamson and W.H. Hall. X-ray line broadening from filed aluminium and wolfram. *Acta Metallurgia*, **1**: 22, (1953).

[123] Y. Zhu, M. Suenaga, J. Tafto, and D.O. Welch. Variable nature of twin boundaries in $YBa_2Cu_3O_{7-x}$ and its alloys. *Physical Review B*, **44**: 2871, (1991).

[124] F. Sandiumenge, S. Pinol, X. Obradors, E. Snoeck, and C. Roucau. Microstructure of directionally solidified high-critical-current $YBa_2Cu_3O_7$-Y_2BaCuO_5 composites. *Physical Review B*, **50**: 7032, (1994).

[125] R. Guzman, J. Gazquez, V. Rouco, A. Palau, C. Magen, M. Varela, J. Arbiol, X. Obradors, and T. Puig. Strain-driven broken twin boundary coherence in

$YBa_2Cu_3O_{7-x}$ nanocomposite thin films. *Applied Physics Letters*, **102**: 081906, (2013).

[126] W.K. Kwok, S. Fleshler, U. Welp, V.M. Vinokur, J. Downey, G.W. Crabtree, and M.M. Miller. Vortex lattice melting in untwinned and twinned single crystals of $YBa_2Cu_3O_{7-x}$. *Physical Review Letters*, **69**: 3370, (1992).

[127] P.J.M. Woltgens, C. Dekker, J. Swuste, and H.W. Wijn. Superconducting phase of $YBa_2Cu_3O_{7-x}$ films in high magnetic fields: Vortex glass of bose glass. *Physical Review B*, **48**: 16826, (1993).

[128] J.A. Fendrich, W.K. Kwok, J. Giapintzakis, V.M. van der Beek, C.J. andVinokur, S. Fleshler, U. Welp, H.K. Viswanathan, and G.W. Crabtree. Vortex liquid state in an electron irradiated untwined $YBa_2Cu_3O_{7-x}$ crystal. *Physical Review Letters*, **74**: 1210, (1995).

[129] A.M. Petrean, L.M. Paulius, W.K. Kwok, J.A. Fendrich, and G.W. Crabtree. Experimental evidence for the vortex glass phase in untwinned, proton irradiated $YBa_2Cu_3O_{7-x}$. *Physical Review Letters*, **84**: 5852, (2000).

[130] R.J. Olsson, W.K. Kwok, L.M. Paulius, A.M. Petrean, D.J. Hofman, and G.W. Crabtree. Bose glass transition in columnar-defected untwinned $YBa_2Cu_3O_{7-x}$. *Physical Review B*, **65**: 104520, (2002).

[131] D.E. Farrell, J.P. Rice, D.M. Ginsberg, and J.Z. Liu. Experimental evidence of a dimensional crossover in $Y_1Ba_2Cu_3O_{7-x}$. *Physical Review Letters*, **64**: 1573, (1990).

[132] M. Coll, R. Guzman, P. Garces, J. Gazquez, V. Rouco, A. Palau, S. Ye, C. Magen, H. Suo, H. Castro, T. Puig, and X. Obradors. Size-controlled spontaneously segregated Ba_2YTaO_6 nanoparticles in $YBa_2Cu_3O_{7-x}$ nanocomposites by chemical solution deposition. *Superconductor Science and Technology*, page Accepted.

[133] L. Civale, B. Maiorov, A. Serquis, J.O. Willis, J.Y. Coulter, H. Wang, Q.X. Jia, P.N. Arendt, J.L. MacManus-Driscoll, M.P. Maley, and S.R. Foltyn. Angular-dependent vortex pinning mechanisms in $YBa_2Cu_3O_7$ coated conductors and thin films. *Applied Physics Letters*, **84**: 2121, (2004).

[134] L. Civale, B. Maiorov, A. Serquis, J.O. Willis, J.Y. Coulter, H. Wang, Q.X. Jia, P.N. Arendt, M. Jaime, J.L. Macmanus-Driscoll, M.P. Maley, and S.R. Foltyn. Understanding high critical currents in $YBa_2Cu_3O_7$ thin films and coated conductors. *Journal of Low Temperature Physics*, **135**: 87, (2004).

[135] B. Dam, J.M. Huijbregtse, F.C. Klaassen, R.C.F. van der Geest, G. Doornbos, J.H. Rector, A.M. Testa, S. Freisem, J.C. Martinez, B. Stauble-Pumpin, and R. Griessen. Origin of high critical currents in $YBa_2Cu_3O_{7-x}$ superconductin thin films. *Nature*, **399**: 439, (1999).

[136] T. Aytug, M. Paranthaman, K.J. Leonard, P.M. Kang, S. Martin, L. Heatherly, A. Goyal, A.O. Ijaduola, J.R. Thompson, D.K. Christen, R. Meng, I. Rusakova, and C.W. Chu. Analysis of flux pinning in $YBa_2Cu_3O_{7-x}$ films by nanoparticle-modified substrate surfaces. *Physical Review B*, **74**: 184505, (2006).

[137] Y.L. Zuev, D.K. Christen, S.H. Wee, A. Goyal, and S.W. Cook. Near-isotropic performance of intrinsically anisotropic high-temperature superconducting tapes due to self-assembled nanostructures. *Applied Physics Letters*, **93**: 172512, (2008).

[138] A. Palau, E. Bartolome, A. Llordes, T. Puig, and X. Obradors. Isotropic and anisotropic pinning in TFA-grown $YBa_2Cu_3O_{7-x}$ films with $BaZrO_3$ nanoparticles. *Superconductor Science and Technology*, **24**: 125010, (2011).

[139] Y.L. Zuev, D.K. Christen, S.H. Wee, A. Goyal, and S.W. Cook. Near-isotropic performance of intrinsically anisotropic high-temperature superconducting tapes due to self-assembled nanostructures. *Applied Physics Letters*, **93**: 172512, (2008).

[140] T. Aytug, M. Paranthaman, K.J. Leonard, S. Kang, P.M. Martin, L. Heatherly, A. Goyal, A.O. Ijaduola, J.R. Thompson, and D.K. Christen. Analysis of flux pinning in $YBa_2Cu_3O_7$ films by nanoparticle-modified substrate surfaces. *Physical Review B*, **74**: 184505, (2006).

[141] M. Miura, B. Maiorov, S.A. Baily, N. Haberkorn, J.O. Willis, K. Marken, T. Izumi, Y. Shiohara, and L. Civale. Mixed pinning landscape in nanoparticle-introduced $YGdBa_2Cu_3O_y$ films grown by metal organic deposition. *Physical Review B*, **83**: 184519, (2012).

[142] N. Haberkorn, M. Miura, J. Baca, B. Maiorov, I. Usov, P. Dowden, S.R. Foltyn, T.G. Holesinger, J.O. Willis, K.R. Marken, T. Izumi, Y. Shiohara, and L. Civale. High-temperature change of the creep rate in $YBa_2Cu_3O_{7-x}$ films with different pinning landscapes. *Physical Review B*, **85**: 174504, (2012).

[143] J. Plain, T. Puig, F. Sandiumenge, X. Obradors, and J. Rabier. Microstructural influence on critical currents and irreversibility line in melt-textured $YBa_2Cu_3O_{7-x}$ reannealed at high oxygen pressure. *Physical Review B*, **65**: 104526, (2002).

[144] J. Gutierrez. *Vortex pinning and critical currents in $YBa_2Cu_3O_{7-x}$ MOD-TFA thin films and coated conductors*. PhD thesis, Universitat Autonoma de Barcelona, (2008).

[145] J. Gutierrez, T. Puig, and X. Obradors. Anisotropy and strength of vortex pinning centers in $YBa_2Cu_3O_{7-x}$ coated conductors. *Applied Physics Letters*, **90**: 162514, (2007).

[146] T. Puig, J. Gutierrez, A. Pomar, A. Llordes, J. Gazquez, S. Ricart, F. Sandiumenge, and X. Obradors. Vortex pinning in chemical solution nanostructured YBCO films. *Superconductor Science and Technology*, **21**: 034008, (2008).

[147] O. Polat, J.W. Sinclair, Y.L. Zuev, J.R. Thompson, D.K. Christen, S.W. Cook, D. Kumar, Yimin Chen, and V. Selvamanickam. Thickness dependence of magnetic relaxation and e-j characteristics in superconducting (Gd-Y)-Ba-Cu-O films with strong vortex pinning. *Physical Review B*, **84**: 024519, (2011).

[148] G. Deutscher and P.G. de Gennes. A spatial interpretation of emerging superconductivity in lightly doped cupprates. *Comptes Rendus Physique*, **8**: 937, (2007).

[149] G. Deutscher. Origin of weak-link behavior of grain boundaries in superconducting cuprates and pnictides. *Applied Physics Letters*, **96**: 122502, (2010).

[150] N.F. Heinig, R.D. Redwing, J.E. Nordman, and D.C. Larbalestier. Strong to weak coupling transition in low misorientation angle thin film $YBa_2Cu_3O_{7-x}$ bicrystals. *Physical Review B*, **60**: 1409, (1999).

[151] D.C. van der Laan, T.J. Haugan, and P.N. Barnes. Effect of a compressive uniaxial strain on the critical current density of grain boundaries in superconducting $YBa_2Cu_3O_{7-x}$ films. *Physical Review Letters*, **103**: 027005, (2009).

[152] M. Oussena, P.A.J. de Groot, J. Porter, R. Gagnon, and L. Taillefer. Vortex channeling along twin planes in $YBa_2Cu_3O_{7-x}$. *Physical Review B*, **51**: 1389, (1995).

[153] H. Safar, S. Foltyn, H. Kung, M.P. Maley, J.O. Willis, P. Arendt, and X.D. Wu. ab-plane anisotropy of the critical currents in twinned $YBa_2Cu_3O_{7-x}$ superconductors. *Applied Physics Letters*, **68**: 1853, (1996).

[154] A. Palau, J.H. Durrell, J.L. MacManus-Driscoll, S. Harrington, T. Puig, F. Sandiumenge, X. Obradors, and M.G. Blamire. Crossover between channeling and pinning at twin boundaries in $YBa_2Cu_3O_7$ thin films. *Physical Review Letters*, **97**: 257002, (2006).

[155] M. Miura, S.A. Baily, B. Maiorov, L. Civale, J.O. Willis, K. Marken, T. Izumi, K. Tanabe, and Y. Shiohara. Vortex liquid-glass transition up to 60T in nano-engineered coated conductors grown by metal organic deposition. *Applied Physics Letters*, **96**: 072506, (2010).

[156] A.El. Tahan, G. Jakob, D. Miu, I. Ivan, P. Badica, and L. Miu. Vortex creep crossover in YBCO/PrBCO superlattices during standard magnetization relaxation measurements. *Superconductor Science and Technology*, **24**: 045014, (2011).

[157] R.P. Feynman, R.B. Leighton, and M. Sands. *The Feynman Lectures on Physics - Mainly electromagnetism and matter*. Addison-Wesley Publishing Company, INC, (1964).

[158] J.E. Villegas, S. Savel'ev, F. Nori, E.M. Gonzalez, J.V. Anguita, R. Garcia, and J.L. Vicent. A superconducting reversible rectifier that controls the motion of magnetic flux quanta. *Science*, **302**: 1188, (2003).

[159] B.L.T. Plourde. Nanostructured superconductors with asymmetric pinning potentials: Vortex ratchets. *IEEE Transaction on Applied Superconductivity*, **19**: 3698, (2009).

[160] C.C. de Souza Silva, J. Van de Vondel, M. Morelle, and V.V. Moshchalkov. Controlled multiple reversals of a ratchet effect. *Nature*, **440**: 651, (2006).

[161] S. Ooi, T. Mochiku, and K. Hirata. Vortex ratchet effect in singre-crystal films of $Bi_2Sr_2Ca_3Cu_2O_{8+y}$. *Physica C*, **468**: 1291, (2008).

[162] J. Villegas, E. Gonzalez, M. Gonzalez, J. Anguita, and J. Vicent. Experimental ratchet effect in superconducting films with periodic arrays of asymmetric potentials. *Physical Review B*, **71**: 024519, (2005).

[163] W. Gillijns, A. Silhanek, V. Moshchalkov, and C. Reichhardt. Origin of reversed vortex ratchet motion. *Physical Review Letters*, **99**: 247002, (2007).

[164] L. Dinis, E. Gonzalez, J. Anguita, J. Parrondo, and J. Vicent. Current reversal in collective ratchets induced by lattice instability. *Physical Review B*, **76**: 212507, (2007).

[165] D. Perez de Lara, A. Alija, E.M. Gonzalez, M. Velez, J.I. Martin, and J.L. Vicent. Vortex ratchet reversal at fractional matching fields in kagomelike array with symmetric pinning centers. *Physical Review B*, **82**: 174503, (2010).

[166] A.V. Silhanek, W. Gillijns, V.V. Moshchalkov, V. Metlushko, F. Gozzini, B. Ilic, W.C. Uhlig, and J. Unguris. Manipulation of the vortex motion in nanostructured ferromagnetic/superconductor hybrids. *Applied Physics Letters*, **90**: 182501, (2007).

[167] C.C. de Souza Silva, A.V. Silhanek, J. Van de Vondel, W. Gillijns, V. Metlushko, B. Ilic, and V.V. Moschalkov. Dipole-induced vortex ratchets in superconducting films with arrays of micromagnets. *Physical Review Letters*, **98**: 117005, (2007).

[168] B. Plourde, D. Van Harlingen, N. Saha, R. Besseling, M. Hesselberth, and P. Kes. Vortex distributions near surface steps observed by scanning squid microscopy. *Physical Review B*, **66**: 054529, (2002).

[169] J.R. Clem and K.K. Berggren. Geometry-dependent critical currents in superconducting nanocircuits. *Physical Review B*, **84**: 174510, (2011).

[170] H.L. Hortensius, E.F.C. Driessen, T.M. Klapwijk, K.K. Berggren, and J.R. Clem. Critical-current reduction in thin superconducting wires due to current crowding. *Applied Physics Letters*, **100**: 182602, (2012).

[171] J. He, N. Harada, H. Naitou, H. Asada, T. Ishibashi, and T.H. Johansen. Flux pinning characteristics of superconducting Nb films with asymmetric artificial pinning centers introduced by nanofabrication. *Physica C*, **468**: 1661, (2008).

[172] C. Olson, C. Reichhardt, B. Janko, and F. Nori. Collective interaction-driven ratchet for transporting flux quanta. *Physical Review Letters*, **87**: 177002, (2001).

[173] A. Sanchez, C. Navau, N. Del-Valle, D.X. Chen, and J.R. Clem. Self-fields in thin superconducting tapes: Implications for the thickness effect in coated conductors. *Applied Physics Letters*, **96**: 072510, (2010).

[174] A. Sanchez, N. Del-Valle, C. Navau, and D.X. Chen. Influence of magnetic substrate in the transport critical current of superconducting tapes. *Applied Physics Letters*, **97**: 072504, (2010).

[175] N. Del-Valle, C. Navau, A. Sanchez, and R.B. Dinner. Transport critical-current density of superconducting thin films with hysteretic ferromagnetic dots. *AIP Advances*, **2**: 022166, (2012).

[176] Y.B. Kim, C.F. Hempstead, and A.R. Strnad. Critical persistent currents in hard superconductors. *Physical Review Letters*, **9**: 306, (1962).

[177] A. Palau, C. Monton, V. Rouco, X. Obradors, and T. Puig. Guided vortex motion in $YBa_2Cu_3O_{7-x}$ thin films with collective ratchet pinning potentials. *Physical Review B*, **85**: 012502, (2012).

[178] A.I. Buzdin. Proximity effects in superconductor-ferromagnet heterostructures. *Review of Modern Physics*, **77**: 935, (2005).

[179] I.F. Lyuksyutov and V.L. Pokrovsky. Ferromagnet-superconductor hybrids. *Advances in Physics*, **54**: 67, (2005).

[180] M.J. Van Bael, K. Temst, V.V. Moschalkov, and Y. Bruynseraede. Magnetic properties of submicron co islands and their use as artificial pinning centers. *Physical Review B*, **59**: 14674, (1999).

[181] D.J. Morgan and J.B. Ketterson. Asymmetric flux pinning in a regular array of magnetic dipoles. *Physical Review Letters*, **80**: 3614, (1998).

[182] M.J. Van Bael, M. Lange, S. Raedts, V.V. Moshchalkov, A.N. Grigorenko, and S.J. Bending. Local visualization of asymmetric flux pinning by magnetic dots with perpendicular magnetization. *Physical Review B*, **68**: 014509, (2003).

[183] A. Palau, H. Parvaneh, N.A. Stelmashenko, H. Wang, J.L. Macmanus-Driscoll, and M.G. Blamire. Hysteretic vortex pinning in superconductor-ferromagnet nanocomposites. *Physical Review Letters*, **98**: 117003, (2007).

[184] C. Visani, P.J. Metaxas, A. Collaudin, B. Calvet, R. Bernard, J. Briatico, C. Deranlot, K. Bouzehouane, and J.E. Villegas. Hysteretic magnetic pinning and reversible resistance switching in high-temperature superconductor/ferromagnet multilayers. *Physical Review B*, **84**: 054539, (2011).

[185] M. Lange, M.J. Van Bael, Y. Bruynseraede, and V.V. Moshchalkov. Nanoengineered magnetic-field-induced superconductivity. *Physical Review Letters*, **90**: 197006, (2003).

[186] I.F. Lyuksyutov. Magnetic nanorod-superconductor hybrids. *Journal of Superconductivity and Novel Magnetism*, **23**: 1047, (2010).

[187] K. Kim, A.E. Ozmetin, D.G. Naugle, and I.F. Lyuksyutov. Flux pinning with a magnetic nanorod array. *Applied Physics Letters*, **97**: 042501, (2010).

[188] Z. Ye, I.F. Lyuksyutov, W. Wu, and D.G. Naugle. Strongly anisotropic flux pinning in superconducting $Pb_{82}Bi_{18}$ thin films covered by periodic ferromagnet stripes. *Superconductor Science and Technology*, **24**: 024011, (2011).

[189] K. Kim, I. Lyuksyutov, and D.G. Naugle. Magnetic nanorod-superconductor hybrid near the superconducting transition temperature. *Superconductor Science and Technology*, **24**: 024013, (2011).

[190] Z. Ye, I.F. Lyuksyutov, W. Wu, and D.G. Naugle. Superconducting properties of $Pb_{82}Bi_{18}$ films controlled by ferromagnetic nanowire arrays. *Superconductor Science and Technology*, **24**: 024019, (2011).

[191] Z. Wei, Z. Ye, K.D.D. Rathnayaka, I.F. Lyuksyutov, W. Wu, and D.G. Naugle. Superconductivity of a sn film controlled by and array of co nanowires. *Physica C*, **479**: 41, (2012).

[192] E. Bartolome, A. Palau, J. Gutierrez, X. Granados, A. Pomar, T. Puig, X. Obradors, V. Cambel, J. Soltys, D. Gregusova, D.X. Chen, and A. Sanchez. Artificial magnetic granularity effects on patterned epitaxial $YBa_2Cu_3O_{7-x}$ thin films. *Physical Review B*, **76**: 094508, (2006).

[193] M. McElfresh, S. Li, and R. Sager. *Effects of Magnetid Field Uniformity on the Measurement of Superconducting Samples*. Quantum Design.

[194] A. Palau, T. Puig, X. Obradors, E. Pardo, C. Navau, A. Sanchez, A. Usoskin, H.C. Freyhardt, L. Fernandez, B. Holzapfel, and R. Feenstra. Simultaneous inductive determination of grain and intergrain critical current densities of $YBa_2Cu_3O_{7-x}$ coated conductors. *Applied Physics Letters*, **84**: 230, (2004).

[195] A. Sanchez and C. Navau. Magnetic properties of finite superconducting cylinders. i. uniform applied field. *Physical Review B*, **64**: 214506, (2001).

[196] G. Via. *Modeling the response of thin superconductors to applied magnetic fields and currents*. PhD thesis, Universitat Autonoma de Barcelona, (2013).

Nomenclature

	Exponent of the log-log $J_c(H_a)$ representation
	Anisotropic Parameter
$_{eff}$	Effective Anisotropic Parameter
	Penetration Depth
$_{ab}$	Penetration Depth along the ab-plane
$_{c}$	Penetration Depth along the c-axis
μ	Regimen-Dependent Exponent
$_0$	Flux Quantum
ρ	Resistivity
θ	Angle between the c-axis and the applied magnetic field
ε	Anisotropic Parameter
	Coherence lenght
$_{ab}$	Coherence Length along the ab-plane
$_{c}$	Coherence Length along the c-axis
A	Crossection of the bridge
AFM	Atomic Force Microscopy
APC	Artificial Pinning Center
AR	Aspect Ratio
B	Magnetic Field Induction
B0	Bridge Oriented 0^o with the Substrate Edges
B45	Bridge Oriented 45^o with the Substrate Edges
BYTO	Ba_2YTaO_6

BZO	$BaZrO_3$
CC	Coated Conductor
CSD	Chemical Solution Deposition
D	Dimension
DK	Double Kink
E	Electric Field
E_c	Electric Field Criterion
F_L	Lorentz Force
F_p	Pinning Force
F_p^{aniso}	Anisotropic Pinning Force
F_p^{iso}	Isotropic Pinning Force
FEBID	Focused Electron Bean Induced Deposition
FEBL	Focused Electron Bean Lithography
FIB	Focused Ion Bean
FM	Ferromagnetic
H^*	Full Penetration Field
H^+	Magnetic Field Transition from single-vortex pinning to vortex-vortex interactions
H_a	Applied Magnetic Field
H_{c1}	Lower Critical Field
H_{c2}	Upper Critical Field
H_{coher}	Cohercitive Magnetic Field of a Ferromagnet
H_c	Critical Field
H_{eff}	Effective Magnetic Field
H_{irr}	Irreversibility Magnetic Field
H_{local}	Local Magnetic Field
$H_{local}^{YBCO\ AR}$	Local Magnetic Field of the YBCO/AR system

$H_{local}{}^{YBCO\ A}$	Local Magnetic Field of the YBCO/A System
H_{mag}	Magnetization Field
H_{max}	Maximum Applied Magnetic Field
H_r	Return Magnetic Field
$H_r{}^{FM}$	Return Magnetic Field of the Ferromagnet
$H_r{}^{grain}$	Return Magnetic Field of a Grain
$H_r{}^{SC}$	Return Magnetic Field of the Superconductor
$H_{Sat}{}^{FM}$	Saturating Field of a Ferromagnet
HAADF	High Annular Angle Dark Field
HTS	High critical-Temperature Superconductor
I	Electrical Current
I_c	Critical Current
I_{max}	Maximum Applied Electrical Current
ICMAB	Institut de Ciencia de Materials de Barcelona
IL	Irreversibility Line
J	Current Density
J^+	Positive Current Density
J^-	Negative Current Density
J_c	Critical Current Density
$J_c{}^+$	Positive Critical Current Density
$J_c{}^-$	Negative Critical Current Density
$J_c{}^{aniso-strong}$	Anisotropic Critical Current Density
$J_c{}^{iso-strong}$	Isotropic-Strong Critical Current Density contribution
$J_c{}^{iso-weak}$	Isotropic-Weak Critical Current Density contribution
$J_c{}^{iso}$	Isotropic Critical Current Density
$J_c{}^{sf}$	Critical Current Density at Self Field

J_c^{strong}	Strong contribution of the Critical Current Density
$J_c^{str}(0)$	Strong contribution of the Critical Current Density at T=0K
J_c^{weak}	Weak contribution of the Critical Current Density
$J_c^{wk}(0)$	Weak contribution of the Critical Current Density at T=0K
J_c^{ZFC}	Critical Current Density after a Zero Field Cool Process
K_B	Boltzman constant
l	Bridge Length
LAADF	Low Annular Angle Dark Field
LAO	$LaAlO_3$
LTS	Low critical-Temperature Superconductor
M	Magnetization
M^{grain}	Magnetization of a Grain
M^{sat}	Saturated Magnetization
MOKE	Magneto Optical Kerr Effect
n	Flux Creep Exponent
PLD	Pulsed Laser Deposition
PMMA	Positive Polymethyl Metacrylate Resist
PPMS	Physical Property Measurement System
R_{grain}	Grain Radius
SC	Superconductor
SEM	Scanning Electron Microscopy
SF	Stacking Fault
SQUID	Superconducting Quantum Interference Device
T	Temperature
t	Time
T^*, T_0	Characteristic Vortex Energies

T^{cross}	Crossover Temperature from Elastic Creep to Plastic Creep
$T_{Curie}{}^{Co}$	Curie Temperature of Cobalt
T_c	Critical Temperature
t_{eff}	Characteristic Time
T_{irr}	Irreversibility Temperature
t_{irr}	Reduced irreversibility temperature
t_r	Reduced Temperature
t_s	Sample Thickness
TAFF	Thermal Activation Flux Flow
TB	Twin Boundary
TEM	Transmission Electron Microscopy
TFA	Trifluoroacetate Route
U	Activation Energy
U_0	Barrier Height
UAB	Universitat Autonoma de Barcelona
V	Voltage Drop
w, W	Bridge Width
Y248	$Y_2Ba_4Cu_8O_{16}$
YBCO	$YBa_2Cu_3O_{7-x}$
YSZ	Yttria Stabilized Zirconium Oxide Single Crystal
ZFC	Zero Field Cool